UNIVERSIDAD COMPLUTENSE DE MADRID
FACULTAD DE CIENCIAS FÍSICAS
Departamento de Estructura de la Materia, Física Térmica y Electrónica

TESIS DOCTORAL
Observations of VHE emission from blazars at cosmological distances

Observaciones de la emisión en muy altas energías de blazars a distancias cosmológicas

MEMORIA PARA OPTAR AL GRADO DE DOCTOR

PRESENTADA POR

Mireia Nievas Rosillo

Directores

José Luis Contreras González
Abelardo Moralejo Olaizola

Madrid, 2019

UNIVERSIDAD COMPLUTENSE DE MADRID

FACULTAD DE CIENCIAS FÍSICAS

Dpto. Estructura de la Materia, Física Térmica y Electrónica

TESIS DOCTORAL

Observaciones de la emisión en muy altas energías de blazars a distancias cosmológicas

MEMORIA PARA OPTAR AL GRADO DE DOCTOR
PRESENTADA POR

Mireia Nievas Rosillo

DIRECTORES

José Luis Contreras González
Abelardo Moralejo Olaizola

Madrid, Junio 2018

Observations of VHE emission from Blazars at Cosmological Distances

Observaciones de la emisión en muy altas energías de blazars a distancias cosmológicas

Mireia Nievas Rosillo

Universidad Complutense de Madrid

Dpto. Estructura de la Materia, Física Térmica y Electrónica

Thesis advisors

Dr. José Luis Contreras González
Dr. Abelardo Moralejo Olaizola

A Thesis submitted for the degree of

Doctor of Philosophy

June 2018

I hereby declare that I am the sole author of this thesis.

The data presented in this thesis are the property of the MAGIC collaboration when not otherwise stated.

Mireia Nievas Rosillo
Madrid, June 2018

I authorize the Universidad Complutense de Madrid to lend this thesis to other institutions or individuals for the purpose of scholarly research.

Mireia Nievas Rosillo
Madrid, June 2018

I dedicate this thesis to
my parents Paco and Paquita,
my sister Irene,
and my partner Marta

Acknowledgements

I want to begin this section by expressing my gratitude to my supervisor José Luis Contreras for his patience, guidance and support, not only professional but also personal. I owe him the opportunity to be part of the UCM group and his always interesting and novel ideas and comments have been essential to bring this thesis to a successful end. I also thank my co-supervisor, Abelardo Moralejo for all projects in which we have collaborated, for his help in the development of the EBL part and for all I learned from him. I want also to acknowledge Jaime Zamorano, a friend, an inspiration and an endless source of ideas during all these years. I really had a good time designing all these little prototypes to measure the sky brightness.

With special thanks to all the present members of Grupo de Altas Energías, my second family during these years: Maria Victoria, Fernando, Juan Abel, Marcos, Luis Ángel, David, Alberto, Pablo, Dani, Jaime, Daniel, John, Lab and Valeria. I do not forget my past (and in several cases also future) colleagues from the group: Simon, Tarek, Konstancja, Irene and Diego. Being a part of the GAE family has greatly enriched my PhD experience.

I also want to praise the MAGIC collaboration, for running such an impressive facility and offering me a great work environment to develop my research. I wish the *magicians* all the success and great discoveries that are still to come. Particular thanks to the MAGIC colleagues I have had the opportunity to met or work with. In particular, I want to acknowledge Julian Sitarek, who has been like my third supervisor during all these years and for giving my the chance to collaborate in the development of MAGIC software and the B0218+357 project. I also thank Pepa Becerra, for being the best host during my stay at the NASA's Goddard Space Flight Center in Maryland and for been such a wonderful workmate in the PKS 1441+25 paper. I want to extend my gratitude to the rest of the team: Elisa Prandini, Elina Lindfors, Jezabel Rodríguez, Núria Torres, Alba Fernández, Marina Manganaro, Dijana Dominis Monica Vázquez, Gaia Vanzo, Leyre Nogués, Marlene Doert, Giovana Pedaletti, Elena Moretti, Alicia López, Daniel Mazin, Giacomo Bonnoli, Michele Doro, Martin Will, Père Munar, Pierre Colin, Juan Cortina, Antonio Stamerra, Tomislav Terzić, David Paneque, Fabrizio Tavecchio, Pratik Majumdar, Dario Hrupec, etc.

This work would not have been possible without the funding of the Ministery of Education (MECD) through the grant 'Formación del Profesorado Universitario'

FPU13/00618. I also acknowledge the national projects FPA-2010-22056-C06-06, FPA 2012-36668, FPA2015-68378-P and FPA2015-69210-C6-3-R for funding my participation in national and international conferences.

I leave these final words for my family, to remark all the love and support during all these years. This thesis is dedicated to all of them, in particular to my parents, Paco and Paquita, my sister Irene and my partner Marta. Thank you.

Contents

I Introduction to γ-ray Astronomy 3

Appendices

Abstract

Observations of VHE emission from Blazars at Cosmological Distances

Mireia Nievas Rosillo

Since the accidental discovery in 1909 by Fath of rare and intense emission lines in the optical spectra of the “spiral nebulae”, the study of the active galactic nuclei nature has been the subject of intense research. Today we think that these violent structures, found in the center of some galaxies, are powered by a very massive black hole of often more than $10^8\,\mathrm{M}_\odot$. They are capable of sustaining very large luminosities of, up to $10^{15}\,\mathrm{L}_\odot$, based solely on an efficient accretion mechanism. It is not uncommon to see collimated jets extending perpendicularly to the accretion disk to distances equivalent to the size of the host galaxy, with intense emission across the entire electromagnetic spectrum. Active galactic nuclei are also extreme particle accelerators, but it is not clear where and how exactly this process takes place. The accelerated charged particles can in turn emit non-thermal radiation via several mechanisms, which can be detected from radio to γ-rays.

This thesis is focused on a particular type of active galactic nucleus known as blazar. Blazars are radio-loud sources with powerful jets oriented in the direction of the observer. This orientation, together with the ultra-relativistic nature of the charged particles found in the plasmas that are immerse in the blazar jet , causes an amplification due to Doppler effect of the emitted radiation. The escaping photons often have energies entering the domain of very high energy (VHE, $E > 100\,\mathrm{GeV}$) γ-rays and can be detected with ground-based Imaging Atmospheric Cherenkov Telescopes (IACTs) such as MAGIC.

Three AGNs have been studied among the $\sim$ 70 blazars known in VHE γ-rays. They are the two most distant flat spectrum radio quasar, B0218+357 and PKS 1441+25 and the most distant BL Lac ever detected with IACTs: PKS 1424+240. The first one stands up because of its uniqueness as the first and only strongly gravitationally lensed VHE blazar. PKS 1441+25 is unique due to the long-lasting flare in VHE that took place in 2015, the good quality of the reconstructed spectrum and the elegant and simple interpretation of the development of the emission with time. In both cases, the VHE emission is understood as being produced in a plasma filled with ultra-relativistic electrons which moves across the jet and can eventually escape the intrinsic γ-ray shroud generated by the broad line region of the quasar.

This region is a source of intense low energy radiation which can interact with γ-rays through pair production. PKS 1424+240 has also been included to investigate its intriguing spectrum, used in the past as evidence of hadronic emission processes taking place in the jet and alternative cosmic γ-ray propagation models and the generation of hypothetical secondary particles. In the three cases, we analyzed their VHE γ-ray emission in the context of multi-wavelength campaigns. The development of the VHE flares was correlated with the behavior of each source in other wavelength bands, finding interesting trends for PKS 1441+25, explained as a coherent emission from a single emitting region. Furthermore, we interpreted the broadband spectra in terms of leptonic models, including external Compton contributions for B0218+357 and PKS 1441+25. We concluded that inverse Compton emission models can successfully explain the observed blazar spectra and their multi-wavelength variability.

Finally, we have combined more than 300 h of MAGIC observations of 12 different blazars together with contemporaneous Fermi-LAT HE ($0.1 < E < 100\,\mathrm{GeV}$) γ-ray data from the same sources to derive limits on the density of extragalactic background light (EBL) photons. These photons, with energies extending from UV to far IR, can interact with γ-ray photons generated in the blazar creating secondary particles. At cosmological distances, the induced energy-dependent attenuation of the blazar γ-ray spectra can be used to statistically derive properties of the EBL spectrum and its evolution with redshift, which has strong implications on the star formation history in the Universe. In order to study the EBL induced attenuation on MAGIC blazars, we developed two independent tools based on a Profile Likelihood method to derive limits on the EBL density based on the observed blazar spectra. Results show that state of the art models of EBL can successfully explain MAGIC observations of blazars. We find that our measurements are close to lower limits on the EBL density predicted by galaxy count surveys. This is interpreted as EBL intensity being dominated by the emission from normal galaxies.

Resumen

Observaciones de la emisión en muy altas energías de blazars a distancias cosmológicas

Mireia Nievas Rosillo

Desde el descubrimiento accidental por parte de Fath en 1909 de lineas de emisión extrañas e intensas en el espectro óptico de las “nebulosas espirales”, el estudio de los núcleos de galaxias activos ha sido objetivo de una intensa investigación. Hoy en día pensamos que estas violentas estructuras, que se encuentran en el centro de algunas galaxias, están alimentadas por agujeros negros muy masivos de frecuentemente más de $10^8\,\mathrm{M}_\odot$. Son capaces de mantener luminosidades de hasta $10^{15}\,\mathrm{L}_\odot$ basándose únicamente en un eficiente mecanismo de acrecimiento. No es extraño encontrar en ellos chorros colimados que se extienden perpendicularmente al disco de acrecimiento hasta distancias equivalentes al tamaño de la propia galaxia anfitriona, con intensa emisión que se extiende a lo largo del espectro electromagnético. Los núcleos activos de galaxias son aceleradores de partículas extremos, pero no se sabe con certeza dónde y cómo se produce este proceso. Las partículas cargadas que han sido aceleradas pueden emitir radiación no térmica mediante varios mecanismos, desde radio hasta rayos gamma.

Esta tesis se enfoca en un tipo particular de nucleo galáctico activo conocido como blazar. Los blazars son fuentes intensas de radio con potentes chorros orientados en la dirección del observador. Esta orientación, junto a la naturaleza ultra-relativista de los plasmas de partículas cargadas que están inmersos en el chorro, amplifican por efecto Doppler la radiación emitida. Los fotones que escapan tienen frecuentemente energías que entran en el dominio de los rayos gamma de muy alta energía (por sus siglas en inglés, VHE, $E > 100\,\mathrm{GeV}$) y pueden ser detectados por telescopios Cherenkov de imágenes atmosféricas (IACTs) como MAGIC.

De entre los ~ 70 blazars conocidos en rayos gamma VHE, hemos seleccionado tres para este trabajo. Son los dos radioquasars de espectro plano B0218+357 y PKS 1441+25 y el BL Lac más lejano hasta ahora detectado con un IACT: PKS 1424+240. El primero destaca por su originalidad como primer y único blazar VHE amplificado por lente gravitatoria fuerte. PKS 1441+25 es único por el estallido de actividad duradero que tuvo en 2015, por la calidad de su espectro reconstruído y por la elegante y sencilla implementación que pudo realizarse del desarrollo de

su emisión con el tiempo. En ambos casos, la emisión de muy altas energías se puede explicar por la emisión de un plasma lleno de electrones ultra-relativistas que se mueve a lo largo del chorro y puede eventualmente escapar de la región de líneas anchas del quasar. Esta región es una fuente intensa de radiación de baja energía que puede interaccionar con los rayos gamma generando pares. También hemos incluído a PKS 1424+240 para investigar su intringante spectro, utilizado en el pasado como evidencia de procesos hadrónicos en el chorro y de modelos de propagación cósmica de rayos gamma mediante la generación de hipotéticas partículas secundarias. En los tres casos, hemos estudiado su emisión en muy altas energías en el contexto de campañas multi-frecuencia. Hemos buscado correlaciones en el desarrollo de sus estallidos de actividad en muy altas energías con el comportamiento de cada fuente en otras longitudes de onda, encontrando interesantes tendencias para PKS 1441+25, explicadas como una emisión coherente desde una única región de emisión. Además, hemos interpretado sus espectros de banda ancha en términos de modelos leptónicos, incluyendo la contribución de emisión Compton inverso externo para B0218+357 y PKS 1441+25. Concluimos que los modelos de emisión de Compton inverso pueden explicar satisfactoriamente los espectros observados de los blazars y su variabilidad multi-frecuencia.

Finalmente, hemos combinado más de 300 horas de observaciones de 12 blazars diferentes con MAGIC, junto a datos en rayos gamma de altas energías ($0.1 < E < 100\,\mathrm{GeV}$) contemporáneos usando Fermi-LAT, con el objetivo de obtener límites a la densidad de fotones del fondo de luz extragaláctica (EBL). Estos fotones, con energías que van desde el UV al IR lejano, pueden interaccionar con los rayos gamma generados por el blazar creando partículas secundarias. A distancias cosmológicas, la atenuación dependiente de la energía inducida en el espectro de rayos gamma del blazar puede utilizarse para obtener por métodos estadísticos propiedades del espectro del EBL y de su evolución con el corrimiento al rojo, que tiene fuertes implicaciones en la historia de formación estelar en el Universo. Para estudiar la atenuación inducida por el EBL en la emisión de los blazars de MAGIC, hemos desarrollado dos herramientas basadas en un perfil de verosimilitud para obtener límites en la densidad de EBL. Los resultados muestran que los modelos más recientes de EBL pueden explicar las observaciones de blazars de MAGIC. Encontramos además que nuestras medidas son cercanas a los límites inferiores a la densidad de EBL predichos por estudios basados en conteos de galaxias, lo cual nos indica que el EBL está dominado por la emisión de galaxias normales.

Preamble

1 Motivation

Despite being known for about half a century, Active Galactic Nuclei are still a complete mystery to us. It is known that these structures are powered by super-massive black holes, which are believed to be present in most galaxies. Yet, not all galaxies are capable of sustaining AGN structures. So, what makes AGNs so unique? And why would we want to study them anyway? The reasons are multiple:

Accretion : Accretion is probably one of the most fundamental processes in astrophysics and is found everywhere: protostars and circumstellar disks, binary objects filling the Roche lobe. AGNs are the only probes we have of accretion at large scale. Studying the nature of accretion flows and their environments has become instrumental to understand the AGN taxonomy.

Cosmic time machines : AGNs are *cosmological time machines.* They are extremely bright and this makes them visible even at very long distances. The study of their properties, and how these properties evolve with lookback time, can bring light on cosmological issues such as: super-massive black hole formation and growth, re-ionization of the intergalactic medium (and the role of AGNs on it) and AGN evolution.

Jet and knots : The good temporal and spatial resolution in radioastronomy has allowed to resolve structures in some AGN jets. The observation of evolving knots and the correlation of these structures with emission in other wavelengths provide unique insight of the physical processes that are taking place. Lacking spectral features to give away the nature of the jet, its composition is still mostly unknown.

Their environment : AGNs are known to modify the star formation in their host galaxy, and may even affect other galaxies in the cluster, through radiation pressure and interstellar and intra-cluster medium heating.

Fundamental physics : AGNs are excellent test benches of fundamental physics and the strong gravity regime. For instance, their variable broadband emission are unique probes of Lorentz invariance.

Astroparticle physics : These large structures constitute the most extreme accelerators we can think of. AGNs are thought to be the source of UHE cosmic-rays above the knee. They are often described with very simple leptonic emission models (e.g. synchrotron-self-Compton), but with surprises like the detection of possible associated neutrino particles (pointing towards significant hadronic contribution).

AGNs as cosmological tools : They help us to test the intensity of the intergalactic magnetic field (IMF) and are at the same time a source of γ-rays and a laboratory to measure the density of photons of the Extragalactic Background Light (EBL) indirectly.

The observation of AGNs in γ-rays provides fundamental information. γ-rays are tracers of the inner parts of the AGN and give us clues about the particle acceleration mechanisms and the processes that generate jets. Besides, the γ-ray sky is plagued with AGNs.

This work is as a continuation of previous efforts to understand the nature of AGN emission, particularly at the highest energies. The document describes observations of blazars, the analysis of the γ-ray data and the interpretation of the results. It also presents novel measurements of the interaction of γ-ray photons coming from blazars with cosmic optical and infrared photon fields using the MAGIC telescopes. The presented results, while not revolutionary, are undoubtedly an improvement over what we knew before.

2 Structure of this work

The document is organized in four parts:

- Part I is an introductory part which serves to present the topic of cosmic rays, describes the main particle acceleration and γ-ray emission and absorption mechanisms and finally presents the most important γ-ray source types that are currently known.
- Part II describes the γ-ray instrumentation with particular emphasis on the *Fermi*-LAT and MAGIC telescopes, which are extensively used in this work.
- Part III summarizes our current knowledge about Active Galactic Nuclei and presents the analysis and interpretation of the observations of three blazars which have been found as bright γ-ray emitters.
- Part IV describes the nature of the cosmic optical and infrared backgrounds (EBL). It presents historical measurements that have been performed to constrain their density, the models that have been proposed, and finally describes the results that were obtained by MAGIC by studying the attenuation that these background fields produce in the γ-ray spectra of blazars.

In addition, an appendix describing analysis details and additional work developed during the thesis which were left out from the main text is provided.

Part I

Introduction to γ-ray Astronomy

> “*Mensus eram coelos, nunc terrae metior umbras. Mens coelestis erat, corporis umbra iacet.*”
>
> —Johannes Kepler's, Self-authored epitaph (1630).

1

The origin of high energy γ-rays

Contents

1.1 Introduction to Cosmic Ray physics

The term *Cosmic Ray* (CR) refers to the population of relativistic particles that reach the Earth from the outer space. The name ‘rays’ has historical connotations because originally they were thought to be photons. Nowadays, we know that most of the high energetic particles that reach us are charged particles and usually the term CR refers only to charged particles, excluding therefore neutrinos and γ-rays.

However, all these particles may share a common origin and studying them is in fact one of the ultimate goals of multi-messenger astronomy. In the High Energy Astrophysics field, we are interested only in γ-rays and CRs with energies between 1 GeV (Sun & solar wind) to more than 10^{20} eV.

1.1.1 The discovery of Cosmic rays

The existence of high levels of ionizing radiation in the atmosphere was a long standing problem in the beginning of the 20th century. First in 1907–1911 the Italian physicist Domenico Pacini and later in 1911–1912 the Austrian physicist Victor Franz Hess [1, 2] started to systematically study its origin. Until then, the radiation was thought to have its origin in rocks in Earth's surface.

Already in 1909 the German scientist Theodor Wulf measured the rate of ionization near the top of the Eiffel tower (at a height of about 300 metres) using a portable electroscope. The ionization rate was expected to decrease steeply with height, but Wulf noted that the ionization rate at the top was just under half of that at ground level – a much less significant decrease than anticipated. Not much later, in a series of balloon ascents, V. F. Hess carried out experiments with an electroscope to measure the evolution of radiation in the atmosphere with altitude. In 1911 his balloon reached an altitude of around 1100 metres and the drop in the amount of radiation was not as large as expected. Then, on April 1912, he made an ascent to 5300 m during a near-total solar eclipse and he realized that not only from ~ 1 km the radiation increased by a factor of ~ 2, but also it did not changed significantly during the eclipse, concluding that the main source of the radiation could not be the Sun or the Earth itself. The intriguing radiation was coming from farther out in space. His discovery was confirmed by Robert Andrews Millikan in 1925, who extended the study from deep under water to high altitudes and also carried out experiments around the globe. He named the new particles 'cosmic rays' in the belief that they were in fact γ-rays originated in Hydrogen fusion processes into heavier elements. Two years later, Jacob Clay discovered during a sea trip from Java to the Netherlands that the intensity of cosmic rays changed with latitude and therefore CRs were affected by geomagnetic field, as expected for charged particles [3]. This idea was further supported by Bothe and Kolhörster [4], who discovered that CRs could penetrate 4.1 cm of gold, suggesting that they are very energetic and ruling out the possibility of being mainly fusion-related photons.

Composition studies started when in 1930, Bruno Rossi predicted an anisotropy induced by Earth's magnetic field that would depend on the charge of the primary cosmic rays [5]. This effect was confirmed by number of experiments [6–8], which detected more CRs coming from the west than from the east. The main component of cosmic rays was hence positive, possibly charged protons with perhaps some electrons, heavier nuclei and muons. Nowadays, the composition in terms of particle flux is known to depend somewhat on energy, consisting approximately in $\sim 90\%$ protons, $\sim 9\%$ helium nuclei and $\sim 1\%$ heavier nuclei and electrons.

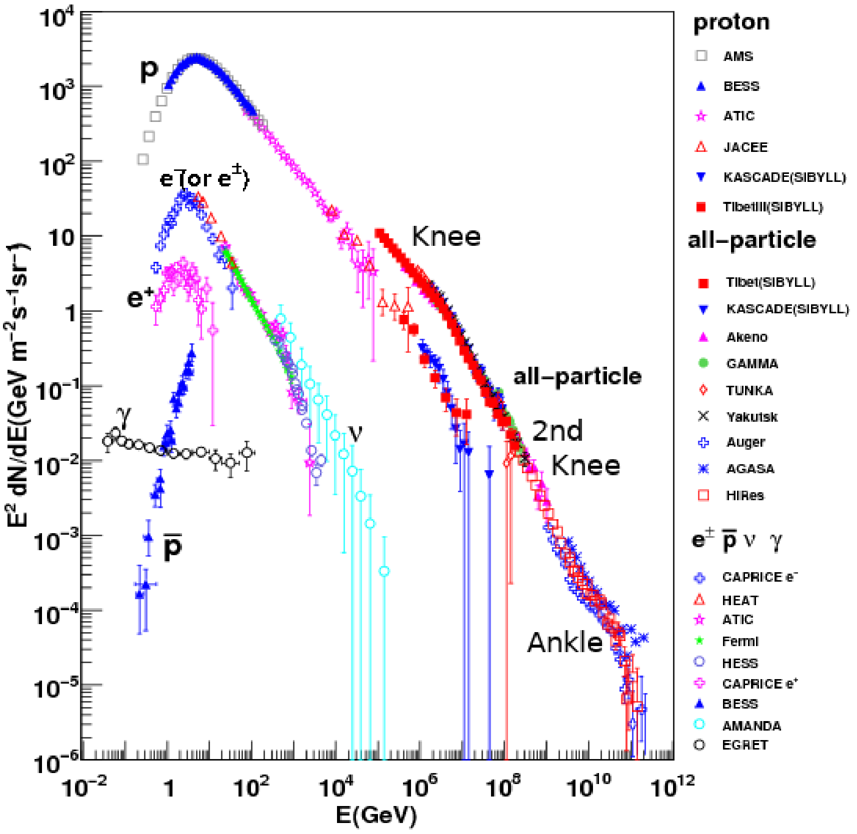

Figure 1.1: Cosmic Ray spectrum with its main components [12].

Particularly interesting for this work was the discovery of atmospheric cascades. In two independent experiments, Bruno Rossi [9] and Pierre Auger [10] detected and investigated Extensive Air Showers (EAS). They observed that several counters placed at large distances from each other registered coincident events, concluding that high energy primary cosmic-rays hitting the atmospheric nuclei initiated cascades of secondary particles that could be detected at ground-level (see Section 3.3).

1.1.2 Spectrum of Cosmic Rays

It is a remarkable fact that through many decades in energy, the spectrum of cosmic rays can be roughly modeled as a Power Law,

$$I_N(E) \sim 1.8 \left(\frac{E}{\mathrm{GeV}}\right)^{\alpha} \mathrm{nucleons\,cm^{-2}s^{-1}sr^{-1}} \tag{1.1}$$

with an spectral index of $\alpha \sim -2.7$. The corresponding energy density of CRs in the Galaxy is $\sim 1\,\mathrm{eV\,cm^{-3}}$, to be compared with $\sim 0.4\,\mathrm{eV\,cm^{-3}}$ from stellar light, $\sim 0.2\,\mathrm{eV/cm^{-3}}$ kinetic energy of the interstellar medium (ISM) in the Galaxy or $\sim 1\,\mathrm{eV/cm^{-3}}$ contained in the Galactic magnetic field [11]. The spectrum of CRs is shown in Figure 1.1, where we can distinguish the following spectral regions:

- From few MeV to the knee: CRs from the Sun or the solar wind.

- Knee: softening at 5×10^{15} eV.
- From the knee to the ankle: typically interpreted as SNe or Galactic CRs. Secondary knee at $\sim 10^{17}$ eV.
- Ankle: hardening at 3×10^{18} eV.
- High energies: starting from the ankle, the Larmor radii in the Galactic magnetic field becomes large enough to leave charged particles unperturbed (charged particle astronomy becomes feasible).
- The GZK cutoff ($\times 10^{20}$ eV) is a theoretical upper limit to the energy of cosmic rays from distant sources. The interaction with the CMB of particles above that limit produces pions via the Λ-resonance $\gamma_{\mathrm{CMB}} + p \to \Lambda^+ \to (p + \pi^0)$ or $(n + \pi^+)$. Neutral pions would then decay in a HE γ-ray cosmic background and $\pi^{\pm}$ fill the medium with $e^{\pm}$ and neutrinos.

Cosmic rays can be produced inside the Galaxy (Galactic CRs or GCRs) [13] or outside (extragalactic CRs) [14]. The general belief is that up to the *knee* they are mostly GCRs with a rather steep spectrum. Somewhere at ~ 1 EeV there is a transition to extragalactic CRs with a harder spectrum, hence the hardening observed after the *ankle*. After the *ankle*, the common belief is that their origin is mostly extragalactic. The main idea to explain this transition is that, being charged particles, CRs propagate in the Galaxy diffusively due to the random nature of the Galactic magnetic field. The curved trajectory of charged particles that move perpendicular to a magnetic field is given by the Larmor radius, which in natural units ($c = \hbar = k_B = 1$), reads

$$r_g = \frac{cp_\perp}{ZeB} \approx 100\,\mathrm{pc}\frac{3\,\mu\mathrm{G}}{B}\frac{E}{Z \times 10^{18}\,\mathrm{eV}} \tag{1.2}$$

Starting from approximately the *knee* the Larmor radius becomes larger than typical Galactic scales (e.g. the height of the Galaxy disc), thus transitioning from a diffusive to an unaffected linear propagation regime, where CR are no longer confined by the Galactic magnetic field. Most CR models coincide in that the composition also changes from a Iron-dominated population to an almost pure proton based CR population [15].

The standard model for Galactic Cosmic Rays (SM GCR) predicts that Supernova Remnants (SNRs, see 2.2.4) are the main sources for these particles. Since they are also very bright γ-ray sources, SNRs are one of the main targets for space and ground-based γ-ray observations.

Extragalactic cosmic rays have been traditionally associated with AGNs, γ-ray bursts (GRBs), radio galaxy lobes and intra-cluster-medium (ICM) in galaxy clusters [16]. Their large energy reduces their deflection by magnetic fields, turning them into valuable tools in multi-messenger astronomy. Nevertheless, experiments such as Pierre Auger have been trying to establish correlation between Ultra High Energy (UHE) CRs and known *Fermi*-LAT high energy γ-ray sources with little success [17–19].

1.2 Particle acceleration mechanisms

Acceleration of charged particles is a long standing problem in Astrophysics and still today the particular processes taking place are not well understood. So far, several processes are being called to explain particle acceleration in astronomy [20, 21].

1.2.1 Direct electric field acceleration

Perhaps the simplest (and at the same time less understood) way to boost the kinetic energy of charged particles is by means of a strong electric field, such as those typically generated during magnetic field reconnections in magnetospheres. It is common to distinguish between two well differentiated cases based on the electric field strength compared to the critical Dreicer field E_D [22], defined as

$$E_D = \frac{kT}{e\lambda_{\mathrm{Coul}}}, \qquad \text{where} \qquad \lambda_{\mathrm{Coul}} \sim 15 \times 10^{-3} \times T_8^2 \times [n/\mathrm{cm}^{-3}]^{-1}\,\mathrm{kpc} \tag{1.3}$$

being $T_8 = T/10^8\,\mathrm{K}$ and λ_{Coul} is the collision (electron-electron or proton-proton) mean free path. In sub-Dreicer fields the acceleration is inefficient when compared with the rate of collision losses and the resulting electrons cannot have energies larger than $\sim 10^2\,\mathrm{keV}$ (the model has been however applied to explain X-ray solar flares [23]). These energies are far from those needed to justify γ-ray production (GeV–TeV). In super-Dreicer fields, which are also present in many simulations of reconnections, particle acceleration is faster than typical collision and thermalisation times τ_{therm}. The results is a runaway effect and the formation of plasma waves or turbulence (PWT), which could potentially accelerate particles via *Fermi process* (see Section 1.2.2).

Nevertheless, there is no evidence of large scale magnetically dominated cosmological flows [24], which means that this mechanisms cannot explain the bulk of particle acceleration processes. Locally, Direct (parallel) Electric field acceleration mechanisms are believed to take place in pulsar gaps [25], however the location and structure of these gaps in the pulsar magnetosphere is still an open issue with direct implications on the VHE γ-ray spectra of ordinary pulsars.

1.2.2 Second Order Fermi acceleration

In the original model of Fermi particle acceleration process (also known as *Second Order Fermi acceleration*, *Stochastic Acceleration* or simply *Fermi process*) [26], charged particles moving at velocities $v \sim c$ along magnetic field lines (B) with a pitch angle μ suffer scattering or stochastic collisions with ‘magnetic gas clouds’ moving at speed u. This process can be interpreted [27] as randomly moving ‘magnetic mirrors’ (irregularities in the Galactic magnetic field) causing an overall reflection and acceleration when they move against the particle trajectory (head-on collision) and braking if there is a head-tail collision.

Fermi argued that the probability of head-on collisions ($\propto v + u\cos\theta$) is higher than head-tail ones ($\propto u - v\cos\theta$)[1], so on average, the gain in energy is proportional to $(u/v)^2 D_{\mu\mu}$ where $D_{\mu\mu}$ is the pitch angle diffusion rate. Since the gain in energy is only $\mathcal{O}(u/v)^2$, this mechanism would be efficient only with collision rates higher than those suggested from typical cloud velocities ($u/v \lesssim 10^{-4}$) and CR mean free paths ($\sim 0.1\,\mathrm{pc}$). Other problems include that the obtained spectrum, while being a power law, is model dependent. Furthermore, some of these collisions result in additional energy losses which are not included in the simplest version of the model.

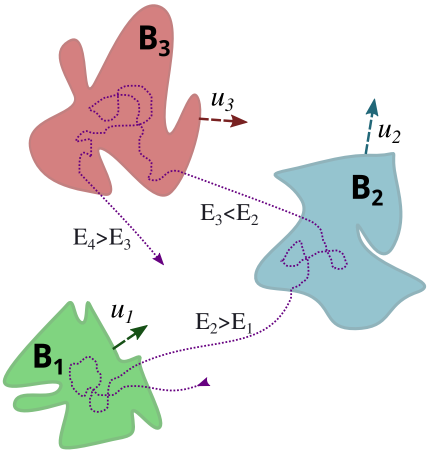

Figure 1.2: Sketch of the *Second Order Fermi process*. The moving charged particle (dotted line) can gain (clouds 1, 3) or loss energy (2).

A particular case of Stochastic Acceleration (SA) that is worth mentioning is the one driven by plasma waves or magnetohydrodynamic turbulence. This scenario has found important uses among astronomers, such as to describe strongly magnetized plasmas (e.g. in solar wind flows and perhaps also in AGN jets [28]), where the Alfv́en velocity $v_A = \sqrt{B^2/4\pi\rho}$ (ρ = mass density) exceeds the sound velocity $v_s = \sqrt{kT/m}$ ($\beta_p = 2(v_s/v_A)^2 < 1$), turning SA driven by Alfv́enic turbulence into an efficient mechanism for accelerating particles which could work in some astrophysical environments.

1.2.3 First Order Fermi acceleration

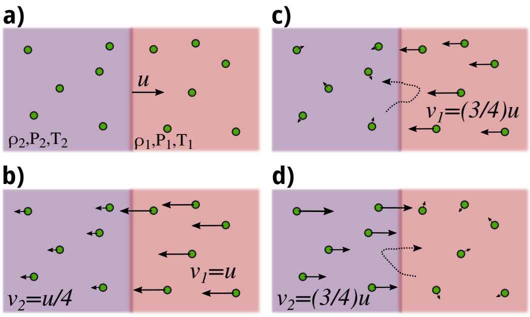

Figure 1.3: Sketch of the *First Order Fermi process*: a) observer frame (shock moves at speed u, b) shock front frame, c) downstream frame [2], d) upstream frame [1]. When a high speed charged particle (dotted line) crosses the front in any direction it sees plasma coming towards it.

An alternative process is the so called *First Order Fermi acceleration* [29, 30] or *Diffusive Shock Acceleration* (DSA) which is recognized as the most important acceleration mechanism in astrophysical plasmas and thought to power Supernova Remnants. The energy gains are larger ($\mathcal{O}(u/c)$) than in SA.

In this scenario, the acceleration takes place near strong non-relativistic shocks (in general, any flow convergence region) moving at speed u. Following the explanation in [27], the shock divides the plasma in two regions: downstream and upstream. In the reference frame of the shock, particles moving from the upstream approach the shock at speed u. For strong

---

[1] An easy way to see this is to imagine yourself driving in the highway, you will cross more cars traveling in the opposite direction than you will on your own.

shocks and a fully ionized plasma $v_{\mathrm{down}}/v_{\mathrm{up}} = 4$. This flow velocity discontinuity means that any particle crossing the shock front from either side will see plasma coming at speed $3/4u$. The overall boost in energy is of $\mathcal{O}(u/c)$.

The predicted spectrum is an almost universal power law $dN(E)/dE \sim E^{-2}$, which while having the wrong index, only depends on the compression ratio of the shock. The only requirement for this mechanism to work are relativistic particles and strong shock fronts, which are believed to occur for instance near supersonic shells of supernova remnants.

Despite being more appealing than *Second Order Fermi Acceleration*, some the details are not correctly reproduced (like the index of the Power Law spectrum) or explained, such as for instance the 'injection problem' or how the seed particles of energies above the thermal energy (Lorentz factors $\gamma_e > m_p/m_e(v_A/c)$) are originated [28]. Additionally, the mechanism is still slow, requiring the particles to cross the shock multiple times to reach the observed energies. Finally, there is an upper limit of $\sim 10^{14}$ eV to the maximum energy reachable with this process (confinement radius in SNRs with magnetic fields of $\sim 1\,\mu$G), while the CR spectrum extends beyond $\sim 10^{20}$ eV. To solve this, it is generally assumed that the magnetic fields can be amplified by several processes.

In both Fermi processes the environment has to be collision-less to avoid severe energy losses.

1.3 Particle interactions and γ-ray production

1.3.1 Thermal emission

Electromagnetic radiation generated by the thermal motion of charged particles in matter (Fig. 1.4a) follows a black body spectrum. It is the dominant radiation coming from sources like stars, interstellar dust, etc.

In an ideal (optically thick and non-reflective) black body in thermal equilibrium, the spectrum and intensity emitted only depend on its temperature following the well known Planck formula [33]:

$$I_{BB}(\nu, T)d\nu = \frac{2\pi h\nu^3}{c^2}\left[\exp\left(\frac{h\nu}{kT}\right) - 1\right]^{-1} d\nu \ \ \mathrm{erg\,cm^{-2}s^{-1}} \tag{1.4}$$

where $I_{BB}(\nu, T)d\nu$ is the spectral energy distribution, h is the Planck constant, T the temperature in Kelvin, c the speed of light in vacuum, ν the frequency and k the Boltzmann constant.

For an optically thick medium, the differential energy spectrum of photons is

$$N_{BB}(E) = 9.899 \times 10^{40} E^2 \left[\exp(E/kT) - 1\right]^{-1} \ \mathrm{ph\,cm^{-2}s^{-1}MeV^{-1}} \tag{1.5}$$

For optically thin media the absorption of photons in a hot plasma needs to be taken into account, resulting in the spectrum of thermal bremsstrahlung

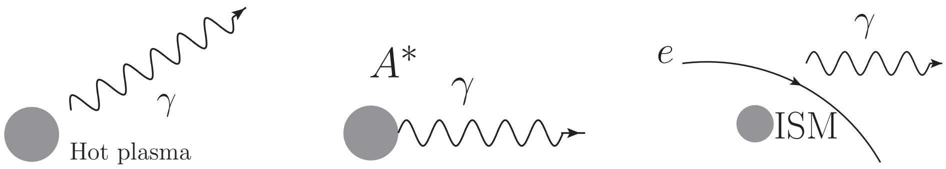

(a) Hot plasma **(b)** Radiactive emission **(c)** Bremsstrahlung

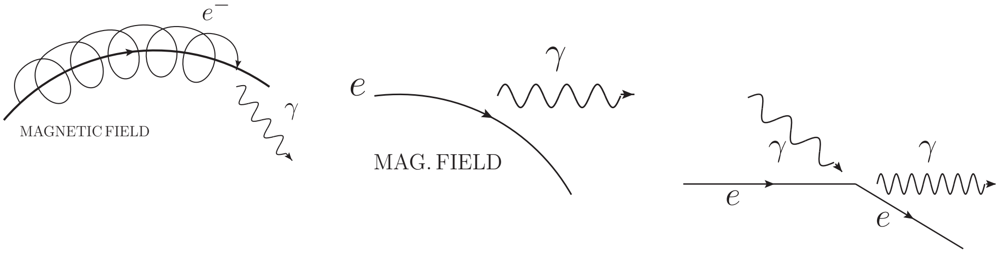

(d) Synchrotron emission **(e)** Curvature radiation **(f)** Inverse Compton

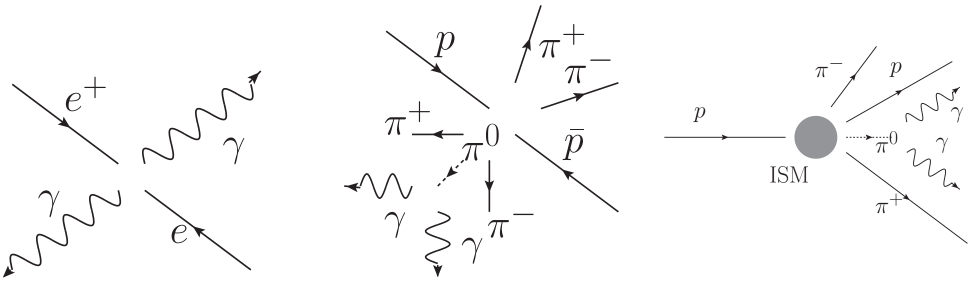

(g) e^- - e^+ annhilation **(h)** p-$\bar{p}$ annhilation **(i)** p-matter interaction

Figure 1.4: Particle γ-ray emission mechanisms. Based on [31, 32].

$$N_{TB}(E) \propto \frac{n_e^2}{T^{1/2}E} \exp(-E/kT) \tag{1.6}$$

The maximum of the emission for the black body case is reached a temperature given by Wien's law

$$E_w(\,\mathrm{MeV}) = 4.7 \times 10^{-10}\,T(K) \tag{1.7}$$

and the average photon energy is

$$\langle E\rangle(MeV) = 2.3 \times 10^{-10}T(K) \tag{1.8}$$

According to these two expressions, temperatures of the order of $10^{10}K$ would be needed in order to have a significant production of thermal γ-rays. These conditions were only reachable during the Big Bang (which would not be observable at those energies due to redshift effects) or in explosive phenomena such as GRBs. For the latter, the medium is already optically thin and the spectrum is explained by thermal bremsstrahlung.

Electronic interactions

1.3.2 Bremsstrahlung

When the trajectory of a charged particle is deflected in the presence of an electric field generated by a nucleus with charge Z (Fig. 1.4c), it emits electromagnetic radiation whose amplitude is proportional to the acceleration suffered by the particle. The classical treatment predicts an acceleration $\propto Ze^2/m$ [34] and is interpreted in reality as a deceleration of the incident particle (usually named after the German word bremsstrahlung, which means 'braking radiation'). The emitted photons follow the same differential spectrum than the one of the electrons (i.e. for a Power Law, $E_\gamma^{-\Gamma}$). It is particularly important for cosmic electrons in SNRs and the interstellar medium. The average differential cross-section (both classical and quantum) is

$$\sigma_b dE_\gamma = 4\alpha r_e^2 Z^2 \frac{dE_\gamma}{E_\gamma} F(E_e, \nu) \tag{1.9}$$

where α is the fine structure constant and $\nu = E_\gamma/E_e$ the fractional energy carried by the photon. If the Coulomb field of the nucleus is not screened by electrons, then

$$F(E_e, \nu) = \left[1 + (1-\nu)^2 - \frac{2}{3}(1-\nu)\right] \left[\ln\left(\frac{2E_e}{m_e c^2}\frac{1-\nu}{\nu}\right) - \frac{1}{2}\right] \tag{1.10}$$

while for complete screening

$$F(E_e, \nu) = \left[1 + (1-\nu)^2 - \frac{2}{3}(1-\nu)\right] \ln(183Z^{-1/3}) + \frac{1}{9}(1-\nu) \tag{1.11}$$

The average cross-section for many bremsstrahlung interactions of the same order is thus $\sigma_b \sim 0.58\,\mathrm{mb/nucleus}$. Typical radiation lengths for hydrogen in the ISM ($\sim 1\,\mathrm{atom\,cm^{-3}}$) are of the order of $10\,\mathrm{Mpc}$.

Nonetheless, bremsstrahlung is an inefficient process that requires a hot (fully ionized) and non-dense (low recombination rate between electrons and ions) medium in order to be relevant. These conditions can be found in the intracluster medium of galaxy clusters and in the X-ray solar flares [35].

1.3.3 Synchrotron emission

In the presence of a homogeneous magnetic field of strength B, an electron of energy E_e whose trajectory forms an angle θ with the magnetic field will emit magnetobremsstrahlung radiation (German world for 'magnetic braking radiation', in a clear analogy to the standard bremsstrahlung). Depending on the energy (speed) of the electron, we can distinguish between

- Gyro radiation ($v \ll c$). The magnetic force is perpendicular to the particle velocity and no power is transferred to the charged particle. The particle traces a helical path and emits radiation with a dipole pattern of gyro frequency $\omega_G = \frac{eB}{m_e c}$ and power given by Larmor's formula $P = \frac{2e^2}{3c}\dot{v}^2$. In astronomy, this radiation is only significantly detected in extremely large magnetic fields (e.g. neutron stars).
- Cyclotron radiation ($v \lesssim c$): When the electron kinetic energy is comparable to $m_e c^2$, the gyro frequency no longer coincides with the orbital frequency and relativistic beaming changes both the emission pattern (departure from the dipole case) and the emitted spectrum (no longer a single line). The total power emitted by the particle is given by the Liénard expressio [36] $P = \frac{2e^2}{3c}\gamma^6 \left[(\dot{\beta})^2 - (\beta \times \dot{\beta})^2\right]$, where γ is the Lorentz factor. The radiation can be described as a sum of dipoles radiating at the harmonics of the relativistic gyrofrequency $\omega_r = \omega_g/\gamma$ suppressed by a factor $(v/c)^{2n}$. If the dipoles overlap, they generate 'wiggles' at each harmonic frequency.
- Synchrotron radiation (Fig. 1.4d): When the electron motion is ultrarelativistic ($\gamma \gg 1$), the dipole pattern is distorted into a narrow cone of radiation and the 'cyclotron wiggles' are totally washed out. Synchrotron emission is one of the most important non-thermal radiative mechanisms in astronomy and is responsible of a significant fraction of the radio and optical (sometimes even X-ray) light we receive from AGNs.

The synchrotron power spectrum (energy flux per frequency interval) is given by

$$P(\nu) = \frac{\sqrt{3}e^3}{m_e c^2} N_e(\Theta) H \sin\theta \frac{\nu}{\nu_c} \int_{\nu/\nu_c}^{\infty} K_{5/3}(\eta) d\eta \tag{1.12}$$

where $N_e(\Theta)$ is the electronic density (number of electrons per solid angle with velocity vectors pointing towards us), $K_{5/3}$ the modified Bessel function of the second kind, ν the frequency of the emitted photon and

$$\nu_c = \frac{3eH\sin\theta}{4\pi m_e c}\left(\frac{E_e}{m_e c^2}\right)^2 \tag{1.13}$$

The above expressions can be approximated for the low and high frequency cases,

$$P(\nu) \sim \frac{\nu}{\nu_c}, \qquad \omega \ll \omega_c \tag{1.14}$$

$$P(\nu) \sim \sqrt{\nu/\nu_c} e^{-\nu/\nu_c}, \qquad \omega \gg \omega_c \tag{1.15}$$

If instead a single electron we have a distribution with electron differential energy spectrum of $I_e(E_e) = K E_e^{-\Gamma}$, the synchrotron photon number spectrum is of the form

$$\frac{dN}{dE} \propto E_\gamma^{[(-\Gamma+1)/2]} \tag{1.16}$$

1.3.4 Curvature radiation

In some astrophysical environments, like pulsar magnetospheres, the very strong magnetic fields force the electron trajectories to follow the magnetic field lines with pitch angles $\theta \sim 0°$. Since the magnetic lines (and therefore the electron paths) are curved themselves (Fig. 1.4e), the charged particles emit ‘curvature’ radiation [37] in the direction of motion with a characteristic energy given by

$$E_c = \hbar\omega \approx \frac{3}{2}\frac{\hbar c \gamma^3}{\rho_c} \tag{1.17}$$

where ρ_c is the radius of curvature of the magnetic field line and $\hbar$ and γ are the reduced Planck’s constant and Lorentz factor. For very high energy (TeV) electrons and positrons moving along a field line of a pulsar ($\sim 10^3$ km), the emitted photons are found at high energy (GeV) γ-rays.

1.3.5 Inverse Compton emission

In the inelastic interaction between a photon and a moving charged particle, energy is exchanged and the particle’s kinetic energy can be boosted at the expense of lowering the photon’s frequency. This process is known as Compton scattering and has important implication in detectors, being the dominant interaction between $\sim 10^2$ keV and $\sim 10^1$ MeV[2] (see Fig. 3.2) and the base of Compton telescopes such as COMPTEL or the future AMEGO/e-ASTROGAM.

The opposite effect (Inverse Compton scattering or IC, see Fig. 1.4f), in which the particle transfers a fraction of its energy to the photon, is fundamental for most γ-ray emitting sources. For relativistic moving particles, any ambient photon is seen Doppler shifted with energy $\gamma h\nu$ in the frame of the particle, where γ is the Lorentz factor. After the interaction, the scattered photon comes out with an energy $\lesssim \gamma h\nu$ which, back in the observer reference system is seen again boosted with energy $\sim \gamma^2 h\nu$ if $\gamma h\nu \ll m_e c^2$ (electron recoil can be neglected, Thomson regime) and $\sim E_e$ if $\gamma h\nu \gg m_e c^2$ (significant electron recoil, Klein-Nishina regime).

The transition from the Thomson to the Klein-Nishina regime (reduced scattering cross-section) happens at $\gamma_{K-N} \sim 1/4(h\nu_0/m_e\, c^2)$. In this regime, electrons lose most of their energy in a single scattering rather than smoothly cooling down due to multiple small losses of energy. These two regimes have important implications in some astrophysical sources:

- For sources with strong external photon fields and VHE electrons such as Flat Spectrum Radio Quasars (FSRQs), electrons see the ambient photons with Doppler shifted frequencies. The interactions are then likely happening in the KN regime ($\gamma h\nu > m_e\, c^2$), where the scattering probability is larger the lower

---

[2] The range depends on the Z of the material, requiring higher energies for heavy nuclei.

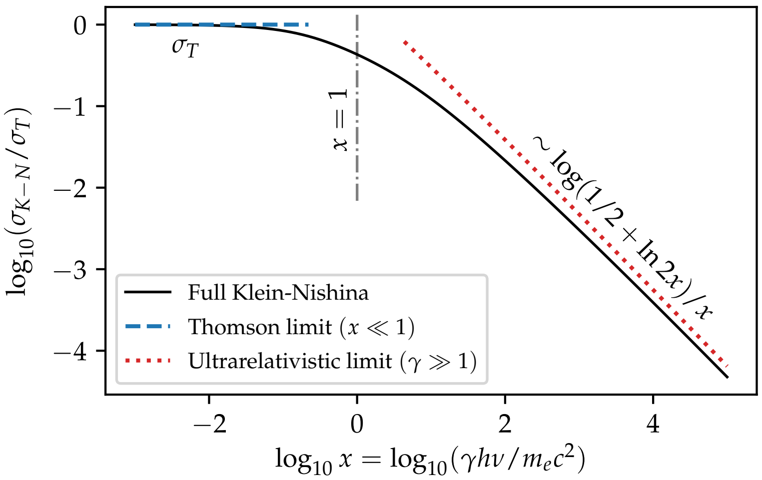

Figure 1.5: Klein-Nishina cross-section as a function of the photon energy in the rest frame of the electron according to formulas 1.18, 1.19 and 1.20.

the frequency of the photon and the energy of the electron are (see Fig. 1.5). The gains attainable by the upscattered γ-rays are limited and the spectrum will probably be curved. This is not the case for high-frequency peaked BL Lacs (HBL) for which most of the low energy photons are generated from synchrotron emission by the same population of relativistic electrons. In the reference frame of the electron, they are seen with energies $\gamma' h\nu \ll m_e\, c^2$, where the Thomson limit applies.

- For typical FSRQs, the large amount of ambient photons makes external Compton cooling very efficient. This significantly limits the energy gains electrons can attain before they cool down.

If we define $x = \frac{\varepsilon}{m_e c^2} = \frac{h\nu}{m_e c^2}$ and $\sigma_T = 8\pi r_e^2/3 \approx 6.65 \times 10^{-25}\,\mathrm{cm}^2$ is the Thomson cross-section, the full Klein-Nishina cross-section can be written down as [27, 33, 38]:

$$\sigma_{K-N} = \frac{3\sigma_T}{8x}\left[\left(1 - \frac{2(x+1)}{x^2}\right)\log(1+2x) + \frac{4}{x} + \frac{2x(x+1)}{(2x+1)^2}\right] \tag{1.18}$$

$$\xrightarrow[x \ll 1]{} \sigma_T(1-2x) \approx \sigma_T \tag{1.19}$$

$$\xrightarrow[\gamma \gg 1]{} \frac{3\sigma_T}{8x}\left(\frac{1}{2} + \log 2x\right) \tag{1.20}$$

The full Klein-Nishina cross-section and its two limit regimes are shown in Figure 1.5. As an example, when the scattering involves photons from the CMB ($T \sim 2.7\,\mathrm{K} \to \langle\varepsilon\rangle \approx 6 \times 10^{-4}\,\mathrm{eV}$, the maximum energy reachable before entering the Klein-Nishina regime ($\gamma \sim 10^9$) is about $\langle E_\gamma\rangle \simeq \frac{4}{3}\gamma^2\langle\varepsilon\rangle \approx 5 \times 10^{14}\,\mathrm{eV}$.

An interesting result arises from the assumption of a population of low energy photons with energy density ρ_{ph}. If the differential electron distribution follows the same power law $I_e(E_e) = KE_e^{-\Gamma}$ (where K is the normalization factor and Γ the index) as in the synchrotron case, then Stecker [39] showed that the up-scattered γ-ray energy spectrum is

$$\frac{dN}{dE} \propto E_\gamma^{-[(\Gamma+1)/2]} \tag{1.21}$$

In general, inverse Compton is an important source of γ-rays from low energies ($E_\gamma \sim 1\,\mathrm{MeV}$) to very high energies ($E_\gamma \sim 1\,\mathrm{TeV}$). Since Compton cooling time decreases linearly with the energy and photon fields exist everywhere (e.g. the 2.7 K CMB), IC turns out to be one of the first choices to model the VHE spectra of astrophysical sources, including AGNs.

1.3.6 Electron-positron annihilation

The collision of an electron e^- and a positron e^+ results in the production of γ-ray photons[3] (see Figure 1.4g). If both particles are at rest, the two[4] photons are produced with an energy of $E = m_e c^2 = 0.511\,\mathrm{MeV}$.

For particles which are in-flight but with low energy, the collision leads to the production of the unstable positronium with 25% chance of being in the singlet ${}^1S_0$ state (mean lifetime of $1.25 \times 10^{-10}\,\mathrm{s}$ and generating photons of 0.511 MeV) and 75% in the ${}^3S_1$ state (mean lifetime of $1.5 \times 10^{-7} s$ and decaying in 3 γ-rays forming a continuum with a maximum energy of 0.511 MeV).

In the ultrarelativistic regime, the collisional cross-section in the electron's reference frame is given by

$$\sigma_A = \frac{3}{8\gamma}\sigma_T[\ln(2\gamma) - 1] \tag{1.22}$$

where $\gamma = E_e/m_e c^2$ is the Lorentz factor of the positron. Note that at large positron energies, the mean free path and lifetime of a positron in the Galaxy can be incredibly large and other processes can affect the positron before it annihilates. For such high energy positrons, the photon emitted in the extreme forward direction captures most of the available energy, while the other gets an energy of $m_e c^2/2 \approx 0.256\,\mathrm{MeV}$.

Comparing the typical annihilation time with the characteristic bremsstrahlung decay time for e^+, one finds that for positrons with $\gamma \leq 30$ the annihilation continuum dominates over bremsstrahlung from already $E(e^+) \sim 15\,\mathrm{MeV}$ for typical particle densities ($\sim 1\,\mathrm{cm}^{-3}$) [40].

Hadronic interactions

Protons also undergo all the non-thermal processes described for electrons (bremsstrahlung, synchrotron, curvature radiation, inverse Compton scattering), but in most cases

---

[3] At high energies, mesons and W and Z bosons can be produced as well.

[4] Single photons can only be produced if the electron is firmly bound to an atom.

their significantly larger mass to charge ratio ($m_p/m_e = 1836$) makes them very inefficient sources of γ-rays compared to electrons or positrons.

Protons are however a source of π^0 mesons through inelastic collisions with matter, annihilations with antinucleons and interactions with background photons. These neutral pions decay into γ-rays with an extremely short mean lifetime of $\tau_{\pi^0} = 8.4 \times 10^{-17}\,\mathrm{s}$ (much shorter than the one for charged π-mesons, $\tau_{\pi^\pm} \sim 10^{-8}\,\mathrm{s}$).

In the case of bremsstrahlung radiation, the power radiated by protons goes as m^{-4} to m^{-6} (depending on the direction of the acceleration with respect to the trajectory of the particles, from perpendicular to parallel respectively). This is the reason why the mechanism tends to be relevant only when the number of $e^\pm$ are far higher than those of the nuclei (e.g. regions with $T \gg 10^{10}\,\mathrm{K}$).

1.3.7 Hadronic collision

For simplicity, we will restrict this section to protons. Protons can interact with other protons (and more generally hadrons) to produce secondary particles of mass m (Fig. 1.4i). The threshold energy for this process to occur is given by [41]

$$E^p_{th} = \underbrace{m_p c^2}_{\text{rest energy}} + 2mc^2(1 + m/4m_p) \tag{1.23}$$

where m_p is the proton rest mass. In the case of $\pi^0 s$ (the simplest interaction that is relevant for γ-ray astronomy), their mass $134.96\,\mathrm{MeV}/c^2$ yields a threshold kinetic energy of about $\sim 280\,\mathrm{MeV}$ or a total proton energy of $\sim 1.22\,\mathrm{GeV}$.

$$p + p \to p + p + \pi^0; \qquad \pi^0 \to 2\gamma \tag{1.24}$$

The main feature of the spectrum of γ-rays that arises from the decay of π^0 is a peak at $E_\gamma = m_\pi c^2/2 \simeq 67.5\,\mathrm{MeV}$ coming from the 2-γ decay channel for π^0. It is remarkable that the formation of this feature is independent of the energy spectrum of the π^0s and their parent protons.

At high energies, the probability of forming charged π mesons from the original p-p interaction becomes comparable to the formation of π^0 and multiple interaction channels can be observed

$$p + p \to \pi^0 + \pi^+ + \pi^- + p + p \to \gamma' s, \nu' s, ... \tag{1.25}$$

$$p + p \to n + p + \pi^+ \to e^-, \bar{\nu}_e, ... \tag{1.26}$$

$$\ldots \tag{1.27}$$

Charged pions have larger mean lives and decay producing ultimately $e^\pm$ and ν. The $\nu_{e,\mu}$ spectra resembles the one of the γ-rays. However, if the radiation or gas densities are large, interactions of these charged pions with nucleons of photons cause a fast energy loss, making the neutrino spectra steeper than the γ-ray spectra.

The total cross-section of the inelastic p-p collisions depends on the energy of the protons, increasing rapidly from the threshold energy to about $E_{kin} \sim 2\,\mathrm{GeV}$ and then only logarithmically as $\sigma_{pp}(E_p) \approx 30[0.95 + 0.06\ln(E_{kin}/1\,\mathrm{GeV})]\,\mathrm{mb}$.

An interesting effect is related with the cooling time, which for inelastic interactions of relativistic protons in a hydrogen medium of density of particles n is almost independent of the energy,

$$t_{pp\rightarrow\pi^0} \sim 10^8(n/1\,\mathrm{cm}^{-3})^{-1}\,\mathrm{yr} \tag{1.28}$$

The γ-ray luminosity relates directly to the total energy of the protons W_p as

$$L_\gamma(E \geq E_\gamma) \sim \eta_N \frac{W_p(\geq 10E_\gamma)}{t_{pp\rightarrow\pi^0}} \tag{1.29}$$

where $\eta_N \approx 1.5$ is assumed if one wants to take into account the presence of heavier than hydrogen nuclei for both the cosmic ray (accelerated particles) population and the interstellar medium.

We can summarize saying that at $\gtrsim 1\,\mathrm{GeV}$ nuclear losses dominate over ionization losses and the photon spectrum practically replicates the one of the parent protons. At very high energies, electron bremsstrahlung is no longer competitive as a mechanism to produce γ-rays because the emissivity ratio depends only on the ratio of electron and proton densities ($q_\gamma^{br}/q_\gamma^{\pi^0} \simeq 4r^{-1}$). In this regime, photons can become tracers of the proton population. This scenario is widely recalled when modeling Pevatrons [42].

In some astrophysical sources, SSC models are too simple to explain the observed spectrum [43, 44]. The same happens with the emission from large scale structures [45]. For these objects, other mechanisms involving hadrons have been recalled, such as proton synchrotron or the interaction of proton and photons producing secondary mesons[5] and leptons[6].

1.3.8 Proton-radiation interactions

Radiation is everywhere and it should not surprise us that very energetic protons can interact with photon fields in the same way that electronic populations do. Many of these processes are highly suppressed by the large mass of the proton when compared to the electron ($(m_e/m_p)^4$ for the inverse Compton) and others have relatively small cross-sections ($e^\pm$ pair production, photodisintegration of nuclei). Perhaps the most interesting case is when the photon energy (in the reference frame of the proton) exceeds the threshold for photomeson energy production, then the interaction of both can led to the highly unstable Δ^+ baryon, which decays into π^0 ($p+\gamma \rightarrow \Delta^+ \rightarrow p+\pi^0$) or π^+ ($p+\gamma \rightarrow \Delta^+ \rightarrow n+\pi^+$). The critical energy for this process to take place is

$$E_{th} = m_{\pi^0}(1 + m_{\pi^0}/2m_p) = 144.7\,\mathrm{MeV} \tag{1.30}$$

In the case of the CMB, the required energy for the protons to produce photomesons lies in the range of 10^{20} eV. At intergalactic distances this process attenuates

---

[5] In the case of neutral pions, they decay through the $\pi^0 \rightarrow 2\gamma$ channel.

[6] They can trigger secondary synchrotron emission and inverse Compton scattering.

the flux of cosmic rays making their spectrum much softer. This is the so-called Greisen-Zatsepin-Kuzmin (GZK) effect. The resulting γ-rays have extremely large energies and they immediately interact through pair-production with the same CMB photons, creating a cascade of secondary particles (leptons). Finally, these leptons interact through inverse Compton scattering, contributing to the high energy diffuse γ-ray background [46, 47].

1.3.9 Proton-antiproton annihilation

Antiprotons can annihilate with protons (Fig. 1.4h) to produce pions, from which the π^0 can decay into γ-rays. This is however a rare mechanism because to produce anti-protons we need the interaction of energetic protons with matter and this channel is subdominant with respect to other channels involving the creation of pions (with no anti-proton creation), being only significant if significant antimatter clumps exist in the Universe [48].

1.3.10 Nuclear γ-ray emission lines

The interactions of protons with elements of the surrounding medium that do not carry enough kinetic energy to trigger γ-rays through pion decays can still excite medium nuclei. If radioactive decay (see Figure 1.4b) takes place afterwards (either with the nuclei at rest or in flight), γ-rays with energies of about a few MeV can be produced.

1.4 γ-ray absorption mechanisms

Similarly to γ-ray production and photon energy boosting mechanisms, HE and VHE γ-ray suffer from a number of mechanism that can degrade their energies or even remove them from the medium, some of them (like pair production at cosmological distances) give us information about Optical and IR cosmic background radiation fields (they are described in chapter 10), others are actually exploited in γ-ray detection techniques and can be found in section 3.1.

2

γ-ray sources

Contents

In this chapter, we describe the most relevant high energy γ-ray source types. We base the review in the most complete catalog we probably have in this energy range: the third *Fermi* Large Area Telescope source catalog (3FGL), which includes 3033 sources above 4σ significance. Nevertheless, we must keep in mind that it is an already outdated catalog, which is based only on four years of LAT data processed with the old `PASS7rep` IRFs. A major improvement in the number of sources and their morphological and spectral characterization accuracy is expected for the future 4FGL, which will be based in more than 7 years of data, the new `PASS8` analysis chain a new set of diffuse models. For reference purposes, Figure 2.1 shows simultaneously the HE γ-ray sky as seen by Fermi-LAT and the current VHE γ-ray sky as seen by the H.E.S.S., MAGIC and VERITAS.

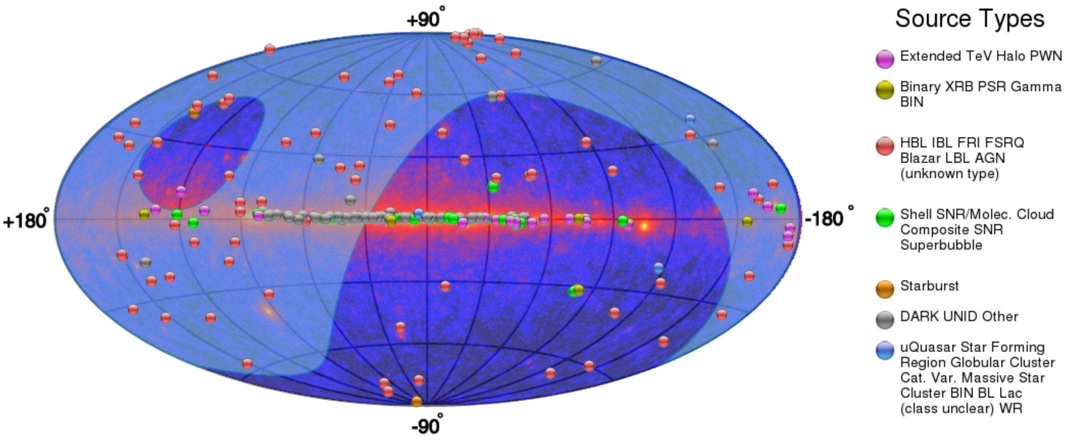

Figure 2.1: Full sky map from TeVCat[49] as of May 2018 showing the sky in HE γ-rays as seen by *Fermi*-LAT, the visibility from the MAGIC site (shadowed region) and the individual sources detected in VHE γ-rays.

2.1 Local γ-ray sources

The most important local γ-ray sources visible in the *Fermi*-LAT band are Terrestrial γ-ray flashes (TGFs) and Solar flares. TFGs are small and frequent ($\sim 1\,\mathrm{min}^{-1}$) γ-ray bursts of $E \lesssim 100\,\mathrm{MeV}$ produced in the atmosphere. They can hit low-orbit satellites.

Solar flares [50] are explosive phenomena visible from radio to γ-rays which are thought to happen during magnetic reconnection events. Particle acceleration happens as the plasma heats up and γ-rays are generated from electron bremsstrahlung (up to tens of MeV), nuclear decays, Hadronic collisions and inverse Compton. Typically, γ-ray flares are associated with Coronal Mass Ejections. After an impulsive phase ($10 - 100\,\mathrm{s}$), a smooth decay can still be a source of significant γ-ray fluxes, as trapped particles precipitate into the solar atmosphere and accelerate through the produced shocks or stochastic turbulence in a closed magnetic loop.

2.2 Galactic Sources

2.2.1 Pulsars

Neutron stars are formed during the gravitational core-collapse of a massive star. The conservation of angular momentum makes the resulting compact object ($\sim 1 - 2M_{\odot}$ in a sphere of $R \sim 10 - 14\,\mathrm{km}$) spin at large velocities ($P \sim 30 - 100\,\mathrm{ms}$) while the one of magnetic flux generates strong magnetic fields ($\sim 10^{8-11}\,\mathrm{T}$). Pulsars are simply neutron stars for which a significant pulsed emission, resembling those of a lighthouse, has been detected in either radio, optical, X-ray or γ-rays. Their rotation powers a radiation field of $\dot{E} \sim 10^{30-32}\,\mathrm{W}$ (10^{4-6} times stronger than the one of the Sun). In about $10^{8}\,\mathrm{yr}$, the period slows down to $\sim 1\,\mathrm{s}$ and the radiation field decreases in intensity to about $10^{22-24}\,\mathrm{W}$.

Old pulsars in binary systems can spin up through angular momentum transfer from a companion star. These pulsars are also known as recycled pulsar and their

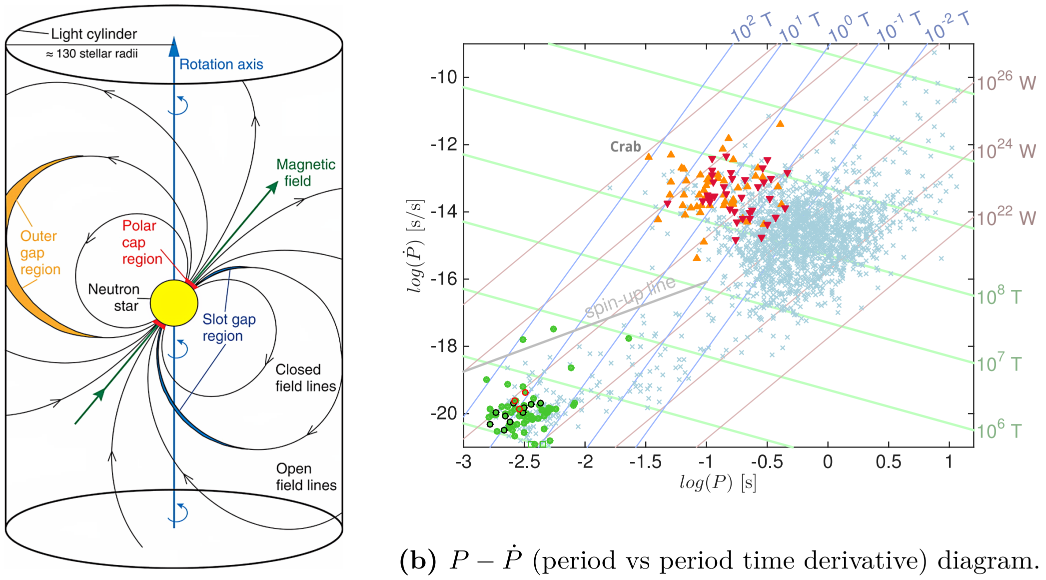

(a) Sketch of the Crab pulsar's magnetosphere (black lines) with the polar cap (red), slot gap (blue) or outher gap (orange) regions. Adapted from [51].

(b) $P - \dot{P}$ (period vs period time derivative) diagram. *Orange triangles*: radio-loud young pulsars detected in γ-rays, *Red triangles*: radio-faint pulsars detected in γ-rays, *Green circles*: radio and γ-loud millisecond pulsars (MSP), *Light blue*: other pulsars, *Green lines*: isolines of constant magnetic field, *Brown lines*: Constant spin-down power, *Blue lines*: lines of constant magnetic field at the light cylinder radius, *Gray line*: spin-up rate expected from mass transfer at the Eddington rate in a binary systems. Extracted from [52].

Figure 2.2: γ-ray pulsar

period drifts down to few milliseconds (hence the name *millisecond pulsars* or MSP). Since the magnetic field is "only" of the order of 10^{4-6} T, their rotational power goes up to only 10^{26-30} W.

The exact mechanism that drives the γ-ray production in pulsars is still an open issue. What most models predict is that the pulsar rotation powers extreme electromagnetic fields that overcome the gravitational well, filling the magnetosphere with charges (typically $e^{\pm}$) through pair production under the strong magnetic fields near the central object. These particles are then dragged at relativistic energies in trajectories following the magnetic lines and are accelerated to very high energies in voids or gaps by the electric fields. The emission of γ-ray emission is then due to synchrotron-curvature or inverse Compton scattering. Finally, far away from the central object, pair-production processes under the strong magnetic and photon fields lead to strong cutoffs in the γ-ray spectrum of these particles.

Where models (Polar-Cap, Slot-Gap, Outer-Gap, etc) differ is in the location of the gaps and which emission mechanism dominates (see Figure 2.2b), which in turn has an impact on the predicted radiation patterns, phaseograms and spectra. For instance, the detection of a power law spectrum from the Crab extending up to very high energies ruled out the Polar Cap model [51]. The detection of TeV emission from this pulsar ruled out synchrotron-curvature (as it would need unrealistic curvature radii of $R_c \sim 20R_{L.Cil}$). The current most-promising scenario [53, 54] predicts a combination of 'curvature radiation' working up to 400 GeV and synchrotron-self-compton emission (SSC) working up to TeV energies. This scenario is at odds with Crab's phaseogram, which suggest similar regions being responsible for the GeV and TeV photons. As of February 2018, only two pulsars are known to exhibit very high energy emission: Crab and Vela [55, 56].

Nevertheless, pulsars are one of the main source populations in the 3FGL. Out of the 3033 sources detected (2023 associated), 143 are pulsars. This number has since then gone up to 205 as statistics increase (more than 7 years for 4FGL[1] vs 4 years in 3FGL). Nearly half of them (92) are milli-second pulsars (MSP, almost all discovered through radio observations) and the rest are young pulsars (close to half identified in radio, another half in gamma and just a few discovered in X-rays).

2.2.2 γ-ray binaries

γ-ray binaries are systems involving a compact object and a massive star [57]. The discovery of 2CG 135+01 in 1978 revealed a binary system composed by a Be star (LS I+61°303 and an unidentified compact object [58]. The source was intriguing back then because it was not only a X-ray emitter, but also a radio source which had periodic bursts [59, 60]. More recently, the source was identified as a microquasar with a relativistic radio-emitting jet and was detected in γ-rays. Its VHE emission was measured to be variable [61] and then identified as periodic [62] with $P = 26.496$ days matching the orbital radio emission with a super-orbital modulation of ~ 4.5 years.

Despite not being detected yet as a VHE emitter, Cyg X-3 deserves a place in this section due to the numerous claims about its VHE emission which were made during the 80s [63–65]. It was discovered in X-rays back in 1967 [66] and its identification as a radio source came soon after [67, 68], with a synchrotron-emitting jet. For a long time, its emission was challenging for existing models [69, 70]. It is believed to be a system composed of a Wolf-Rayet (WR) star [71] and a compact object of $< 10\,\mathrm{M}_\odot$ (a neutron star or a black hole). The orbital period is ~ 4.8 h and the current belief is that the intense photon field from the WR is the cause of the lack of significant VHE γ-ray emission.

As of 2018, there are 9 binary objects identified in VHE γ-rays. TeV J2032+415 was the first one, originally discovered by HEGRA in 2002 [72] and initially proposed as a Pulsar Wind Nebula (PWN) [73, 74]. It was not until recently, with measurements of long-term spin-down rate changes in the pulsar [75], that the source was re-classified as a binary object with an orbital period of $20 - 30$ years. Microquasar LS5039 [76, 77] with an orbital period of only $P \sim 3.9$ days is particularly interesting. It was also discovered by H.E.S.S. [78] and proposed as a miniaturized model of an archetypal Active Galactic Nuclei (AGN), with particle acceleration occurring in relativistic outflows far away from the compact object so that the acceleration happens outside the γ-photosphere of the massive star($\tau_{\gamma\gamma} = 1$). The mass loss from the massive component falls into an accretion disk similar to the one of an AGN, hence the

---

[1] Not yet published

microquasar name. Alternatively, for some sources a shocked *pulsar wind* scenario with a cometary tail of material mimicking a microquasar jet has been proposed.

2.2.3 Novae

In low mass binary star systems, the more massive star evolves faster (going through the giant phase, see Figure 2.3) and leaves a white dwarf and a Planetary Nebula (PNe) behind. When the lower mass companion leaves the main sequence its volume increases dramatically and a significant fraction of the mass of the giant may end up be located outside its Roche lobe [79]. Under these circumstances a mass transfer stream from the giant to the white dwarf is established. The falling material forms then an accretion disk around the latter. Runaway thermonuclear explosions on its surface drive the astrophysical phenomena known as a 'classical nova'.

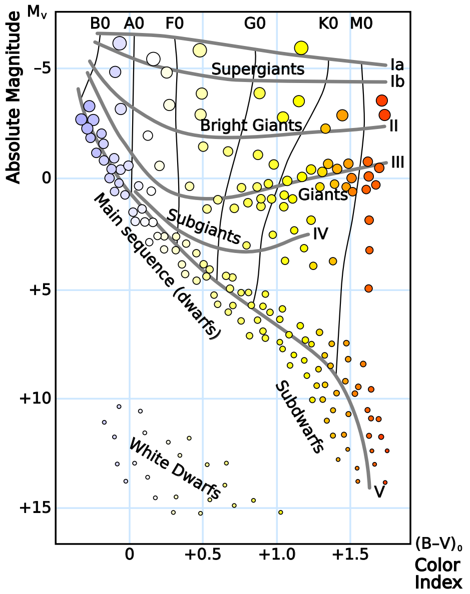

Figure 2.3: Hertzsprung–Russell diagram: classification of stars according to their luminosity and temperature.

A different class of novas are the γ-ray symbiotic binary systems. The first of such objects, V407 Cygni, were detected by *Fermi*-LAT [80]. In contrast with classical novas, in a symbiotic system the ejecta from the white dwarf surface expand within the circumstellar wind of the red giant companion and high-energy particles are accelerated in a blast wave inside a high-density environment. The γ-ray emission in this case is believed to be due to π^0 decay in p-p interactions (Hadronic models) or a combination of high energy electron bremsstrahlung and inverse Compton scattering of the photons from the red giant (Leptonic models).

Coming back to classical novae, five have been detected by *Fermi*-LAT so far [81, 82]. Two mechanisms of γ-ray emission have been proposed so far. The first involves radioactive nuclei emission and positron-annihilation. Nonetheless, no individual novae has been detected using these traces [83]. The second mechanism involves particle acceleration and ejecta quickly expanding into the interestellar medium. In classical novae, the companion star is typically a main-sequence or subgiant star. Then, γ-ray emission cannot be due to stellar winds like in giants. Instead, it is assumed that a bow shock driven by the ejecta, or turbulence and weak internal shocks created in the inhomogeneous ejecta, could be the source of particle acceleration. The emission could then be of either leptonic or hadronic nature.

That said, observations of classical and symbiotic novae in VHE have only resulted in non-detections [84, 85]. From the analysis of upper limits, the contribution of Hadronic emission (protons) can be no more than 15% of the leptonic power.

2.2.4 Supernova Remnants

The explosion of a typical Supernova (SN) provides particles with a total kinetic energy of $W_{SN} \sim 10^{51}$ erg. In the Galaxy they occur at a rate of $\dot{n} \sim (1/50 - 1/100)\,\mathrm{yr}^{-1}$. The resulting structure, known as Supernova Remnants (SNRs), can be classified as: i) bare shell-like objects (e.g. Cas A); ii) composite shells (also known as plerions) with a central pulsar wind nebula (PWN, e.g. G21.5-0.9 or the Crab); iii) mixed type remnants with 'plerionic' emission only in some wavelengths (typically X-ray, sometimes also radio) enclosed by a radio shell (e.g. W28 or W44).

Emission from the remnant

SNRs are considered one of the most promising source populations of galactic Cosmic Rays accelerated via Diffuse Shock Acceleration (DSA). The total inferred cosmic ray luminosity in the Galaxy is $L_{CR} \sim 2 \times 10^{41}$ erg/s, which can be explained if SN occur at a rate of one in 50 years and hadrons carry at least 10% ($\epsilon_{CR} = 0.1$) of the kinetic energy released in the explosion [86]. Moreover:

- The spectrum of CRs is well reproduced by these SNR ($\sim E^{-2.1-2.4}$) assuming that the confinement time in the Galaxy decreases with energy as $t_{\mathrm{esc}} \propto E^{-s}$ ($s \approx 0.3 - 0.6$) and that protons can be accelerated at least up to the knee ($\sim 5 \times 10^{15}$ eV for protons, $\sim 10^{17}$ eV for Fe).
- Leptons can be accelerated up to TeVs according to X-ray observations, indicating Strong magnetic fields and implying possible shock-driven hadron acceleration.
- IC scattering efficiency is reduced at multi-TeV energies due to Klein-Nishina effect.
- Pion-decay signatures have been found in γ-ray spectra of old SNRs in *Fermi*-LAT.

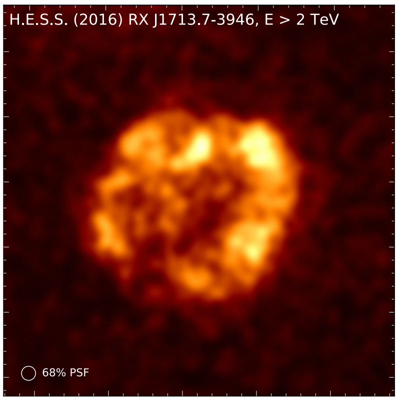

Figure 2.4: SNR RX J1713.7-3946 as seen by H.E.S.S. [87].

Hadron acceleration mechanisms can work only during a relatively short period of time. In the first phase of the SNR expansion, also known as free-expansion phase, $M_{\mathrm{ejecta}} > M_{\mathrm{swept\ up}}$ and the ejecta has a nearly constant velocity. The maximum energy reachable by the particles is $E^{CR}_{\mathrm{max}} \propto t_{\mathrm{age}}$. The SNR transitions then to the Sedov-Taylor or adiabatic phase as soon as $M_{\mathrm{ejecta}} < M_{\mathrm{swept\ up}}$. During this phase the shock slows down and the energies reachable by the accelerated particles progressively degrades as $E_{max} \propto t_{age}^{-\alpha-1/5}$) [88]. In this scenario, the highest "PeV" energy particles are accelerated in the very beginning of the Sedov phase when the shock speed is high and escape as the shock slows down. Progressively, lower

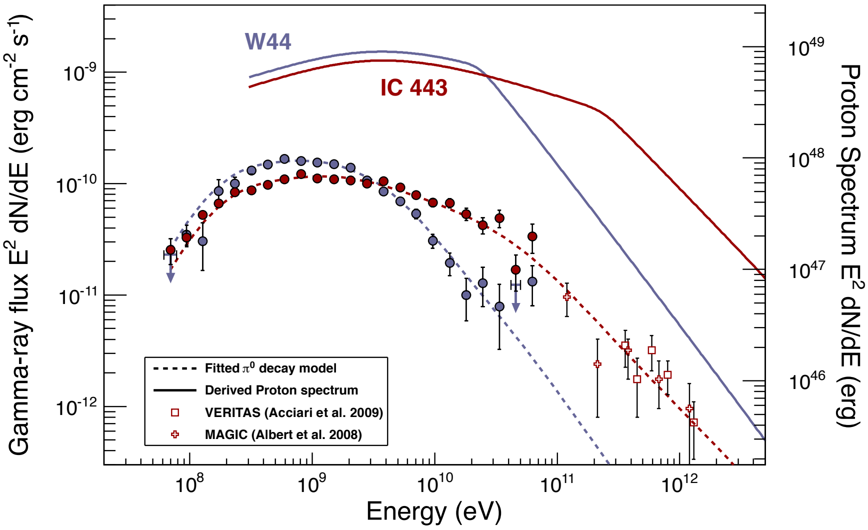

Figure 2.5: Hadronic models for two SNRs [89].

energy particles can leave the SNR too. This may explain the lack of SNRs having strong emission above 10^2 TeV, as the PeVatron phase lasts for a very short time.

CR chemical composition, while coarsely reproduced by SNR models, seems more likely to be originated in a mixture of massive star ejecta and normal interstellar medium, suggesting that OB stellar associations, their stellar winds and superbubbles/cavities produced in Super Nova (SN) explosions may be the source of CRs.

VHE γ-rays have been detected in several bright SNRs [90]. While leptonic emission models can approximately describe the observed γ-ray spectra through inverse Compton scattering of CMB photons, recent observations of very young shell-like SNRs like Tycho [91] and Cas A [92] showed that hadronic emission is sometimes preferred. In hadronic models, decays of secondary π^0-mesons can potentially explain the bulk of the γ-ray emission[93]. The detection of TeV γ-rays in bright SNRs [87] was a promising way to test this model. Nevertheless, the idea of SNR explaining the CR spectra up to knee energies faces its own problems, as the rate of expansion seems to be too slow in young SNRs [94]. For older SNRs like RX J1713.7-3946, the much larger collection area at higher energies of CTA will be needed to fully solve the puzzle of their hadronic/leptonic emission [95].

Emission from the Pulsar Wind Nebulae

Pulsar wind nebulae (PWNe) are a type of nebulae found in some SNRs (plerions). They are clouds of largely magnetized ($u/K \gg 1$ where u is the Poynting flux and K the lepton kinetic energy flux) $e^{\pm}$ plasma that extend up to several parsec. They are powered by the energetic winds or outflows of a young pulsar embedded in a supernova remnant. These winds generate a reverse (or termination) shock which collides with the surrounding environment, triggering particle acceleration via DSA [96]. PWNe are dominated by non-thermal emission, namely synchrotron at low energies (the index varies with the radius) and inverse Compton upscattering of

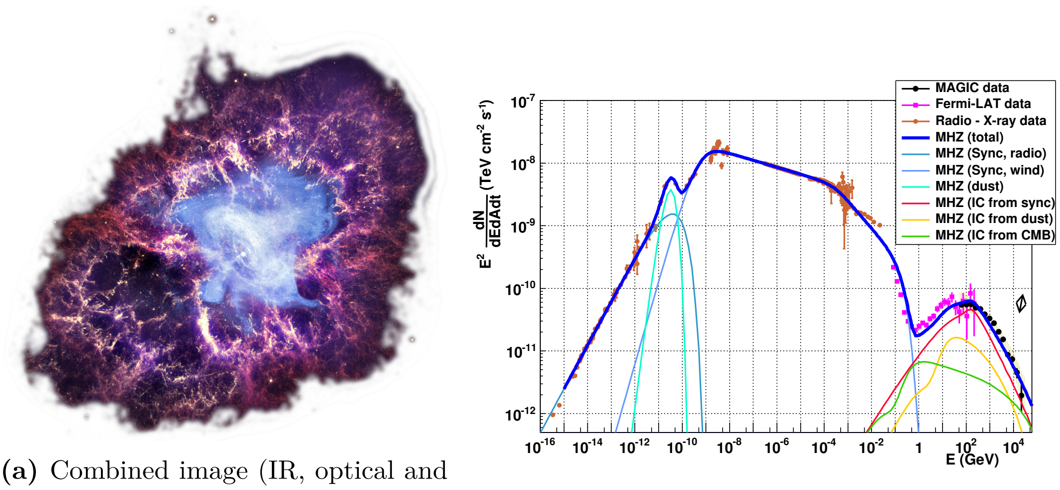

(a) Combined image (IR, optical and X-ray) of the Crab's SNR (red, purple) and PWN (blue). Credits: NASA, ESA and JPL-Caltech.

(b) Multi-component emission model for the Crab Nebula including thermal dust radiation from Meyer, Horns, and Zechlin [99]. Figure adapted from [100].

Figure 2.6: Broadband emission from the Crab Nebula.

ambient photons (including Far Infrared, CMB, SSC) at high energies. Interestingly, Compton dominance (ratio of the maximum energy flux from inverse Compton and from synchtrotron) seems to grow as the PWNe ages [97, 98].

PWNe are the most abundant Galactic VHE gamma-ray source class with 34 identifications as of November 2017[2]. They are found related to young and energetic pulsars that power highly magnetized nebulae ($B \sim 1 - 100\,\mu$G).

These sources can be divided according to their age. Young PWNe (Crab like) show a correlation between the X-ray emitting region morphology and the γ-ray one while in old PWNe (Vela-X like) often the pulsar powering the nebula is found misaligned with respect to the TeV emission and the X-ray and VHE γ-ray morphologies are different.

Current PWNe models distinguish between two populations of electrons. On one hand, low energy relic electrons, with energies too low to generate significant synchrotron emission in X-rays, but capable of producing VHE γ-rays through inverse Compton scattering of ambient photons (eg: CMB, starlight). This inverse Compton scattering traces the electron plasma, independently of the inhomogeneous and time evolving magnetic fields [101]. X-ray emitting electrons on the other hand trace more recent stages of the PWNe evolution. The emitting region is more compact and severe radiative losses originated from the strong magnetic field are expected. This may explain the above commented difference between young and old PWNe.

2.2.5 The Fermi Bubbles

The Fermi bubbles [102] are two large γ-ray lobes that were discovered [103] while searching for the γ-ray counterpart of the WMAP haze [104] (the residual microwave

---

[2] `http://tevcat2.uchicago.edu/`

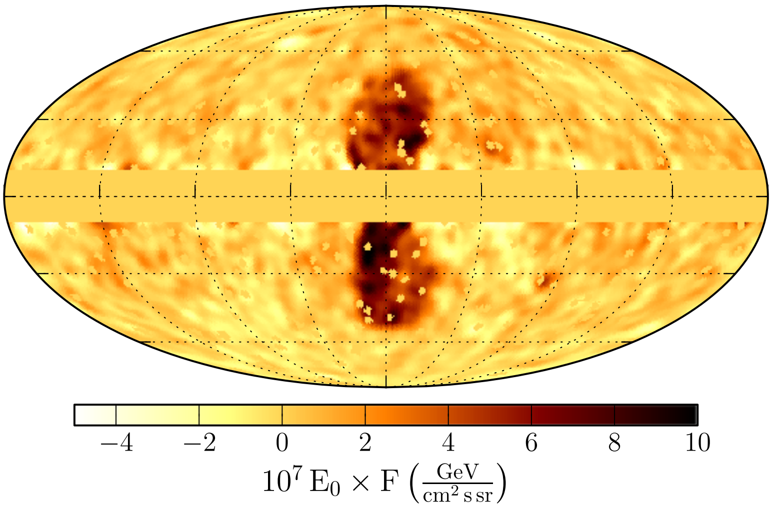

Figure 2.7: Fermi Bubbles as seen by the LAT at $E = 10 - 500\,\mathrm{GeV}$ [102].

emission around the Galactic center that remains after subtracting synchtrotron, free-free, thermal dust and the CMB components from the WMAP data).

The bubbles resemble the jets in Centaurus A and the starburst features of M82. They extend $\sim 55°$ above and below the Galactic center (GC) and are not symmetrical, but enhanced towards the south-east side of the bubbles. They have sharp edges, suggesting a transient nature, and an uniform spectrum with an index of $\Gamma \sim 2$ and a cutoff or significant softening above $\sim 100\,\mathrm{GeV}$.

Several possible origins have been suggested:

- Present emission of a jet from the GC black hole [105].
- Recent AGN activity [106], perhaps in the form of spherical outflow from the black hole [107] or a sequence of shocks from accretion events [108].
- Winds from SN explosions and accumulation of CR from regular star formation or from starburst activity in the past (star driven) [109]. The SN explosions could be even unrelated to the Galactic center, although this scenario is disfavored by the lack of strong synchrotron emission from WMAP and Planck observations.

The γ-ray production mechanisms is also unclear, with both leptonic (inverse Compton scattering of high-energy electrons on radiation fields [110]) and hadronic (collision of CR protons with diffuse gas in the bubbles [109]) models being able to roughly explain the observations, although they both have their own limitations. Leptonic models are appealing as they explain both radio and γ-ray observations using a common electronic population. If the emission is predominantly leptonic, a low energy component could be explained naturally as being due to synchrotron emission. Observations in X-rays using ROSAT [110] and Suzaku [111] and in radio with S-PASS [112] and VHE have been conducted to look for multi-wavelength counterparts. Leptonic models are however in tension with the fact that no shock

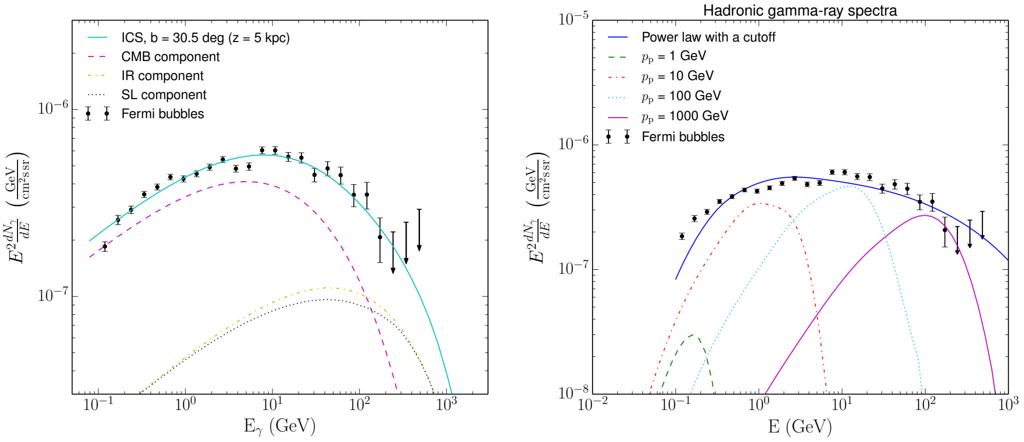

(a) Leptonic **(b)** Hadronic

Figure 2.8: Spectral Energy Distribution (SED) of the Fermi bubbles. Adapted from [102].

front at the boundary of the bubbles has been observed.

In hadronic models, a π^0-cutoff is expected below 100 MeV. This is however not observed in the *Fermi*-LAT spectrum. This mismatch can be however resolved by incorporating secondary IC emission from leptons produced in the hadronic interactions [113].

2.3 Extragalactic Sources

2.3.1 Neighbour galaxies: LMC, SMC, M31 and M33

The Large and Small Magellanic clouds are two irregular (or dwarf barred spiral) galaxies that are visible from the southern hemisphere. They belong to the Local Group of galaxies and are the place of intense star formation. The presence of a bridge of gas connecting them shows that both are gravitationally bound.

Already from COS-B [114, 115] and CGRO [116] times, significant γ-ray emission from the Magellanic clouds was predicted based on cosmic ray interactions with the interstellar medium (ISM). The main channel for these hadronic interactions would be the neutral pion decay (other channels such as decay of hyperons and K and η-mesons account for only $10-20\%$ of the emission and are thus typically neglected) with electron bremsstrahlung as the second process in relevance [117]. It was not until EGRET that significant γ-ray excess coming from the direction of the LMC was detected using 4 weeks of data. The interpretation of these γ-rays ($F_{E>100\,\mathrm{MeV}} = (1.9 \pm 0.4_{stat}) \times 10^{-7}\,\mathrm{ph\,cm^{-2}s^{-1}}$) as being due to hadronic interactions suggested a CR density similar to that of the Milky Way and made the LMC the first normal galaxy detected (apart from our own) in HE γ-rays. The SMC was detected as well several years later with EGRET's successor, *Fermi*-LAT, after 17 month of continuous all-sky observations. The emission in this case is at the level of $F_{E>100\,\mathrm{MeV}} = (3.7 \pm 0.7_{stat}) \times 10^{-8}\,\mathrm{ph\,cm^{-2}s^{-1}}$. No variability signatures were detected and the estimated CR density was of the order of $\lesssim 15\%$ of those of the

Galaxy, even less if the large population of HE pulsars in the SMC are taken into account. Such low densities suggest a small confinement volume in that galaxy.

More recent observations of the LMC with *Fermi*-LAT and H.E.S.S. have confirmed the diffuse and extended emission that EGRET detected, which corresponds to a large-scale GeV CRs with a density of 30% of the Galaxy density. This emission seems to be correlated with heavy star-formation tracers such as Hα from Wolf-Rayet stars, e.g. 30 Doradus). The observations have revealed also individual sources [118]:

- PSR J0540-6919: Pulsed γ-ray emission leading to the discovery of the first extragalactic γ-ray pulsar and the most powerful one (γ-ray luminosity of $\sim 5.7 \times 10^{36}\,\mathrm{erg\,cm^{-1}}$, ~ 20 times the Crab pulsed luminosity and up to 4 times its X-ray luminosity). It accounts for $\sim 60\%$ of the GeV emission previously attributed to the 30 Doradus nebula [119]. A similar period and magnetic field strength makes it be known as the Crab-twin.
- PSR J0537-6910 / N157B: With a period of $P \approx 16\,\mathrm{ms}$, its origin is thought to be in the SN explosion of a $\sim 25 M_\odot$ star linked with the LH99 OB association. The γ-ray emission (also detected by H.E.S.S. [120]) is thought to be due to the large spin-down power of the pulsar and the rich IR photon field environment. The total luminosity between 100 MeV and 100 GeV is $5.2 \times 10^{36}\,\mathrm{erg\,s^{-1}}$.
- Unassociated emission with a soft spectrum of $\Gamma = 2.8 \pm 0.1$, possibly from the HII regions NGC 2029/2032, SNR DEM L 241 or the Seyfert I galaxy 2E 1445.
- SNR N 132D, also seen by H.E.S.S. [120]. It has an age of 2500 yr and is the brightest remnant of the LMC in X-rays. Its luminosity and hard spectrum ($\Gamma = 1.4 \pm 0.3$ at LAT energies, 2.4 ± 0.3 at H.E.S.S. energies) makes it challenging for leptonic models.

Similarly, *Fermi*-LAT has observed other large star-forming galaxies in the Local group such as M31 and M33 [121] and in other groups (M82, NGC253) [122], the last two also seen by IACTs. They are however at least one order of magnitude more distant and cannot be spatially resolved in individual sources, so the origin of their γ-ray emission is still unclear.

2.3.2 GRBs

Gamma-Ray Bursts (GRBs [123]) are short ($1\,\mathrm{s} < \tau \lesssim 10^2\,\mathrm{s}$) and intense pulses of γ-rays that are found almost isotropically. They are linked to star-forming regions and their origin is thought to be either neutron star mergers or very massive star collapses (hypernovae). Although seen also in low frequencies (e.g. optical), we will focus only on the high energy component, which typically spreads from few keV to at tens of GeV [124]. So far, no GRBs have been detected in VHE. Their luminosity ($\sim 10^{51-52}$ erg/s) and strong beamed emission makes them the most luminous objects in the sky (comparable to SNe) and allows them to be detected at large distances (often $z > 1$). They exhibit a bimodal burst duration distribution [125], which separates long bursts ($T_{90} > 2\,\mathrm{s}$) from short bursts ($T_{90} < 2\,\mathrm{s}$), where

T_{90} was defined as the time needed to accumulate from $5 - 95\%$ of the counts in the $50 - 300\,\mathrm{keV}$ band of the BATSE monitor. GRBs have long lasting (up to years) low energy afterglows from radio to X-rays.

The current most accepted scenario to explain GRB emission is the so called fireball model [126]. A compact "inner" hidden engine produces a wind (long energy flow) which interacts with the ISM or with internal shocks, converting part of the kinetic energy to radiation in an optically thin region (prompt emission). The remaining kinetic energy will most likely dissipate via external shocks, producing the observed afterglow.

GRB typically exhibit two components in their spectral energy distribution [125]. Pure leptonic scenarios could explain the fast variability, but have problems to explain the hard spectrum, the high radiative efficiency (if synchrotron emission is assumed), the low energy extension (down to keV) and the emission afterglow (if inverse Compton is invoked). In order to explain the afterglow, external shocks have been proposed. They would form in the interaction between the jet and the surrounding medium and can potentially explain the relative stability of the high energy component as opposed to the fast variability found at lower energies. Hadronic scenarios in the form of proton synchrotron emission and/or IC of secondary $e^{\pm}$ pairs produced in internal cascades have been also proposed. The delayed component is explained naturally as the time required to accelerate protons and produce cascades. Fast pulses at high-energies are however left unexplained.

2.3.3 Active Galactic Nuclei

Among the γ-ray galaxies described before, those powered only by hadronic interactions with the ISM account for only a few, close, objects. The vast majority of galaxies detected in GeV and TeV are powered by massive black holes and they are popularly known as Active Galactic Nuclei (AGNs). They constitute the main topic of this work and are discussed in detail in chapter 6.

Part II

Instrumentation for High Energy Astrophysics

> “*Galileo Galilei, a most humble servant of Your Serene Highness, (...) appears before You with a new contrivance of glasses [occhiale], drawn from the most recondite speculations of perspective, which renders visible objects so close to the eye and represents them so distinctly that those that are distant, from example, 9 miles appear as through they were only 1 mile distant.*”
>
> —GALILEO GALILEI, Letter to the Doge (Venice, 1609).

3

Detection Techniques

Contents

3.1 Detection of γ-rays from space

Only small portions of the electromagnetic spectrum can be transmitted through the Earth's atmosphere without absorption or distortion. They are known as atmospheric windows (see Figure 3.1) and can be subdivided in two parts: a) radio window, with wavelengths ranging from several meters to a few millimeters (radio window) and b) infrared-optical window, from tens of micrometers to hundreds of nanometers, for which atmospheric scattering and absorption heavily depends on the particular wavelength of the radiation. The discontinuous transmission properties of the latter is one of the reasons taken into account in the definition of photometric bands.

Below $200 - 300\,\mu$m, Earth's atmosphere becomes fully opaque. The only

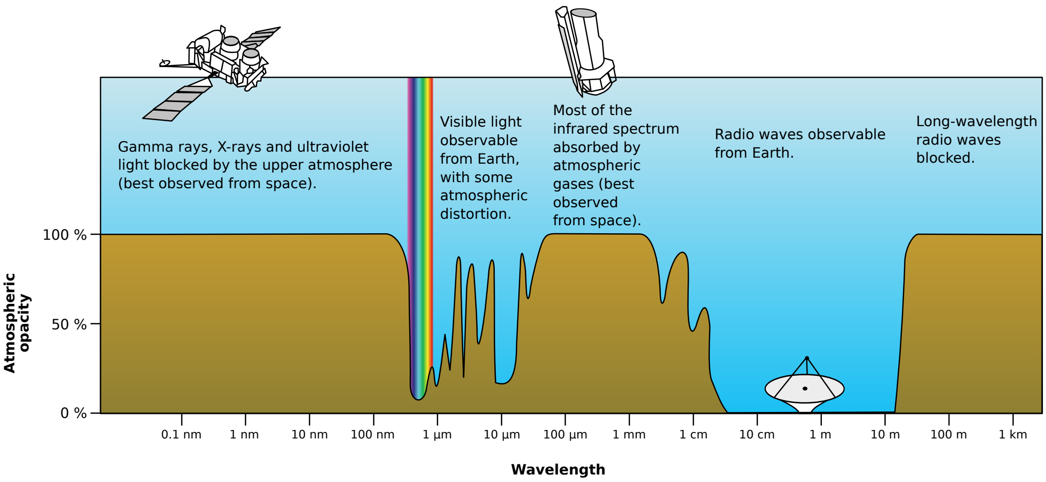

Figure 3.1: Atmospheric windows. Credits: NASA

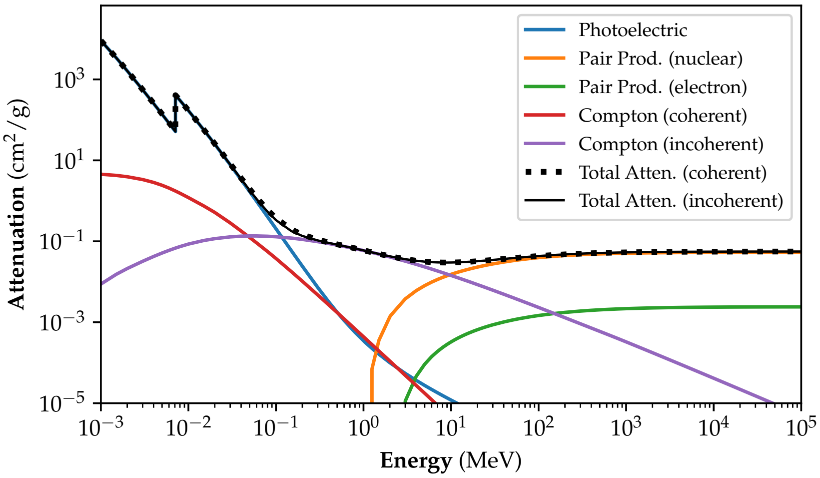

Figure 3.2: Cross Sections as a function of energy for different photon interactions in Iron. Data from NIST[1]

possibility to observe directly the Universe in this energy range is by means of high altitude balloons and spacial probes. This is no exception for γ-ray measurements, which started to develop in parallel with X-ray astronomy back in the 60s and 70s. Contrary to X-rays, high energy (HE) γ-rays cannot be focused, hence the effective detection area is restricted to that of the detector itself, which for space missions is of the order of $\sim 1\,\mathrm{m}^2$. Since particle (and photon) fluxes decrease rapidly as energy increases, HE missions are restricted to below $\sim 100\,\mathrm{GeV}$ (see chapter 4). For higher energies, much more elaborated detectors need to be built on Earth that detect the incoming γ-rays indirectly (see section 3.4.4). Additionally, γ-ray experiments suffer from large and troublesome backgrounds of charged cosmic rays.

The detection techniques used in γ-ray astronomy were already known from

---

[1] `https://www.nist.gov/pml/xcom-photon-cross-sections-database`

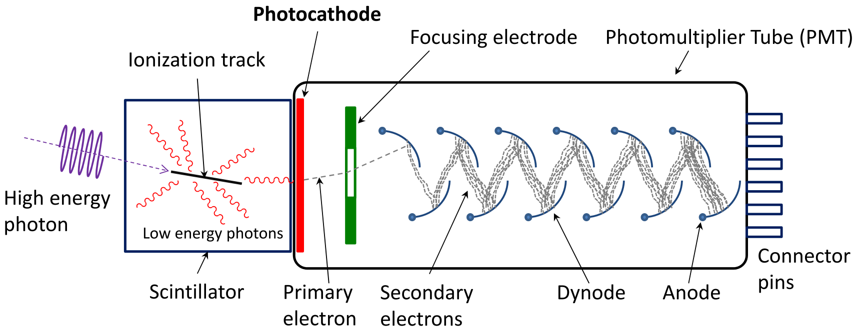

Figure 3.3: Schematic view of a photomultiplier coupled to a scintillator, illustrating detection of gamma rays. Credits: Wikipedia's user *Qwerty123uiop*.

particle physics and exploit our knowledge of γ-ray interaction processes (already discussed in section 1.3). As it can be seen in Figure 3.2, low energy photons primarily interact through the *photoelectric effect*. The photon is fully absorbed ejecting an electron with maximum energy $h\nu$ from the inner shells of an atom. X-rays and Auger electrons are then emitted as the vacant is filled in cascade. The *Compton effect* (see 1.3.5) is the mean interaction channel from ~ 0.1 MeV up to ~ 10 MeV. The process takes place when photons are (inelastically) scattered by atomic electrons. An energy transfer happens between both particles. Above a few MeV *pair production* takes over (see also 1.3.6) and becomes the only way to detect the incoming particles of $E > 100$ MeV. For electron-positron pair production to occur, the energy of the incident particle must be at least twice the rest energy of the electron (511 keV) and the interaction must happen near a nucleus (larger masses giving higher interaction probabilities). Greater energies translate into higher kinetic energy of the new particles.

In scintillation detectors (the prototypical γ-ray detector) the three processes mentioned above can take place. The incident γ-ray leaves a trace of charged particles (electrons) and scattered γ-rays that can excite atoms in the scintillation tube, which in turn emit UV and optical radiation as they decay into the fundamental state. These low energy photons can then be detected with a photomultiplier tube (PMT). For the pair production and photoelectric effects, all the energy is deposited and can be measured. For the Compton effect, part of the energy remains on the scattered photon and can escape. This is particularly true for thin scintillators, which can be opaque for charged particles but nearly transparent to γ-rays, making them ideal for background rejection in γ-ray telescopes.

3.2 Ground based γ-ray experiments

Since γ-ray fluxes strongly decay with energy, space-based missions stop being competitive at $\gtrsim 10^2$ GeV. The flux of charged particles falls as $\sim E^{-2.7}$ and for photons the situation is not much better. For instance, the inverse Compton peak of the Crab pulsar wind nebula, the standard candle in VHE γ-ray astronomy, can be roughly fitted by a modified Log Parabola from ~ 1 GeV to at least ~ 20 TeV [100].

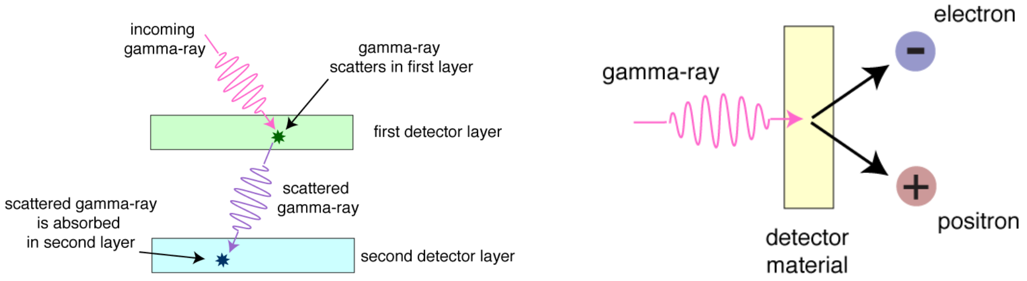

(a) Sketch of a Compton scattering detector. Credits: NASA's Imagine the Universe.

(b) Sketch of a pair production detector. Credits: NASA's Imagine the Universe.

Figure 3.4: Detection of γ-rays through Compton and pair production processes.

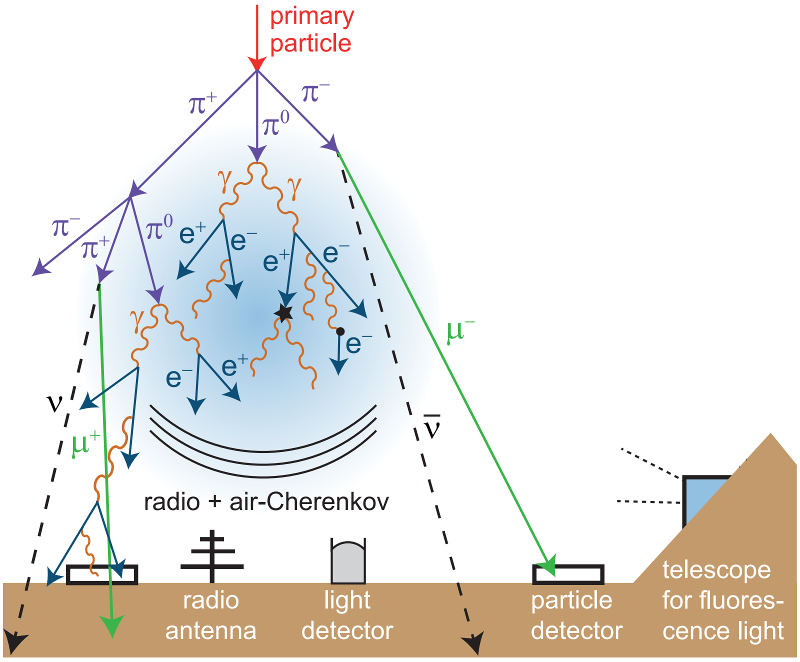

Figure 3.5: Schematic view of a cosmic ray (hadronic) initiated cascade and the possible instruments that can be employed to characterize it [127].

$$E^2\frac{dN}{dE} = 10^{\log f_0 + C(\log(E/E_{IC}))^a} \tag{3.1}$$

where $C = -0.120 \pm 0.008$, $\log(f_0) = -10.248 \pm 0.006$, $E_{IC} = (48 \pm 2)\,\mathrm{GeV}$ and $a = 2.5 \pm 0.1$. At $\sim 50\,\mathrm{GeV}$ (the threshold energy of the 2FHL) the differential energy spectrum is $dN/dE \sim 2.3 \times 10^{-8}\,\mathrm{ph/cm^2/s/TeV}$. At $\sim 5\,\mathrm{TeV}$, it is $\sim 4.8 \times 10^{-13}\,\mathrm{ph/cm^2/s/TeV}$. The number of events decreases $\sim 5 \times 10^4$ times in this energy range.

Ground based instruments have typical collection areas of $\sim 10^5\,\mathrm{m}^2$ (to be compared to $\lesssim 1\,\mathrm{m}^2$ in space-based telescopes) and take advantage of the absorption of γ-ray photons by the atmosphere. The interaction of a high energy photon or any high energy particle with an atmospheric atom generates a large number of secondary particles in cascade, also known as *extensive air showers* or EAS [128–131] (see Figure 3.5).

3.3 Extensive air showers (EAS)

3.3.1 Electromagnetic showers

Two processes are the ultimate responsible for the development of atmospheric electromagnetic showers: a) Pair production $e^{\pm}$ in the electric field of the atmospheric nuclei and b) Bremsstrahlung emission by $e^{\pm}$ in the same electric field [132], releasing new high energy photons. The resulting bremsstrahlung spectrum is roughly

$$\frac{dN_{ph}}{dE_{ph}} \propto E_{ph}^{-1} \tag{3.2}$$

Photons generated with large enough energies trigger subsequent $e^{\pm}$ pair creation, which in turn undergo more bremsstrahlung. The shower maximum is reached when the ionization and radiation energy losses become equal [34], slowly dying afterwards.

The characteristic mean free path for pair production and bremsstrahlung is:

$$X_0 = \left[4\alpha r_e^2 \frac{N_A}{A} Z^2 \ln\left(183 Z^{-1/3}\right)\right]^{-1} \mathrm{g\,cm^{-2}} \tag{3.3}$$

where $\alpha = 1/137$ is the fine structure constant, r_e the classical electron radius and N_A the Avogadro number. In the atmosphere, this quantity is roughly $\sim 37\,\mathrm{g\,cm^{-2}}$ for electrons.

The shower development can also be approximated by analytical expressions (see Approximation B from [133]). We start by defining the atmospheric depth T and the shower age s as

$$s = \frac{3T}{T + 2\ln\left[\frac{E_\gamma}{E_C}\right]} \qquad \text{and} \qquad T = T_0 e^{-H/H_0} \tag{3.4}$$

where E_γ is the energy of the incident γ-ray, $E_C = 83\,\mathrm{MeV}$ is the so called 'critical energy', $H_0 = 8.4\,\mathrm{km}$ is the scale-height of the atmosphere and $T_0 = \frac{X_{air}}{X_0 \lambda \cos\theta}$ ($X_{air} \sim 1013\,\mathrm{g\,cm^{-2}}$) is the column height of air at sea level. Values of $s = 0$, 1 and 2 mark the beginning, maximum and dying point of the shower and $s \to 3$ for $T \to \infty$.

The longitudinal development of the shower can then be approximately described by the Greisen equation (see [134], section 1.3):

$$N_e(E_p, t) = 0.31\left[\log\frac{E_\gamma}{E_C}\right]^{-1/2} e^{T[1-(3/2)\log s]} \tag{3.5}$$

The atmosphere is a thick and very inhomogeneous calorimeter of ~ 27 radiation lengths, to be compared with $\sim 10\,X_0$ for γ-ray satellites. Due to the rapid decrease in density with altitude, the shower development is faster near the ground than it is at $\sim 10\,\mathrm{km}$. For an isothermal atmosphere in hydrostatic equilibrium, the shower

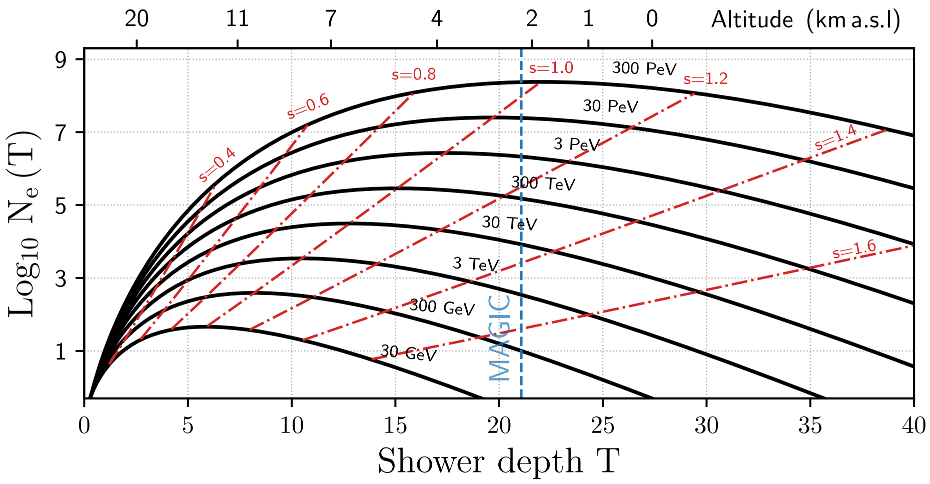

Figure 3.6: Longitudinal development of a γ-ray shower in the Greisen approximation 3.5. Reproduced from [31, 32].

maximum slowly decreases in altitude with energy ($X_{max} \propto \log E_\gamma$) and the number of particles at the shower maximum is proportional to the energy of the primary. Altitude has hence an effect on the range of possible energies covered by instruments detecting EAS, with higher altitude instruments generally having lower energy thresholds.

Similarly, the lateral distribution in the region $0.5 \lesssim s \lesssim 1.5$ can be roughly described by the Nishimura-Kamata-Greisen function [135]:

$$f(r) = \frac{\Gamma(4.5-s)}{\Gamma(s)\Gamma(4.5-s)} \frac{N_e}{2\pi r^2} \left[\frac{r}{r_m}\right]^{s-2} \left(1+\frac{r}{r_m}\right)^{s-4.5} \tag{3.6}$$

where r is the distance from the shower centre, N_e the number of electrons at a given depth level and $r_m \sim 21(X_0/E_c)$ MeV the Moliére radius (a key parameter in the multiple scattering theory), $r_m \sim 78$ m at sea level. From this expression, the density of electrons can be expressed as $\rho_N(r, E, T) = N_e(E, T)/r_m^2 f(r)$.

In the real world, additional processes can play a role in the shower development of electromagnetic cascades [136]: multiple scattering of charged particles, ionization and atomic excitation leading to energy losses in $e^\pm$ with energies below E_C, positron annihilation with ambient electrons resulting in a $10-20\%$ excess of high energy negative charges [137], which in turns produces coherent microwave radiation through the 'Askaryan effect', and further broadening of the cascade in the East-West direction due to Earth's magnetic field.

3.3.2 Hadronic showers

Hadronic particles and nuclei also create particle showers when they interact with atmospheric nuclei. The interaction is in general more complicate to describe because hadron originated showers are subject to fragmentation (nuclear fragments resulting from collisions with atmospheric nuclei, nucleons, π and K mesons). Electromagnetic components from the decay of π^0 and neutrinos and muons $\mu^\pm$ from the decay of charged mesons ($\pi^{\pm}$ and $K^{\pm}$) are some of the possible end products. The long mean life of the muon together with its small bremsstrahlung cross-section leads to high probabilities of these particles to reach the ground. The resulting shower tends to be more irregular and clumpy. The difference in shape and development is, in fact, a powerful γ-hadron discrimination tool. The presence of a muon signal is also used to assist in γ-hadron separation [138]. Another characteristic of hadronic showers is that their absorption length is larger ($\lambda_h \approx 90\,\mathrm{g/cm^2}$) than the one for γ-rays, making them able to penetrate deeper into the atmosphere. The last important difference is their origin. Since hadrons are originally charged particles, they are deflected by magnetic fields and they do not point towards the direction of their original sources, but they are isotropically distributed.

3.4 Types of detectors

EAS can be detected by particle detectors, by the Cherenkov radiation produced by their ultrarelativistic particles or through fluorescence detectors (see Figure 3.5).

3.4.1 Particle detectors

The most direct way to characterize an EAS is by means of its particles and secondary γ-rays, using air shower detectors or particle counter matrices. Direct detection of the shower from a γ-ray is only possible at energies of $\sim 10^{14}\,\mathrm{eV}$ and beyond (e.g. CASA-MIA [139] or LHAASO-KM2 [140]) or by placing the instruments at very high altitudes. This effectively reduces energy thresholds to more reasonable few TeVs ($\sim 10^{12}\,\mathrm{eV}$) in sparse sampling detectors (e.g. HEGRA [141], Tibet AS [142]) or hundreds of GeV ($\sim 10^{11}\,\mathrm{eV}$) using compact sampling water Cherenkov detectors (e.g. MILAGRO [143], ARGO-YBJ [144] or HAWC [145]). The advantage of detectors of this kind is their very wide FoVs, sampling a large fraction of the sky simultaneously and their robustness and stability due to the lack of moving/tracking parts. One has to add the large duty cycles, as they can in fact be operated during the day. The disadvantage, compared to Imaging Air Cherenkov Telescopes, is their limited instantaneous sensitivity.

3.4.2 Fluorescence detectors

Extensive Air Showers traversing the atmosphere excite nitrogen molecules, which in turn emit fluorescence light at $\lambda \sim 300-430\,\mathrm{nm}$. The number of fluorescence photons emitted is roughly proportional to the energy deposited by the incident particle due to electromagnetic losses. The fluorescence yield, defined as the number of photons emitted in a given waveband per energy loss by charged particles, depends on pressure, temperature and humidity of the air, but for typical atmospheric conditions is a few photons per MeV deposited energy [146, 147].

The technique has been widely used to characterize ultra-high-energy ($\gtrsim 10^{18}\,\mathrm{eV}$) cosmic rays. Previously used by Fly's Eye detector [148, 149] and HiRes [150], the study of the fluorescent yield of UHE cosmic rays became one of the main goals of

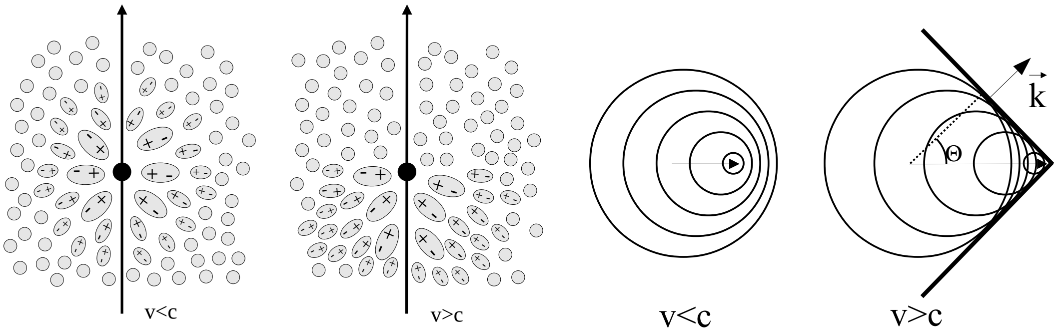

(a) Environment polarization from non-relativistic and ultra-relativistic particles [32].

(b) Wavefront generated from a non-relativistic and ultra-relativistic particles.

Figure 3.7: Cherenkov polarization and wavefront generated from moving charges [155].

the Pierre Auger observatory [146, 151] and the Telescope Array [152]. There are proposals to extend their use to the Cherenkov Telescope Array (CTA) [153].

Since typical cosmic ray showers have lengths of $\sim 10\,\mathrm{km}$, it is important to design the fluorescence telescopes with very wide field of views ($\sim 30\,\mathrm{deg}$) in order to cover the longitudinal development of the shower. Cameras are typically composed of PMT pixels. The timing sequence of triggered pixels helps to reconstruct the direction of the event and allows to discriminate legit showers, for which pixels are triggered sequentially, from local background events, where the pixels are triggered simultaneously). As opposed to Cherenkov flashes, the total fluorescence emission from the shower as seen by the detector lasts few μs[2]. The significantly longer integration times require further night sky background shielding (using UV-pass filters). The energy reconstruction of the shower is done by fitting and integrating the Gaisser-Hillas function to the energy deposit profile [154].

3.4.3 Atmospheric Cherenkov detectors

Ultra-relativistic particles in the shower, traveling faster than the (local) speed of light in a material (of refraction index $n > 1$), produce coherent polarization of the dielectric medium (see Figure 3.7a), which in turn emits beamed Cherenkov light in the forward direction. The emitted radiation forms a cone with characteristic angle given in first approximation (neglecting photon recoil) by the Huygens principle: $\cos\theta_c = [\beta n]^{-1}$ (see Figure 3.7b). Since there is a minimum $\beta = v/c$ for which the emission takes place, this translates into a threshold energy for the charged particle, given by

$$E_{C,th} = \frac{m_0 c^2}{\sqrt{1-\beta_{min}^2}} = \frac{m_0 c^2}{\sqrt{1-1/n^2}} \tag{3.7}$$

The total Cherenkov yield is given by [156]:

$$\frac{d^2N}{dx\,d\lambda} = \frac{2\pi\alpha z^2}{\lambda^2}\sin^2\theta(\lambda) = \frac{2\pi\alpha}{\lambda^2}\left(1-\frac{1}{\beta^2 n^2(\lambda)}\right) \tag{3.8}$$

---

[2] Each pixel sees the fluorescence flash for about $\sim 10^2$ ns

Interestingly, the total amount of Cherenkov light produced in an EAS is almost proportional to the energy of the primary particle (~ 500 photons per GeV of primary γ-ray assuming fast electrons, $z = 1$ and $\beta \approx 1$), making the atmosphere a good calorimeter, specially for γ-rays and electrons.

Cherenkov radiation was first studied in solid and liquid media by P. A. Cherenkov in 1934 [157, 158] and classically described in terms of Maxwell's equations by Frank and Tamm [159]. It was not until ten years later that Cherenkov radiation was predicted to occur also in the atmosphere [160] and to contribute to up to 10^{-4} of the night sky background (NSB). It was finally observed using a system which consisted on a reflector, a PMT and an oscilloscope by Galbraith and Jelley in 1953 [161].

The spectrum of the Cherenkov radiation extends from $\lesssim 300\,\mathrm{nm}$ to more than 700 nm. At these wavelengths, the atmosphere is optically thin, although absorption at $\lambda < 290\,\mathrm{nm}$ by the stratospheric O_3 and N_2 (similarly in the IR by H_2O and CO_2) together with Rayleigh and Mie scattering can cause significant attenuation of the Cherenkov light.

The refractive index depends in general on the air density, which has a marked evolution with altitude. This results in an angle θ which becomes larger as the shower develops towards the ground, saturating at around 1.3° at sea level. Since Cherenkov-emitting particles travel faster than the light in this medium, the photons emitted at the base of the cascade reach the ground just before those emitted in the top. The superposition of 'emitting cones' in a very short time window boosts the instantaneous photon density and generates a slight accumulation of photons towards the edge of the shower image, followed by a rapid drop in the luminosity. EAS photons can be observed from the Ground as very short flashes of the order of 10 nanoseconds.

Cherenkov photon density is low, requiring to operate typically under clear moonless nights, although Cherenkov experiments have recently overcome (at least partially) this limitation with the use of improved analysis techniques: UV pass filters and LIDARs to reconstruct partially extinct showers, reaching reasonable duty cycles.

Atmospheric Cherenkov detectors are typically subdivided in two groups. The first group consist on arrays of sampling detectors, which measure part of the Cherenkov light pool at Ground level. Examples are AIROBICC [162] or heliostats like STACEE [163].

The second, and most fruitful ones, are the *Imaging Atmospheric Cherenkov telescopes* (IACTs). Following the work of Michael Hillas in 1985 [164], it became clear that complete images of the extended air shower could be exploited to retrieve information about the incident primary particle. Results from the new developed technique were firstly obtained with the Whipple Observatory's 10 m reflector and its 37 pixel camera [165], but it was not until HEGRA that stereoscopic observations showed their huge benefits in terms of background rejection and improved shower reconstruction.

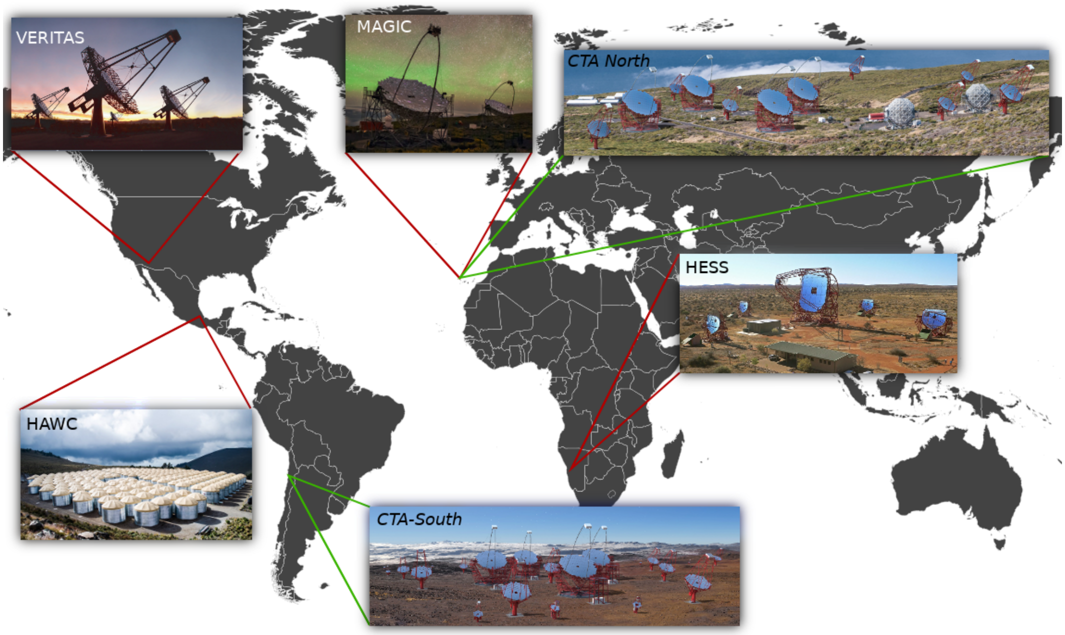

Figure 3.8: Location of current (MAGIC, H.E.S.S, VERITAS, HAWC) and next-generation (CTA-North and CTA-South) VHE γ-ray experiments.

3.4.4 Imaging Atmospheric Cherenkov Telescopes

IACTs are designed to detect the brief Cherenkov pulses, and hence they are optical telescopes with very fast cameras. In order to collect as much light as possible in very short integration windows and have high temporal resolution, the required optics must have very large apertures. Their optical system, in contrast with the one of typical optical telescopes, is made to have very wide field of view ($> 3°$) and is not focused at infinity, but at several kms the height of typical Cherenkov showers.

The shape of the images, its time development and, when available, stereoscopic observations of the cascade are very powerful tools to reconstruct the 3D shape of the atmospheric shower and its direction.

At the same time, stereoscopic observations together with optimized integration windows help to discriminate between true γ-ray Cherenkov events and accidental triggers generated by fluctuations of the PMT signals caused by the night sky background or NSB (Galactic diffuse emission, zodiacal light, airglow, Moon light, artificial light, etc), which greatly depends on atmospheric conditions, position in the sky and time.

Finally, pure γ-ray event Monte Carlo simulations (see Figure 3.10), together with a good knowledge of the instrumental response to those events are essential to reconstruct the energy of the incident γ-ray and its 'hadronicity' (probability of being a hadron).

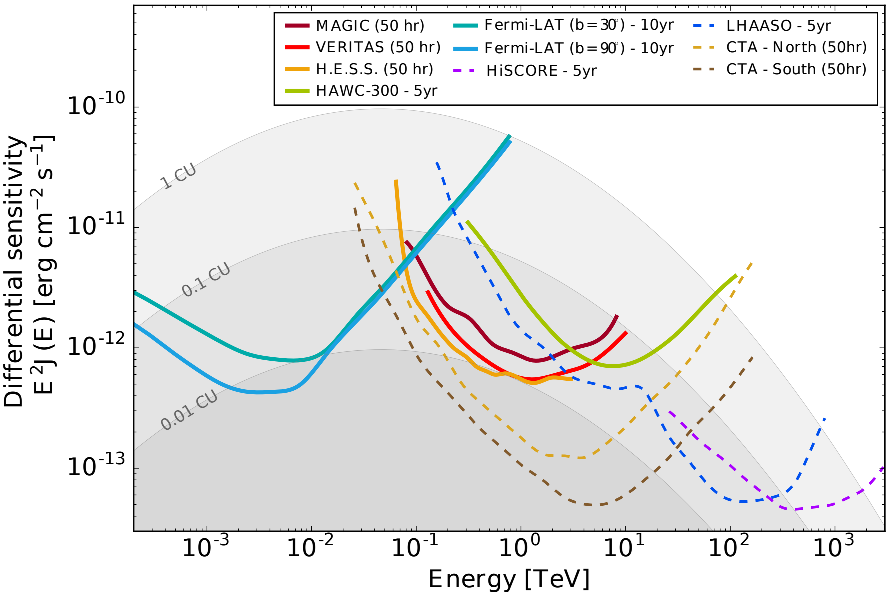

Figure 3.9: Approximate differential $5\,\sigma$ sensitivity of several γ-ray experiments, both current (solid lines) and future (dashed lines). Gray shaded regions indicate 1, 0.1 and 0.01 times the Crab nebula reference spectrum. Adapted from [166].

3.5 Future space and ground-based γ-ray missions

In chapters 4 and 5 we will discuss in detail two current generation γ-ray experiments: the first collecting HE γ-rays (LAT) and the second focused on VHE γ-rays (MAGIC). Both instruments have been used to obtain most of the results in this work. However, as we reach their sensitivity and performance limits, astronomers and astroparticle physicists have moved into the design of new and improved instrumentation.

3.5.1 AMEGO, e-ASTROGAM and GAMMA-400

The medium energy (MeV) γ-ray sky has traditionally been poorly explored, even more as there has been no instrument since CGRO was de-orbited operating in this energy regime apart from INTEGRAL, capable of reaching only $\sim 10\,\mathrm{MeV}$. These energies are expected to contain very interesting physics, including a large population of unidentified objects, possible dark matter annihilation channels and the most powerful FSRQs, whose high energy peak lies at these wavelengths as we will see in chapter 6. In order to address this problem, there are currently two proposed missions (e-ASTROGAM [167] and AMEGO [168][3]) which share similar goals: close the gap between low energy γ-ray instruments like NuSTAR or INTEGRAL and *Fermi*-LAT and provide polarization and nuclear line spectroscopy capabilities.

In the meantime, the *DArk Matter Particle Explorer mission* (DAMPE) [169] was successfully launched in December 17th, 2015. The goal of this general purpose survey-mode instrument from the Chinese Academy of Sciences is to perform combined

---

[3] See also `https://pcos.gsfc.nasa.gov/physpag/probe/AMEGO_probe.pdf`

high energy cosmic-ray and γ-ray measurements. It was recently commissioned and is currently operational[4]. Similarly, the GAMMA-400 mission [170, 171] is meant to be launched in the beginning of the next decade with characteristics similar to those found in *Fermi*-LAT (energy range of $20\,\mathrm{MeV} - 1\,\mathrm{TeV}$) but with improved energy and angular resolution.

3.5.2 The LHAASO and High score experiments

LHAASO (Daocheng site, Sichuan province at $\sim 4400\,\mathrm{m}$ a.s.l) is expected to be the most sensitive project to study Galactic cosmic-ray physics through a combination of photon and charged particle EAS observations in the energy range between 100 GeV and 100 PeV. The commissioning will begin in 2018 with $\sim 25\%$ of the detector and the instrument is expected to be operational by 2021.

At even higher energies, the *Hundred*i Square-km Cosmic ORigin Explorer* (HiSCORE) with its a non-imaging air-shower detector will be sensitive to cosmic rays in the range $100\,\mathrm{TeV} - 1\,\mathrm{EeV}$ and to γ-rays from 10 TeV to several PeVs.

3.5.3 The Cherenkov Telescope Array

Current generation of VHE ground-based facilities (particularly IACTs) have helped us to greatly improve our knowledge of EAS and the γ-ray sky. With the aim of significantly improving the performance of existing instrumentation, the γ-ray community has joined efforts in the Cherenkov Telescope Array (CTA) collaboration to build a global observatory for very high energy γ-ray astronomy.

CTA will be an open, proposal-driven observatory with full-sky coverage, for which one site per hemisphere is needed. In order to cover the energy band from $20\,\mathrm{GeV} - 300\,\mathrm{TeV}$ with a sensitive of one order of magnitude better than current instruments, ~ 100 telescopes in the South and ~ 20 in the North will be deployed with 3 basic telescope sizes:

- Large Size Telescopes (LST) with a $\sim 23\,\mathrm{m}$ diameter mirrors will cover the lowest energies and bring the energy threshold down to 20 GeV.
- Medium Size Telescopes (MST) and the double-mirror Schwarzschild Couder Telescope design (SCT) with about $10 - 12\,\mathrm{m}$ mirrors will be responsible of the core sensitivity of CTA between $\sim 100\,\mathrm{GeV}$ and $\sim 10\,\mathrm{TeV}$.
- Finally, Small Size Telescopes (SST-1m), ASTRII and GCT SST-2m [172] with $2 - 4\,\mathrm{m}$ mirrors will extend the sensitivity range up to $\gtrsim 100\,\mathrm{TeV}$ in the southern hemisphere.

Their wide field cameras ($> 4.5^\circ$ in all cases) will provide shower reconstruction at large impact distances to enlarge the collection area, improve the resolution and increase the field of view. They will also give us a much more uniform response than current generation instruments, boosting survey capabilities. At the same time, the

---

[4] See for instance `http://www.astronomerstelegram.org/?read=11246`

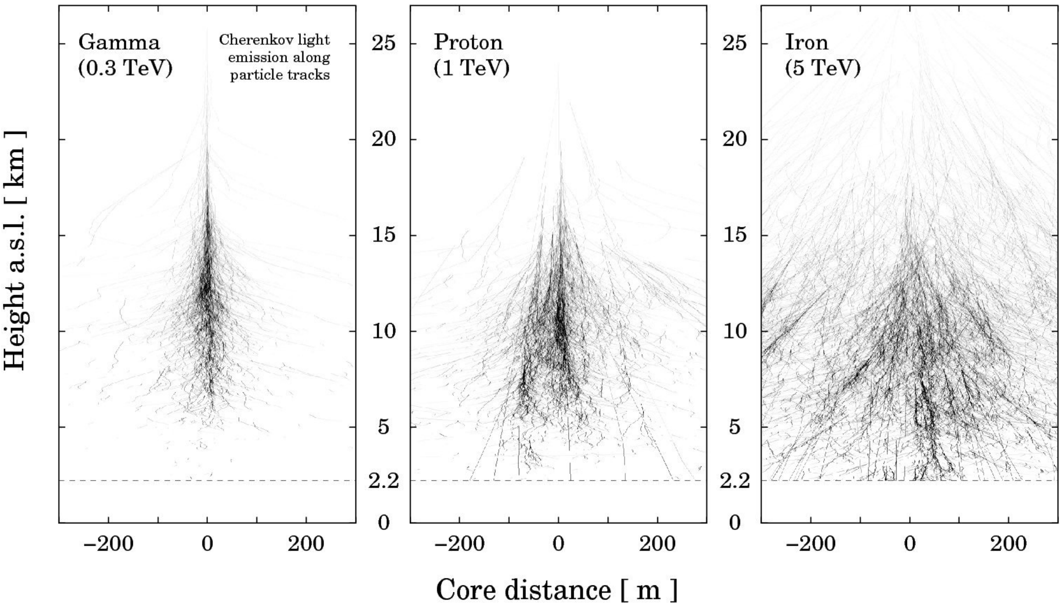

Figure 3.10: CORSIKA shower simulations for a γ-ray with energy of 300 GeV, a 1 TeV proton and a 5 TeV Iron nucleus. The pictures show the trajectories of high energy particles. Cherenkov light is emitted along the particle tracks. Reproduced from [176].

large number of telescopes observing the Cherenkov yield of the EAS will vastly improve the sensitivity, energy and angular resolution of CTA and provide a great tool to study γ-ray related phenomena [173–175].

Figure 3.8 shows the location of the current generation of IACTs: H.E.S.S in the Khomas Highland of Namibia, MAGIC in the Canary island of La Palma (Spain) and VERITAS in southern Arizona (United States). The two sites of the future Cherenkov Telescope Array (CTA) are also shown: the North site in La Palma and the South site in Paranal, Chile.

4
The Fermi Large Area Telescope

Contents

This chapter will describe the *Fermi* satellite and its instruments, particularly focusing on the Large Area Telescope, the current most sensitive instrument available to observe the Universe in the High Energy γ-ray band ($0.1 - 100\,\mathrm{GeV}$). In order to understand the design and capabilities of the *Fermi*-LAT, we first briefly describe its precursors.

4.1 Precursors

One of the first successful measurements of γ-ray emission from extra-terrestrial origin was made by the OSO-3 satellite [177]. It employed a multi-layer scintillation detector and a ‘sandwich’ of NaI and tungsten layers for energy measurements.

Its main success was to discover the γ-ray emission from the Galactic plane at $E \sim 100\,\mathrm{MeV}$. The next milestone was achieved thanks to NASA's SAS-2 [178, 179]. The mission was operational for only 6 months in 1973 and had an angular resolution of few degrees and a field of view of $\sim 35°$. Almost in parallel, ESA's COS-B [180, 181] was launched in a highly eccentric orbit to optimize observation time, at the cost of long and short term performance changes. The satellite was able to collect data from 1975 to 1982. Both missions carried spark-chamber experiments capable of detecting γ-rays of more than $20 - 30\,\mathrm{MeV}$. Multiple thin tungsten plates were interleaved between the spark chamber modules to trigger pair production and measure the incoming γ-ray energy. Anti-coincidence acting scintillation domes helped to reduce the charged particle background. The trace of the created electron and positron were used to determine the incoming γ-ray trajectory (hence the name 'tracer'). Its energy content was measured by means of bremsstrahlung processes in a 'calorimeter'. With this method, a degradation of angular resolution happens due to multiple scattering of electrons in the tracer. In the best case, it can be of $\sim 0.15°$. Typical energy resolutions are of the order of $\sim 15\%$.

The *Arthur Holly Compton Gamma Ray Observatory* (CGRO) is the second of the Great Observatories, launched by NASA in April 5, 1991. The goal of the observatory was to perform broad-band γ-ray observations with improved angular resolution, broader energy range, much better sensitivity than any of the previous missions and to provide the first full-sky γ-ray survey. In order to achieve this, CGRO counted with four instruments:

- The *Burst and Transient Source Experiment* (BATSE) optimized for all-sky measurements of bursts at $\lesssim 1\,\mathrm{MeV}$.
- The *Oriented Scintillation Spectroscopy Experiment* (OSSE) for source monitoring.
- The *Imaging Compton Telescope* (COMPTEL), which was optimized for the range $1 - 30\,\mathrm{MeV}$. It was based on the detection of Compton scattering from γ-rays with a low-Z liquid scintillator to reconstruct the properties of the primary particle.
- The *Energetic Gamma Ray Experiment Telescope* (EGRET), precursor of the *Fermi*-LAT and the highest energy instrument of CGRO. It featured a pair-production based detector, sensitive to γ-rays of up to $\sim 30\,\mathrm{GeV}$. The device was similar to SAS-2 and COS-B in using spark chambers, but with a much larger collection area.

CGRO was de-orbited in 2000 and replaced with ESA's INTEGRAL (low energy γ-rays, 2002), NASA's SWIFT (designed for bursts and soft X-rays, 2004), AGILE (HE γ-rays of $30\,\mathrm{MeV} - 50\,\mathrm{GeV}$ with sensitivity similar to those of EGRET but using solid-state detectors instead of a spark chamber) and *Fermi*-LAT (described in the following sections).

4.2 The LAT hardware

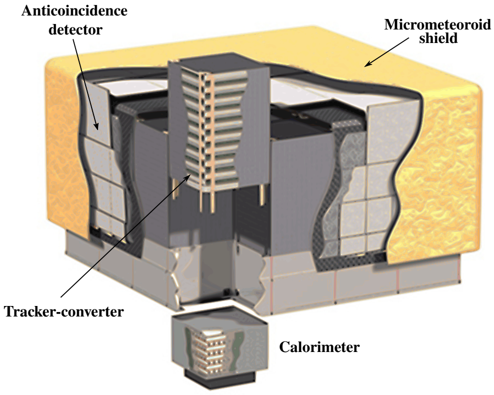

Figure 4.1: *Fermi*-LAT sketch [182].

Formerly known as *Gamma-ray Large Area Space Telescope* (GLAST) [182], the Large Area Telescope (LAT) is the primary instrument on the *Fermi Gamma-ray Space Telescope (Fermi)*. Similarly to its predecessors, EGRET and *Agile*, the LAT is a pair-conversion telescope consisting on a precision converter-tracker and a calorimeter, each with 4 × 4 modules. An anticoincidence detector (ACD) covers the tracker and a programmable trigger and data acquisition system (DAQ) utilizes information from the 3 previous instruments to form a trigger. The use of silicon-strip detectors, an evolution of the spark chamber used in previous missions, allows to get rid of consumables (such as gas) and the need of external triggers.

Fermi follows an almost circular orbit (at 525 – 544 km altitude) and spends $\sim 15\%$ of its time inside the South Atlantic Anomaly (SAA), where the fluxes of energetic particles are larger than usual due to Van Allen radiation belt becoming closer to Earth. During that time, data acquisition is halted.

On-board event processing is optimized to reject cosmic-ray triggered events (by a factor of $\sim 10^6$ with the combination of data filtering, hardware trigger and ground-based processing) while keeping as many true γ-ray events as possible ($\sim 75\%$ efficiency). The goal is to reduce the rate of events transmitted to the ground to a rate compatible with LAT's average downlink speed of ~ 1 Mbps.

4.2.1 Converter-tracker

A high-Z material (tungsten) is used for the 16 planes that form the converter-tracker and allows the incident γ-rays to be converted into $e^{\pm}$. The 16 modules operate independently for increased redundancy. Position-sensitive detectors are interleaved in the converter planes to record the passage of charged particles, allowing the tracks to be measured and the incident directions of the incident γ-rays to be reconstructed. The instrument is designed in such a way that the tracker has a very wide FoV and most events recorded enter the calorimeter for energy estimation.

The probability distribution for the reconstructed direction of γ-rays from a point source, better known as Point Spread Function or *PSF*, is mainly limited by multiple scattering of the $e^{\pm}$ and bremsstrahlung production. Thin converters are needed to achieve good PSF at low energies, were missed hits are translated into angular resolution losses. Similarly, a thick enough tracker is needed to maximize the effective area at high energies. The optimal balance between the two is achieved by dividing the tracker in two regions. The "front" section of the tracker has thin converters of 0.03 radiation length thickness, providing good PSF at low energies. The “back” section has a ~ 6 times thicker converters in order to maximize the effective area at the cost of a worse PSF. The converter has a total of 1.5 radiation lengths on-axis.

The first-level trigger is derived from coincidence of successive layers in the tracker. It has nearly no electronic noise and a $\sim 100\%$ trigger efficiency for charged particles.

4.2.2 Calorimeter

Fermi-LAT’s calorimeter is in charge of measuring the energy deposition from the incident γ-ray that produced the $e^{\pm}$ pair and generating an image of the electromagnetic shower development profile. The latter is used for background discrimination and helps to estimate the energy leakage fluctuations. It is instrumental to have good energy resolution at high energies. Each one of the 16 calorimeter modules has 96 CsI(Tl) crystals, optically isolated from each other and arranged horizontally in 8 layers of 12 crystals each. Their size is a compromise between electronic channel count and desired segmentation within the calorimeter (in order to give good resolution for shower spatial imaging). They provide a total 8.6 radiation lengths for the calorimeter and 10.1 radiation lengths for the complete instrument. The total weight of the calorimeter is $\sim 1800\,\mathrm{kg}$.

The CsI crystals are read with PIN photodiodes, which measure the scintillation light that is transmitted to each end. In order to increase the dynamic range, two photodiodes of different collection areas are used, being the large sensitive to energies of $2\,\mathrm{MeV} - 1.6\,\mathrm{GeV}$ and the small to energies of $100\,\mathrm{MeV} - 70\,\mathrm{GeV}$. Longitudinal segmentation of the shower enables to extend the energy range up to TeV by fitting analytical profile models. The method is almost only limited by fluctuations in the shower leakage.

4.2.3 Anticoincidence detector

The main goal of the ACD is to shield against charged-particle background, hence requiring high detection efficiency for these particles ($\gtrsim 0.9997$). Light from 89 plastic scintillator tiles and 8 ribbons is collected with PMTs providing good uniformity ($\sim 95\%$). The whole system is protected by a low-mass micrometeoroid shield. Secondary particles from the electromagnetic shower can Compton scatter in the ACD and create false vetoes from recoil electrons. In order to reduce the effective area for this effect, the ACD is segmented and only the segment nearest to the incident photon is considered. From a given threshold energy ($\sim 10 - 20\,\mathrm{GeV}$), onboard automatic rejection is switched off and a more powerful offline analysis is done instead.

4.2.4 Data acquisition and trigger

The Data Acquisition system or DAQ, known as Global-trigger/ACD-module/Signal distribution Unit or GASU, consists of: i) a Command Response Unit (CRU), in charge of sending and receiving commands and distributing DAQ clock signal; ii) a Global-Trigger electronics module (GEM), which generates readout signals based on the ACD and each of the 16 tower electronics modules (TEMs); iii) the ACD electronics modules (AEM) and iv) the Event Builder Module (EBM) which sends complete LAT events to the Event Processor Units (EPUs). The two EPUs then reduce (filter) the event rate of $2-4$ kHz to a more manageable ~ 400 Hz on-board, so that the data can effectively be downlinked for processing on the Ground. Dead time per event readout is $26.50\,\mu$s, which is the time needed to send the trigger information from the GEM to the EBM and fetch the calorimeter readout. Non-detector based trigger inputs to the GEM are used for calibration and diagnostic purposes.

4.3 Instrument modeling

Instrument simulation consisting on Monte Carlo simulations of LAT response to astrophysical signals was essential to understand its performance and optimize its design. Simulations can be subdivided in i) particle generation and tracking, where the interaction codes and models are based on the Geant4 (G4) Monte Carlo toolkit; ii) a parametrically calculated instrument response based on energy deposition and location in active detector volumes in the ACD and iii) a set of trigger primitives. Event reconstruction, classification, background rejection analysis and the rest of the analysis pipe is then applied to the simulated events the same way it is used for the real data.

4.4 Event reconstruction and classification

Event reconstruction is strongly based on Monte Carlo simulations. First, spatially adjacent hit tracker strips are clustered together. Each cluster determines a spatial location. Track hypotheses are generated and compared to sensor readouts. The possible tracks are based on either: i) *Calorimeter-Seeded Pattern Recognition* (CSPR), which relies on the event's energy deposition on the calorimeter; ii) a *Blind Search Pattern Recognition* (BSPR), which is useful for events that have little energy deposition in the calorimeter and for further refinement of the tracks found with the first method.

Energy reconstruction begins by applying pedestals and gains to the raw digitized signals. It then calculates the total energy deposited in each calorimeter crystal and the position along the crystal. The centroid of the three-dimensional array of energies and locations is computed along with energy moments and a first version of the total energy is estimated (track refinements are needed for the final value). The trajectory provided by the best track is used to estimate the leakage on the sides and back of the calorimeter and through the internal gaps between the calorimeter modules.

A combination of algorithms which work at different energy ranges (parametric correction, shower profile and maximum likelihood fit) is applied to events and an energy resolution of $\sim 2\% - 4\%$ is obtained above 5 GeV. For low energies, the energy deposited in the tracker becomes non-negligible and it becomes mandatory to use the tracker as a sampling calorimeter where the number of hits correlates with energy deposition, which is then added to the calorimeter energy measurement.

The background model, used for on-board trigger and filtering, includes cosmic-rays (from AMS and BESS experiments) and Earth's albedo for both charged particles (based on data from NINA, NINA-2, Mariya) and γ-rays (derived from EGRET's data re-analysis) in the range $10 - 10^6$ MeV.

Event classification is based on classification tree (CT) generated probabilities. These CTs are also used to do the final energy estimation for those cases where more than one method (PC, LF or SP) is available. Events can be classified in types according to where the pair creation takes place in the tracker (*Front* and *Back* events) or, newly introduced with Fermi's *Pass 8* data release, by how good is their Point Spread Function (PSF) or their energy reconstruction as measured by Energy Dispersion (EDISP). Additionally, hierarchical classes of events with different background rejection strengths are created for different analyses. In *Pass 8*, the loosest cuts are found in the various *TRANSIENT* classes, meant mainly for Gamma-ray Bursts (GRBs) and fast transients, where we expect low integration times and high γ-ray event rates. The *SOURCE* class, used for most analyses and appropriate for point sources, was originally designed so that the residual background was similar to typical extragalactic γ-ray background fluxes. More restrictive classes such as *CLEAN*, *ULTRACLEAN* or *ULTRACLEANVETO* are designed to have $2 - 4$ times lower background rates than *SOURCE.* They provide a slightly better sensitivity for very hard sources at high galactic latitudes and are particularly suited for extended diffuse γ-ray sources that require very low levels of cosmic-ray background. More details about these sources can be found in Cicerone[1].

With GRBs as one of the main scientific targets of *Fermi*-LAT, the satellite incorporates an onboard science processing system. It provides a prompt detection and location of GRBs, combining the *Fermi* Gamma-ray Burst Monitor (GBM) and LAT's own on-board algorithms. It also offers self-triggering capabilities, which allow to keep GRBs within the LAT FoV and send alerts to the Gamma-ray burst Coordinate Network (GCN) once a cluster of tracks (events) is detected in a small part of the sky during a short interval of time.

Fermi-LAT's data downlinked from the spacecraft is considered of *Level 0.* At this step, ground-based data analysis is performed at the LAT Instrument Science Operation Center (ISOC). The data is automatically processed via pattern recognition and reconstructions to assess the nature of the events (γ-rays or cosmic-rays), their energy and the arrival direction and times. The resulting products are known as *Level 1* data and a refined search for GRB and transients happens after this step. *Level 1* data consists on a Events File (*Photon File*, covering from *SOURCE* to *ULTRACLEAN*, and *Extended File* covering looser cuts) and Spacecraft File, which contains spacecraft's attitude information. High-level science data products and transient source analysis results from the Automated Science Processing (ASP) are finally delivered to the *Fermi* Science Support Center (FSSC) and made public to the community. ASP is of capital important for GCN notices and ATELs about

---

[1] `https://fermi.gsfc.nasa.gov/ssc/data/analysis/documentation/Cicerone/Cicerone_Data/LAT_DP.html`

GRBs, solar flares and flaring blazars. Since LAT started operations in 2008, transient and flare searches have inspired other works, such as the *Fermi All-sky Variability Analysis* (FAVA)[2].

4.5 Data analysis

In this section we cover the fundamental steps of any *Fermi*-LAT data analysis, which is normally done with the public *Fermi*'s ScienceTools (ST). The description of the different steps is described in detail in the Fermi GSFC webpage: `https://fermi.gsfc.nasa.gov/ssc/data/analysis/`. Ultimately, using frameworks such as `fermipy` or `enrico` allows the analyzer to encapsulate all these steps in very convenient analysis threads.

4.5.1 The LAT data server

The *Fermi*-LAT collaboration distributes fully reconstructed photons with information about their energy, arrival direction and time together with response functions describing the reconstruction accuracy of the event once it triggered the LAT. The data is published in the LAT data center in two forms:

- *LAT Data Query form*, which allows the user to download photons in specific regions in the sky, observation dates and energy ranges. By default, events from the Photon database are collected, which represent tighter cuts and contain event classes 'source', 'clean' and 'ultraclean'. Alternatively, the Extended photon database can be checked, which add events of the transient-class and thus represent much looser cuts.
- *Weekly files*, containing all photons from any position in the sky, are published in separated files for every week since the beginning of the mission.

Together with the events files, a spacecraft file is needed, which contains information about the pointing of the telescope as well as non-instrument-specific data. *Fermi*-LAT photon and spacecraft files are stored in `fits` format.

4.5.2 Event selection

The first step of the analysis, applied to both unbinned and binned likelihood analyses, is the event selection, performed using the `gtselect` macro. This tool takes as input a fits file containing *Fermi*-LAT events sorted in rows. The possible parameters for data filtering include the event class, event type, coordinates (and aperture radius), energy range and maximum zenith distance for which events are kept. They are useful to remove noise coming from Earth limb. Any event that does not meet these criteria is removed at this step.

---

[2] `https://fermi.gsfc.nasa.gov/ssc/data/access/lat/FAVA/`

4.5.3 Good time intervals

The second step is the computation of Good Time Intervals (GTIs) using the spacecraft file. GTIs are defined as time ranges for which the data is considered valid and after running this step using `gtmktime`, a new entry is appended to the filtered event (`fits`) file containing a list of such time intervals. The criterion to flag LAT data as valid include times for which LAT was properly working and collecting data. In reality, any field defined in the spacecraft file is subject to possible cuts.

4.5.4 Counts map

Once the events have been selected and the GTIs are appended to the data, count maps need to be generated for the desired region of interest (ROI). This is done with `gtbin`, which is a multi-purpose program also capable of producing light curves from event data and spectra among other products. Once the ROI and spacial binning has been specified, the output is a `fits` image that can be checked any time with `ds9`, `python` or any other software capable of dealing with astronomical formats.

4.5.5 Exposure calculation and source model

Since the LAT instrument response functions (IRFs) depend on the angle between the pointing direction and the source position, the flux measured (in counts) from a given source changes as the source moves across the FoV. At this point, the data analysis path strongly differs in the *binned* with respect to the *unbinned* procedure. While the latter is generally more sensitive as it considers each event separately with its own IRFs, the amount of computing time and memory required is also significantly larger, enough to make *binned* analysis (with 'averaged' IRFs) appealing when one analyzes large data samples.

Unbinned analysis

Starting with the *unbinned* case, we have first to calculate the *livetime cubes.* Their purpose is to measure the accumulated time during which LAT is collecting data in a three dimensional grid (2 dimensions for the sky position and one for the inclination angle). For this task, `gtltcube` is typically used. Similarly, exposure maps have to be computed using `gtexpmap`, which takes `gtltcube` output and computes the predicted number of photons within a given ROI for the diffuse components in the source model. The exposure returned by this macro is the integral of the total response (effective area × energy dispersion × PSF) over the entire ROI.

A source model `XML` file has to be defined at this step. It contains all the sources that are expected to exist in the ROI (including the source(s) of interest) together with their spectral and spatial information, which may depend on one or more free parameters (for instance, normalization flux and spectral indices in the case of a Power Law spectra).

Finally, `gtdiffrsp` is called to compute the integral over solid angle of a diffuse source model convolved with the IRFs for each of the photons in the events file.

The end result is an additional column for each diffuse source (diffuse responses) added into the events file.

Binned analysis

Alternatively, *binned* analyses require to calculate first a three-dimensional version of the counts map (two spacial dimensions and third one for the energy) using the `CCUBE` option of `gtbin`. Then, the source model `XML` file is defined the same way it was done for the *unbinned* analysis.

The calculation of livetimes and exposure can be done in this case with `gtltcube` and `gtexpcube2`. The end result is a set of exposure maps for different energies. Just like in the *unbinned* case, the exposure needs to be computed again if the event class or data filtering change. Finally, the analysis requires a model of the *count maps* with the sources from the `XML` convolved with the exposure and PSF to be computed for use in the maximum likelihood. This step is performed with `gtsrcmaps`.

4.5.6 Maximum Likelihood

The last step in the *Fermi*-LAT data reconstruction is the maximum likelihood fit, which is in charge of fitting all free parameters of the `XML` model to the observed data using the previously computed IRFs. While the tool (`gtlike`) is the same for the *binned* and *unbinned* cases, the input files it takes change. The end result is an output `XML` model with best-fit values for the free parameters and errors calculated.

From this point, it is easy to produce spectral points or a light curve since it would just involve repeating this prescription for each desired bin and then combining the result in data files or plots. More advanced tasks, such as the generation of *Test Statistics* (TS) maps, *model* maps, *residual maps* or folded light curves (for periodic sources) are also possible, but they will not be covered here.

4.5.7 The `enrico` framework

As it was mentioned in the beginning of this section, there are several tools that have been written to simplify the *Fermi*-LAT data analysis. In this section, we briefly describe one of them, `enrico` [183], as I have contributed significantly to its development since I joint the γ-ray community[3]. Written in Python, this software is portable (it does not depend on the architecture or a precise version of the *Fermi*-LAT ScienceTools) and is well documented[4]. Some of the features of the program include:

- `enrico` wraps the Science Tools analysis tools under more meaningful tools:
  - `enrico_config`: generates an easily-readable and editable configuration file divided in sections.
  - `enrico_xml`: automatically builds a `XML` source model file based on published catalogs such as the 3FGL [184].

---

[3] See `https://github.com/mireianievas/enrico`

[4] `http://enrico.readthedocs.io`

  - `enrico_sed`: generates a *spectral energy distribution* and offers the possibility to generate also spectral points automatically, providing as output plots and data files summarizing the most important results.
  - `enrico_lc`: generates a *light curve* by dividing the sample in time bins.
  - `enrico_foldedlc`: generates a *folded light curve* (periodic sources).
  - `enrico_tsmap`: generates a *test statistics* map.
- Supports both *binned* and *unbinned* analyses.
- Interacts with *job queue* systems such as Torque-PBS, allowing for high parallelization of the analysis.
- Results are easily reproducible.

As mentioned before, during the last years, I have become one of the main contributors to `enrico`'s code. Apart from correcting errors, several features have been implemented:

- *Summed likelihood analysis*: by dividing the events in groups according to their PSF or EDISP types (see Section 4.4) and using specific IRFs for each, the sensitivity of the analysis is improved. Similarly, the analysis can be split in two energy ranges, performing i) *binned* likelihood analysis for the low energy regime, where statistics are higher and computing time becomes a limitation; ii) *unbinned* likelihood analysis for the high energy regime, where the few available events can really profit from an individual treatment.
- *EBL absorbed models*: by specifying a non-zero redshift and a given EBL model, the assumed spectral shape for the source of interest is absorbed before doing the maximum likelihood fit, which can improve the accuracy of the reconstructed spectrum at high energies.
- The *8-years* source catalog can be used to generate the *XML* source model file.
- *Spectral energy distribution* bins can be generated not only logarithmically spaced in energy but also with alternative schemes, based for instance on the event statistics per bin.
- A *decorrelation energy* is computed as part of the analysis and the fit parameters are recalculated at that energy, where errors and parameter correlations are minimized.

5
The MAGIC telescopes

Contents

5.1 Introduction

The Major Atmospheric Gamma-ray Imaging Cherenkov telescopes (MAGIC hereafter) is a set of two Imaging Atmospheric Cherenkov Telescopes (IACTs) located at 2200 m.a.s.l in the Canary Island of La Palma (Spain). The first telescope (MAGIC-I) started operations in 2004, followed five years later by MAGIC-II. The

Figure 5.1: Image of the MAGIC stereoscopic telescopes with MAGIC-I in the background (left) and MAGIC-II in the foreground (right) [185]. Credits: Robert Wagner.

system was upgraded in 2011-2012 to make both telescopes more alike, simplify their maintenance and boost the stereoscopic performance. The system was built in the same location of a former γ-ray experiment, HEGRA, and uses the same principles as the imaging Cherenkov telescopes (CTs) of that experiment. Together with H.E.S.S. [186] and VERITAS [187], it is the most sensitive instrument in its energy range ($50\,\mathrm{GeV} - 50\,\mathrm{TeV}$). The design goals of MAGIC include a low energy threshold (for which large area mirrors and fine pixelization are essential) and a fast repositioning system to allow for prompt follow-up of Gamma-Ray Bursts just seconds after space-based alerts are issued.

Despite being sensitive to visible light, MAGIC differs from typical optical telescopes in that it is optimized for dim ($\sim 10^2\,\mathrm{photons/m^2/TeV}$) and very short ($\sim 1\,\mathrm{ns}$) flashes produced by extensive air showers (EAS) emitting Cherenkov radiation in the UV and optical wavelength bands (see section 3.4.4). The telescopes form images of the EAS in moderately pixelized ($\sim 10^3$) cameras. By analyzing their shape, the arrival direction and energy of the primary particle can be estimated. The reconstruction gets more precise when multiple stereoscopic images of the air shower are used in the analysis simultaneously.

The small duration of the Cherenkov light flashes, together with the intensity and variability of night sky background (NSB) forces us to use fast and sensitive Photomultiplier Tubes (PMTs) as light sensors for each pixel. Coupled with fast electronics for triggering, signal sampling and stereoscopic event matching, the cameras provide good discriminating performance against background events, local muons shining only one of the telescopes and after-pulsing signals. The telescopes are triggered by multiple (adjacent) pixels registering signals above a certain threshold. For each of these triggers, a signal extraction method based on a “sliding window” approach is used for each pixel. The end result are clean time-resolved sample images of the shower which can be calibrated to convert ADC counts into number of photons.

5.2 Hardware description

5.2.1 Structure and mirrors

The MAGIC telescopes dishes have 17 m diameter segmented mirrors, which corresponds to a $\sim 240\,\mathrm{m}^2$ reflecting surface [188]. They form a nearly parabolic shape whose overall focal ratio is $f/D \sim 1$. This was needed to maintain the temporal structure of the nanosecond Cherenkov flashes and thus reduce the required integration time, keeping the noise at minimum levels and improving the signal to noise ratios. MAGIC-I is composed of 964 square (0.5 m side) panels, spherical shaped honeycomb core sandwiched between two outer Al-layers. In the case of MAGIC-II the individual panels are larger ($247\ \times 1\,\mathrm{m}^2$) and the outermost 104 mirrors were made out of glass [189]. The reflecting surfaces are subject to extreme weather conditions and have to endure rapid and dramatic changes in humidity, UV radiation and temperature. Over the years these effects have significantly reduced the reflectivity and even disfigured the surface of some of them. In order to maintain the good performance of the instrument, the most degraded mirrors needed to be replaced in 2016.

The structure of the telescopes is made out of carbon fiber and epoxy tubes in order to make the instrument as lightweight as possible. The success of the design inspired the next generation large size telescopes (LSTs of CTA), which profit from the same basic design ideas that were employed in MAGIC. The total weight of each telescope including motors is about 60 tons and a fast repositioning to any point in the sky becomes possible in just ~ 20 s. The light structure creates a slight bending in the structure and the overall mirror shape. In order to maintain the precise parabolic shape of the dish, each mirror has a set of actuators (Active Mirror Control, AMC) that are automatically adjusted during telescope operations.

The alt-azimuth drive systems of the MAGIC telescopes are designed to allow for a fast repositioning time while maintaining good pointing accuracy and smooth tracking. They are based on two azimuth and one altitude motors for each telescope, which are controlled by a *star guider* system. The *star guider* consists on an optical charged-coupled device (CCD) camera coupled with a commercial lens which is placed in the dish and points in the direction of the MAGIC camera. By identifying stars in the field of view (FoV), it continuously calculates the exact pointing of the instrument, making small differential corrections in the drives whenever needed.

5.2.2 Camera

The current design of the MAGIC cameras, after the upgrade of 2012, is very similar in both telescopes. It is based on $1039\ \times 1$ inch hemispherical PMTs from *Hamamatsu* (model *R10408*). Their QE is of $\sim 32\%$ in the blue band and they have a response time of approximately 1 ns. Winston cones are installed on top of the PMTs to reduce the blind area between them and the maintenance is simplified by grouping pixels in clusters of 7. This setup provides a total of 3.5° Field of View (FoV). The total number of trigger pixels is 547 grouped in macrocells, covering the inner 2.5°.

The average Cherenkov pulse width (FWHM) is ~ 2.5 ns. Pulse injection signals (closely resembling true Cherenkov pulses) can be injected anytime at the PMT base of every pixel to allow for daytime tests of the whole electrical and readout chain.

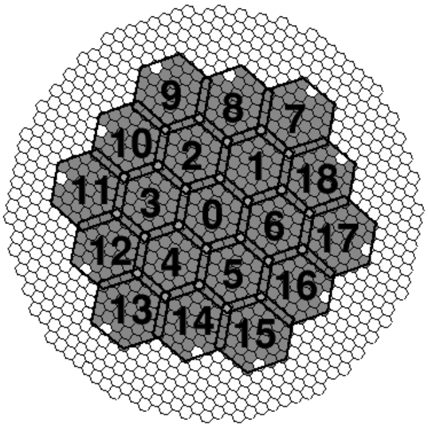

Figure 5.2: Camera of both MAGIC-I and MAGIC-II together with the different trigger macrocells.

The main difference of MAGIC-I and MAGIC-II PMTs is the gain distribution in the second camera, which ranges from $1.0 \times 10^4 - 6.0 \times 10^4$. MAGIC-II's PMTs are typically operated at $3 - 4 \times 10^4$ gains, which allows to work under moderate moonlight without damaging the PMT dynodes. This gain spread is compensated with a *FlatFielding* process by applying different High Voltages (HVs) to each PMT. Due to aging, the applied HV needs to be slowly increased as time passes and is thus greater for MAGIC-II than for MAGIC-I. Careful selection of PMTs for the upgraded MAGIC-I camera, with half of the pixels having higher gains together with analog attenuation of the higher gain pixels using resistors, helped to reduce the spread of MAGIC-I gain distribution compared to MAGIC-II.

A cooling system is mounted in both cameras to regulate their temperature (and make the response of the PMTs more stable).

Finally, the whole system is protected with a plexiglas window and movable lids to shield the PMTs against dust and light.

5.2.3 Readout

Analog signals are transmitted continuously from the PMTs to the readout and trigger electronics located in the control house (also known as *Counting House, CH*) using ~ 162 m long optical fibers grouped in 19 bundles (72 fibers each) per telescope. The total spread of propagation time in the bundles is 138 ps (RMS) and is corrected for the trigger automatically. Manual offline corrections can also be applied using reference calibration signals.

PMT signals are split in the MAGIC Optical Nano-Second Trigger and Event Receiver (MONSTER/receiver boards) into analog-readout and sum-trigger and digital branches. When an optical signal coming from the camera is received, it is converted back to analog electrical signals and digitized to provide the Level-0 (L0) individual pixel trigger signal using discriminators. Three parameters can be set in the L0 trigger level for each channel: a) the discriminator thresholds (DTs), b) the delay, and c) the width of the output pulse of the discriminators. The individual pixel rate (IPR) is monitored at 1 Hz to react to stars in the FoV by modifying the L0 parameters.

The readout for both telescopes is based on the Domino Ring Sampler version 4 (DRS4 hereafter) chip, which largely improves the old DRS2 chip used during the first years of MAGIC-II operations in terms of dead time ($< 1\%$), linearity ($1 - 600$ phe), intrinsic noise and a negligible channel-to-channel cross-talk. The system is also less expensive and bulky than the old FADC/Aquiris digitizer used previously in MAGIC-I, a requirement to fit all the electronics in the available space of the CH.

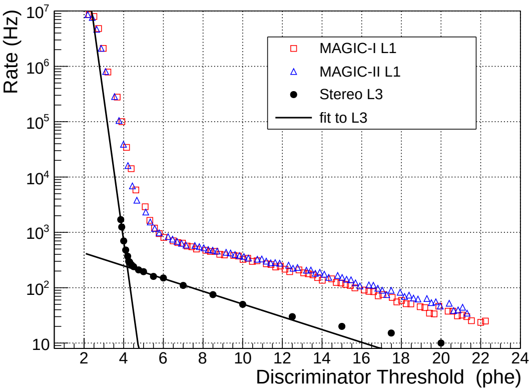

Figure 5.3: Trigger rates and accidental triggers (NSB) as a function of the DTs [190].

The sampling electronics is composed by a motherboard or PULSAR board (developed at University of Chicago) and a DRS4 mezzanine designed at INFN/Pisa laboratory. Conceptually, the DRS4 is an ultra-fast analog memory composed of a ring buffer built out of 1024 switching capacitors which are read in the event of a trigger using a conventional 14-bit analog to digital converter at low speed (32 MHz). A raw pedestal level of $\sim$ 2500 ADC is introduced to account for negative signals (NSB fluctuations and pulse undershooting). The Region of Interest (RoI) mode of the DRS4 helps to reduce the time overhead for readout and contributes to give a total dead time of just 27 μs. The tunable sampling frequency of the DRS4 chip is currently set at $\sim$ 1.6 Gsamples/s[1] and a linear response in an input range of 1 V. The mezzanine noise ($\sim$ 7.5 ADC or $\sim$ 450 μV at board input) is dominated by the noise from the DRS4 chip. In total, the digitization electronics contribute to $\sim$ 50% of the total noise.

The calibration of the chip response has three major corrections: a) mean cell offset, b) readout time lapse, c) signal arrival times. The first two are applied by the DAQ software (a multithreaded C++ program running on 2 computers, one per telescope) while the last is applied offline.

The *mean* cell offset calibration requires the raw mean ADC count values to be measured for each capacitor using a *pedestal calibration run* (the baseline of a single capacitor varies up to $\sim$ 15% from cell to cell). Pedestal runs are taken once at the beginning of the night and then subtracted from readout values. The mean offset decreases following a simple power law as a function of time, behavior that is very similar among all DRS4 chips, making it possible to refine this correction with a simple analytical expression.

DRS4 chips exhibit variable time spreads ($1 - 4$ ns) on the delay of the recorded signal pulses depending on the position in the ring buffer. This effect is chip-dependent and is corrected (recovering the actual arrival time) using *calibration runs*. Several runs of this type are taken every night during data taking.

---

[1] A reduction from the original 2.0 Gsamples/s was needed in 2014 to drastically reduce the so called *dead-zone*, in which no coincidences can be triggered, by increasing the buffer size.

5.2.4 Trigger

The first trigger level (L0) is a simple amplitude discriminator operating on the 547 trigger pixels of each telescope. This *pixel-level* digital trigger signal is sent to the second trigger level or telescope trigger (L1), which is just a digital filter arranged in 19 partially overlapping macro-cells of 36 channels each. The choice of triggering or not the telescope is based on one of the implemented logics: 2 next-neighbor logic (2NN), 3NN, 4NN and 5NN (selected at the beginning of every observation). L1 is issued once a macrocell reports a coincidence trigger using the selected logic. Both L1 trigger signals (one per telescope using normally a 3NN logic) are sent to the stereo trigger (L3) with a proper stretching ($\sim 100\,\mathrm{ns}$) and delay according to the pointing position in the sky to account for differences in the arrival times between the two single-telescope signals. The artificial width of the signals makes sure that the trigger efficiency does not practically get reduced with any misalignment in the timing for any of that telescope and triggers up to $\sim 200\,\mathrm{ns}$ away can issue an L3 trigger.

Alternative trigger schemes are also available. The first, being a nearly complete replacement of the L1 trigger, would be the *Sum-Trigger-II* [191]. It follows the design of the old *analog sum trigger* that was available in MAGIC-I and consists in the sum of signals of clusters of pixels (macrocells). The main advantage of this system is that it significantly lowers the energy threshold and improves the signal to noise ratio at low energies as all pixels in a macrocell contribute to the trigger decisions, not only those above a given threshold as in the classical trigger. The design however needs to deal with inhomogeneity among the different channels of the macrocell (different performance for each PMTs, slightly different optical fiber lengths, etc), smaller trigger regions and intrinsically weaker Cherenkov pulses when one observes low energy cascades. Data acquisition rates are also significantly larger than in the typical 3NN-L1 + L3 trigger. The second, alternative to the standard L3 stereo trigger, would be the *Topo-Trigger* [192]. It features a topological trigger, which is able to reject $\sim 85\%$ events based on their relative orientation in the telescope cameras while keeping $\sim 99\%$ of the true γ-rays, boosting the collection area by $10 - 20\%$ at the energy threshold.

5.2.5 Calibration system

A calibration box exists in each of the two telescopes. It is based on Q-switched Nd:YAG lasers emitting at $\lambda \sim 355\,\mathrm{nm}$ that produce $\sim 0.4\,\mathrm{ns}$ width pulses. The intensity is adjusted with filters (which help to substantially increase the dynamic range) and uniformity achieved by using an Ulbricht sphere. The system originally installed in MAGIC-II was technically superior to the led-based calibration box available in MAGIC-I, so during the upgrade both calibration boxes were built based on laser-technology but with several upgrades: adding a humidity sensor and heating system inside the box, a laser status check system, a fast photodiode for monitoring the laser light output, improved dynamic range and better uniformity. 2000 events are recorded during each calibration run, which happens just before data runs. The extracted charge per pixel and its variance are used to determine the conversion factors between ADC counts and number of photoelectrons (phe). The F-factor method used to derive such conversion factors is accurate assuming that only long-term drifting happens due to aging of the crystals and no short-term ($\sim 10\,\mathrm{min}$) changes are seen in the laser light intensity.

5.2.6 Timing system

Each recorded event needs to be labeled with precise and absolute time stamps when the trigger signals reach the readout system. A commercial timing system coupled to a timing rack module provides all the electronics needed to export such timing information as low voltage differential signal (LVDS) to the readout. The drift in the timing information is only of $\sim 65\,\mathrm{ns/month}$, with a total precision of $\sim 200\,\mathrm{ns}$.

5.2.7 LIDAR

The MAGIC telescopes are normally operated together with a custom-made micro-LIDAR system [193] which allows to characterize the vertical transmission profile of the atmosphere and derive corrections for the development of the shower in the MAGIC analysis chain. Such corrections make it possible to extend the duty cycle of the telescopes and operate under adverse atmospheric conditions with reduced systematic errors in energy and flux.

5.2.8 Computing

The computing infrastructure of the MAGIC telescope consists on four racks containing computers, storage and network equipment connected by Gigabit ethernet and Fibre Channels (for the connection between DAQ computers and storage units). Power switches make it possible for each system to be controlled remotely. The cluster of machines are split in the on-site analysis machines, the subsystem machines, the storage area network (SAN) and a dedicated machine connected to the European Grid Infrastructure.

The central control of the MAGIC telescopes is in charge of `SuperArehucas` (SA++), a software written in Labview, running in a dedicated PC, which communicates with the different MAGIC subsystems and gives a general status for all of them in just one screen.

A dedicated machine inside the computing infrastructure is devoted to the MAGIC *online analysis* (MOLA) [190]. MOLA is a multi-threaded C++ program, part of the *MAGIC Analysis and Reconstruction Software* (MARS [194]), which does a real-time analysis of the data coming from the two DAQs. One analysis thread is devoted to each mono reconstruction, performing a simplified calibration, signal extraction and cleaning of the atmospheric shower images. A third thread matches the events in both telescopes and performs the stereoscopic reconstruction and background suppression, generating γ-ray excess event sky-maps, θ^2 plots and light curves for two non-overlapping energy (event size) bands. The output is continuously monitored by the MAGIC operators in order to decide whether observations need to be extended or in case alerts to other VHE experiments are to be issued. The sensitivity of the online analysis is considered to be $\sim 1.0\%$ of the Crab Nebula flux in 50 h above ~ 200 GeV, compared to $\sim 0.66\%$ of the standard offline analysis with MARS.

5.2.9 Observation modes and file types

MAGIC observations are normally carried on in the so called *wobble* mode [195], during which two or four positions symmetrically distributed at typically 0.4° offset are tracked during 1 run ($\sim 15-20$ min) each, cyclically. Both the on-source (ON) region and background control regions (OFF) are extracted simultaneously from the same dataset, turning dedicated off observations unnecessary. The slightly lower efficiency is compensated with a better control over the systematic uncertainties due to sky changes with time and a much better use of the available exposure. Alternatively, the *on* mode can be employed for particular observations, requiring then to also observe *off* regions.

Events are gathered and recorded in runs identified with an unique and increasing number. For historical reasons, the files are further split in sub-runs at the lowest data levels to deal with limitations on the maximum file size allowed by old filesystems. During observations, three type of runs can be recorded:

- ***Pedestal runs (P):*** Taken at the very beginning of the source *slot* and after typically 1 hour of observation time, they contain accidental triggers (random triggers caused by NSB and the readout).
- ***Calibration runs (C):*** Taken after Pedestal runs, they record the flashes emitted by the calibration lasers and are used to derive the calibration constants.
- ***Data runs (D):*** They contain triggers from shower candidates fulfilling the predefined trigger scheme, flagged LIDAR triggers and interleaved pedestal and calibration events that are fired at a given low rate (typically 25 Hz) in order to improve the calculation of calibration constants and account for time evolution of these quantities.

The names of the files stored in MAGIC contain the following metadata:

- Date of the observation (`YYYYmmdd` format).
- Telescope (M1, M2). Skipped if the data is stereoscopic.
- Run number (possibly followed by subrun number up to *star* files).
- Run type: `_D_` for RAW data, `_P_` for RAW pedestal, `_C_` for RAW calibration runs, `_Y_` for calibrated files, `_I_` for reconstructed mono events, `_S_` for stereo reconstructed events and `_Q_` for fully characterized events (including energy estimation and event classification).
- Name of the source and pointing (wobble configuration): offset and orientation.
- An extension, which can be `raw` or `raw.gz` for RAW files and `root` for the rest of the products.

For instance, `20171021_M2_05067988.012_D_GRB171020-W0.40+180.raw.gz` denotes a RAW data file taken on October 21th (2017) with MAGIC-II and it is identified by run number 05067988 and subrun 12. The source is a GRB number 171020[2] and the telescopes were pointing 0.4° away from the source (offset) and at 180° rotation from the RA axis (position in the ring defined by the wobble offset).

5.3 MAGIC's Reconstruction and Analysis Software

In this section, we briefly describe the standard MAGIC analysis chain. It is mainly based on the Mars Data Analysis Manual, available in the MAGIC wiki page (`http://wiki.magic.pic.es/index.php/Mars_Data_Analysis_Manual`)

In order to derive physical properties from observations of γ-ray sources, a complex reduction and analysis process must be done on the MAGIC data. The low level analysis (calibration, report 'merpping', cleaning and stereo reconstruction) are typically performed as part of the MAGIC *On Site Analysis* (OSA) directly in La Palma, while the latest steps (γ/hadron separation, energy and direction reconstructions) together with the generation of science products (θ^2 plots, skymaps, spectra and light curves) are usually done offline.

5.3.1 MAGIC's On Site Analysis

The goal of the MAGIC *On Site Analysis* (OSA) is to run the analysis chain on the real data that is being recorded and make the results available to the collaboration as soon as possible (normally during the day) by transferring both the raw and processed data to the *Port d'Informació Científica* (PIC) data center. The analysis (which comprises calibration, image cleaning, Hillas' parametrization and stereoscopic reconstruction) is performed in parallel with the data acquisition, but is totally decoupled from it. There are several advantages of doing this process on the site:

- Offline analysis of the data is significantly sped up since there is no need (in general[3]) to repeat the calibration, image cleaning, parametrization and stereoscopic reconstruction of the events. Additionally, the storage and bandwidth needed to download OSA's stereo products is reduced by a factor of ∼ 200 compared to the compressed raw data.
- Data quality checks, allow both real-time (operator alerts) and long-term studies. The result is a continuous monitoring of the performance and status of the telescope subsystems, anticipating possible hardware failures.
- Shower reconstruction checks, which include both how Cherenkov showers are simulated and how the software is able to reconstruct high level products. Regular checks on well-known sources such as the Crab Nebula, the standard candle in VHE, are also performed thanks to this system.

---

[2] GRBs are normally named after the date they are detected.

[3] Exceptions to this include data taken under *strong 'Moon'* conditions, obtained with non-standard flat-fielding and High Voltage (HV) settings and non-standard trigger schemes.

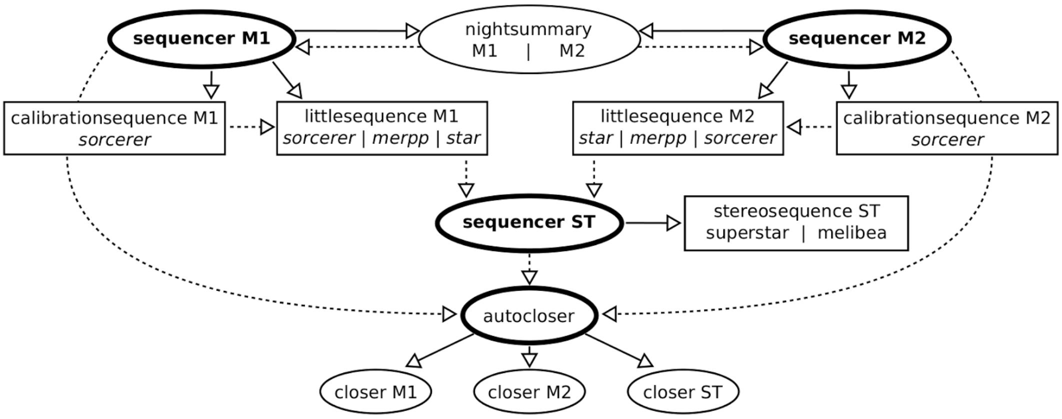

Figure 5.4: MAGIC's on-site analysis scheme (credits: David Carreto Fidalgo)

OSA consist on a software package mainly written in `Python`[4] (version 2.7+), a set of `GNU Bash`[5] scripts, `Unix cron`[6] jobs and a `PBS/Torque`[7] resource manager to allow for high parallelization of the analysis using the 40 cores available for data analysis in La Palma's analysis cluster.

The first OSA activity is the raw data copy and compression process (`rawcopy`), which looks every hour for new raw data and CC reports on the DAQ storage for both MAGIC-I and MAGIC-II and copies the newly found files to the analysis storage (shared between the different analysis machines). The goal of using two different file systems is to interfere with the DAQ as little as possible.

Immediately afterwards, (`sequencer`) is executed. This program organizes the jobs hierarchically, gathers information (thanks to the `nightsummary` macro) about the observing conditions and parameters and submits to `Torque` run-wise jobs containing the calls to `MARS` executables (written in CERN's `ROOT` [196]):

- `sorcerer`: calibration of raw compressed data. It is run twice, once for the *pedestal* and *calibration runs* to extract the calibration constants and (only then) for the *data runs* to apply the previously derived constants and calibrate the data.
- `merpp`: central control (CC) reports are attached to the calibrated files.
- `star`: cleaning and parametrization of the images by means of Hillas parameters.
- `superstar`: combines the data from the M1 and M2 *star* files and computes the stereo reconstruction of the shower.
- `melibea`: using a pre-generated Random Forest (RF) files and Lookup Tables (LUTs), estimates the energy, arrival direction and the nature of the incident particle. The Random Forest files are carefully re-created and tested every time the MAGIC's Monte Carlos are updated.

---

[4] `https://www.python.org/`

[5] `https://www.gnu.org/software/bash/`

[6] `https://en.wikipedia.org/wiki/Cron`

[7] `http://www.adaptivecomputing.com/products/open-source/torque/`

A summary of these processing activities is shown in Figure 5.4. The first three steps of the list are executed for each telescope separately in one processing block per source and run number, while the last two are run once the *star* files have been correctly generated. Optionally, the analysis is finished by running for each source `odie`, `caspar`, and `flute`, which generate θ^2 plots, skymaps and spectra and light curves respectively. We will describe these tools more in detail in the following sections.

Finally, once the data has been fully processed for a particular run in either MAGIC-I, MAGIC-II or the Stereo, the results are validated by the `autocloser` macro and the *run* is flagged as 'closed' in the `MySQL` analysis database. This flag triggers the archival of the OSA files and the data transfer to the PIC data center.

During my work inside the MAGIC collaboration, significant effort was devoted to improve the processing times in OSA and make the software as automatic and robust as possible. In particular, `nightsummary` received important changes so that it could effectively register information about the particularities of the data acquisition. This allowed to select the optimal `sorcerer` and `star` input cards according to external conditions such as the presence of bright *Moon* or UV-pass *filters* in front of the camera. It also incorporated the detection of *GRB* observations, which often are accompanied with fast re-positioning of the telescope and source file name changes without stopping the DAQ or changing the *run* number. The *merpping* process was also improved with an automatic generation of simplified report entries (including only *Drive* reports recovered from the *Drive computers*) in case the original Central Control reports were missing for a particular subrun (e.g. due to a SA++ crash). Together with the introduction of the `autocloser` macro previously mentioned, these actions resulted in a continuous improvement of the performance of the system over the years as seen in Figure 5.5. In 2017, 75% of the nights were fully analyzed in stereo by 12 PM UTC (compared to 44% in 2013) and 94% of the nights are processed by midnight of the next day (69% in 2013).

In general, the analysis results used in MAGIC publications are obtained from OSA's `superstar` files. This data level still allows for a careful data selection and the use of optimized RFs while keeping OSA's calibration and cleaning, simplifying the analysis and improving data manageability.

5.3.2 Calibration

The calibration is the process of extracting signal properties such as arrival time and signal intensity for each pixel and time slices (60 samples of 0.5 ns are recorded) in the shower and converting detector measurements (counts) into physical quantities (photo-electrons or phe).

The program in charge of doing this process is called `sorcerer` (*Simple, Outright Raw Calibration; Easy, Reliable Extraction Routines*). The program begins by subtracting the pedestal from the received signal and performing corrections for non-linearities in the amplitude and timing of each pixel, process that depends on the position of the event in the DRS4 as described in section 5.2.3. This step is applied

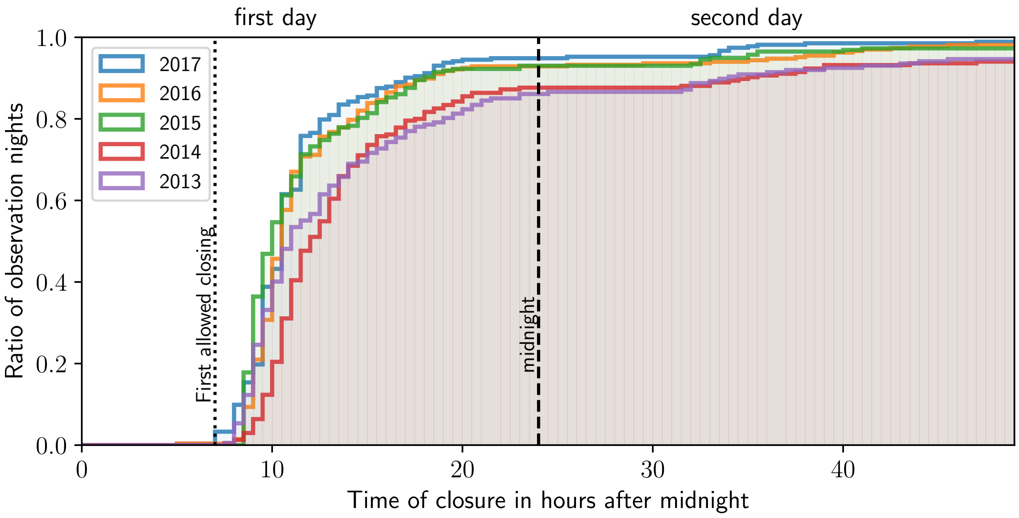

Figure 5.5: MAGIC's on-site analysis performance measured as the percentage of nights closed by a given time (in hours) after midnight of the night for which data is taken.

twice, first for *calibration runs* (the so called C-mode of `sorcerer`) and afterwards for *data runs* (Y-mode). Additional pedestal triggers are recorded at a rate of 25 Hz during *data runs* to account for the possible evolution of the NSB or sky conditions.

The conversion factors between counts and phe are obtained from the calibration pulses, which are registered mainly in the *calibration runs*. This initial calibration is continuously updated during normal *data runs* by firing the calibration box again at a rate of 25 Hz[8], with the aim of monitoring the signal transmission and readout performance. Assuming Poissonian statistics for the number of photons, uniform phe detection efficiency and an excess readout noise which does not depend on the signal amplitude, the number of phe is given by the F-factor [197, 198] method as:

$$\langle N_{\rm phe} \rangle = \frac{F^2 \times Q^2}{\sigma_Q^2 - \sigma_P^2} \tag{5.1}$$

where σ_Q is the standard deviation of the measured signal and σ_P the electronic noise (resolution of the signal extractor, estimated as the standard deviation of the pedestal signal) and Q is the mean charge after pedestal subtraction. F is the so called excess noise factor, which is measured in the laboratory. With this definition, the conversion factor between measured charge and number of phe is simply $C = N_{\rm phe}/Q$.

As we mentioned before, the calibration needs to be performed in two steps:

- ***C-mode***: Two loops over the *pedestal run* are performed followed by a loop over the *calibration run* (to derive pedestal signals with its RMS and measure integrated charge, arrival times for each pixel, absolute position in the DRS4). Then the F-factor is applied and finally quality checks are performed on individual pixels.

---

[8] To be added to the 25 Hz interleaved pedestal events.

- ***Y-mode***: A single loop over the data is performed calibrating times and charges using the coefficients obtained in C-mode. The information stored in the pedestal and calibration signals is updated on-the-fly using interleaved pedestal and calibration events.

Right after the calibration is finished, the reports coming from the different MAGIC subsystems are attached to the already `ROOT` formatted data *subruns* as headers using `merpp`.

5.3.3 Image cleaning and parametrization

The image of the shower usually covers a small part of the total camera surface. The rest of the pixels do not contain useful information, but just random noise (fluctuations) from NSB, electronic noise or light from stars. They need to be screened out before characterizing the shower image in terms of geometrical parameters to avoid spoiling the results. Both steps are done at once in `star`. The program also performs optical (coma) aberration corrections (PSF increases as we get away from the camera centre) and allows to suppress bad pixels and to add artificial noise to the MCs (useful to analyze data taken under strong Moon conditions [9]).

Image cleaning

The traditional cleaning algorithm used in MAGIC before the upgrade was the *Time-constrained Absolute Image Cleaning.* With this method, pixels containing less than a given threshold charge (in phe) were rejected. Typically, two thresholds were provided, one for the core pixels (currently $q_c = 6$) and another for the boundary pixels ($q_b = 3.5$). The procedure was divided in three steps:

1. Pixels with $q > q_c$ are initially selected.
2. The core pixels are identified. Sets of 2 or more adjacent pixels are used to form one or more islands. The mean arrival time in the main island is computed.
3. Core pixels with arrival times outside a fixed time window ($4.5 - 9\,$ns) with respect to the mean arrival time of the island are rejected.
4. Pixels next to the selected pixels with $q > q_b$ are also preserved if the arrival time difference with respect to neighbor core pixels is less than 1.5 ns.
5. The charge of the rest of the pixels is set to zero.

Following the upgrade of MAGIC-I and MAGIC-II, a new image cleaning method was introduced: *Sum Image Cleaning.* With this method, the signals are first clipped (to reduce biases due to after-pulses and strong NSB fluctuations) in amplitude and possible combinations of 2, 3 or 4 compact neighboring pixels are identified. If the sum of signals is above a threshold and within a $\sim 1\,$ns time interval these pixels are

---

[9] A similar level of noise in the MC and real data is needed for such cases

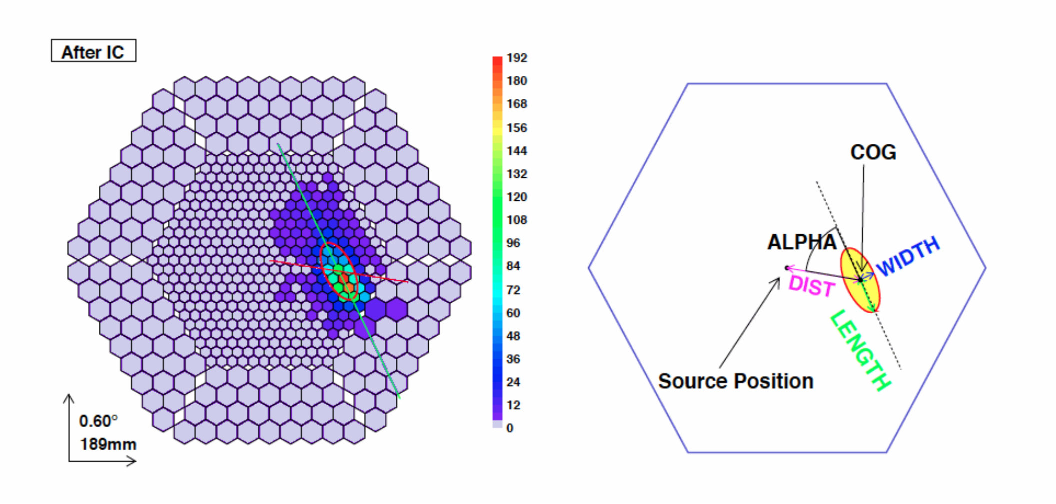

Figure 5.6: Parametrization of a shower image after image cleaning. Credits: W. Wittek.

flagged as shower image pixels. Both the threshold and time window width are more strict the smaller the group is. Then, the core pixels are identified with a recipe similar to the Absolute Image Cleaning using the same q_c and q_b thresholds. The given charge thresholds and time constraints are optimized with γ-ray and telescope simulations to bring an equilibrium between energy threshold and noise.

Image parametrization

The data can be further compressed by keeping only the essential information for the shower image analysis, which is its geometrical shape represented as a list of parameters. After this step, the information (arrival times and charges) contained in each pixel is no longer needed.

Most of the parameters, named usually after Hillas [164], are derived from a principal component (moment) analysis (up to third orden) of the phe distribution in the image (see Figure 5.6). Some of them are referred to a particular position in the camera, typically the nominal source position. Others take into account the arrival time of the Cherenkov signal.

- ***Size***: total number of phe in the shower image (roughly $\propto E_{\text{primary}}$).
- ***CoG***: center of gravity of the image ($\bar{X}$ and $\bar{Y}$).
- ***Width***: half width of the minor axis of the shower ellipse (transversal development).
- ***Length***: half length of the major axis of the shower ellipse (longitudinal development).
- ***Conc-n***: fraction of phe contained in the n brightest pixels (compactness).
- ***Leakage1/2***: fraction of signal in the most external pixels of the camera with respect to the total image size (fraction of the shower lost).

- ***M3long***: third longitudinal momentum along the major axis of the ellipse (asymmetry along that axis, to determine the head of the shower).
- ***Asym***: difference in the positions of the peak of the charge distribution and the *CoG* along the major axis.
- ***Number of Islands***: fragmentation of the air shower.
- ***Alpha***: angle between the line from the nominal source position to the *CoG* and the image major axis.
- ***Dist***: distance from the image CoG to the nominal source position.
- ***Time gradient***: slope of the linear fit of arrival times as a function of position along the major axis.
- ***Time RMS***: spread in the arrival times across the image.

Typically, hadronic showers have larger widths, lengths, are less compact and more fragmented. On the other hand, γ-ray induced showers typically point towards astronomical sources (hence smaller alpha values than hadronic showers are expected).

5.3.4 Stereo reconstruction

Stereoscopic observations of an EAS greatly improves the capabilities of 3D shower reconstruction methods. In MAGIC, this step is done with `superstar`, which stores its reconstructed parameters in a separate data structure called *MStereoPar* container. In particular, stereo allows to determine the *reconstructed incident direction* and *shower core impact point* on ground of the primary particle as the intersection of the main axes of MAGIC-I and MAGIC-II shower ellipses. Both parameters are determined at the same time with the above mentioned recipe, which is accurate unless the planes containing the shower and the telescopes position are parallel to each other (shower coming across the imaginary vertical plane that connects both telescopes).

Once the shower axis is reconstructed, the impact parameters can be computed for both telescopes and the height of the shower maximum (position at which the shower is the brightest) can be estimated.

5.3.5 Data selection

Data selection is necessary in every MAGIC analysis in order to reduce systematic uncertainties associated to that analysis. Data selection can be subdivided in:

- Telescope operating mode filtering (mono, stereo, trigger modes, PMT High Voltage settings, UV-pass filters).
- Data quality filtering such as removal of data with bad mirror focusing, data acquisition settings or car flashes affecting the DTs.
- Selection based on NSB (strong moon observations require special calibration and cleaning settings and the addition of artificial noise to the MC).

- Filtering based on atmospheric transparency (using either the LIDAR or the pyrometer information).

Atmospheric conditions can affect the air shower development and detection. If the refractive index varies, e.g. by a change in the atmospheric pressure, then the amount of Cherenkov photons produced is modified. Suboptimal atmospheric conditions also change Rayleigh and Mie scattering and cause absorption and multiple scattering of the Cherenkov light, turning the images dim and blurry. The end result is that the estimated source spectra is not only wrongly reconstructed in the flux, but also the energies of the events are not the correct ones. However, thanks to MAGIC's LIDAR, filtering based on atmospheric transparency is usually relaxed and data with limited transparency ($0.55 < T < 0.85\%$) can still be used (with corrections) in standard analyses.

Data selection is currently done in MAGIC using two macros: `pasta` and `quate`. The first is a very simple program which provides average, minimum or maximum estimates of just one single parameter at a time for a single MAGIC data file. It can be useful to make quick data quality checks and discard whole data files based on meaningful parameters such as the average *zenithal distance* (ZD), the *discriminating thresholds* (DTs) which are useful to remove data taken under strong Moon or the *event rate* and *pyrometer cloudiness*, which are correlated with the atmospheric conditions and transparency. A more complete program is `quate`, which generates full reports containing information about multiple parameters (including more advance data such as LIDAR transmission) and allows to select data in time slices, making it possible to select small good time intervals inside a whole *superstar* file.

5.3.6 Estimation of primary particle properties

This is perhaps the most delicate part of a VHE γ-ray analysis, and it comprises several analysis parts which are all performed using just two programs: `coach` (the 'trainer') and `melibea` (the 'executor').

Gamma/hadron separation

As mentioned in section 5.3.3, the shower image parametrization is a powerful tool to discriminate among the different kind of events that can trigger IACTs: accidental triggers, muons, hadrons and γ-rays. Stereoscopic operations can effectively reduce the first two by a significant fraction, leaving hadrons and primary electrons as the main background in γ-ray observations and as the target for separation methods.

MAGIC currently uses a *Random Forest* [199] (RF) method to compute a global *hadronness* parameter based on multiple decision *trees*. This parameter correlates with the chance probability for the event of being a hadron-like cascade. It is a machine learning method based on MC information. The RF training needs the following information as input:

- A pure sample of γ-rays, which in MAGIC needs to be simulated with *CORSIKA*

[200] events passed through the Telescope simulation code [201, 202] and the same low level reconstruction pipelines as the real data.

- A pure (or nearly pure) sample of hadronic recorded cascades. They are typically hard to simulate since they involved richer physics. In MAGIC hadronic events are extracted from previously non-detected source data or by observing *Dark Patches*, where no significant γ-ray signal is expected.
- A list of shower parameters containing the relevant separation information to grow the decision trees and make it possible to separate γ-rays from hadronic showers in bins of size, zenith angle, azimuth[10], etc.

Energy estimation

Energy estimation in MAGIC can be done with two different methods. The first (and current standard) is the *Look-Up Table* (LUT) method, which is just a multi-dimensional table in which axes are given by a list of image parameters (values are binned) and the matrix is filled with the mean energy (and RMS) of MC events. Then, in order to estimate the energy of a real event, one only needs to look up for the proper entry in the table. In reality, due to limited MC statistics, it is often needed to reduce to parameters to only a few and begin with a rough estimation of the energy using the shower size (zero order) and only then fill the table with corrections of E/size instead of the true energy (first order). Finally, small corrections are applied based on atmospheric optical depth, geomagnetic field and image leakage.

Alternatively, a more sophisticated RF method can also be used in this step with `melibea` and its validity is currently being tested in MAGIC. The main advantage of using RF is its better performance at high energies (starting from few hundreds of GeV) in terms of Energy resolution even when accepting events with larger leakage, although at low energies the simple LUTs matrices still perform better.

DISP method

The goal of the *DISP* method (from *Distance between the Image centroid and the Source Position*) [203, 204] is to reconstruct, on a event-by-event basis, the angle between the direction to the shower maximum and the incident direction of the γ-ray or source position. The method uses the shape of the image, characterized mainly by its width and length[11], to infer the position of the source using a single telescope. It was originally designed for mono operations and extensively used by the Whipple and HEGRA experiments, but it has been successfully extended to stereo in MAGIC.

The main limitation of the method comes from the identification of the head and the tail of the shower, for which the *time gradient* and the *M3long* parameters are typically used. This is known as Ghost busting. In Mono, $10-20\%$ of the events are wrongly characterized, but the use of stereo parameters in the RF helps to greatly improve the performance of the DISP method and its accuracy. The exclusion of

---

[10] Magnetic fields depend on the shower direction and can deform its shape.

[11] DISP parametrization in MAGIC is based on MC simulations and RFs.

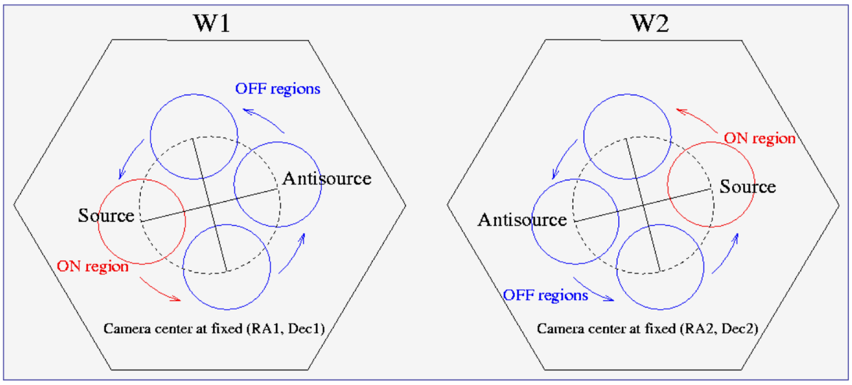

Figure 5.7: Definition of ON and OFF regions in the Wobble observation mode.

badly reconstructed events (those for which MAGIC-I and MAGIC-II reconstructed directions greatly differ) helps also in the γ/hadron separation.

5.3.7 Detection tools

VHE γ-ray astronomy relies on probabilistic methods to determine whether a source is detected or not. Frequentist often quantify this by using the so called *Likelihood Ratio Test* (LRT), where two hypothesis are compared in terms of their *Likelihood*. The null hypothesis (H_0) typically refers to the case of having only background events in our sample, while an alternative hypothesis (H_1) admits the possibility of having a non-zero excess due to legitimate astronomical sources. The ratio of likelihoods relates with the chance probability of the excess being due to a spurious fluctuation.

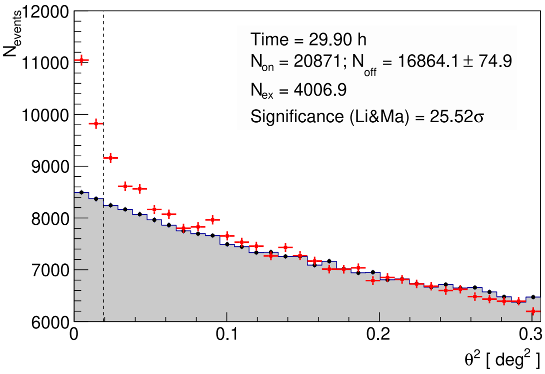

Figure 5.8: θ^2 distribution of ON and OFF events (scaled to account for the different exposure in the ON and OFF region)

In MAGIC, the standard method used to calculate the significance of source detections is the Li&Ma method [205], which is implemented in `odie`. The program starts by building histograms with the number of events as a function of the square distance (in deg^2) to a given position in the sky. These are known as θ^2 plots in VHE experiments (see Figure 5.8). The chosen position is typically either the nominal position of the source or a given set of *off* (background control) positions, symetrically distributed with respect of the center of the camera (see Figure 5.7). Then, taking into account the PSF, a cut is applied to define a signal region in the histograms. This reduces the histograms to more manageable event counts, n_{on} and n_{off}. The joint likelihood for these regions, assuming Poissonian distribution of the number of events, can be expressed as

$$L(g,b;n_{on},n_{off}) = \frac{(g+b)^{n_{on}}}{n_{on}!}e^{-(g+b)} \times \frac{(b/\alpha)^{n_{off}}}{n_{off}!}e^{-b/\alpha} \tag{5.2}$$

where n_{on} and n_{off} are the number of events contained in the *on* and *off* regions, α is the ratio of *on* to *off* exposure, g is the excess events (signal) in the *on* region and b the background signal in the *on* region (nuisance parameter). Then, the LRT becomes

$$\lambda(g;n_{on},n_{off}) = \frac{L(g,b*;n_{on},n_{off})}{L(g',b';n_{on},n_{off})} \tag{5.3}$$

where g',b' maximize the likelihood when both are set free and b* maximizes it when g is fixed. The significance of detecting a signal then becomes simply $S = \sqrt{-2\log\lambda(g=0;n_{on},n_{off})}$. In the case of having just one signal and background channels (counting experiments), this expression accepts an exact solution, which is known as the formula number 17 of Li&Ma [205]

$$\begin{aligned} S = \sqrt{2}\Bigg\{ & n_{on}\log\left[\left(\frac{1+\alpha}{\alpha}\right)\left(\frac{n_{on}}{n_{on}+n_{off}}\right)\right] + \\ & + n_{off}\log\left[(1+\alpha)\left(\frac{n_{off}}{n_{on}+n_{off}}\right)\right]\Bigg\}^{1/2} \end{aligned} \tag{5.4}$$

Its validity holds if n_{on} and n_{off} are above ~ 10 counts. In MAGIC, it is common to add a sign to this significance depending on whether the excess is positive or negative. Alternative methods try to incorporate extra information about the shape of the signal and background regions. To mention two straightforward examples:

- Li&Ma with fitted *off* signal. If the camera response is well modeled and is roughly uniform, one expects the *off* signal to depend only on the angular response of the optical system, i.e. to evolve smoothly with the square distance to the defined signal region. Fitting the *off* region with a simple smooth analytical shape is then equivalent to improve background statistics and increase detection sensitivity.
- Using the PSF knowledge of the instrument and the distribution of the events, as described in our published work [206] and presented in Appendix A.

5.3.8 Sky maps

Sky maps are two-dimensional representations of the incoming direction of γ-like events. They are usually projected in the camera coordinates (to investigate the sensitivity of the instrument) or more commonly in the sky (either in azimuthal or equatorial coordinates).

Events in MAGIC are recorded one by one and their positions are reconstructed afterwards with an error that depends on the γ-ray PSF[12]. The software that generates

---

[12] Not to be confused with the optical PSF of the telescope

sky maps in MAGIC is `caspar` (see Figure 5.9). It is capable of doing:

- Exposure estimation taking into account the movement of the source in the camera.
- Background map generation.
- Smearing of the resulting image with a given kernel to highlight the source against the noise of the photon-limited sample.
- Estimation of `caspar`'s test statistics (TS) using the prescriptions from `odie`.

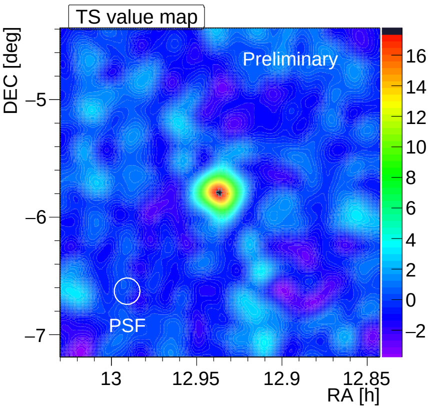

Figure 5.9: 'Smeared' TS sky map.

5.3.9 Spectra and light curves

The results that have been discussed until know are measured in terms of instrumental units (counts). In order to estimate the flux coming from a γ-ray source in physical units, we need the effective observation time t_{eff} (taking into account the possible dead time) and the effective γ-ray collection area A_{eff}, which in general depends on the energy of the primary, its arrival direction and the pointing of the telescope with respect to the source position. This quantity is one of the keys of the Instrument Response Functions (IRFs). If we call $\Phi = \frac{d^2N}{dA \cdot dt}$ the γ-ray flux (γ-ray rate per unit area), then we shall define two important quantities:

$$\underbrace{\frac{d\Phi}{dE} = \frac{d^2N}{dA \cdot dt \cdot dE}\,\mathrm{cm^{-2}s^{-1}TeV^{-1}}}_{\text{Differential Energy Spectrum}} \qquad \underbrace{\nu F_\nu = \lambda F_\lambda = E^2\frac{d\Phi}{dE}\,\mathrm{TeV\cdot cm^{-2}s^{-1}}}_{\text{Spectral Energy Distribution}} \tag{5.5}$$

In order to measure fluxes and generate spectra and light curves, MAGIC has a specific tool called `flute`, which takes care of doing the following calculations:

Event counting

The first step to estimate the flux of incoming γ-rays is to count the number of events that survived the analysis chain. An important number of the resulting events are coming from background cosmic-rays, which need to be subtracted to obtain the excess events. Since IRFs are energy dependent, the data is usually first divided in bins of *estimated energy* (E_{est}) and then θ^2 histograms are generated with events falling into each energy bin. Finally, a signal region that optimizes the sensitivity and minimizes systematic effects is chosen to count the number of *on*, *off* and *excess* events in the selected energy bin. Knowing the efficiency of the selected cuts (percentage of γ-rays contained in the signal region) in a pure MC γ-ray sample, the number of *excess* events can then be corrected.

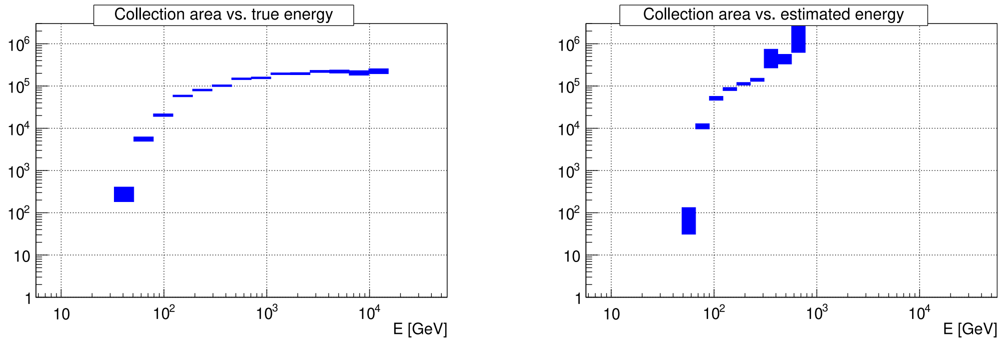

(a) As a function of true energy. **(b)** As a function of estimated energy.

Figure 5.10: Effective Area calculation in terms of E_{true} and E_{est}.

Effective time

Each time an event triggers the telescopes, there is a dead time or period for which the data acquisition system is busy 'building' the event and the system cannot accept any new events. If we call λ the rate of events, the effective time as it is measured in MAGIC follows the simple relation $t_{\rm eff} = t_{\rm elapsed}/(1+\lambda \cdot d)$ where d is the dead time per event, which for the DRS4 based readout is $\sim 26\,\mu$s.

Collection area

The effective area ($A_{\rm eff}$) is computed in MAGIC by applying the same cuts and analysis procedures to a sample of MC simulated γ-rays as it was done in real data. The simulation of γ-rays needs to be done by distributing the 'impact points' homogeneously in a large area $A_{\rm MC}$ with the IACTs in the center. The area must be large enough so that no 'external' (not simulated) γ-rays would manage to trigger the telescopes and survive the analysis while keeping it small enough so that the simulation efficiency is acceptable.

Since MC events are generated with a specific spectral shape[13] and $A_{\rm MC}$ is known, it is in principle straightforward to determine the response of the instrument to the detection of simulated events of different energies with the relation

$$A_{\rm eff}(E) = (N_{\gamma,\rm surv}/N_{\gamma,\rm sim}) \times A_{MC}(E) \tag{5.6}$$

As with other IACTs, MAGIC's $A_{\rm eff}$ increases with energy and reaches a plateau around $\sim$ 1 TeV. The effect of observing a source at higher zd are twofold: i) the atmospheric depth is larger, which in turns increases the extension of the light pool and therefore the effective area; ii) the showers are dimmer due to the larger extinction, implying a higher energy threshold E_{th}. Azimuth can also have a significant effect on the effective area since the magnetic field changes with the observing direction. This effect becomes non-negligible at medium and high zenithal distances ($zd > 35°$). It must be noted that $A_{\rm eff}$ cannot be expressed in principle as a function of $E_{\rm est}$ but instead it is a function of the true energy of the events ($E_{\rm true}$), which is unknown for observed γ-rays.

---

[13] MC spectra follow a hard Power Law with $\Gamma \sim 1.6$ to improve statistics at high energies.

Migration matrix

The reconstructed energy of the events is not, strictly speaking, the true energy of events. Some sort of modification, often known as spillover correction, needs to applied to the data to account for the mean energy mismatch between the two quantities. Fortunately, the same reconstruction artifacts are found in MC simulated γ-ray events analyzed with the procedure we used for the real data. These events would have an associated E_{est}, which we can use to build a *migration matrix* that correlates E_{est} and E_{true} for MC simulated γ-rays (see Figure 5.11).

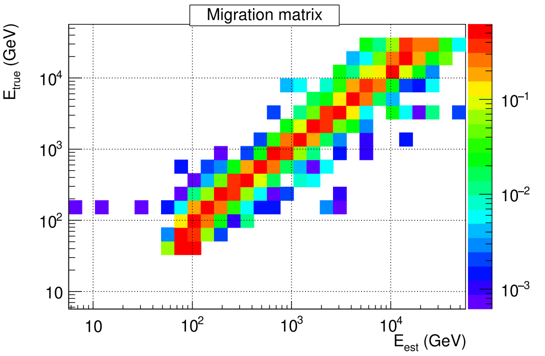

Figure 5.11: Migration matrix from `flute`.

In `flute`, the effect of the migration matrix is taken into account by modifying the definition of the effective area so that events are counted in bins of E_{est} while simulated events are counted on the same bins of E_{true}. Since the effective area calculation depends on the simulated spectrum, which in general will differ from the one of the considered sources. One has to re-weight the spectrum of simulated γ-rays to match that of the source of interest and obtain reliable effective areas. Finally, `flute` provides the differential energy spectrum and spectral energy distribution in terms of E_{est}. Note however that this is a circular problem because the spectrum is in principle unknown. Fortunately, a simple iterative procedure can be easily applied to solve this problem. Figures 5.10a and 5.10b show A_{eff} as a function of E_{true} and E_{est} for a source with a very steep spectrum.

(Un)folding

The alternative to the simple spill over correction of `flute` is to *unfold* the spectrum. The procedure becomes almost unavoidable when one wants to report actual spectral points and take into account the finite resolution of MAGIC's energy reconstruction. It is a numerically difficult procedure involving matrix inversions and approximations. The solution is often ambiguous as each procedure results in different spectra, sensitive to noise and fluctuations and requires to use *regularization* methods to smooth out the data. It also results in correlated errors. There are two tools in MAGIC to perform this step, `CombUnfold` and `TRUEE`.

Because of all the drawbacks that have been mentioned before, specific tools have been written to avoid the need of *unfolding* and *regularization* in some cases by using a *Forward folding* procedure. An example of this is the study of the imprint of the Extragalactic Background Light (EBL) in the γ-ray blazar spectra using the macros `fold` and `fitebl` (see chapter 11).

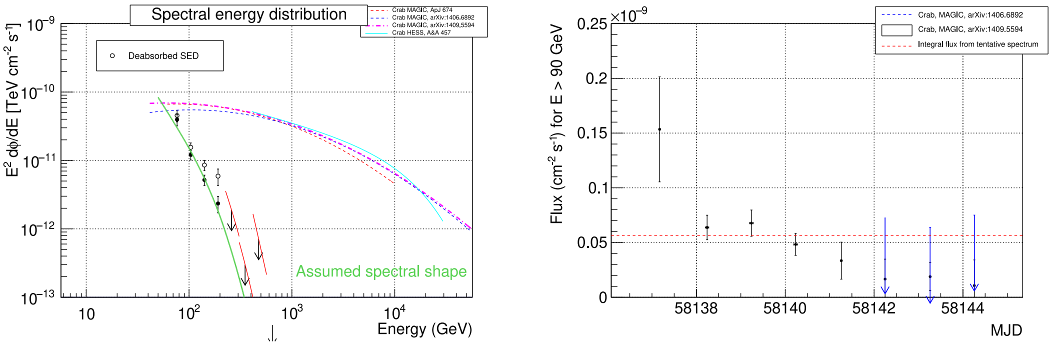

(a) Spectral Energy Distribution (SED). **(b)** Light Curve (LC).

Figure 5.12: Examples of SED and LCs generated with `flute`.

Light curves

Apart from generating spectra, `flute` is capable of generating *light curves* by dividing the data in time bins. The events are then used to build the spectrum for each bin (assuming that the shape is constant among all time bins and only the normalization changes) and the flux is integrated in the specified energy range (in cm^{-2}s^{-1}) and plot against time. Examples of spectra and LCs generated with `flute` are shown in Figures 5.12a and 5.12b.

Upper limits

When the observation of a source does not result in a detection, an upper limit must be calculated instead of its flux. In MAGIC, `flute` uses the so called *Rolke method* [207] to determine confidence intervals for the number of excess events. The code uses a profile likelihood method assuming that on events are Poisson distributed and the background distribution is approximately Gaussian. The advantage of this method is that it allows to apply efficiency corrections and estimate the effect of systematic uncertainties on the efficiency.

Systematics

The main systematic uncertainties affecting flux measurements are found in the reconstructed energy of the events. Two main components contribute to this effect:

- *Instrument performance.* MAGIC is a telescope operating under changing weather conditions. The optical properties of the telescopes (reflectivity, PSF) vary with time as dust accumulates in the reflecting surfaces and storms affect the optical alignment of the parts. PMTs are also unstable by nature and their efficiency degrades with time.
- *Earth's Atmosphere*, which is a dynamic and non-perfect calorimeter with short and long term variability. If the atmosphere becomes optically thicker, then the density of Cherenkov photons that can be seen from the telescopes changes. This creates a mismatch between the simulated shower development in MC

γ-rays and the actual observations. This in turn would affect not only the estimated energy of the shower, but also the measured fluxes as a significant fraction of the showers would fail to trigger the instrument and the rest would be reconstructed incorrectly.

After the upgrade of the MAGIC stereo system, we estimate that the systematic uncertainties can be divided in $< 15\%$ in energy scale, $11 - 18\%$ in flux normalization and ± 0.15 in the slope of the energy spectrum assuming a power-law shape. The details of how these systematic uncertainty are estimated are described in Aleksić et al. [204].

Part III

AGN studies with MAGIC

> *The typical planetary spectrum, where Eβ is fainter than N2, is found in the rare cases of apparently stellar nuclei of spirals; for instance, in N.G.C. 1068, 4051, and 4151. Here also the emission spectra are localized and do not extend over the nebulae.*
>
> —Edwin Hubble, 1926 [208].

6

Active Galactic Nuclei

Contents

6.1 A brief history of AGN studies

Emission lines in rare spiral nebulae

The beginning of AGN studies can be found early in the twentieth century when, trying to clarify the nature of the "spiral nebulae", Fath [209] noticed that most of these diffuse sources had continuum spectra with stellar absorption lines consistent with unresolved stars at great distances, well differentiated from bright nebulae and their intense emission lines. One rare case arise, NGC 1068, for which he noted a composite spectrum with strong emission lines on top of a continuum filled with absorption lines. Following his work, other 'rare' spiral nebulae with nuclear emission lines were spotted.

Seyfert objects

A more systematic study of spiral nebulae with bright nuclei and their classification started when, in 1943, Seyfert [210] observed very wide emission lines, attributed to Doppler shifts which reached up to $8 \times 10^3\,\mathrm{km\,s^{-1}}$. He noticed that these sources clustered in two groups. The first (*Seyfert 1*) had similar and very broad ($3 \times 10^3\,\mathrm{km\,s^{-1}}$) line profiles for both forbidden lines and hydrogen lines. The second (*Seyfert 2*) had narrow hydrogen and forbidden lines, but in the case of hydrogen lines, he observed very broad wings of up to ($7.5 \times 10^3\,\mathrm{km\,s^{-1}}$). This contrasted dramatically with the narrow emission lines of diffuse nebulae (HII regions) in irregular and spiral galaxies.

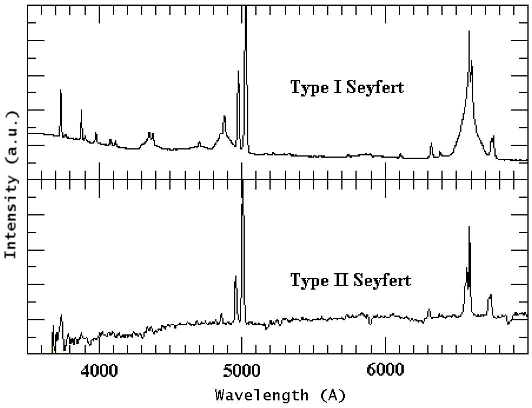

Figure 6.1: Comparison between Sy 1 and Sy 2 spectra. Adapted from `http://www.uni.edu/morgans/astro/course/Notes/section3`.

The advent of radioastronomy

AGN finally grabbed astronomers' attention with the advent of Radio Astronomy. Using a rotatable antenna and short-wave receiver, Jansky [211] detected static of unknown origin coming from the Galactic plane which was particularly strong towards its center [212]. By the end of World War II, Hey, Parsons, and Phillips [213] used their 6-degree beam to constrain the emitting region size in the Cygnus region. The angular resolution continued to develop and in 1949, further work from Bolton, Stanley and Slee [214, 215] led to the first identification of several radio sources: Taurus A with the Crab nebula (a supernova remnant from SN1054, Messier 1), Virgo A with Messier 87 and Centaurus A with NGC 5128.

The first morphological studies were done in Jodrell Bank [216]. Sources were divided in Class I (typically in the plane of the Milky Way and with puzzling morphologies [216, 217]) and Class II (compact, isotropically distributed and probably extragalactic).

The non-thermal nature of the emission was firstly suggested by Reber [219]. In the 40s, the belief was that the emission was free-free radiation (thermal bremsstrahlung) from ionized gas in the interestellar medium. Alfvén and Herlofson [220] proposed in 1950 that the radio emission was in fact synchrotron radiation from cosmic-ray electrons trapped in the magnetic fields generated by a star, hence calling these sources "radio stars". Similar arguments were used by Kiepenheuer, Ginzburg and Syrovatskii,

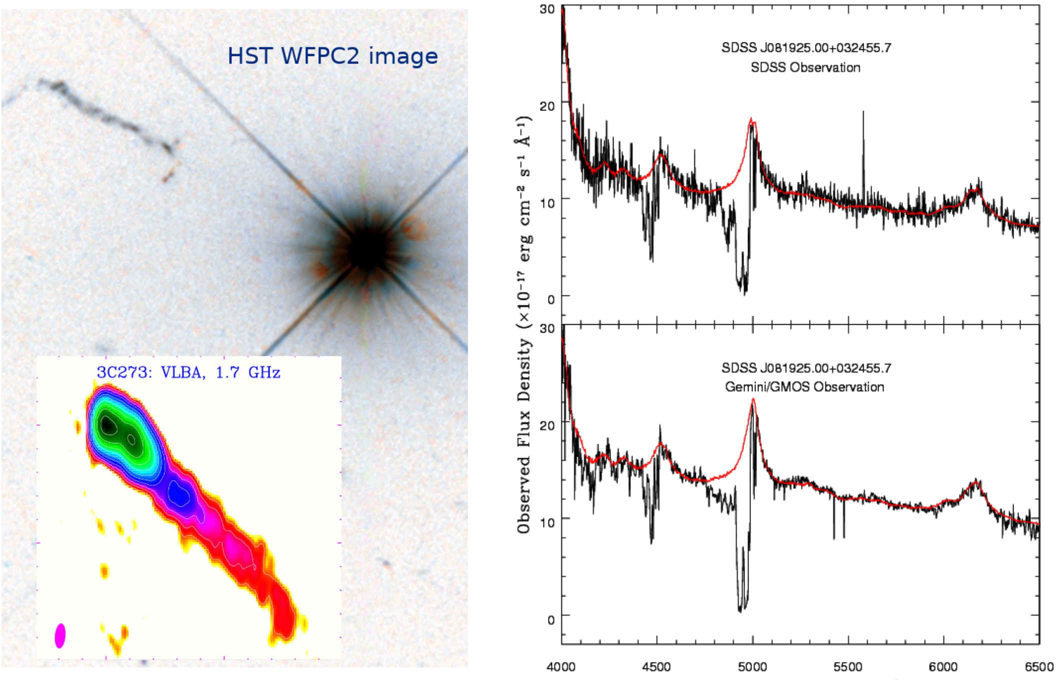

(a) Optical (Source: *Hubble's Wide Field and Planetary Camera 2* and Radio image of QSO 3C273 SDSS obtained with VLBA at 1.7 GHz).

(b) SDSS and Gemini/GMOS spectra of BAL QSO J081925.00+032455.7 ($z = 2.138$) and its absorption-less reconstruction [218].

Figure 6.2: Examples of observational features of AGNs

explaining the Galactic radio background as synchrotron (magnetobremsstrahlung) emission from cosmic rays in the Galactic magnetic field [221–223].

Multiwavelength observations

The final push towards understanding the nature of AGNs was an almost simultaneous effort in multiple energy bands: the publication of the third Cambridge (3C) survey at 159 and 178 MHz [224, 225], the discovery in the optical band of compact galaxies and compact galaxy nuclei [226, 227] and the compilation of the Markarian catalog [228]: a list of galaxies with abnormally bluer colors and a bright ultraviolet continuum towards their core.

Quasi-stellar sources

Quasi stellar radio sources (QSRS), quasi-stellar sources (QSS, QSO) or simply quasars were discovered after studying the optical counterpart of 3C 295 [229], 3C 48 [230] (with peculiar colors and striking variability of up to 0.4 mag) and 3C 273 [231]. They all exhibited a compact (star-like) unresolved shape with faint to no nebulosity and unprecedented spectra, with broad emission lines at non-expected wavelengths, photometric variability and intense ultraviolet emission. The general consensus was that these radio sources were peculiar stars but there was a remote possibility that they were distant unresolved galaxies.

Further radio observations of quasar 3C 273 during a lunar occultation [231–237] showed a two component source: a preceding (3C273A) star-like object with spectral index $\Gamma \approx -0.9$ (typical of Class II radio sources) and a 'faint wisp' (3C273B) with a very unusual spectrum ($\Gamma \approx 0.0$), which resembled a jet of $1-2''$ width extending away from 3C273A. Schmidt [231] concluded through line identification that the source was most probably the nuclear region of a galaxy at a cosmological redshift $z = 0.158$.

The data suggested that a central object was the source of the optical continuum. This object would be surrounded by the emission-line region and radio emitting region. The inferred size of the jet of 3C 273 was $\sim 50\,\mathrm{kpc}$ (length), comparable in size to the Milky Way. The quasar seemed to harbor a collapsed region of $\sim 10^9 M_\odot$ [238].

In 1965, Sandage [239, 240] reported the discovery of a large sample of radio-quiet QSO-like objects (interloopers or quasi-stellar galaxies, QSG). More quasars were rapidly discovered in an apparent race towards higher redshifts [241–243]. Measurements of intergalactic HI through the detection of Lyα emission had important implications on the rate of expansion of the Universe, making quasars excellent Cosmology laboratories. Multiple discoveries were made soon after, such as the existence of absorbers between the quasar and us ($z_{abs} < z_{em}$) [244] that even generated a forest of absorption lines, the presence of some sources for which z_{abs} seemed to be greater than z_{em} (interpreted as material that was 'falling' into the QSO [245]) or the opposite, broad absorption lines on the short-wavelength side of corresponding emission lines (BAL objects, accounting for 10% of radio-quiet QSOs) that seemed to indicate expanding shell of gas around the central object [246].

Emission lines

By the end of the 50s, it was clear that the emission lines in Seyfert galaxies were most probably originated in a small volume ($\sim 100\,\mathrm{pc}$) close to a very hot ($T \approx 2 \times 10^4\,\mathrm{K}$) central region with a total mass of $\sim 10^5 M_\odot$.

For a long time, it was not well understood why some sources showed broad wings in permitted lines but not in forbidden lines (Seyfert 1 or Sy 1) while others did not show such wings and both forbidden and permitted lines had the same widths (Seyfert 2 or Sy 2) [247]. The classification was convenient as it only depended on spectral features. Photometric and morphological properties further supported such division. Lines such as Hα and [N II] tend to blend in Seyfert 2, while for other galaxies with strong emission lines they are sharp and clearly resolved. Sy 2 also have very high [O III]:Hβ ratios, which implies that narrow line galaxies and Sy 2 have different ionizing sources. Both Seyfert groups have excesses in UV bands that cannot be due to stellar radiation.

Since the 60s, two models were proposed to explain the origin of the broad Balmer lines. The first model, from Woltjer [248], assumed a separate region of fast moving (possibly gravitationally bound) gas to explain the line broadening. An alternative model was suggested by Burbidge et al. [249], who believed that the large widths arose from electron scattering in a region with optical depths of $\tau_e \sim 0.1$. The problem was that such scattering region needed to be so dense and compact that it would wash the continuum variability that is characteristic of many of these objects. The idea of the two zones, one inner and small with dense and fast moving clouds ("Broad Line Region", BLR) and one larger with slower moving and less dense clouds ("Narrow Line Region" or NLR) gained momentum from photoionization models [250]. The model was further supported by forbidden line widths, which were naturally explained as occurring in the less dense NLR. Photoionization became then accepted as the main source of heating and ionization in the emission-line gas.

Source of energy

The idea of QSO being powered by a supermassive black hole (SMBH) was originally proposed in 1964 by Salpeter [251] and Zel'dovich [252]. The large masses derived for the emitting region in the previous decade, largely in excess of Chandrasekhar's critical mass $M_{\rm crit} \approx 1.4\,{\rm M}_{\odot}$, implied that these central structures would end up collapsing within their Schwarzschild radius, forming a SMBH. Nothing can escape from the Schwarzschild sphere of radius $r = 2\,{\rm GM/c}^2 \equiv 2\,{\rm m}$, but the strong gravitational effects can be indirectly observed.

When a QSO is active, the accreted gas forms a flat disk with a differential rotation velocity profile. Such system, similarly to the accretion disk of a protostar [253], releases energy through "friction". Magnetic transport of angular momentum dominates over turbulent transport for low molecular viscosity (as it happens in Alfvén's theory of the primaeval solar nebula). Even with accretion rates as low as $10^{-3}\,{\rm M}_{\odot}\,{\rm yr}^{-1}$ the system can dissipate $\sim 10^{42}\,{\rm erg\,s}^{-1} \sim 10^{9}\,{\rm L}_{\odot}$ as the material falls into the last stable orbit at $r = 6\,{\rm m}$. With a released energy of $0.057\,c^2$ per unit mass, accretion can significantly brighten the nucleus of a galaxy. In fact, an accretion rate of $1 M_{\odot}\,{\rm yr}^{-1}$ and an efficiency F (mass flux) of converting matter into light of 10% can generate as much light as a whole galaxy. In order to explain QSO luminosities, with accretion disk effective temperatures of $10^5\,{\rm K}$ (leading to photoionization and broad line emission), it would be required to have larger accretion rates ($10^{3-4}\,{\rm M}_{\odot}\,{\rm yr}^{-1}$), not sustainable in the long term as pointed out by Lynden-Bell [254]. He concluded that the Universe was probably filled with "dead quasars".

6.2 Emission properties

The spectrum of an Active Galactic Nuclei is a complicated sum of excitation lines (already discussed), thermal and non-thermal emission components (see Figure 6.3). The latter was first suggested to account for:

- Fast variability events [256] and the correlation between the variability at $10\,\mu$m and the one measured in radio [257–259].
- The presence of power-law energy distribution that were also observed in radio galaxies and the Crab Nebula (interpreted there as synchrotron radiation).
- The strong optical polarization [260]. For some sources (e.g. NGC 1068) the polarization degree is significantly larger in the UV than in the IR.

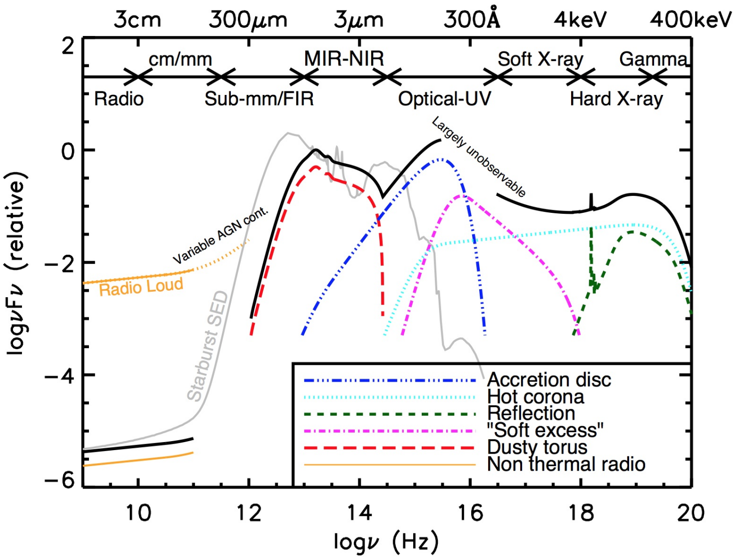

Figure 6.3: Broadband spectral energy distribution from non-jetted AGNs. Adapted from Harrison [255].

Thermal components are present in many (but not all) AGNs in optical and IR. They are generated mainly by heated material the dusty torus and the accretion disk and can contribute to a good fraction of the bolometric luminosity in some cases.

6.2.1 Optical radiation

Inverse Compton scattering was first invoked by Shklovskii [261], who defended that submillimeter and far-infrared synchrotron radiation coming from a region of just $\sim 10^{16}$ cm could be boosted to the optical band through inverse Compton scattering with relativistic electrons of $\sim 10\,\mathrm{MeV}$. He stated that Seyfert galaxies and QSO were similar objects and despite being radio quiet, they might be observable at higher radio frequencies.

Hoyle [262] exploited the idea of inverse Compton playing a major role in order to question the cosmological nature of the measured redshifts. He argued that if relativistic electrons are inelastically scattered by low-energy photons, this would result in a divergence on the energy of the photons due to scattering events stacking one on top of another. Instead, he suggested that the bulk of the light seen in optical-IR was due to synchrotron emission. He also argued that for objects as small as 10^{17} cm, the broad line region would be opaque in the continuum, concluding that either quasars were close ($\sim 10\,\mathrm{Mpc}$) objects or the physical models at the time were wrong. Furthermore, if the region was indeed at cosmological distances, IC losses would dominate over synchrotron radiation loss unless the magnetic fields involved were very strong.

The puzzle was finally solved by Woltjer [263], who proposed that electrons move in a narrow cone (~ 10) around the magnetic field lines of a radial field and hence the emission would be highly anisotropic, reducing the efficiency of IC cooling. He concluded that such a situation might link QSO with extended radio sources.

Thermal components in the optical band were proposed after observing that about half of the quasars become bluer as their luminosity increases [264], interpreted as gas heating [265]. If optical/UV traces mainly processes related to the accretion disk, then thermal fluctuations driven by stochastic processes such as magnetic turbulence becomes a plausible source of such variability [266].

6.2.2 Infrared radiation

In parallel with non-thermal emission model development for radio and optical, the improved IR instrumentation made obvious that a thermal component might be present at mid IR, at least for some sources [267, 268]. For them, mid IR radiation was less polarized, there was an excess of emission with respect to a pure non-thermal power law spectrum at $3 - 5\,\mu$m and the spectrum showed a minimum at $1\,\mu$m, interpreted as dust grain evaporation ocurring above $1500\,$K.

For Seyfert 2 galaxies, the presence of a dusty component which was re-emitting absorbed UV light at longer wavelengths could explain the observed line reddening and the excess at $3 - 5\,\mu$m [269]. The situation however was less clear for Seyfert 1 and quasars. Their optical and infrared continuum showed no significant reddening and the non-thermal continuum extended up to UV, providing radiative ionization of the gas and recombination lines [270, 271].

In the far IR, variability correlated with the polarization degree [272]. High polarization objects varied up to a factor 2 in a few months. These objects were consistent to the “blazar” source class. “Normal quasars” and Seyfert galaxies showed no more than 15% changes and if any, variability was present only in much longer time scales.

6.2.3 Radio emission

The angular resolution of radio interferometers rapidly improved in the 60s with the aim of studying milliarcsec features predicted by monthly-scale variability detected on some AGN and causality arguments. Very long baseline interferometry (VLB, VLBI) was introduced by analog or digital posterior correlation of magnetic taped signals from two antennas separated by very long distances. Starting from 1967 it was possible to observe AGNs with baselines of 200 km [273, 274], quickly growing to cover a distance comparable to Earth’s diameter (California, United States - Parkes, Australia).

Rees [275] predicted in 1966 “superluminical” motion for extragalactic radio sources, where the emitting region could move at close to the speed of light towards the observer and with very low pitch angles. The effect was spotted for 3C 279 with the Goldstone (California) - Haystack (Massachusetts) baseline, which in October 14-15, 1970 [276] showed a symmetrical double source separated $1.55 \pm 0.03\,$mas and just 4 months later [276] this separation increased to $1.69 \pm 0.02\,$mas. The resulting linear separation rate was 10 ± 3 times the speed of light for $z_{3C\,279} = 0.538$ and $H = 75\,\mathrm{km\,s^{-1}\,Mpc^{-1}}$. Such “superluminical” expansions were also

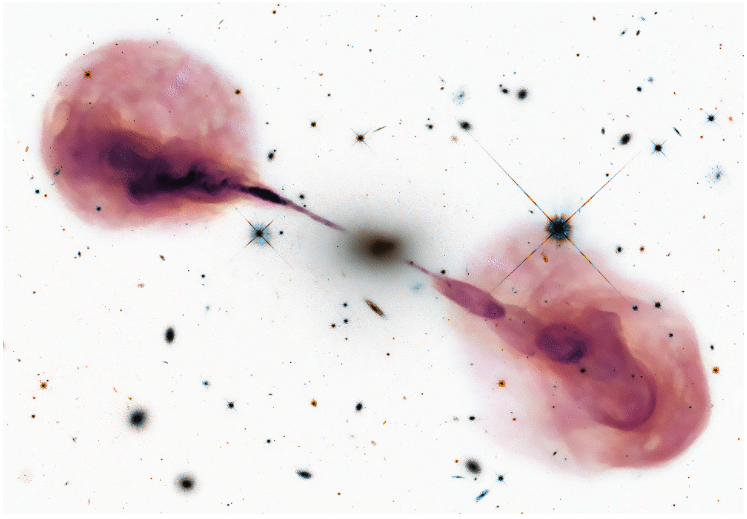

Figure 6.4: Composite image of Her A (3C 348) in optical (HST) and radio (VLA) showing the giant radio lobes emanating from the elliptical host galaxy. Credits: NASA, ESA, S. Baum and C. O'Dea (RIT), R. Perley and W. Cotton (NRAO/AUI/NSF), and the Hubble Heritage Team (STScI/AURA)

observed for 3C 273 [277]. Original interpretations included spatial distribution of the emitting sources, phased time variations, multiple images of a gravitational lensed object, wrongly measured distances of 3C 279, large underestimation of the Hubble constant, etc. Interestingly, the possibility of having the jet at a pitch angle of $\theta \lesssim 6\,\mathrm{deg}$ was considered unlikely, but the idea rapidly found further support thanks to relativistic jet models [278].

Radio emission is an accurate tracer of the non-thermal nuclear emission and it allows for morphological studies. In that regard, the pioneering work from Fanaroff and Riley [279] was essential to understand the nature of the radio emission and its origin. They discovered that radio galaxies (RG) tend to cluster in two well differentiate groups, those with the largest emission placed close to the central object (Class I), and those with 'hot spots' further away from the central region (Class II). They also observed that objects of Class II were statistically more luminous than Class I sources and that the division seemed to be related to cosmological evolution [280].

6.2.4 X-ray emission

One of the first astronomical X-ray experiments was carried out using a sounding rocket equipped with Geiger counters sensitive to energies of $\sim 155 - 620\,\mathrm{eV}$ [281]. The rocket reached an altitude of 225 km and the observations, above 80 km, lasted 350 s. The experiment resulted in a significant detection of soft X-rays, incompatible with the Sun or the scattering by major solar system bodies. The strongest signal was recorder in the directions of the Galactic center, Cas A and Cygnus A (all of them intense radio sources). The emission was interpreted initially as synchrotron radiation, idea quickly discarded because of the large electron energies required to produce it. Inverse Compton [282] or Bremsstrahlung [283] were proposed instead.

By the end of the 60s, several active galaxies were detected as X-ray emitters, including the RGs M87 and Cen A (NGC 5128) and the QSO 3C 273 [284–286]. The latter had a X-ray luminosity of $\sim 10^{46}\,\mathrm{erg\,s^{-1}}$, comparable with its optical luminosity. More systematic X-ray studies were only possible with the dedicated X-ray satellite Uhuru [287], which detected several Seyfert galaxies [288, 289] with fluxes of $10^{42.5-44.5}\,\mathrm{erg\,s^{-1}}$ in the range $2-10\,\mathrm{keV}$ [290, 291]. In particular, for Sy 1 the X-ray emission seemed to be correlated with Hα line luminosity and optical/infrared continuum powers, but no correlation with radio was found [290].

The detection of long and short-term X-ray emission changes in Centaurus A [292, 293] using Uhuru, OSO-7 and Copernicus data motivated variability studies in other sources. In a survey made using Ariel V data over 5 yr, the X-ray emission from 28 active galaxies was investigated, concluding that half of the sample was variable with yearly changes of a factor of 2 in flux [294]. Short term variability ($1\,\mathrm{h} \lesssim t \lesssim 1\,\mathrm{week}$) was also observed on a number of them. These properties seemed to indicate that X-rays originated well deep in the nucleus ($\sim 0.1\,\mathrm{pc}$) of the galaxy and X-ray observations were the key to understand its nature.

HEAO-2 (better known as Einstein Observatory) was the next big step in the development of X-ray astronomy. With its improved sensitivity, it allowed to study QSOs as a class of X-ray emitters. Tananbaum et al. [295] found variability time scales of $\lesssim 10^3\,\mathrm{s}$ for some sources, implying masses of $10^{5-8} M_\odot$ for the central black hole. They also found that the radio and X-ray emission for radio-loud quasars was correlated and that they were intrinsically more luminous in X-rays than their radio-quiet counterparts [296, 297].

Finally, a correlation of X-ray and UV fluxes (at $1350\mathring{A}$) was also observed. The *Big Blue Bump* [298] (characteristic of many AGNs, particularly non jetted sources) was consistent with a sum of thermal emission from an accretion disk plus a significant reprocessing of X-ray radiation. The same non-blazar objects typically exhibited structured X-ray emission (see Figure 6.3), with two prominent features found: a soft excess below $\sim 1\,\mathrm{keV}$ and a Compton hump (reflection of coronal X-rays by a cold disk) with a continuum coming from Compton upscattering of disk photons by the hot corona [299]. At even higher energies, most of the sources showed strong spectral cutoffs.

6.2.5 Gamma-ray emission

After the initial success from Explorer XI in detecting γ-ray events of unknown origin [282], the attempts made with OSO-3 (1967-68), SAS-2 (1972-73) and COS-B (1975-82) [300] to identify the first γ-ray sources only resulted in a few AGNs identifications. Most of the sources had spectra that reached $\sim 1\,\mathrm{MeV}$, with the sole exception of 3C 273, for which COS-B detected an emission reaching $\geq 35\,\mathrm{MeV}$. As soon as the Energetic Gamma ray Experiment Telescope (EGRET) was operational in 1991, it became evident that blazars completely dominated the population of γ-ray emitting AGNs.

The third (and final) catalog of high-energy γ-ray sources detected by EGRET

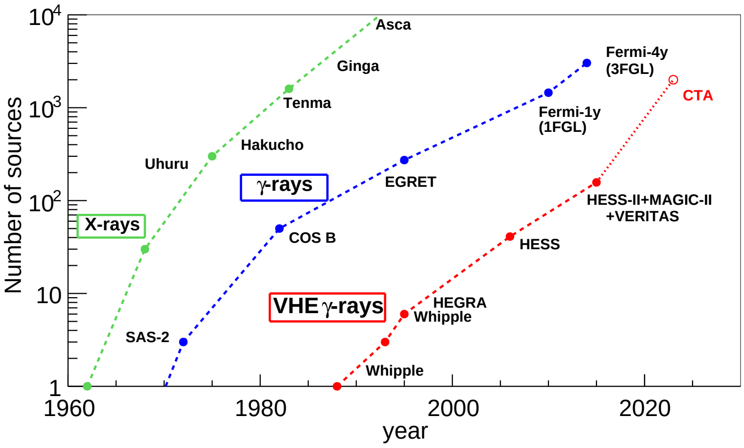

Figure 6.5: X-ray and γ-ray astronomy development. Adapted from [307].

included slightly more than 4 years of exposure. 271 sources were detected above 100 MeV, including a hint from Centaurus A, 66 high confidence blazars and hints from other 27 blazars. Most of the sources were bright radio-loud quasars (FSRQs, $\alpha_r \geq -0.5$), but the BL Lac object Markarian 421 was detected as well. Additionally, several high latitude γ-ray sources were detected and they were thought to be blazars with less powerful (undetected) radio emission. A nearly isotropic emission was also detected after subtracting the modelled Galactic emission [301, 302] which was believed to originate also from blazars [303].

For many of the EGRET blazars, the energy spectrum was dominated by the high energy component, with γ-ray luminosities typically ranging from $10^{47-48}\,\mathrm{erg\,s^{-1}}$ to more than $10^{49}\,\mathrm{erg\,s^{-1}}$. Variability was detected in many of them, with time scales from days to months, implying (assuming isotropic emission) emitting region sizes of the order of the Schwarzschild radius for a $10^{10} M_\odot$ black hole.

The γ-ray emission was interpreted as originating from shock waves forming along the jet, producing a very energetic and variable synchrotron emission. In this scenario, optical variability was expected to precede the radio knot detection due to synchrotron self-absorption hiding the knots initially [304]. The same models however failed to explain the EGRET detected spectra [305].

In the mid 90s, external Compton models were established [306]. They provided a satisfactory explanation to the large γ-ray fluxes observed in FSRQs by assuming that the Comptonization of external photon fields (e.g. coming from the UV disk) could dominate the SSC emission.

In parallel, the first very high energy (VHE, $E > 100\,\mathrm{GeV}$) emission from an extragalactic source (Markarian 421) was detected in 1992 by Whipple [308]. Its VHE signal was about ~ 0.3 times that of the Crab Nebula at similar energies, the standard candle in VHE due to its stable and relatively high luminosity between few GeV and tens to TeV. This detection was quickly followed by Markarian 501 in 1995 [309]. From there, Earth-based γ-ray astronomy gained popularity as the population of sources grew. This was possible thanks to the technical developments of the new generation IACTs (HEGRA, H.E.S.S., CANGAROO, MAGIC and VERITAS) with: i) larger cameras with more extended trigger regions to detect bigger events and showers at larger impact parameters; ii) finer pixelization to improve gamma-hadron separation by means of the shower shape; iii) larger mirrors to lower the energy threshold; iv) stereoscopic observations to improve background rejection and sensitivity; v) new analysis methods like machine learning (e.g. RF), model analysis, statistical procedures like unfolding/regularization.

The population of extragalactic VHE sources is dominated by BL Lacs. From the 74 extragalactic sources detected as of November 2017, there are 68 blazars (56 BL Lacs, 6 FSRQs, 6 of unknown type), 4 Fanaroff-Riley I radio galaxies and 2 starburst galaxies. These proportions are different than the ones from *Fermi*-LAT in HE gamma rays 100 MeV – 100 GeV, which has roughly the same amount of FSRQs and BL Lacs. VHE observations are hence needed to have a less biased view of the physical phenomena that is present in this huge cosmic engines.

6.3 Taxonomy

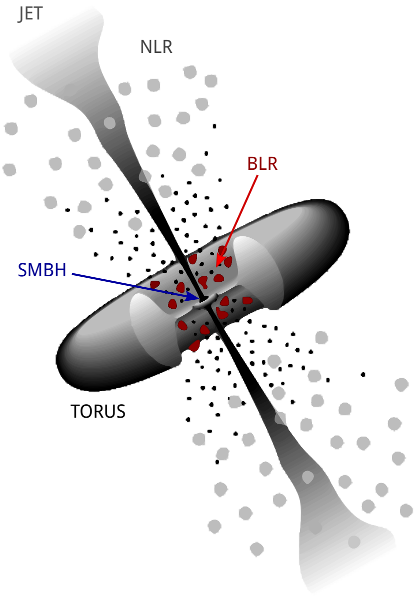

Figure 6.6: Schematic diagram of a radio-loud AGN.

Active Galactic Nuclei are a very heterogeneous group of sources which can be classified attending to very different criteria. Their continuum IR to X-ray emission has approximately the same properties for all sources. However, the presence or absence of prominent radio emission means fundamental differences in the host galaxy type, black hole spin, jet properties, etc.

According to their radio emission, about 10–20% of AGN are *radio-loud* ($F_{5\,\mathrm{GHz}}/F_B \gtrsim 10$) [310], a percentage that increases with luminosity ($\sim 50\%$ for $M_B \lesssim -24.5$). *Radio-loud* objects are characterized by large scale radio jets or lobes that take up a good fraction of the total bolometric luminosity as kinetic power. They are mainly hosted by giant elliptical galaxies and are thought to be ultimately generated by recent merger activity. If such a merger takes place, the coalescence of two similar-mass super massive black holes can result in a very massive rapidly spinning *Kerr* black hole, whose rotational energy and accretion can power the jet. *Radio-quiet* objects have insignificant radio components in comparison and are predominantly found in spiral galaxies or in mergers where the black hole mass ratio is large, which result in slowly spinning holes. The fundamental physical differences between the two types is the reason why, more than an unification model, we should talk about radio-loud and radio-quiet unification models.

The rest of the classification relies mostly on the observing angle. The axial symmetry of the problem causes AGN to be perceived as dramatically different sources depending on the angle at which they are observed as the emitted light is subject to different phenomena (absorption, anisotropy and beaming). In the original paper from Urry and Padovani [311], a major distinction is made between objects with broad lines or *Type 1* (Sy1, QSOs, BLRG/SSRQ/FSRQs), narrow line objects or *Type 2* (Sy 2, NELG, IR quasars, NLRG of FR-I and FR-II classes) and finally unusual objects or *Type 0* objects (BAL QSOs, BL Lacs and FSRQs).

6.3.1 Radio-quiet sources

Radio-quiet sources are typically classified in *Type 1* radio-quiet sources (Seyfert 1 and radio-quiet QSO) and *Type 2* sources (Seyfert 2). They typically harbor $\sim 10^7 M_\odot$ black holes and their bolometric luminosity is $L_{bol} \sim 10^{44}\,\mathrm{erg/s}$ for Seyfert 1 and 2 galaxies and slightly larger for radio-quiet quasars ($M_{\mathrm{SMBH}} \sim 10^8 M_\odot$, $L_{bol} \sim 10^{45}\,\mathrm{erg/s}$) [312].

Most *Type 1* radio-quiet AGNs show strong and high-ionization narrow emission lines and broad lines (including forbidden lines). Subgroups are commonly defined to account for the relative strength of broad lines (e.g. Sy 1.5 having stronger broad lines than Sy 1.9).

Type 2 radio-quiet AGNs contain strong narrow lines in NIR, optical and UV. They are further subdivided in *hidden Type 1* Sy, for which broad lines can be seen in polarized spectra and the diffuse *true Type 2* Sy. These AGNs are challenging to identify because strong narrow emission lines are also a characteristic of star-forming galaxies, more numerous than AGNs. When no hard X-ray data is available, the best strategy to separate them is by means of emission-line diagnosis, being common practice to use ratios of line fluxes (involving same-element or hydrogen recombination lines to reduce abundance effects). These lines should be strong (easy to measure even at large distances), easy to identify and should differentiate between HII regions (star formation) and AGNs generated features. Some widely used optical/UV lines include C IV 1549$\AA$, He II 1640$\AA$, Lyα, [O III] 5007$\AA$, [N II] 6583$\AA$, [S II] 6724$\AA$, [OII] 7234$\AA$, etc.

More recent classification schemes tend to explicitly mention LINERs (AGNs with low ionization and narrow emission lines from a gas ionized by a nonstellar source [313, 314]) and Lineless AGNs (very weak or totally undetected emission lines).

6.3.2 Radio-loud sources

Radio galaxies (RGs) normally exhibit giant radio lobes and jets. They host slightly more massive black holes ($\sim 10^8 M_\odot$[1]) and larger luminosities ($\sim 10^{46}\,\mathrm{erg/s}$[2]) than their radio-quiet counterparts [312]. Like in Seyferts, they can be split in *Narrow Line Radio Galaxies* (NLRGs) and *Broad Line Radio Galaxies* (BLRGs).

RGs can be also subdivided according to the jet morphology. In Fanaroff-Riley I (FR-I) sources, the ratio between the distance of the brightest radio spots to

---

[1] They exhibit larger mass distribution spread than radio-quiet sources.

[2] The actual bolometric luminosity is hard to estimate due to the unknown relativistic boosting.

the total radio structure size is less than 0.5 (inner jet dominates the emission). For FR-II, this ratio is larger. In general, FR-II are more luminous ($L_{178\,\mathrm{MHz}} > 2 \times 10^{25}\,\mathrm{W\,Hz^{-1}sr^{-1}}$) than FR-I.

Aligned or beamed radio-loud sources form a family of AGNs on their own, known as blazars. When seen through the jet, their apparent luminosity can reach $\sim 10^{49}$ erg/s due to the extreme *relativistic aberration*. Blazars can be further classified according to the strength of their spectral features in BL Lacs (continuum dominated) and the generally more luminous Flat Spectrum Radio Quasars (FSRQs) or Optically Violent Variable quasar (OVV), which often exhibit strong emission lines. Blazars are the dominating class in γ-rays, and will be described more in detail in Section 6.4.

6.4 Blazars

Blazars, originally misidentified as irregular variable stars, were found to be highly variable at all wavelengths (as opposed to most AGNs, which are less variable in far IR than they are in UV) following no apparent patterns.

The prototypical example of this class is BL Lacertae (BL Lac), originally discovered in 1929 [315] and described back then as a variable star with a apparent magnitude ranging from $13 - 16^{mag}$. BL Lac was identified in 1968 with the radio source VRO 42.22.01 by Schmitt [316], noting that the object had a marginal envelope. The absence of optical features and its strong optical polarization suggested a nonthermal nature of the bulk of the radiation, and at the same time did not help to classify the source and measure its distance [317]. Its extragalactic nature was proposed after the identification of the host galaxy [318, 319], with a redshift of $z = 0.07$. The identification of its host galaxy and absorption features was done by taking the spectra of an annular aperture centered at the central object to obscure the bright nucleus [320]. The discovery of other sources with similar properties (violent variability, strong polarization and their unusual spectra) invited astronomers to group them in a new class of BL Lac-like objects [321]. The new source type seemed to be related to a subset of quasars known as optically violently variable (OVV, known also as Flat Spectrum Radio Quasars or FSRQs).

The FSRQ family comprises $\sim 10\%$ of the radio-loud sources. They are characterized by changes in their optical fluxes as high as a factor ~ 2 in one week. Contrary to other quasars (and similarly to BL Lacs), optical linear polarization often reaches fractions of up to $\sim 10\%$. The main differences with respect to BL Lacs were the presence of strong emission lines and the apparent deviation from the pure non-thermal nature, with hints of a hot accretion disk at shorter wavelengths and heated dust components at longer wavelengths.

Blazars are the dominating class in γ-rays. In some cases, the ‘amplified’ non-thermal emission coming from the ultrarelativistic plasma can overcast the spectral features that we described for radio-quiet or misaligned radio-loud sources.

6.4.1 The nature of non-thermal emission in blazars

The extreme luminosities and the rapid variability provide evidence that the high energy emission originates in relativistic jets that are roughly pointing toward us. Through causality arguments, the emitting region can be constrained in size and its precise placement can be derived from estimations of the magnetic field strength, charged particle density, etc.

It is common practice, and generally does not limit the generality of the results, to assume that the emitting plasma (popularly known as 'blob') has a spherical shape with radius $R \sim 10^{15-18}\,\mathrm{cm}$. If we assume that this blob is moving at speed $\beta = v/c \sim 1$, it is subject to relativistic motion relative to a fixed observer with bulk Lorentz factors Γ and doppler shifts δ given by

$$\Gamma = \frac{1}{\sqrt{1-\beta^2}}, \qquad \delta = \frac{1}{\Gamma(1-\beta\cos\theta)} \tag{6.1}$$

where θ is the angle between the jet axis and the line of sight. The observed flux is enhanced by a factor of δ^4, variability time scales shortened by a factor of δ^{-1} (explaining also superluminical motions) and the energies upshifted by δ.

The plasma is usually considered to be composed mainly by leptons, although it may include other particles. Leptons are normally assumed to have Lorentz factors $\gamma \in [\gamma_1, \gamma_2]$, following an energy spectrum described by a smoothly Broken Power Law with indices α_1 and α_2 (with the break at γ_{br}). If we assume a plasma with electron density K_e embed in a tangled magnetic field B, the low energy component of the emission (radio through optical or even X-rays) can be naturally explained as synchrotron emission. Polarization measurements further support this interpretation. For the high energy component, the situation is less clear and two possible scenarios have been proposed: leptonic and hadronic.

Leptonic emission

In the leptonic scenario, the plasma is dominated by relativistic leptons (electrons and positrons). Protons, if existing, are assumed to have low enough energies or densities so that they do not significantly contribute to the observed spectrum. The highly relativistic leptons can undergo inverse Compton (IC) scattering with synchrotron-emitted photons coming from the same population of leptons (synchrotron-self-Compton, SSC) [322] or with ambient photons (external Compton or EC) [306, 323].

The simplest one-zone leptonic models are normally sufficient to reproduce the observational features of many simple blazars and explain the correlation seen between the low and high energy emission. On the other hand, it faces problems to reproduce very fast variability in the VHE emission (requiring very large bulk Lorentz and Doppler factors) and very small emitting regions for FSRQs [324]. The large separation of the low and high energy components seen in some blazars is difficult to explain as well (see chapter 7 and [325]).

In order to address these problems, several models have been proposed, including

Rad.	Quiet			Loud *(jet, lobes)*			
Fea.	Seyfert (*mostly Spirals)*		QSO	Radio Gal. *(misaligned)*		Blazars *(aligned, beamed)*	
Opt.	Sy 1 *broad* *lines*	Sy 2 *narrow* *lines*	*star* *like*	FR-I *core* *dom.*	FR-II *lobe* *dom.*	BL Lac *weak* *lines* *[FR-I]*	FSRQ *strong* *lines* *[OVV/FR-II]*

Table 6.1: AGN classification according to optical-radio criteria. *Rad.* stands for radio, *Fea.* for features, *Opt.* for optical emission and *dom.* for dominated. Note that, as usual with taxonomical classifications, the source families proposed are not unique and leave out multiple sources (e.g. SSRQs, BAL QSOs).

multi-zone and inhomogeneous SSC and EC models, time-dependent leptonic models, structured jet models such as the spine-sheath model from Tavecchio and Ghisellini [326], and internal-shock models [327].

Hadronic emission

In hadronic models, protons can also be accelerated to ultrarelativistic energies. While electron synchrotron emission dominates at low energies, the high energies would be produced by a combination of proton synchrotron, π^0 decay and synchrotron and inverse Compton from secondary particles.

Hadronic models have traditionally received limited attention due to the complex cross-section calculations (particularly for p-γ) and the amount of degrees of freedom involved. Calculations are typically done by means of MC simulations with codes like SOPHIA [328]. They are however fundamental to understand recent multi-messenger results [329, 330].

Their main criticism is that they do not successfully explain the often observed correlation between the low energy component variability, presumably coming from electrons (which can accelerate very quickly) and the high energy component coming from hadronic processes, which should be much more slowly varying. For a review of hadronic emission models, see Böttcher et al. [331]

6.5 AGN unification models

In the previous section, we have described the basic observational features of Active Galactic Nuclei (AGNs), as they were discovered in the different wavelength bands and an approximate classification of AGNs according to them (see Table 6.1).

6.5.1 The main components of an AGN

A simplistic prototypical picture of an AGN with its main parts is shown in Figure 6.7. Its main ingredients [311, 333] are:

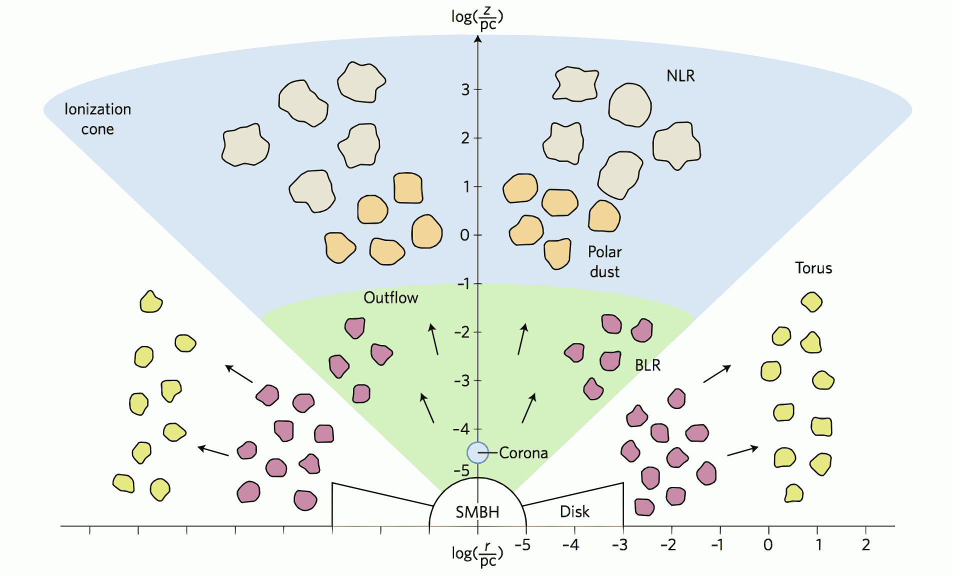

Figure 6.7: Sketch of the structure of a radio-quiet AGN showing typical spatial scales for the Disk, Torus, Broad Line Region (BLR), Narrow Line Region (NLR) and showing the approximate position of the X-ray corona. Different colors are used to indicate differences in composition or density. Adapted from Ramos Almeida and Ricci [332].

- A central *super massive black hole (SMBH)* of typically $M_{\mathrm{SMBH}} \sim 10^{6-10} M_{\odot}$, whose gravitational potential powers the whole structure.
- A sub-pc rotational dominated accretion flow (*accretion disk*) formed by matter that is falling into the black hole due to angular momentum losses caused by viscosity or turbulence. The disk, visible in the optical, UV or even soft X-rays, can be optically thick (geometrically thin or thick) or thin (also referred as radiation inefficient or advection dominated accretion flows). The large accretion rates translate into Eddington ratios of $L_{AGN}/L_{Edd} > 10^{-5}$.
- Clouds with high density, dust-free, gas quickly moving under the black hole's gravitational field and close to it ($d \sim 10^{-2} - 1\,\mathrm{pc}$). They form a *broad line region*, with significantly Doppler-broadened emission lines.
- A *dusty torus* [334] or *warped disk* [335] at $0.1 - 10\,\mathrm{pc}$, optically thick to optical and ultraviolet radiation. AGN tori seem to have a two-phase nature: clumps of high density dust clouds embed into a lower density dusty medium [336, 337]. This component blocks infrared through ultraviolet light generated inside the torus if the AGN is seen significantly tilted with respect to its axis.
- A lower density, lower velocity and dusty gas which extends from just outside the torus and up to $\sim 10^{2-3}\,\mathrm{pc}$ following the direction of the 'ionization cones'. 'Ionization cones' are conical structures along the torus axis filled with ionizing photons that can escape from the obscuring torus. The lower speed movements translates into significantly narrower (less Doppler broadened) emission lines, hence the name *narrow line region*.

- A (hard) *X-ray corona* close to the central object, probably caused by a sea of hot electrons above the disk, which may take energy away from the black hole itself when it rotates.
- Outflows of energetic particles which occur along the poles of the disk or torus, with tangled magnetic fields forming radio-emitting jets, which can led to giant radio sources in the case of galaxies of early types (giant elliptic and lenticular galaxies, e.g. Centaurus A or M87) but with no significant radio emission in most late type galaxies (spiral and irregular, e.g. NGC 1068, Mrk 279). In radio-loud objects, non-thermal emission across the jet is usually strongly collimated and beamed when the source is observed face-on (blazars).

The prototypical unified model [311, 338, 339] that builds with these basic ingredients has a clear axial symmetry and it implies different observable properties depending on just few parameters: the angle from which the AGN is observed and the source luminosity or black hole spin, naturally leading to different taxonomy-driven classifications, as seen in Table 6.1. There are two strong arguments supporting this idea: the detection of obscured and hidden nuclear and broad line components and the study of selection effects.

6.5.2 Hints of obscured/hidden nuclear components

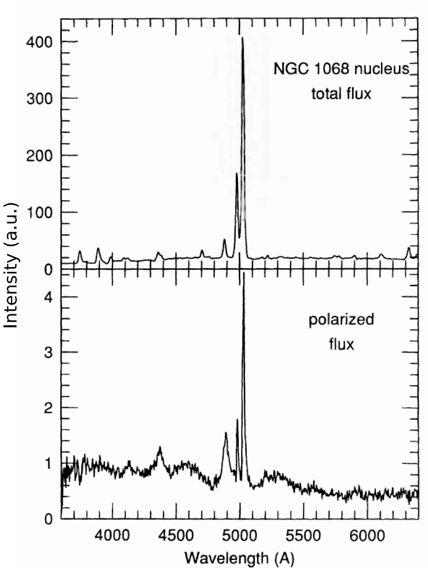

Figure 6.8: NGC 1068, the prototypical Sy 2 galaxy, seen through spectropolarimetry. The polarized component of the spectrum exhibits broad lines like Sy 1 galaxies [340].

Obscuration is mostly seen in Type 2 objects [341], particularly in Sy 2 and to lesser extent in FR-II. A fraction of the light of many of these objects is strongly polarized, and the spectrum of the polarized component has broad lines, resembling the behavior of Sy 1 galaxies (see Figure 6.8). Polarization seems to be the result of free electron scattering (wavelength independent) rather than dust grain scattering (which would be wavelength dependent) and seems to trace a hidden BLR. Spectropolarimetry and imaging polarimetry of several Radio Galaxies (RG) have since then shown hidden polarization continuum and broad lines that seem to be coming from hidden nuclear regions, supporting the unification of both source types.

The optical depth of the dusty component heavily decreases towards X-ray (higher energies) and IR (lower energies), making observations in these bands better probes of the nuclear regions in Type 2 AGN. Compact and bright IR cores and perpendicular polarization components have been spotted in several narrow-line radio galaxies of high and low luminosities. In other cases, broad wings are seen for Paschen lines [342] in the IR, while for optical bands no such broadened emission is seen because of the larger optical depths. The X-ray continuum is also weaker for Type 2 AGN when compared to Type 1, which is expected for more obscured objects with higher column densities.

Finally, anisotropic continuum emission tracing ionizing light cones [343, 344] is sometimes seen in optical imaging of narrow-line regions in Type 2 AGNs, suggesting obscured quasar-like luminosity. Ionizing beam powers are within the range for BL Lacs (continuum photons are preferentially emitted toward the ionization cones).

6.5.3 Selection effects

The combination of relativistic beaming and obscuration produces strong selection effects, making it almost impossible to derive fully unbiased samples. The number of blazars found in radio surveys heavily depends on the frequency where the sources are found, varying from $\lesssim 1\%$ in the 3CR (178 MHz) [345] to $\sim 50\%$ in the 1Jy (5 GHz) [346]. Far-infrared surveys are not a solution either, as they introduce an important bias against dust-free AGNs, the non-thermal far-infrarred emission may be beamed and obscuration may vary from one source to another. X-ray and γ-ray emission seems to be also largely biased towards beamed sources.

6.5.4 Unification of radio-loud sources

In the unification scheme, FR-I and FR-II appear as the ‘tilted’ counterparts to low power and high power blazars (BL Lac and FSRQs) respectively. In order to test this hypothesis, several authors have carried same-redshift surveys, which are equivalent in flux-limited samples to a selection in radio luminosity and narrow-line luminosity [347]).

FR-II and radio-loud QSO

For high power sources (FR-II and FSRQs or more in general radio-loud quasars), these surveys show that radio-loud quasars are systematically more [O III] (5007$\AA$) luminous than FR-II radio galaxies. This is expected since the [O III] emission, partly polarized and thought to come from a region subject to torus obscuration, is angle dependent [348, 349]. This is not the case for the [O II] (3727$\AA$) line emission, more isotropic and assumed to be produced further away from the nuclear region. Its luminosity in quasars and FR-II radio galaxies is indeed comparable. The unification scheme is further supported by the study of host galaxies in both populations at $z \lesssim 0.4$, which suggest that in both cases the host is a luminous elliptical galaxy.

In summary, flat spectrum radio quasars (FSRQs) and FR-II radio galaxies are basically the same objects. The strong continuum in radio quasars is justified in terms of Doppler boosting, while the presence of broad lines in the first and the lack of them in FR-IIs is understood as evidence of obscuration of the nuclear region by a thick molecular torus in the latter. Finally, the model explain why the slightly off-axis sources known as steep spectrum radio quasars (SSRQs) exhibit intermediate properties between FSRQs and FR-IIs.

FR-I and BL Lacs

Initially, BL Lacs were classified in radio-selected BL Lacs (dubbed as RBLs) and X-ray selected BL Lacs (XBLs). RBLs were found to be systematically more luminous than XBLs and FR-Is. Both RBL and XBLs show correlation between their radio and optical luminosities, but no correlation is observed with the X-ray luminosities. These results suggest that either XBLs are also slighly off-axis and thus are not as core-dominated as RBLs or XBLs are intrinsically less luminous than RBLs [350, 351]. Finally, there is strong evidence that BL Lacs and FR-I are similar objects and appear as low luminosity siblings of radio-loud quasars and FR-II respectively [352–357]. In particular, the observed extended radio powers at 5 GHz are similar in BL Lacs and FR-Is[356], which is expected by the beaming hypothesis.

In the unification framework, BL Lacs are the beamed version of FR-Is. The strong continuum in the former could in principle swallow the weak narrow lines typical of FR-Is.

It is worth to mention that the aforementioned separation between RBL and XBL BL Lacs is often misleading, with many sources like Mrk 501 fitting properties of both categories. This has motivated a recent re-classification of BL Lacs in low-energy cutoff BL Lacs (LBL) and high-energy cutoff BL Lacs (HBL) [351]. The line between them is typically drawn at $\alpha_{\Gamma X} = \log(F_{5\,\mathrm{GHz}}/F_{1\,\mathrm{keV}})/7.68 = 0.75$ (objects with lower values $\alpha_{\Gamma X}$ are HBLs, while higher values would point towards LBLs).

Relationship between FR-II/FSRQs and FR-I/BL Lacs

A number of factors make also the separation of FR-I and FR-II rather blurry and complicates any attempt of unifying them. First, there are RBLs with radio morphologies more consistent with FR-IIs than with FR-Is [358]. At the same time, a number of FR-IIs have low-excitation spectra (e.g. weak or undetectable [OIII] compared to H lines [359]), which is a characteristic of low power sources. Recent X-ray surveys [360] have in fact revealed a population of BL Lac objects identified with relativistic beamed FR-II radio galaxies. Finally, samples of BL Lacs and radio quasars with measured black hole masses and jet powers fully support the dicotomy between FR-I and FR-II, but support the unification schemes for FR-I with BL Lacs and FR-II with radio quasars separately [361].

Evolution serves to complete the puzzle of radio loud sources. FR-II objects are found in young and small host galaxies, normally isolated. Their relativistic jets tend to reach the full extend of the radio lobes. They also exhibit large accretion rates and have a quickly spinning black hole. These sources are thought to evolve with time into FR-I radio sources. The latter are grown up and old sources, found typically on rich clusters and with radio emission clustered towards the central object. The estimated accretion rates are significantly lower and their black hole spins more slowly. The deceleration of powerful jets in FR-IIs due to increased density of the intergalactic medium or a decreased accretion activity in the central region could explain this evolution pattern.

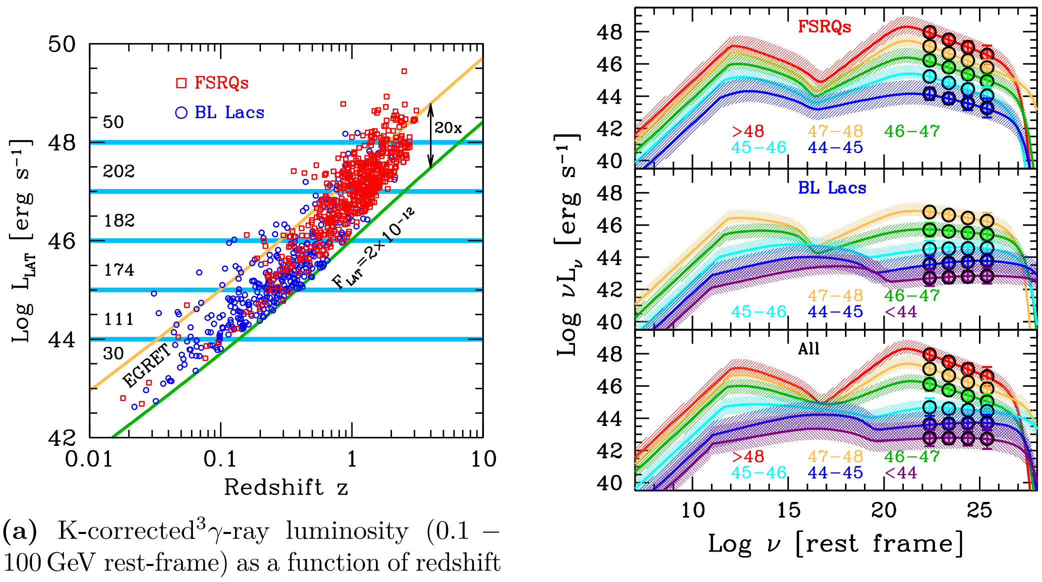

(a) K-corrected[3] γ-ray luminosity (0.1 − 100 GeV rest-frame) as a function of redshift for BL Lacs (blue) and FSRQ (red), featuring the sensitivity limit of two generation γ-ray telescopes: EGRET and LAT (3LAC catalog).

(b) Average Spectral Energy Distribution (SED) for sources of different γ-ray luminosity in the blazar sequence (represented in different colors).

Figure 6.9: The blazar sequence. Adapted from Ghisellini et al. [362]

6.5.5 The blazar sequence

Although similar in many aspects to Faranoff-Riley radio galaxies, BL Lacs and FSRQs deserve particular attention in this work due to the large number of these sources that can be detected in γ-rays.

Blazars have traditionally been subdivided between BL Lacs (emission line widths of less than 5 Å) and FSRQs (broader lines) [311]. Alternatively, the ratio of the luminosity of the broad lines to the Eddington luminosity can be used to trace a line between FSRQs ($L_{\mathrm{BLR}}/L_{\mathrm{Edd}} \gtrsim 10^{-3}$) and BL Lacs [363, 364]. The disadvantage of this physical approach is that the black hole mass must be known in order to estimate L_{Edd}.

Any flux-limited sample tends to cluster the most luminous sources at higher distances. For BL Lacs, this traditionally motivated the distinction of low redshift (Type 0) BL Lacs and high redshift (Type 1, or quasar-like) BL Lacs, sometimes refereed as transitional objects. This distinction was motivated by the detection of weak broad emission lines in high redshift BL Lacs, suggesting that perhaps high redshift BL Lacs might be related somehow to FSRQs [365], so that high redshift radio quasars (strong lines) evolve into less luminous and continuum-dominated BL Lacs (with Lorentz factors decreasing with redshift [366]).

There is however no real evidence that such evolution exists for BL Lacs. Their properties, apart from the mentioned detection of weak lines, do not seem to correlate

---

[3] Correction to the magnitude of an astronomical object at redshift z to estimate its equivalent rest frame emission.

with their redshift. BL Lacs are indeed more similar among themselves than high redshift BL Lacs are to FSRQs. BL Lacs have dramatically different extended radio powers and line luminosities than FSRQs and the Lorentz and Doppler factors do not seem to be different enough as to support the idea of the continuum swallowing the emission lines in BL Lacs but not in FSRQs.

The broad band spectrum, when measured from radio to γ-ray as shown in Figure 6.9b, shows interesting tendencies between BL Lacs and FSRQs. The overall spectral energy distribution (SED) of blazars can be roughly described by two broad humps. The first is dominated by synchrotron emission and radiation from the different components (lines, disk, torus). It peaks between IR to X-rays. The second is mainly due (in leptonic models) to inverse Compton scattering and peaks in the MeV-TeV γ-ray band. Correlated variability of the different spectral bands have been observed in some (but not all) cases, suggesting that most of the emission is generated in the same region.

The low and high energy humps are placed at significantly longer wavelengths for FSRQs ('red' blazars) than they are for HBLs (XBLs), with LBLs (RBLs) found in between. It is however not yet clear whether this effect is intrinsic (more efficient radiative cooling for instance) or due to selection effects [367]. If the latter is the case, one would be able to observe bluer and redder blazars at any luminosities with more sensitive instruments. At the same time, the X-ray spectrum softens (steeper spectrum) and the bolometric luminosity and Compton Dominance (the ratio of γ-ray to bolometric luminosity) are lower in HBL than in LBLs or FSRQs. The γ-ray spectrum anti-correlates with the X-ray spectrum, becoming harder as bolometric luminosity decreases. In the original blazar sequence from Fossati et al. [368] and Ghisellini et al. [369], the classification was done attending to the bolometric luminosity and using the radio luminosity as a tracer for it.

The idea of having different cooling efficiencies in FSRQs and in BL Lacs was motivated by the observation of broad line clouds and tori in FSRQs, more luminous than for BL Lacs, which could re-isotropize part of the disc radiation. Therefore, the inverse Compton hump tends to be comparatively more luminous for FSRQs due to the presence of external photon fields [306]. At the same time, the larger cooling rates of FSRQs (prompt Comptonization of low energy electrons with ambient photons) explain the redder spectrum. For BL Lacs (particularly HBLs), the less prominent (or total absent) lines or tori leaves synchrotron photons as the only seed photons for the inverse Compton, enabling the leptons to potentially gain more energy. At the same time the Compton dominance is lowered by the absence of external photon fields.

Given that viewing angles (and beaming δ) seem to be similar for BL Lacs and FSRQs [370–372], the larger luminosity in FSRQs indicates (for a given black hole mass) larger accretion rates. In fact, the accretion disk can become very luminous and is often spotted in the spectrum of FSRQs at high redshifts.

Finally, when considered separately, FSRQs only show trends with luminosity in some of these parameters (Compton dominance and X-ray slope). Changes in the Compton Dominance imply that the magnetic field strength decreases for the bright FSRQs and larger X-ray slopes can be interpreted as stronger self-absorption. The situation is more complex for BL Lacs, for which increasing power implies more efficient cooling and reddening of its spectra. The lack of reddening in FSRQs with increasing luminosity can be interpreted in terms of radiative cooling, which would occur mainly in the BLR and the molecular torus due. Since cooling is almost independent on the jet properties (it only depends on the Γ factor through the Klein-Nishina cross-section), it is approximately the same for FSRQs of different powers [362].

7

B0218+357

Contents

In July 2014, QSO B0218+357 experienced a violent flare which was observed by the *Fermi*-LAT and the MAGIC telescopes. The details about the analysis and interpretation of the MAGIC data were published in [325] and are detailed in this chapter.

7.1 Introduction

QSO B0218+357, also known as S3 0218+35 in the *Third "Strong" (radio) Source survey*, is classified as a flat spectrum radio quasar (FSRQ, [373]). Like in many other cases, its classification and redshift determination were made by identifying some spectral features in the optical band, mostly emission lines, which are systematically redshifted because of the expansion of the Universe. With this method, a redshift of $z_s = 0.944 \pm 0.002$ [374] could be derived, recently updated to $z_s = 0.95 \pm 0.01$ [375, 376]. QSO B0218+357 is also a gravitationally lensed blazar. The lens is a face-on spiral galaxy (known as B0218+357G) located at a redshift of $z_l = 0.68466 \pm 0.00004$ [377].

Gravitational lensing

In gravitational macro lensing (also known as strong lensing), a massive object or set of objects (typically a galaxy or a cluster of galaxies) bends the trajectory of the emitted photons in such a way that photons reaching the Earth seem to arrive from an apparent direction that does not correspond to the true position of the source. It is common to observe deformed or multiple images of the same source as a result of gravitational lensing [379]. Additionally, the lens modifies the flux reaching the observer with a magnification defined as the ratio between the number of deflected photons and the number of photons emitted in a given small solid angle centered at the observer. This deflection depends on the geometrical configuration of the lens and may be different for the individual images. Finally, the difference in light travel distances between the various images introduces image-dependent time delays for the arrival time of the source photons.

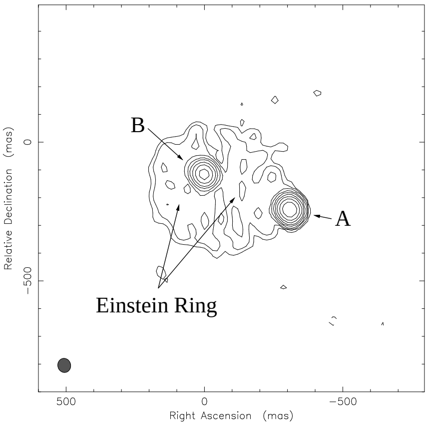

Figure 7.1: B0218+357 region as seen by MERLIN/VLA, with two different images from the blazar [378]

Gravitational microlensing differs from the strong lensing effect in that the bending of lights is not produced by a large mass body, but by its individual components, such as stars. While the individual effect for each component is small, in complex systems the stacked microlensing can have large effects (variability) caused by the relative movement of the structured lens with respect to the observer and the blazar.

The variability seen in the different images has thus a correlated component due to the macrolensing (which traces the intrinsic variability of the source) and an uncorrelated component coming from microlensing effects [380]. While the distribution and properties of the individual stars of the lens cannot be accessed directly, important properties about the structure of the lens, mass of the star and sizes of the γ-ray emitting region can be derived statistically from simulations.

Lensing in B0218+357

Observations of the spatial distribution of B0218+357 with high resolution radio instruments show 2 independent components with an angular separation of 335 mas and an Einstein ring of a similar size [381], as seen in Figure 7.1. The same configuration has been observed in optical with the Hubble Space Telescope (HST).

Time variability correlation of the two radio components shows a delay of 10-12 days between the behavior of one image (B, trailing) with respect to the other (A, leading) [382–385]. This delay is explained as due to the different light paths of the two images. Because of the spatial configuration of the lens, the two images have different fluxes, with the delayed component being 3.57-3.73 times weaker than the leading component [383]. This factor depends on the radio frequency [386] due (presumably) to free-free absorption in the lensing galaxy [387]. In the optical band, the leading image is strongly absorbed [388]. As a result, it is less bright than the trailing one.

B0218+357, like other AGNs of its class, is a variable source in many energy bands. In 2012, the source went through a series of outbursts in HE γ-rays [389]. Even though *Fermi*-LAT does not have the necessary angular resolution to disentangle the two emission components, the statistical analysis of the light curve shows a time delay of 11.46 ± 0.16 days.

The average magnification factor, as opposed to the one in radio and optical, was ~ 1, with small changes with time interpreted as microlensing effects of individual stars in the lensing galaxy [390]. Microlensing on larger scale structures has been considered as well [391]. The radio follow-up observations of B0218+357 after the gamma-ray flare of 2012 did not reveal any correlation between the two bands [392]. This is a common situation in many, but not all, blazars and leaves the debate open of what is the origin of the γ-ray and radio activity.

The source became active again in 2014 July 13rd and 14th in the GeV band, as seen by *Fermi*-LAT. In contrast with the high state of 2012, no subsequent flares were seen in the next days. The spectrum was also much harder than in the flare of 2012. The high state occurred during MAGIC's moon break, but follow-up observations were triggered for the delayed component with the hope of capturing the echo. This resulted in the discovery of VHE gamma-ray emission from B0218+357 [393].

In this chapter the analysis, results and publication of the data from the July 2014 flare are discussed. The MAGIC dataset was complemented with quasi-simultaneous data coming from multi-wavelength partners (*Fermi*-LAT, *Swift*-XRT, *Swift*-UVOT and KVA-*R*).

7.2 Instruments, observations and analysis

7.2.1 MAGIC

MAGIC5 performance at low energies is among the best in current generation IACTs due to the combination of low energy threshold and good sensitivity. Still, due to EBL absorption (see chapter 11) of VHE γ-ray photons, studies of sources at moderate redshifts $z > 0.3$ in these extreme energies are very challenging and only a handful of them are presently known to emit radiation above 100 GeV[49].

The sensitivity[1] achieved by MAGIC in the energy range $E \gtrsim 100\,\mathrm{GeV}$ is at the level of 1.45% of Crab Nebula flux in 50 h of observations. Its angular resolution is of the order of 0.09°, i.e. insufficient for spatially resolving the emission from the two lensed image components of B0218+357.

---

[1] Flux for a Crab-like spectrum that gives an excess with significance $N_{ex}/\sqrt{N_{bkg}}$ of $5\,\sigma$.

Date	Exposure	S (σ)	Remarks
2014/07/23	0.59	0.40	
2014/07/24	0.75	-0.25	
2014/07/25	1.13	4.18	‡
2014/07/26	0.98	2.13	
2014/07/27	0.97	0.21	
2014/07/28	1.04	0.79	
2014/07/29	1.04	1.87	
2014/07/30	1.09	0.46	
2014/07/31	1.11	1.56	
2014/08/01	0.85	-0.02	
2014/08/02	0.84	-1.20	
2014/08/03	0.53	1.52	

Table 7.1: MAGIC observations of B0218+357 during the campaign of 2014. The exposure is quoted after quality cuts. S denotes the significance in number of standard deviations (σ). ‡: Expected arrival time of the delayed component.

The telescopes could not immediately follow the flare alert published by *Fermi*-LAT in mid July 2014 from B0218+357, as it occurred during the full Moon time. The Moon makes not only not safe to operate the telescopes (as permanent damaging can happen to the PMT camera if operated in nominal HV conditions when there is too much optical light collected on the pixels), but the energy threshold is severely affected due to the much larger noise from the scattered moonlight) [394]. The MAGIC observations started 10 days later, with the aim of studying the possible emission during the delayed flare component. The observing conditions were not ideal and the study could only be carried out at medium zenith angles ($20° - 43°$), at the cost of an increased energy threshold with respect to low zenith distance data. The available time was only about one hour at the end of each night. In order to check the source flux baseline, the observations were performed not only for the expected arrival of the delayed flare, but covering 14 consecutive nights around the predicted delayed component, from July 23 (MJD=56861, two nights before the expected delayed emission) to August 5, 2014 (MJD=56874). The list of nights in which the source was observed is shown in Table 7.1. The total exposure time was 12.8 h. As it is usual for point-like sources, a strategy based on 4 wobble position observations [195] was employed with an offset of 0.4° from the center of the camera.

The data reduction (stereo reconstruction, gamma/hadron separation, estimation of the energy and arrival direction of the primary particle) was performed using the standard analysis chain of MAGIC [194, 204]. The sky position of B0218+357, contrary to the Crab Nebula used to estimate the performance of the MAGIC telescopes [204], is not projected against the Milky Way optical background. Therefore the 30% smaller night sky background registered by the MAGIC telescopes for B0218+357 with respect to Galactic sources allowed us to apply image cleaning thresholds lower by 15% with respect to the ones used in the standard analysis presented in Aleksić et al. [204]. This particularity helped to further reduce the energy threshold. With all this in mind, the resulting energy threshold of the analysis is found to be about 85 GeV (measured following the techniques explained in Appendix C.2.1).

The lower than usual image cleaning thresholds were validated by applying the same procedure to the so called pedestal events, i.e. events which contain no showers but night sky and electronic noise. An acceptable fraction of about 10% of such images survived the image cleaning, meaning that the data is not dominated by noise. The analysis was done using a dedicated set of MC simulations of gamma rays with the night sky background and the trigger parameters tuned to reproduce as accurately as possible the actual observation conditions.

7.2.2 Fermi-LAT

The *Fermi*-LAT [182] γ-ray telescope is generally operated in scanning mode, providing coverage of the full sky every three hours. Starting on December 2013 and until December 2014, a new observing strategy that emphasized coverage of the Galactic center region was adopted. B0218+357 data presented in this paper were obtained during this time interval. As a consequence, the coverage on the blazar position was on average a factor of 0.6 of the maximum one. Additionally, at the time of the expected delayed emission, Fermi performed a ToO (Target of Opportunity) observation on B0218+357 to enhance exposure toward the source position. The ToO lasted approximately 2.7 days (2014-07-24 00:30:01 UTC to 2014-07-26 18:24:00 UTC, MJD= 56862.02 – 56864.77).

Fermi-LAT data were extracted from a circular region of interest (ROI) of 15° radius centered at the B0218+357 radio position, R.A. = 35.27279°, Decl. = 35.93715° [J2000; 395]. The analysis was done in the energy range 0.1 – 300 GeV using the standard *Fermi Science Tools* (version `v9r34p1`) in combination with the `P7REP_SOURCE_V15` LAT Instrument Response Functions.

The campaign comprises data data collected between MJD=56849–56875 (2014 July 11 – 2014 August 6) for the light curve. For the spectral analysis only data spanning the two days during the expected maximum of the delayed emission (MJD=56863.125–56864.5) were used. The data was filtered using `gtmktime` following the FSSC recommendations[2]. According to this prescription, time intervals when the LAT boresight was rocked with respect to the local zenith by more than 52° (usually for calibration purposes or to point at specific sources) and events with zenith angle $> 100°$ were excluded to limit the contamination from Earth limb photons.

The spectral model of the region included all sources located within the ROI with the spectral shapes and the initial parameters for the modeling set to those reported in the third *Fermi*-LAT source catalog [184] as well as the isotropic (`iso_source_v05.txt`) and Galactic diffuse (`gll_iem_v05.fit`) components[3].

For the light curve, the source spectrum was modeled with a power-law shape

---

[2] `http://fermi.gsfc.nasa.gov/ssc/data/analysis/documentation/Cicerone/`

[3] `http://fermi.gsfc.nasa.gov/ssc/data/access/lat/BackgroundModels.html`

with normalization and index free to vary. To assess the detection significance, the Test Statistic (TS) value was used. It is defined as $\mathrm{TS} = -2\log(L_0/L)$, where L_0 is the maximum likelihood value for a model which does not contain the target source in the sky region considered (the 'null hypothesis') and L is the maximum likelihood value for a model which incorporates such target source at the specified location. The TS quantifies the probability of having a point gamma-ray source at the location specified and corresponds roughly to the square of the number of standard deviations assuming one degree of freedom [396]. As in our analysis the second model had two more degrees of freedom (i.e. normalization and index were left free), therefore TS=9 (25) corresponds to significance of ~2.5 (4.6) σ, respectively. During the analyzed period, B0218+357 was not always significantly detected. Flux upper limits at the 95% confidence level were calculated for each time interval where TS was < 9.

7.2.3 Swift

B0218+357 was observed by the *Swift* satellite during 10 separated epochs, each with an exposure of about 4.5 ks. The observations did first follow the original *Fermi*-LAT alert of enhanced activity in GeV gamma rays, and then were resumed at the expected time of arrival of the delayed component so that broadband spectral information could be gathered. The data were reduced with the `HEASoft` package version 6.17. The *Swift* X-ray Telescope (XRT, [397]) is a CCD imaging spectrometer, sensitive in the 0.2–10 keV band. The data was reduced using the calibration files available in the version 20140709 of the *Swift*-XRT CALDB. The `xrtpipeline` task was employed to process the data, using standard screening criteria on the observations performed in pointing mode. Observations were done in Photon Counting (PC) mode with count rates about 0.02 counts/s. The low rate of events ensured that there was no significant pile-up in the resulting image, which would otherwise spoil the spectrum. On the other hand, the weak X-ray emission compelled us to merge different epochs to create a good quality spectrum. To this purpose, different event files were combined with the task `xselect`, summing the corresponding exposure maps with the task `image`. The merged source and background counts were extracted with the task `xrtproducts` from a circular region of 35" for the source and 120" (ring shaped) for the background. The spectra was grouped with the corresponding background, redistribution matrix (rmf), and ancillary response files (arf) with the task `grppha`, setting a binning of at least 20 counts for each spectral channel in order to be able to use the χ^2 statistics. The spectra were analyzed with `Xspec` version 12.8.1. A value for Galactic absorption of $N_{\mathrm{H}} = 5.6 \times 10^{20}\,\mathrm{cm}^{-2}$ [398] was adopted.

Simultaneous observations by the 30 cm f/12.72 Ultraviolet Optical Telescope (UVOT, [399]), on board of *Swift*, did not result in a significant detection of the emission from the source in the UV range.

7.2.4 KVA

The optical R-band observations were done using the 35 cm Celestron telescope attached to the KVA 60 cm telescope (La Palma, Canary islands, Spain). The observations started on 2014, July 24 (MJD=56862.2) and continued on an almost nightly basis until 2014, August 5 (MJD=56874.2). Further follow-up observations were performed in August and September. The data were analyzed using the semi-automatic pipeline developed at the Tuorla Observatory (Nilsson et al. 2016, in prep.). The magnitudes were measured using differential photometry. An absolute calibration of the optical fluxes was done using stars with known magnitudes present in the field of view of the instrument (see Table 3 of Nilsson et al. [400] and references therein). B0218+357 is rather faint in the optical range (about 19 mag) and the telescope is relatively small, therefore several images from the same night were combined for the measurement of the average flux. For the spectral analysis the optical flux was deabsorbed using a galactic extinction of $A_{\mathrm{R}} = 0.15$ [401].

7.3 Influence of the lensing galaxy

Macro-lensing is rather stable and predictable, and any important variability in the observed flux can be interpreted as intrinsic variations in the original source. Microlensing, on the other hand, can cause large variability of the flux magnification for smaller emission regions in the source [390]. It is also harder to model because it heavily depends on the internal configuration of the lens.

Using a simple Singular Isothermal Sphere model (SIS, see e.g. [379]) we roughly estimated the absolute magnification of the leading and trailing images. A more rigorous lens modeling performed by Barnacka et al. [402] yielded a model consistent with SIS.

The ratio between the observed angular distances to the lens of the leading and trailing radio images of the source was measured to be ~ 4 [403]. In the framework of SIS model this results in the individual magnifications of the two images to be $\mu_{\mathrm{leading}} \approx 2.7$, $\mu_{\mathrm{trailing}} \approx 0.67$.

Using the flux ratio between the two images measured in the radio frequency range, the same model allowed us to also compute the absolute magnifications independently. With the value of $\mu_{\mathrm{leading}}/\mu_{\mathrm{trailing}} \approx 3.6$ [383] very similar results with $\mu_{\mathrm{leading}} \approx 2.8$, $\mu_{\mathrm{trailing}} \approx 0.77$ were obtained. Averaging both methods we assume $\mu_{\mathrm{leading}} \approx 2.7$, $\mu_{\mathrm{trailing}} \approx 0.7$ in the further calculations. The radio emission in blazars is believed to originate from regions much larger than the ones involved in gamma-ray production. Therefore, the values given above for the individual magnifications of images are not affected by possible microlensing on individual stars of the lensing galaxy B0218+357G. In the same sense, models fitting the galaxy with an exponential disk profile show that the galaxy lens contribution is subdominant, about 30-50 times weaker than the lensed image [403]. Still, the galaxy host contribution may be significant, particularly for image A, which is heavily absorbed in optical. In fact, the possibility that a significant part of the emission arises from a large star formation region associated to a molecular cloud cannot be ruled out.

On the other hand, microlensing can significantly modify the fluxes observed in the HE and VHE energy ranges [390, 404]. The flux magnification due to microlensing depends on the size of the emission region, which might vary with the energy (e.g.

due to cooling effects). This might modify the observed spectrum and, in principle, can affect the EBL constraints by making the intrinsic spectrum inaccessible through simple emitting models. However, during the flaring period of 2014 the magnification ratio observed in *Fermi*-LAT was comparable to, or larger than, the radio one. This suggests that the microlensing, if present, might have a bigger effect on the leading rather than on the trailing image, which was observed by MAGIC. Namely, if a microlensing event amplified the observed emission during the delayed flare with a given magnification of $\mu_{\mathrm{star,trailing}}$, the leading flare must have been also amplified with even larger magnification $\mu_{\mathrm{star,leading}} \gtrsim \mu_{\mathrm{star,trailing}}$ by an independent microlensing event to keep the observed ratio of fluxes. Assuming that the probability that the trailing image flux is magnified with a factor of $\mu_{\mathrm{star,trailing}}$ is p_{trailing}, the probability that both images are independently magnified resulting in the observed flux ratio is much smaller, roughly $\lesssim p^2_{\mathrm{trailing}}$.

Absorption in the lensing galaxy can also affect the observed fluxes at different energies. Falco et al. [388] interpreted the different reddening of the two images of B0218+357 as an additional absorption of the leading image with the differential extinction $\Delta E(B-V) = 0.90 \pm 0.14$. In fact the absorption is so strong that it inverts the brightness ratio of the two images in the optical range, making the trailing image brighter. Also, in the leading image, the H_2 column density was estimated at the level of $0.5 - 5 \times 10^{22}\,[\mathrm{cm}^{-2}]$ by an observation of a molecular absorption [405]. In addition, the dependence of the radio flux ratio on the frequency could also stem from free-free absorption [387]. No absorption has been measured for the trailing image. Observations of the 21 cm absorption feature in B0218+357 points to a HI column density of $10^{21}(T_s/100\,\mathrm{K})/(f/0.4)\,[\mathrm{cm}^{-2}]$, where T_S is the spin temperature and f is the fraction of the flux density obscured by HI [377].

In γ-rays, absorption is expected to occur in FSRQs and other bright blazars. The presence of strong external photon fields can lead to pair production processes, extinguishing the γ-ray emission. External absorption can be also present from interactions of γ-rays from the source with optical photons from the host, the lens or our own Galaxy. This effect is in most cases negligible for distant sources compared to the extinction caused by the EBL because of the large integrated optical depth from the latter [406, 407].

7.4 Results

In this section we discuss the spectral and temporal characteristics of the B0218+357 emission obtained in different energy bands.

7.4.1 *MAGIC*

The VHE gamma-ray emission was detected (the usual definition of detection of $> 5\,\sigma$ is used) on the nights of 25 and 26 of July 2014 (MJD=56863.2 and 56864.2 respectively, see Table 7.1), during the expected arrival time of the delayed component of the flare registered by *Fermi*-LAT. The detection cuts were optimized using a reference Crab data sample to provide the best sensitivity in the 60 − 100 GeV estimated energy range (see [204]). The total observation time during those 2 nights of 2.11 h yielded a statistical significance, computed according to Li and Ma [408], Eq. 17, of $5.7\,\sigma$ (see Fig. 7.2).

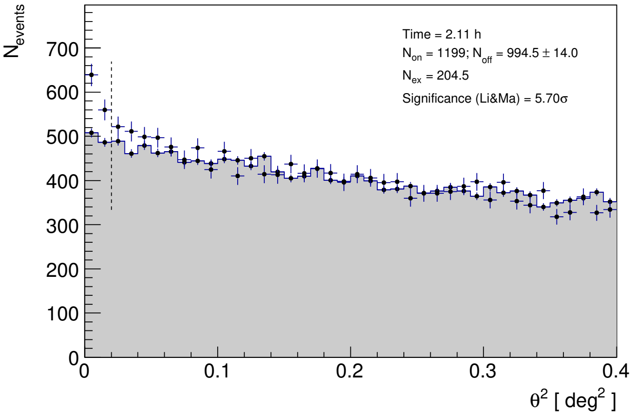

Figure 7.2: Distribution of the squared angular distance, θ^2, between the reconstructed event position and the nominal source position (points) or the background estimation position (shaded area). The vertical dashed line shows the value of θ^2 up to which the number of excess events and significance are computed.

The light curve above 100 GeV is shown in Fig. 7.3. A fit with a Gaussian function gives the peak position at MJD=$56863.86 \pm 0.30_{\mathrm{stat}}$ and a standard deviation (related to the duration of the flare) of $0.75 \pm 0.34_{\mathrm{stat}}$ days. The corresponding fit probability is 21%. The two flaring nights give a mean flux above 100 GeV of $(5.8 \pm 1.6_{\mathrm{stat}} \pm 2.4_{\mathrm{syst}}) \times 10^{-11}\,\mathrm{cm}^{-2}\,\mathrm{s}^{-1}$. The relatively large systematic error comes from the assumption that the systematic uncertainty is dominated by a symmetrical 15% uncertainty in the energy scale [204], which is related to the total optical throughput of the instrument and the atmosphere). Note however that this is a very conservative value, and the real one may be significantly lower (particularly towards higher light throughput values, as it is unlikely that the atmospheric transmission was underestimated by as much as 15% in the Monte Carlo simulations).

The SED obtained from the two nights 25 and 26 of July (MJD = 56863.2 and 56864.2) is presented in Fig. 7.4. The reconstructed spectrum spans an energy range of 65−175 GeV and can be roughly described as a power-law with a fit probability of 47%, being its parameters $E_0 = 100\,\mathrm{GeV}$, $f_0 = (2.0 \pm 0.4_{\mathrm{stat}} \pm 0.9_{\mathrm{syst}}) \times 10^{-9}\,\mathrm{cm}^{-2}\mathrm{s}^{-1}\mathrm{TeV}^{-1}$ and $\alpha = 3.80 \pm 0.61_{\mathrm{stat}} \pm 0.20_{\mathrm{syst}}$. Note however that the fact that a power-law is a good fit to the observed data might only means that the measured spectrum is not detailed enough to significantly exhibit spectral curvature (due to intrinsic effects or EBL absorption), which is expected to be the case for most (if not all) extragalactic sources.

The quoted systematic uncertainty on the spectral index takes into account also the small background estimation uncertainty for a weak low-energy source (see Eq. 3 of [204]). As the redshift of the source is close to 1 the spectrum is severely affected by the absorption of VHE gamma rays in the EBL. Correcting the observed spectrum for such absorption modeled according to [409], an intrinsic spectral index of $2.35 \pm 0.75_{\mathrm{stat}} \pm 0.20_{\mathrm{syst}}$ was obtained. The corresponding normalization of the emission at 100 GeV is $(4.6 \pm 0.8_{\mathrm{stat}} \pm 2.1_{\mathrm{stat}}) \times 10^{-9}\ \mathrm{cm}^{-2}\mathrm{s}^{-1}\mathrm{TeV}^{-1}$. The

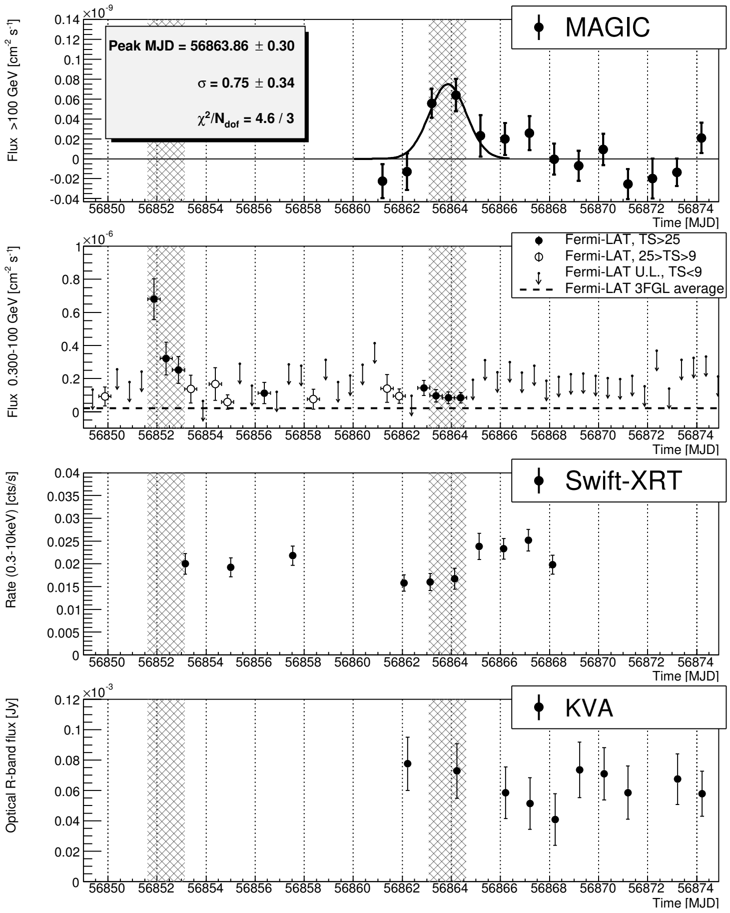

Figure 7.3: Light curve of B0218+357 during the flaring state in July/August 2014. **Top panel:** MAGIC (points) above 100 GeV and a Gaussian fit to the peak position (thick solid line). Note that the fit to a Gaussian is not motivated by any physical principle, but it is just a convenient way of modeling a signal, giving meaningful parameters such as the amplitude of the signal, its temporal position and the characteristic duration of the flare. **Second panel** from the top: *Fermi*-LAT above 0.3 GeV with the average flux from the 3rd Fermi Catalog [184] marked with a dashed line. Notice that, during the days where the trailing emission was expected *Fermi*-LAT was in pointing mode, increasing the total exposure and allowing the significant detection of lower flux levels. **Third panel from the top:** *Swift*-XRT count rate in the 0.3-10 keV range. **Bottom panel:** KVA in R band (not corrected for the contribution of host/lens galaxies and the Galactic extinction). The two shaded regions are separated by 11.46 days.

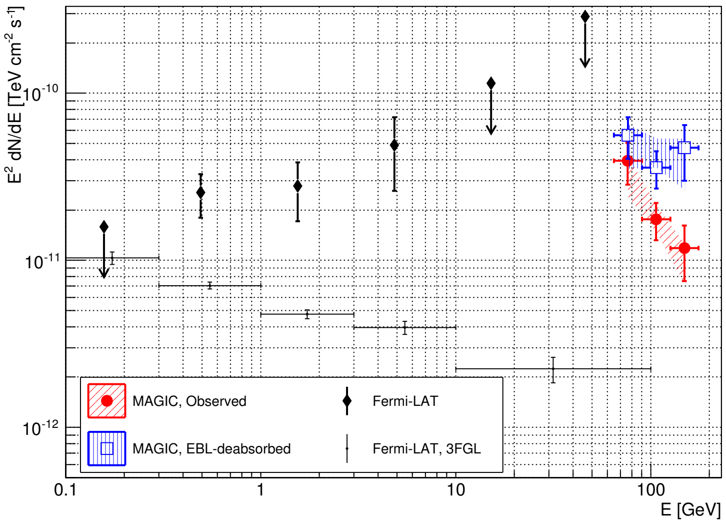

Figure 7.4: Gamma-ray SED of B0218+357 as observed during the two flaring nights, 25 and 26 of July, by MAGIC (red filled circles) and after deabsorption in EBL according to the [409] model (blue open squares). The shaded regions show the 1 standard deviation of the power-law fit to the MAGIC data. Black diamonds show the *Fermi*-LAT spectrum (PASS7) from the same time period. Black points show the average emission of B0218+357 in the 2015ApJS..218...23A catalog [184].

spectral points are obtained using the Bertero unfolding method [410], while the fit parameters are obtained using forward (un)folding [411].

7.4.2 Fermi-LAT

The GeV light curve of B0218+357 is shown in the second panel of Fig. 7.3. A minimum energy 0.3 GeV was used in the light curve (instead of 0.1 GeV) in order to increase the signal to noise ratio in the flux measurements: the spectrum of this source during this flaring episode is very hard (see below), while the diffuse backgrounds fall with energy with an index of > 2.4 (meaning its contribution is more important at the lowest energies), and in the PASS7 release the PSF of LAT at 0.1 GeV is about twice larger than that at 0.3 GeV.

Significant GeV gamma-ray emission was detected by *Fermi*-LAT both during the leading flare and during the expected arrival time of the delayed emission (TS of 615 and 129 respectively). The spectrum contemporaneous to the MAGIC detection, derived between MJD=56863.07 and 56864.85, can be described by a power-law function with slope $\gamma = 1.6 \pm 0.1$. The corresponding flux above 0.1 GeV is $F_{>0.1\mathrm{GeV}} = (1.7 \pm 0.4) \times 10^{-7} \mathrm{cm}^{-2}\,\mathrm{s}^{-1}$. For comparison, the leading flare was marginally harder, $\gamma = 1.35 \pm 0.09$, with ~ 4 times higher flux $F_{>0.1\mathrm{GeV}} = (6.7 \pm 1.0) \times 10^{-7} \mathrm{cm}^{-2}\,\mathrm{s}^{-1}$ The spectral index measured by *Fermi*-LAT during the outburst of 2014 is much harder than the one of the flare in 2012 ($\gamma \sim 2.3$) [389] and the average state of this source reported in the 3FGL [184].

At the redshift of the source ($z = 0.944$), the EBL is expected to cause a negligible absorption of the observed LAT photons.

7.4.3 Swift

The X-ray light curve of the source is shown in the third panel of Fig. 7.3. The whole observed light curve shows a small hint of variability. A fit to a constant gives $\chi^2/N_{\rm dof} = 21.3/9$, corresponding to a probability of 1.1%. The source did not show an enhanced flux in the X-ray range during the trailing gamma-ray flare. The average count rate from the two observations during the enhanced gamma-ray flux results in $(79.2 \pm 7.7)\%$ of the rate averaged from the remaining 8 pointings. The rate obtained in the 0.3–10 keV energy range is similar to the one obtained during the 2012 flaring period $(0.027 \pm 0.003$, [412]).

Given that the source is a weak X-ray emitter and the observed variability is not very strong, all the pointings were combined in order to decrease the statistical uncertainty to reasonable values for the spectral modeling of the source. Moreover, the lack of strong variability also implies that the observed emission is the sum of the two images of the source, with at least one of them affected by the hydrogen absorption. In order to provide higher accuracy per spectral point, the spectrum was rebin to have at least 50 events per bin.

Driven by the observed lens configuration of two emitting components, the X-ray spectrum was modelled as a sum of two power-law components, with the same intrinsic normalization and spectral slope, but magnifications fixed to 2.7 and 0.7 respectively (see section 7.3). Following the detection by [405] of the molecular absorption line in the brighter image, hydrogen absorption was included at the redshift of the lens in the first (brighter) component. However, due to large uncertainty in the hydrogen column density, it was left as a free parameter of the model. With such assumptions, the X-ray intrinsic spectrum can be well described ($\chi^2/N_{\rm dof} = 42.2/34$) by:

$$\frac{dN}{dE} = (2.69 \pm 0.29) \times 10^{-4} \left(\frac{E}{\rm keV}\right)^{-1.90\pm0.08} [{\rm keV^{-1}cm^{-2}s^{-1}}], \qquad (7.1)$$

where the reported uncertainties are statistical only. The corresponding column density $(2.4 \pm 0.5) \times 10^{22}\,{\rm cm^{-2}}$ is within the bounds given by Menten and Reid [405].

The X-ray spectrum can be alternatively described by a simpler model, considering only absorption of the total emission (i.e. same absorption is affecting both images). The resulting spectrum is then slightly harder, with an index of 1.59 ± 0.10. The corresponding effective hydrogen column density is smaller, $(0.57 \pm 0.17) \times 10^{22}\,{\rm cm^{-2}}$. The fit probability is however worse in this case, with $\chi^2/N_{\rm dof} = 54.7/34$. Therefore, for the SED modeling (see section 7.5) the spectrum obtained using the assumption that the absorption affects only the leading image was employed.

7.4.4 KVA

The bottom panel of Fig. 7.3 shows the optical light curve of B0218+357 in the R band. In all of our observations the source was fainter than 19 magnitudes. The resulting error bars for the flux points were therefore relatively large and no significant variability was detected. The observed galaxy flux was estimated within our measurement aperture (5.0 arcsec radius) and a calibration with a similar size aperture. Using the data in Lehár et al. [413] a lens galaxy flux of $F_{\mathrm{galaxy}} \approx 13\,\mu\mathrm{Jy}$ was derived. The resulting flux (corrected for both the Galactic absorption and the lensing galaxy contribution) for the observation during the flare is then $70 \pm 20\,\mu\mathrm{Jy}$.

7.5 Modeling of the broadband emission

In order to model the broadband emission spectrum of B0218+357, the magnification factors affecting the different energy ranges must be obtained first. As no strong variability was seen in either the optical or the X-ray range, the observed emission in those energies was assumed to be the sum of both lensed images. However, the optical leading image is strongly absorbed [388], thus the total magnification in the optical range is close to μ_{trailing}.

The absorption in soft X-rays was already corrected in the analysis (see Section 7.4.3). The extinction is expected to be negligible from $E \gtrsim 2\,\mathrm{keV}$. Therefore the magnification in the X-ray energy range was assumed to be $\mu_{\mathrm{leading}} + \mu_{\mathrm{trailing}} \approx 3.4$. The strong variability in the GeV and sub-TeV gamma-ray range and the much harder GeV spectrum during the MAGIC observations point to the magnification in the GeV energy range at this time to be close to μ_{trailing}. The resulting broad-band SED of B0218+357, (de)magnified according to the numbers derived above and corrected for the X-ray and gamma-ray absorption, is shown in Fig. 7.5. Historical data from ASDC (ASI Science Data Center, see `http://www.asdc.asi.it/`) is reported in green, tracking particularly well the low energy component. These historical data are the sum of the emission of the source transmitted through both of its images, however especially in the optical and UV range the leading component is affected by strong absorption. In order to derive the intrinsic flux of the source, a correction factor to the flux $1/(\mu_{\mathrm{trailing}} + \mu_{\mathrm{leading}} \times T_A(f))$ was applied, where $T_A(f)$ is the frequency-dependent fraction of the leading image flux surviving the attenuation. In order to estimate $T_A(f)$, a differential extinction of the leading image of $\Delta E(B - V) = 0.90 \pm 0.14$ [388] was used to scale the dust extinction curve of the Milky Way [399, 414], taking also into account the redshift of the lens. In the X-ray band the $T_A(f)$ shape was determined from the hydrogen column density obtained in section 7.4.3.

The SED is dominated by the emission at GeV – sub-TeV energies, which is relatively common in flaring FSRQs (see e.g. [415, 416]), due to the presence of an external photon field that floods the environment with seed optical photons. Although the corrections for lensing are uncertain, the intrinsic GeV spectrum appears to be hard for this flaring state.

Interestingly, the gamma-ray flare seen by MAGIC was not accompanied by a similar increase in either optical or in X-ray flux. This is unusual for FSRQs, where a correlation is often seen. Comparison of the optical data to the archival measurements, shows that there was no large change in the position of the low energy peak during the high-energy flare. The high energy peak position however moved from the sub-GeV range in low state to tens of GeV during the flare. This apparently decoupling of the low energies and the high energies invites us to explore models that are beyond the over-simplistic one-zone leptonic model.

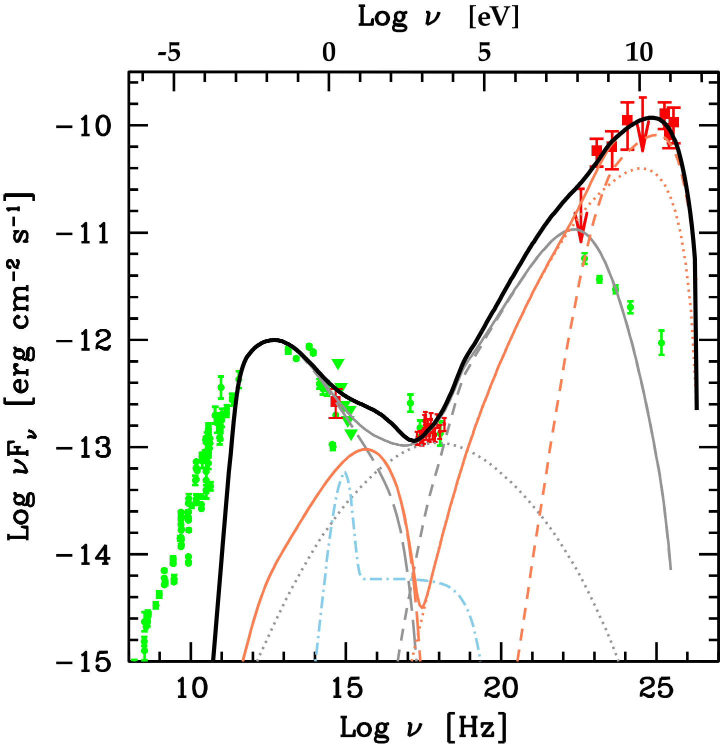

Figure 7.5: Broadband SED of B0218+357 modeled with a two-zone model. The reconstructed fluxes (red squares) are corrected for different magnifications in different energy ranges (see the text). Historical measurements (ASDC) are shown with green circles and triangles (flux upper limits). Gray curves depict the emission from the region located within the BLR, while orange curves refer to the region located beyond the BLR. Long dashed curves show the synchrotron radiation, dotted the SSC emission and short dashed the external Compton emission. Dashed-dotted light blue line represents the accretion disk emission and its X-ray corona. The solid black line shows the sum of the non-thermal emission from both regions.

7.5.1 One zone leptonic models

FSRQs are characterized, among other things, by the presence of large radiation fields coming from their accretion disk, a broad line region (gas moving at high speed and thus contributing to a net broadening of optical emission lines) and a dusty molecular torus. Contrary to what happens in their low power counterparts (the BL Lac class) their SEDs cannot be easily described with simple one-zone SSC models. In particular, the two SED peaks have a large separation in frequency and furthermore this separation depends on the source activity. As detailed in [417] in such a case one-zone models inevitably require unphysically large Doppler factors and very low magnetic fields. For the specific case of B0218+357, in order to explain the high energy peak at $\nu_C \sim 10^{25}$ Hz, the Lorentz factors of the electrons emitting at the peak would need to reach (or exceed in case the scattering is in the Thomson regime) $8 \times 10^4 \nu_{C,25} \delta^{-1} (1 + z_s)$, where δ is the Doppler factor of the emitting region and $\nu_{C,25}$

is the frequency of the Compton peak in units of 10^{25} Hz. Since the same electrons are responsible also for the synchrotron radiation of the low energy peak, a very low value of the magnetic field is required: $B = 5.6 \times 10^{-5} \nu_{s,12} \nu_{C,25}^{-2} \delta^{-1} (1 + z_s)$[G], where $\nu_{s,12}$ is the synchrotron peak frequency in units of 10^{12} Hz. If the high-energy component is interpreted as synchrotron-self-Compton (SSC) emission, the ratio of the high-energy peak luminosity to the synchrotron luminosity has to be equal to the ratio between the synchrotron photon energy density and the magnetic field energy density. This condition, coupled to the value of the magnetic field derived above, allows us to derive the required Doppler factor (see [417] for details): $\delta \gtrsim 35 L_{s,46}^{1/8} \nu_{s,12}^{-1/4} \nu_{C,25}^{1/2} \Delta t_{1d}$, where $L_{s,46}$ is the synchrotron luminosity (measured in the units of $10^{46}\,\mathrm{erg\,s^{-1}}$) and Δt_{1d} is the variability timescale in units of days. With such a large value of the Doppler factor it is rather unlikely that the radiation energy density in the jet frame is dominated by the synchrotron one.

Instead, as usually assumed in the modeling of a FSRQ (e.g. [418]), it is most plausible that the high-energy component is produced by the scattering of external photons (from the broad line region, BLR, the disk or the molecular torus).

In the case of such an external Compton (EC) scenario, some constraints can be derived considering that the SSC emission, expected now to peak in the X-ray band, cannot have a flux exceeding the value fixed by the XRT data. Similarly to the discussion above for the SSC case, a constraint on the Doppler factor can be derived: $\delta \gtrsim 75 L_{s,46}^{1/8} \nu_{s,12}^{-1/4} \nu_{C,25}^{1/2} \Delta t_{1d}$. The extremely large values of the Doppler factors, plus the lack of simultaneous optical and X-ray variability to the GeV and sub-TeV flare, strongly disfavor one-zone models, pointing instead to a two-zone model, as discussed in [419].

Another important element to consider for the modeling is the huge opacity for gamma rays characterizing the innermost regions of a FSRQ. In particular, gamma rays with energies exceeding a few tens of GeV produced within the radius of the BLR would be strongly attenuated. Therefore, the highest energy part of the spectrum, observed by MAGIC, should have been emitted close to or beyond the BLR radius (see e.g. [416] and references therein). This in principle also has some consequences in the variability time-scales, because regions that are further away tend to be less spatially compressed, thus giving longer variability timescales. Unfortunately in B0218+357 variability can also come from microlensing effects.

7.5.2 Two zone external Compton model

Considering the arguments given above, the broadband emission of the source was reproduced with a two zone model, inspired by the scenario c) of Tavecchio et al. [419]. The two emission regions are moving with the same bulk Lorentz factors and the same opening angles along the jet. The first region is assumed, in analogy to other FSRQs, to be fully embedded in the BLR. The opacity condition forces however the second emission region, the production site of the VHE gamma rays, to be outside of the BLR. The reader is referred to section 8.3.3 for a detailed discussion of VHE γ-ray emission in FSRQs. The γ-ray emission is the sum of the SSC and

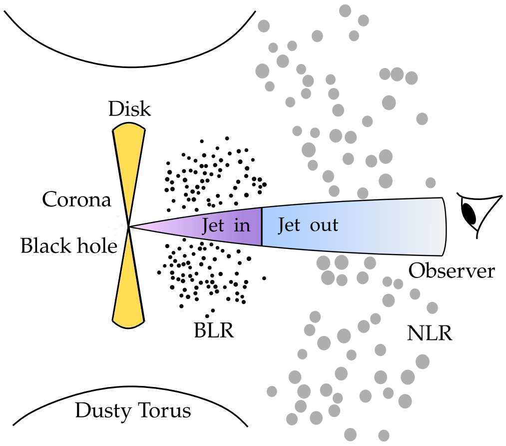

Figure 7.6: Illustration of the structure of B0218+357 according the model described in section 7.5.2. The low energy hump in the SED (NIR to X-ray) would be mostly originated through synchrotron and external radiation fields. Hard X-ray emission is generated through inverse Compton scattering involving photons from the BLR in the Jet in zone (purple), with a minor contribution from direct emission from the accretion disk (yellow) in optical and the black hole corona (red dots) in X-rays. Additional external Compton takes place just outside the BLR (Jet out, blue) and leads to significant γ-ray emission.

EC components on the radiation field of BLR and dusty torus. Both radiation fields are included in the calculations of both emission zones, however the BLR radiation field dominates the EC in the zone closer to the black hole ("Jet in", responsible for the optical and X-ray radiation), and the less energetic radiation field of the torus dominates the farther zone ("Jet out", accounting for the γ-ray radiation). The luminosity of the accretion disk is taken to be $L_{\mathrm{d}} = 6 \times 10^{44}$ erg s^{-1} [420]. This value is quite low if compared to a typical FSRQ. The radius of the BLR and that of the torus, calculated accordingly to the scaling rules of Ghisellini and Tavecchio [421], are $R_{BLR} = 7.7 \times 10^{16}\,\mathrm{cm}$ and $R_{torus} = 2 \times 10^{18}\,\mathrm{cm}$.

The EC and SSC processes in the farther region (see orange curves in Fig. 7.5) allow the radiation to escape the strong absorption of sub-TeV emission in the BLR radiation field. The size of the emission region is sufficiently small to account for the one-day variability timescales observed in this energy band (see Fig. 7.3). On the other hand the optical and X-ray emission comes mostly from the inner region. The lack of strong variability in those energy bands, seen in Figure 7.3, points toward the stability of the emission from this region on the timescales of at least a fortnight. This picture is self-consistent with the procedure of (de)magnification of the flux described in section 7.4.3. In general, blazar emission models reproducing the innermost regions of the jet (distance from the black hole below $\sim 1\,\mathrm{pc}$) cannot account for the radio emission (frequencies at which the region is optically thick) which, instead, is produced by farther, optically thin regions of the jet. The spatial separation of "Jet in" and "Jet out" might in principle introduce a delay between the emission observed from them. If the same population of electrons, traversing along the jet, encounters first "Jet in" and afterwards "Jet out", the expected delay is given by: $\sim (1 + z_s)\Delta R_{dist}/(c\Gamma D)$, where ΔR_{dist} is the distance between the two regions. Using the modeling paramaters reported in Table 7.2 one would obtain a time delay of only $\sim$6.9 h, which is significantly shorter than the duration of the flare, and very small on the temporal scale of Fig. 7.3. Moreover the delay would not be observable if, as assumed above, the emission from the "Jet in" region is quasi-stable.

The parameters for the region inside the BLR (Table 7.2) are in the range of those

	$\gamma_{\min}$	$\gamma_{\rm b}$	$\gamma_{\max}$	n_1	n_2	B [G]	K [cm^{-3}]	R [cm]	R_{dist} [cm]
in	2.5	300	3×10^4	2	3.9	1.1	1.5×10^5	7×10^{15}	7×10^{16}
out	10^3	7×10^4	2×10^5	2	4.3	0.03	3×10^7	10^{15}	2×10^{17}

Table 7.2: Input parameters for the emission model shown in Fig. 7.5 "Jet in" (in) and "Jet out" (out) indicate the emission regions located inside or outside the BLR respectively. The parameters are: the minimum ($\gamma_{\min}$), break ($\gamma_{\rm b}$) and maximum ($\gamma_{\max}$) Lorentz factor and the low energy (n_1) and the high energy (n_2) slope of the smoothed power law electron energy distribution, the magnetic field B, the normalization of the electron distribution, K, the radius of the emission region, R, the distance from the central BH at which the emission occurs, R_{dist}. The Doppler factor was set to $\delta = 20$ in both cases. The corresponding bulk Lorentz factor for both components is $\Gamma = 17$. Doppler factors are calculated assuming that the observer lies at an angle $\theta_{\rm v} = 2.8°$ from the jet axis. As with other AGNs, fitting simultaneously so many parameters with data that have non uniform systematic uncertainties and spectral point cross-correlations becomes challenging. In the end, the values shown here were chosen to reproduce the observed spectrum without going to un-physical values in the parameter space (see [372] for typical leptonic model value ranges)

typically derived for a FSRQ with leptonic models (e.g. [372]). For the outer regions there is a strong constraint on the luminosity of the synchrotron component, which – given the large Lorentz factors of the electrons required to produce the high-energy component – peaks in the UV – soft X-ray band. To keep the synchrotron component below the limits and, at the same time, reproduce the powerful high-energy IC component, the magnetic field must be kept to quite low values. This is similar to the case of PKS 1222+216 discussed in Tavecchio et al. [419]. As in that case, a possibility to explain such low values could be to assume that this emission region is the product of processes involving magnetic reconnection, in which magnetic energy is efficiently converted to electron energies (e.g. [422]).

7.6 Constraints on EBL

The VHE γ-ray observations of distant sources can be used to constrain the EBL density. A wide range of methods have been applied in the past, starting from comparing the spectral shape in the unabsorbed GeV range with the one in the TeV range [423] to testing a grid of generic EBL spectral shapes and excluding the ones resulting in a pile up (i.e. convex spectrum) or a too hard intrinsic spectrum [424].

Indirect measurements of the EBL density with γ-ray instruments are sparse and in general burdened by systematic uncertainties. The $1\,\sigma$ error band of Ackermann et al. [425] for sources with redshift $0.5 < z < 1.6$ allows for about a factor of two uncertainty in optical depth for EBL absorption. More recently, PKS 1441+25 observations with MAGIC and VERITAS resulted in constraints on the scaling factor of optical depth predicted by the current EBL models to be $\lesssim 1.5 - 1.7$ [426, 427] (see chapter 8). Together with direct measurements of 'galaxy counts', which provide very constraining lower limits, these estimations allow to explore cosmological evolution of the EBL and the energy range where uncertainties are still large, such as the near-UV regime.

This work can be considered a precursor of the more extensive analysis of chapter 11. It presents an independent measurement of EBL absorption at $z = 0.944$ using *Fermi*-LAT and MAGIC data collected from B0218+357 during the flare of 2014. Since the two instruments measured a similar time scale of the flare it is plausible to assume that the GeV and sub-TeV emission originates from the same emission region. This assumption is further supported by the SED modeling presented in section 7.5. As a caveat, the dependence of the size of the emission region on the energy, combined with microlensing, might affect the observed GeV spectrum (see section 7.3), introducing additional systematic uncertainties in the derived constraints on EBL. The spectrum observed by MAGIC from B0218+357 gives us a chance to probe the EBL at wavelengths of $\sim 0.3 - 1.1\,\mu$m.

A joint spectral fit combining *Fermi*-LAT and MAGIC points was done following Abramowski et al. [428] and using a set of possible spectral shapes. The method is similar to the one followed in sections 8.4 and 11.2. To cover better the energy range of the EBL induced cut-off for this study, finer binning of the MAGIC data than the one presented in Fig. 7.4 was used, resulting in 5 bins. The intrinsic spectral shapes are attenuated by EBL according to the optical depths presented in Domínguez et al. [409]. The optical depths are allowed to vary according to a global scaling parameter α. The following spectral models (*power law* [PWL], *power law with a cut-off* [EPWL], *log parabola* [LP], *log parabola with a cut-off* [ELP]) are used:

$$\begin{aligned}
\mathrm{PWL}: dN/dE &= AE^{-\gamma}, && (7.2)\\
\mathrm{EPWL}: dN/dE &= AE^{-\gamma}\exp(-E/E_{cut}), && (7.3)\\
\mathrm{LP}: dN/dE &= AE^{-\gamma-b\log E}, && (7.4)\\
\mathrm{ELP}: dN/dE &= AE^{-\gamma-b\log E}\exp(-E/E_{cut}), && (7.5)
\end{aligned}$$

with the additional source physics-driven conditions: $E_{cut} > 0$, $b > 0$.

For each spectral shape the χ^2 value of the best-fit is calculated as a function of α, where the minimum χ^2 indicates the preferred scaling according to our data. The $1\,\sigma$ statistical uncertainty bounds can be obtained as the range of α in which the χ^2 increases in one unit from the minimum value.

The fit probability as a function of the EBL scaling parameter is shown in the middle panel of Fig. 7.7. Out of the phenomenological function shapes (Eq. 7.2-7.5) the highest fit probability is obtained with the simple power-law spectral model. Using this spectral model, an estimation of the EBL scaling parameter of $\alpha = 1.19 \pm 0.42_{\mathrm{stat}}$ was obtained for a redshift of 0.944. Such an assumption of a single power-law between 3 and 200 GeV, even though slightly preferred by the best fit probability, might be at odds with the FSRQ emission models. The spectral models allowing for an intrinsic curvature/cutoff exhibit a lower dependence of χ^2 on the EBL scaling for the low values of α resulting in less constraining bounds. Notably, all the tested spectral shapes provide a $1\,\sigma$ upper bound below the value for a simple power-law

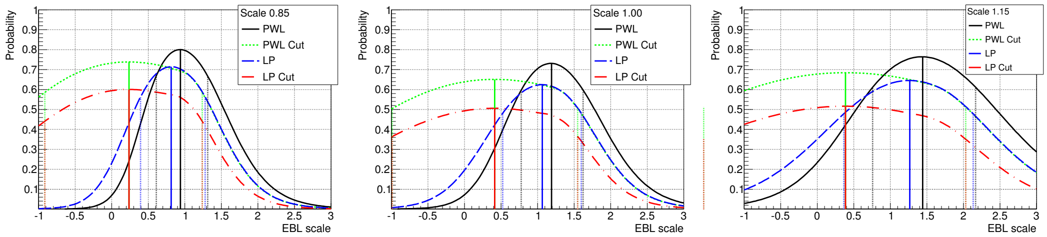

Figure 7.7: Probability of a SED fit as a function of the EBL scaling parameter. Different styles and colors of the lines represent different spectral shapes: power law (solid, black), power law with an exponential cut-off (dotted, green), log parabola (long dashed, blue), log parabola with exponential cut-off (dot-dashed, red). The vertical lines show the scaling for which the best probability is obtained (solid) and +1 change in χ^2 of the fit from this maximum (dotted). Nominal light scale of MAGIC is assumed in the middle panel. The light scale is decreased (increased) by 15% in left (right) panel.

spectral shape. Spectral shapes with an additional intrinsic cut-off result in only a small increase of χ^2 from the scaling factor of 1 (nominal EBL) to 0 (no EBL). Therefore no strict lower bound can be derived on α.

Systematic uncertainties can affect the obtained results. In particular, the use of MAGIC and *Fermi*-LAT data means that a shift in energy scale or flux normalization between the spectra obtained from the two experiments could affect the best fit and confidence bands. Due to the very steep spectrum in the sub-TeV range, the dominant systematic effect is the 15% uncertainty of the energy scale of MAGIC [204], which can shift the reconstructed flux in up to 40%. This effect is much larger than the pure flux normalization uncertainty reported in [204]. The uncertainty of the spectral slope, due to the limited energy range of the spectrum, has a negligible effect. Finally the systematic uncertainty of *Fermi*-LAT (see e.g. [429], where 2% accuracy on the energy scale is reported) is also negligible compared to the ones of MAGIC in the case of this source. Therefore in order to investigate the systematic uncertainty on the EBL scaling parameter a full analysis using the telescope response with a modified light scale (by ±15%) was done following the approach in [204] and [430].

In all three cases (see Fig. 7.7) the best probability of the fit is obtained with a simple power-law fit. However, the corresponding EBL scaling parameter shifts by 0.25 for a power-law case. Also the statistical error for an increased light scale in this case is slightly larger. Therefore, if an intrinsic curvature (log-parabola spectral shape, and/or an exponential cut-off) is allowed, the corresponding 95% C.L. upper limit is given by $\alpha < 2.7$. This limit is less constraining than the one obtained with PKS 1441+25 [426].

The analysis is repeated substituting the EBL model of [409] by other currently considered models: [431], [432], [433], [434] to check for model-wise systematics. For all of them, the highest fit probability was obtained with a power law spectrum. The results of the best scaling parameter of the optical depth of these models are summarized in Table 7.3.

As in the case of the model of Domínguez et al. [409] the limits on the optical depth scaling factor for a power-law intrinsic spectral shape are reported and a

Model	α (PWL)	α (all)
Franceschini, Rodighiero, and Vaccari [431]	$1.19 \pm 0.42_{\mathrm{stat}} \pm 0.25_{\mathrm{syst}}$	< 2.8
Finke, Razzaque, and Dermer [432]	$0.91 \pm 0.32_{\mathrm{stat}} \pm 0.19_{\mathrm{syst}}$	< 2.1
Domínguez et al. [409]	$1.19 \pm 0.42_{\mathrm{stat}} \pm 0.25_{\mathrm{syst}}$	< 2.7
Gilmore et al. [433]	$0.99 \pm 0.34_{\mathrm{stat}}\,^{+0.15\,\mathrm{syst}}_{-0.18\,\mathrm{syst}}$	< 2.1
Inoue et al. [434]	$1.17 \pm 0.37_{\mathrm{stat}}\,^{+0.10\,\mathrm{syst}}_{-0.13\,\mathrm{syst}}$	< 2.2

Table 7.3: Limits on the optical depth scaling α in various EBL models. The second column specifies the limit for the model providing the best peak fit probability from the collection in (Eq. 7.2-7.5), a power law in all cases. The last column specifies the 95% C.L. limit allowing all considered spectral shapes and 15% energy scale systematic uncertainty.

more conservative 95% C.L. upper limit for intrinsic spectral shapes allowing an arbitrary steepening or a cut-off. The combined *Fermi*-LAT and MAGIC spectrum is consistent with all five EBL models considered here.

7.7 Conclusions

MAGIC detected VHE gamma-ray emission from B0218+357 during the trailing component of a two-image gravitationally lensed QSO flare in July 2014. It is currently the most distant source detected with a ground-based gamma-ray telescope, and the only gravitationally lensed source detected in VHE gamma rays. The VHE gamma-ray emission lasted two nights, achieving the observed flux of $\sim 30\%$ of Crab Nebula at 100 GeV. Using the EBL model from Domínguez et al. [409], the intrinsic spectral index in this energy range was found to be $2.35 \pm 0.75_{\mathrm{stat}} \pm 0.20_{\mathrm{syst}}$. The VHE gamma-ray flare was not accompanied by a simultaneous flux increase in the optical or X-ray energy range. The X-ray emission was modeled as a sum of two components with different magnifications, the weaker one absorbed with column density of $(2.4 \pm 0.5) \times 10^{22}\,\mathrm{cm}^{-2}$. The combined *Fermi*-LAT and MAGIC energy spectrum is consistent with the current EBL models. These constraints are however not very strong, with the EBL density scaling parameter being less than 2.1-2.8 of the one predicted by the tested models. The broadband emission of B0218+357 was modeled with a two-zone external Compton model. According to it, the quasi-stable optical and X-ray emission originates mostly in the inner zone. The enhanced gamma-ray emission during the flare is produced in the second zone, located outside of the BLR.

8

PKS 1441+25

Contents

The flat-spectrum radio quasar PKS 1441+25, with a redshift of $z = 0.940$, is the second most distant source detected in very high energy γ-rays. The discovery of photons of more than 100 GeV with MAGIC followed the detection of flaring activity from the source by the *Fermi*-LAT space telescope. The interpretation of the MAGIC observations, in the context of extensive coordinated observations of the source in other wavelength bands was presented in Ahnen et al. [426]. This chapter completes that work, adds polarization measurements and puts the flare in the context of the long-term behavior of the source in the *Fermi*-LAT.

8.1 Introduction

PKS 1441+25 (RA : 14 43 56.8922, DEC : + 25 01 44.491) [435] is a known high-energy (HE, 0.1 GeV $<$ E $<$ 100 GeV) γ-ray emitter flat spectrum radio quasar (FSRQ) [436–438] located at $z = 0.9397 \pm 0.0003_{stat}$[1]. In January 2015 it became active from γ rays to the near-infrared, the overall flux being significantly higher than catalog values in all wavelengths [440–443]. In April of the same year, a new outburst took place, leading to the detection of the source with a hard spectral index with *Fermi*-LAT. Together with the discovery of enhanced multi-wavelength (MWL) emission from the source, MAGIC observations were triggered. They resulted in the first detection of this source at very high energy γ-rays [444], later followed up by VERITAS [445]. This detection made PKS 1441+25 the 5th FSRQ with a firm classification detected at VHE, and the most distant known VHE source, along with QSO B0218+357 ($z = 0.944 \pm 0.002$)[325].

In this chapter, the MWL campaign carried on PKS 1441+25 is discussed in the context of an external Compton model with its parameters evolving through four different states of activity, dubbed periods A (MJD 57125.0–57130.0), B (57130.0–57135.5), C (57135.5–57139.5) and D (57149.0–57156.0). Upper limits on the extragalactic background light (EBL) photon density are also obtained using VHE data.

8.2 Observations and analysis

8.2.1 VHE gamma-ray observations

The MAGIC telescopes (see chapter 5) monitored PKS 1441+25 from 2015 April 18 to 27 (MJD 57130–57139) for a total of 29.9 hr and then in May 8-9 (MJD 57150–57151) for 1.8 h, with a gap imposed by the full-moon break. The observations were performed in wobble mode with a 0.4° offset and four symmetric positions with respect to the camera center [195]. The data were collected in the zenith angle range of $3° < zd < 38°$ to optimize the energy threshold, estimated in 45 GeV according to the prescriptions of Appendix C.2.1.

The analysis of the data was done using the standard MAGIC analysis framework *MARS* [204, 446] and Monte Carlo (MC) simulations matching the night-sky background levels.

PKS 1441+25 was detected with a significance of $25.5\,\sigma$, corresponding to a γ-ray like excess of $N_{ex} = (4.01 \pm 0.16) \times 10^3$ evs (see Figure 8.1) during periods B+C. Note that the statistics in this case are much larger than in the case of B0218+357 (chapter 7), meaning that potentially more information can be derived from the data. No significant emission was found in period D.

The differential VHE spectrum was measured from 40 to 250 GeV and 50 to 160 GeV in periods B and C respectively. At first approximation, a power-law (PWL) could describe both observed and EBL-corrected spectra using the model of [409]:

---

[1] `http://skyserver.sdss.org/dr10/en/get/SpecById.ashx?id=6780257851631206400`, [439]

Date	Exposure	S (σ)	Remarks
2015/04/18	2.10	7.13	†, B
2015/04/19	4.55	12.06	B
2015/04/20	4.76	11.83	B
2015/04/21	3.02	9.4	B
2015/04/22	3.31	10.64	B
2015/04/23	2.33	6.41	B
2015/04/24	3.54	4.37	C
2015/04/25	1.73	3.19	C
2015/04/26	1.23	1.32	C
2015/04/27	1.34	2.21	C
2015/05/08-09	1.83	0.58	D
2015/06/10-17	4.55	6.91	‡

Table 8.1: MAGIC observations of PKS 1441+25 during the outburst of 2015. The exposure is quoted after quality cuts. Third column denotes the statistical significance. The remarks column indicates the different periods of activity defined in the section 8.1. † indicates limited atmospheric transmission and ‡ describes data not published in the original paper.

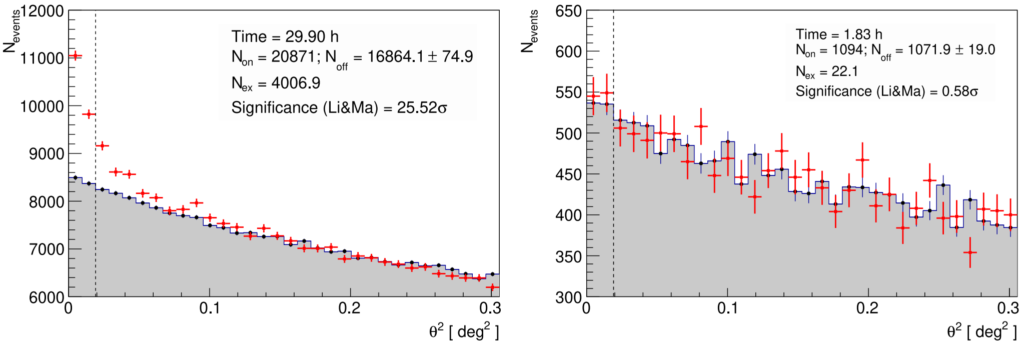

Figure 8.1: Distribution of reconstructed γ-ray like events as a function of the distance to the source position (ON events, blue points), to symmetrically distributed OFF positions w.r.t. to the camera center (OFF events, gray histogram). *Left panel:* April 2015 (high state, periods *B,C*), *Right panel:* May 2015 (low state, period *D*).

$$\frac{dF}{dE} = f_0 \left(\frac{E}{100\,\text{GeV}} \right)^{-\Gamma}, \tag{8.1}$$

where the normalization constant f_0, the spectral index Γ and the goodness of the fit (χ^2/ndf and p-value), different for each period, are:

1. Period B:
    - (i) Observed: $f_0 = (1.14 \pm 0.06_{stat} \pm 0.20_{sys}) \times 10^{-9}$ cm^{-2}s^{-1}TeV^{-1} and $\Gamma = 4.62 \pm 0.11_{stat} \pm 0.18_{sys}$ ($\chi^2/ndf = 22.9/6$, $P = 8.4 \times 10^{-4}$).
    - (ii) EBL-corrected: $f_0 = (2.7 \pm 0.1_{stat} \pm 0.5_{sys}) \times 10^{-9}$ cm^{-2}s^{-1}TeV^{-1} and $\Gamma = 3.18 \pm 0.15_{stat} \pm 0.18_{sys}$ ($\chi^2/ndf = 5.6/6$, $P = 0.47$).

2. Period C:
   - (i) Observed: $f_0 = (0.82 \pm 0.09_{stat} \pm 0.13_{sys}) \times 10^{-9}$ cm^{-2}s^{-1}TeV^{-1} and $\Gamma = 3.7 \pm 0.4_{stat} \pm 0.2_{sys}$ ($\chi^2/ndf = 2.7/3$, $P = 0.44$).
   - (ii) EBL-corrected: $f_0 = (1.7 \pm 0.2_{stat} \pm 0.3_{sys}) \times 10^{-9}$cm^{-2}s^{-1}TeV^{-1} and $\Gamma = 2.5 \pm 0.4_{stat} \pm 0.2_{sys}$ ($\chi^2/ndf = 4.3/3$, $P = 0.23$).

From a likelihood ratio test (LRT), a model with intrinsic curvature such as a log-parabola (LP) is preferred at $4.2\,\sigma$ during period B. It is defined as:

$$\frac{dF}{dE} = f_0 \left(\frac{E}{100\,\mathrm{GeV}}\right)^{-\Gamma_{LP} - b \log_{10} \frac{E}{100\,\mathrm{GeV}}}, \tag{8.2}$$

3. Period B, LP:
   - (i) Observed: $f_0 = (1.39 \pm 0.09_{stat} \pm 0.24_{sys}) \times 10^{-9}$cm^{-2}s^{-1} TeV^{-1}, $\Gamma_{LP} = 4.69 \pm 0.16_{stat}$ and $b = 3.2 \pm 1.0_{stat}$ ($\chi^2/ndf = 5.2/5$, $P = 0.39$).

Such an additional complexity is not needed to describe the less significant and detailed data in period C.

A full description of the MAGIC systematic uncertainties can be found in [204] and references therein. It should be noted however that for very step sources, systematic uncertainties due to possible errors in the reconstructed energy dominate. Additionally, the unfolding and regularization of the spectrum in such cases becomes challenging if we are interested in preserving possible spectral features (in this case, curvature). Instead, we decided to use the comparatively more robust and simple forward folding approach.

8.2.2 HE gamma-ray observations

In nominal survey mode the LAT (described in chapter 4) monitors the entire γ-ray sky every 3 h in the energy range from 20 MeV to at least 300 GeV [204]. Pass 8 SOURCE class events were collected from 2015 April 8 to May 23 (MJD 57120–57165) between 100 MeV to 500 GeV and within a 10° Region of Interest (ROI) centered at the location of PKS 1441+25. In order to reduce contamination from the Earth Limb, a zenith angle cut of $< 90°$ was applied. The analysis was performed with the `ScienceTools` software package version v10r0p5 using the `P8R2_SOURCE_V6`[2] instrument response functions and the `gll_iem_v06` and `iso_P8R2_SOURCE_V6_v06` models[3] for the Galactic and isotropic diffuse emission, respectively. No separation of event classes (FRONT+BACK, PSFs, EDISPs) was done.

The (binned) likelihood fit was performed using `gtlike`, including all 3FGL sources [184] within 20° from PKS 1441+25. The spectral indices and fluxes were left free for sources within 10°, while sources from 10° to 20° had their parameters fixed to

---

[2] `http://fermi.gsfc.nasa.gov/ssc/data/analysis/documentation/Cicerone/Cicerone_LAT_IRFs/IRF_overview.html`

[3] `http://fermi.gsfc.nasa.gov/ssc/data/access/lat/BackgroundModels.html`

the catalog value. Both the flux and the spectral index of PKS 1441+25 were left free for the light curve calculation, while the parameters for the rest of the sources in the ROI were fixed except the diffuse components. Five photons of energies $10 - 50\,\mathrm{GeV}$ were detected with a probability of association with PKS 1441+25 larger than 99.6 %, calculated with `gtsrcprob`. Due to the finite statistics in the *Fermi*-LAT band, the spectrum of PKS 1441+25 could be described by a PWL (as in the 3FGL catalog) and no significant curvature was found. During the flare (period B+C), the spectral index is $\Gamma = 1.75 \pm 0.06$, significantly harder than the 3FGL value $\Gamma_{3FGL} = 2.13 \pm 0.07$.

8.2.3 Hard X-ray observations

NuSTAR (Nuclear Spectroscopic Telescope Array; [447]) is a hard X-ray telescope operating in the energy range between 3 and 79 keV. PKS 1441+25 was observed with *NuSTAR* on 2015 April 25–26 (MJD 57137.1, period C) for a total (on-source) exposure of 40 ks. The data were processed using the standard `nupipeline` script (version 1.4.1) available in the NuSTARDAS software package [448]. The source spectrum extends up to $\simeq$ 25 keV, and was described by a PWL with spectral index $\Gamma = 2.30 \pm 0.08$ ($\chi^2/ndf = 10.4/7$). No significant variability was detected during the observation.

8.2.4 X-ray and optical–UV observations

A *Swift* [449] target of opportunity started on 2015 April 15. *Swift*-XRT [397] observed the source in photon-counting mode. Standard filtering and analysis of the data were employed. The source exhibited a soft X-ray photon index (evolving with time from 1.94 ± 0.16 to 2.55 ± 0.24) and was described by an absorbed PWL model, with the Galactic absorption fixed to $N_H = 3.2\times\ 10^{20}\,\mathrm{cm}^{-2}$ [398] during April–May 2015. As a comparison, a similar set of observations performed on 2010 June 12 (MJD 55359) could be described with a PWL with spectral index 1.2 ± 0.3. This dramatic change in the X-ray spectrum can be attributed as an overall shift towards higher energies of both the synchrotron and IC humps during a high state. This effect is also visible in the *Fermi*-LAT band.

The *Swift*-UVOT [399] is a 30 cm optical/UV telescope on board the *Swift*satellite. The flux in several bands was estimated using aperture photometry, meaning that a set of measurement rings are placed in the image centered on the source position and then a background measured over an external ring (background region) was extracted from the total flux measured in the central aperture (source region). Aperture corrections were then applied to take into account the parts of the PSF that lay outside of the source region. Optical light is generally absorbed and re-emitted at longer wavelengths by the presence of interstellar dust. The correction for this effect, known as de-reddening, was performed using a *color excess* value of $E(B-V) = 0.033$, extracted from the SDSS-based reddening map from [401], and then estimating the total extinction in the V band (A_V) using $R_V = A_V/E(B - V) = 3.1$ [450].

8.2.5 Optical observations

Optical R-band observations started on MJD 57130 and were performed using the 35 cm Celestron telescope attached to the KVA[4] 60 cm telescope (La Palma, Canary Islands, Spain) and the 50 cm Hans-Haffner-Telescope (Hettstadt, Würzburg, Germany)[5]. The data were analyzed using differential photometry, for which the source flux measured in non-physical units was compared with the flux measured over a star with known magnitude in the field of view. The resulting flux was corrected for Galactic extinction applying a similar procedure as in the *Swift*-UVOT data analysis [401]. The host galaxy contribution was found to be negligible compared to the flux of the source during these observations. It is remarkable that the optical emission showed a high degree of polarization, reaching a maximum of 37.7 % on MJD 57132 [451]. Changes in the optical polarization associated to γ-rays have been widely studied in the past and are thought to be produced in high ordered jet magnetic fields or magnetic reconnections [452–454].

8.2.6 Optical polarimetry

In order to complete the work described in [426] and following [427], polarimetric data was gathered from several instruments. The SPOL spectrometropolarimeter [455] at the 1.54 m Kuiper Telescope, the 2.3 m Bok Telescope in the Steward Observatory and the 6.5 m Multiple Mirror Telescope (MMT) provided spectral measurements of the Stokes parameters Q and U in the $5000 - 7000$ Å range. The data. with spectral dispersion of ~ 4 Å, allow to compute the polarization angle (EVPA) and the degree of polarization (PD) from the values of $\langle Q \rangle$ and $\langle U \rangle$. Uncertainties were estimated assuming that photon noise was dominant. Additional data was obtained The RINGO3 [456] optical imaging polarimeter at the fully-robotic Liverpool Telescope by selecting the green band (d, $650 - 760 nm$). Finally, ALFOSC polarimeter data [457] from the Nordic Optical Telescope (NOT) was included for completeness.

8.2.7 Near infrared observations

NIR observations in the J, H, and K_S bands started on MJD 57141 with CANICA[6], a direct camera at the 2.1 m telescope of the Guillermo Haro Observatory located at Cananea, Mexico. The flux was estimated by means of differential photometry using reference stars from the 2MASS catalog [458].

8.2.8 Radio observations

The observations of PKS 1441+25 with the Metsähovi 13.7 m radio telescope started on MJD 57135. The measurements were made with a 1 GHz-band dual beam receiver centered at 37 GHz. A detailed description of the observation and analysis methods can be found in [459]. Less dense observations were performed with the

---

[4] `http://users.utu.fi/kani/1m`

[5] `http://schuelerlabor-wuerzburg.de/?p=Sternwarte`

[6] `http://www.inaoep.mx/~astrofi/cananea/canica/`

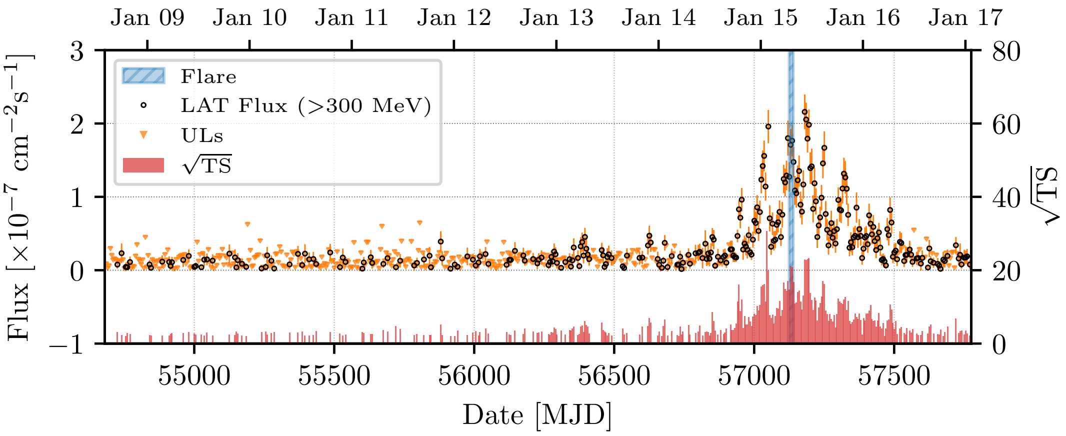

Figure 8.2: Long term light curve of PKS 1441+25 in the HE band. The shaded area marks the flaring episode described in this chapter (periods A-C).

40 m OVRO radio telescope [460] in the 15 GHz band, which provided information about the long-term evolution of the source.

8.3 Results

8.3.1 Long term γ*-ray flux evolution*

In Figure 8.2, the long-term Light Curve of PKS 1441+25 is presented with an emphasis on the LAT flux (> 300 MeV) and the TS value (which does relate with the statistical significance of the detection).

In order to increase the analysis sensitivity of each time-bin, the events were split in groups according to their PSF event type (types 0–3) and appropriate IRFs were employed for each type. The procedure is described more in detail in Section 9.2.2 and is known to improve the overall sensitivity for *Fermi*-LAT by $\sim 10\%$ [461]. The spectral parameters of the source (flux and spectral index) were left free in the minimization.

From the figure, it can be seen the source activity began to increase at the end of 2014 with a big outburst in January 2015, during which the spectral index did not change with respect to the low state value ($\Gamma = 2.120 \pm 0.017$). In April, another outburst took place, this time with a harder spectrum ($\Gamma = 1.75 \pm 0.06$ during period B+C).

8.3.2 Multi-wavelength *flux evolution*

The MWL light curve is presented in Fig. 8.3. In the VHE band, the no-variability hypothesis can be discarded as it results in a $\chi^2/ndf = 52.5/11$ ($P^{B-D}_{const} = 2.2 \times 10^{-7}$) for $B{+}C{+}D$. A constant fit is also unlikely for the flare in April ($B{+}C$) with a $\chi^2/ndf = 26.0/9$ ($P^{B+C}_{const} = 2.1 \times 10^{-3}$). We gauge the characteristic variability time scale by heuristically fitting the VHE light curve with a Gaussian function. The fit provides a standard deviation $\sigma = 5.5 \pm 1.6$ days (from which a halving flux time of $6.4{\pm}1.9$ days can be derived) and a peak flux of $(8.8{\pm}0.6){\times}10^{-11}\,\mathrm{cm^{-2}\,s^{-1}}$ ($\chi^2/ndf =$

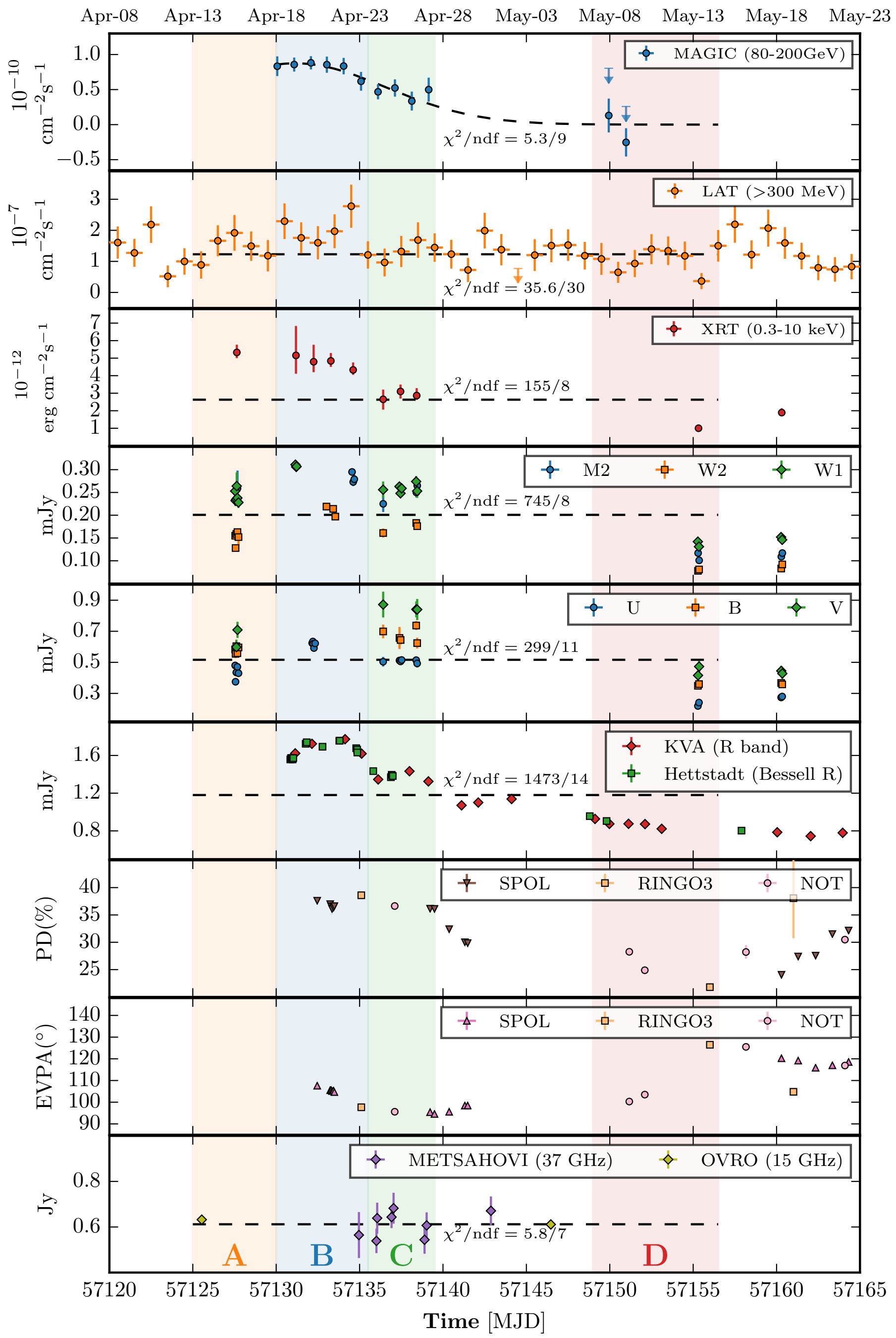

Figure 8.3: Light curve of PKS 1441+25 at different wavelengths. The shaded areas marked as A, B, C, D depict the different states of the source considered in section 8.3.3. Only filters "UVOT-M2", "UVOT-B" and "KVA-R" are used in the fit in the optical–UV bands. The polarization measurements were obtained from SPOL [462], RINGO3 [456] and ALFOSC (NOT Telescope).

Band	VHE/HE γ-rays		X-rays	UV		Optical		NIR
Instr.	MAGIC	LAT	*Swift*-XRT	UVOT		UVOT	KVA	CANICA
E/filter	$> 80\,\mathrm{GeV}$	$> 300\,\mathrm{MeV}$	$0.3 - 10\,\mathrm{keV}$	W1	W2	B	R	
F_{var}	0.53	0.59	0.49	0.72	0.54	0.44	0.39	0.058

Table 8.2: Mean fractional variability values F_{var} obtained for several wavelength bands, obtained from equation 8.3. First two rows indicate the energy band and instruments that were used to calculate it, third row indicates the energies or photometric filters and the last row presents the value of the F_{var}.

5.3/9, $P^{B-D}_{Gaussian} = 0.80$). For X-rays, a halving flux time of 7.6 ± 1.7 days was found. No intra-night variability was detected in either γ-rays, X-rays or optical data.

The average flux in B was larger than in C by a factor of $F_B/F_C = 1.80 \pm 0.27$ in VHE. A similar pattern was found in X-rays ($F_B/F_C = 1.58 \pm 0.17$), optical ($F_B/F_C = 1.23 \pm 0.02$) and a hint in the HE (1.40 ± 0.29). The larger value in VHE could be explained by the development of the flare and the shape of the spectrum. As the flux increased, the IC peak moved up in energy entering the region where the effective areas of VHE ground-based instruments rapidly increase.

An alternative approach to estimate the variability that tries to separate unexplained variability from the random errors due to noise in the measurements is the so called mean fractional variation [463], defined as

$$\mathrm{F}_{\mathrm{var}} = \frac{\sqrt{\sigma^2 - \delta^2}}{\langle f \rangle} \tag{8.3}$$

where $\sigma^2 = \frac{1}{N}\sum_{i=1}^{N}(f_i - \langle f \rangle)^2$ is the variance of the flux, $\delta^2 = \frac{1}{N}\sum_{i=1}^{N}\delta_i^2$ is the mean square uncertainty of the fluxes and $\langle f \rangle$ is the mean flux. The resulting energy-dependent $\mathrm{F}_{\mathrm{var}}$ values are presented in Table 8.2.

In Radio (Metsahovi), the changes in the flux are smaller than the error bars of each measurement, making F_{var} not useful to characterize the variability. It is interesting to note that F_{var} actually traces the position of the maximum of the low and high energy humps, with the largest values found in *Fermi*-LAT and *Swift*-UVOT.

Panels 7th and 8th of Figure 8.3 show the percentage of optical polarization (PD) and its angle (EVPA), based on Stokes parameters measured by several instruments. The large polarization fraction values, comparable to those observed for other FSRQs such as 3C 279 [452] and much larger than for typical BL Lacs [464], point toward a well ordered magnetic field in the emitting region. If one assumes a localized shock and a magnetic field compression such as in [465], a small drop in the PD and a rotation in EVPA is expected as the shock compresses the toroidal component of the magnetic-field and makes it stronger. At the same time, the initial poloidal contribution to the polarization is diminished. This is not the case of PKS 1441+25, where a small increase in PD is actually observed during the high state with a

Period	MJD	$\gamma_{\rm min}$	$\gamma_{\rm b}(10^4)$	$\gamma_{\rm max}(10^6)$	n_2	B (G)	K_3	ν_{IC}	CD
A	57125.0–30.0	80	1.0	1.0	3.55	0.15	2.80	24.2	24
B	57130.0–35.5	80	1.0	1.0	3.70	0.15	4.00	24.1	25
C	57135.5–39.5	50	0.8	1.0	3.75	0.17	3.35	24.0	21
D	57149.0–56.0	50	0.5	0.2	3.90	0.23	2.00	23.6	13
Archival	-	20	10^{-2}	3×10^{-2}	3.05	0.35	70	22.4	7

Table 8.3: Input parameters for the emission models shown in Fig. 8.4. K_3 is the electron density in units of $10^3\,\mathrm{cm}^{-3}$. Parameters that are not specified in the table are kept fixed. The IC peak frequency (in logarithmic scale) and the Compton Dominance (CD) are also reported in the last two columns.

change in EVPA. It suggests that the polarization is not heavily affected by the magnetic field compression in the shock, but by changes in the relative dominance of synchrotron emission with respect to the thermal emission coming from the IR torus, BLR and the accretion disk. In this scenario, synchrotron and thermal emission are comparable in intensity during the low state as seen in Figure 8.4, leading to reduced PD values. During the high state, synchrotron emission becomes dominant, which explains the greater optical polarization.

8.3.3 Broadband spectral energy distribution

The MWL spectral energy distributions (SEDs) shown in Fig. 8.4 indicate a shift of both synchrotron and inverse-Compton (IC) peaks to higher energies during the 2015 observation campaign with respect to the archival data, accompanied by a significant variation of the X-ray and HE γ-ray spectral indices. This behavior resembles the less extreme outburst seen in PMN J2345–1555 [466], and can be explained by a change in the emitting region location: within the broad line region (BLR) in the quiescent state to beyond the BLR during the outburst, where the external photon field is dominated by the optical–UV from the BLR or the IR thermal emission of a dusty torus, respectively (conventional framework for γ-loud FSRQ, see e.g. Tavecchio et al. [419] and Ghisellini, Maraschi, and Tavecchio [467]).

The consequences of this scenario are three-fold: (1) since the radiation energy density of the IR component is much lower than the one associated with the optical–UV photons from the BLR, the electron radiative cooling (which is basically independent of the photon frequency under the Thomson approximation) is less effective and the energy reachable by the acceleration process could be higher, accounting for the shift of the SED peaks toward higher energies; (2) the IC scattering of IR photons rapidly enters the Klein-Nishina regime, which significantly softens the VHE γ-ray spectra as described in section 1.3.5; (3) given the much lower energy of the external photons, absorption of γ rays by pair production occurs only above several hundreds of GeV (e.g. [468]), enabling the detection of FSRQs at VHE. For an emission region well within the BLR, strong absorption features are expected for energies above tens of GeV (see e.g. [469, 470]), which are not observed in the data from 2015.

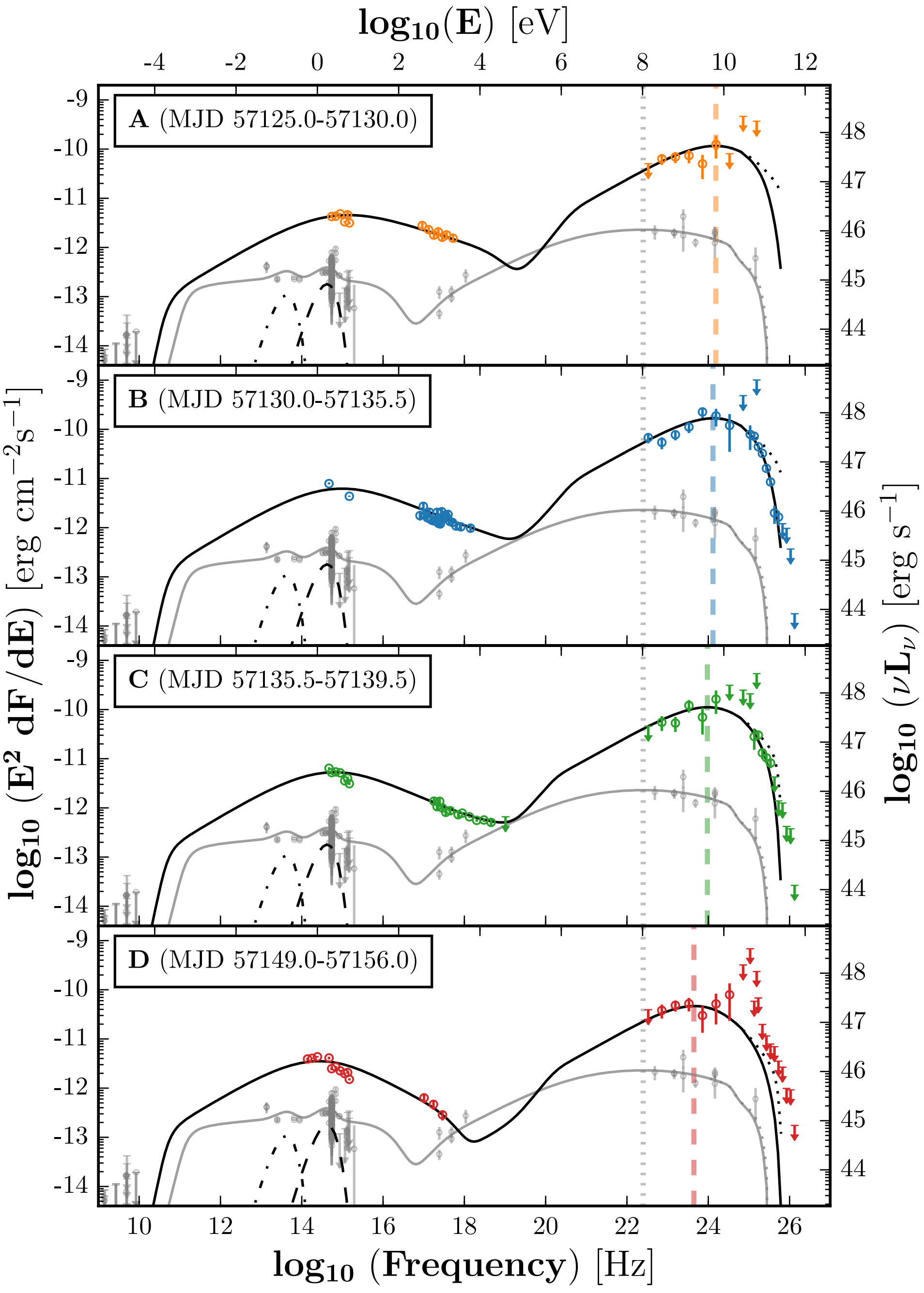

Figure 8.4: MWL SEDs for PKS 1441+25 for the four states of the source indicated in Fig 8.3. The broadband emission model for the observed (solid line) and EBL-de-absorbed (dotted line) spectrum, using the model of Domínguez et al. [409], together with the disk (dashed) and torus (dash–dotted) emission component are shown. Archival data extracted from ASDC (`http://tools.asdc.asi.it`) are shown in gray. The VHE spectral points are not corrected for EBL absorption. Vertical lines indicate the IC peaks.

Within this framework, the proposed SED model for the 2015 observations assumes that the emission region is located at a distance $d > R_{\mathrm{BLR}}$ from the central compact object. Adopting the simple scaling proposed by [467], R_{BLR} depends only on the disk luminosity, $R_{\mathrm{BLR}} = 10^{17}(L_{\mathrm{disk}}/10^{45})^{1/2}$ cm. The latter can be inferred from the luminosity of the optical broad lines, $L_{\mathrm{disk}} \simeq 2.0 \times 10^{45}\,\mathrm{erg\,s^{-1}}$ [372], resulting in $R_{\mathrm{BLR}} = 1.4 \times 10^{17}\,\mathrm{cm}$. In the same way, the size of the dusty torus can be inferred from a similar scaling law, $R_{\mathrm{IR}} = 3.5 \times 10^{18}$ cm. The resulting emission is calculated using the code described in [471]. The emission region is assumed to be spherical (in the source frame) with radius R, in motion with bulk Lorentz factor Γ at angle θ_{v} with respect to the line of sight. It contains a tangled magnetic field with intensity B and a population of relativistic leptons described by a smoothed broken PWL energy distribution between Lorentz factors γ_{min} and γ_{max}, with a break at γ_b, slopes n_1 and n_2 and normalization K estimated at γ=1. The external photon field (dominated by the IR torus emission) is assumed to follow a black body spectrum with luminosity $L_{IR} = \xi L_{\mathrm{disk}}$ [$\xi = 0.6$, following 467] and temperature T, diluted within a region of radius R_{IR}.

The model also includes γ-ray absorption within the IR radiation field of the torus. Assuming that the IR torus emission is well represented by the low-state model of Figure 8.4, one can estimate its temperature using Wien's law, giving a value of $T \approx 10^3$ K. The maximum absorption is then reached at $E = (m_{\mathrm{e}}c^2)^2/2.8kT \simeq 1\,\mathrm{TeV}$ in the source frame, with an optical depth $\tau_{\gamma\gamma} \approx (\sigma_{\mathrm{T}}/5)(U_{IR}/h\nu_{IR})R_{\mathrm{IR}} \approx 250$. Given the large optical depth and the relatively broad spectrum of the target photons, the absorption is appreciable at few hundreds of GeV, i.e. 5 % at 200 GeV and 50 % at 300 GeV in the observer frame. Note also that an additional softening of the spectrum can be due to the fact that the emission in the VHE band is produced by scattering occurring in the Klein–Nishina (KN) regime [e.g. 472–474].

To decrease the number of free parameters, the bulk Lorentz and Doppler factor are fixed to $\Gamma = 15$ and $\delta = 20$, close to the average obtained for a large sample of γ-loud FSRQ [372]. This implies a viewing angle of the jet $\theta_{\mathrm{v}} = 2.7^{\mathrm{o}}$, and the aperture angle is fixed to $\theta_{\mathrm{j}} = 0.1$ rad (5.7^{o}).

The emission region was assumed to be located beyond but not very far from the BLR, $d = 5 \times 10^{17}\,\mathrm{cm}$, implying $R = 5 \times 10^{16}\,\mathrm{cm}$. The low-energy slope n_1 is fixed to the standard value of 2. The remaining parameters are chosen to reproduce the synchrotron and IC components (see Table 8.3). To account for the different flux states, an evolution in both the electron distribution and the magnetic field is required. For comparison, the archival data (representation of the quiescent state) were modeled considering the emitting region partially within the BLR (standard framework) at $d = 1.4 \times 10^{17}$ cm, so that the $\gamma\gamma$ optical depth is small as indicated by the highest energy point of the 3FGL spectrum. The ratio between the peak luminosities (Compton Dominance, CD), are reported in Table 8.3. During the outburst, ν_{syn} lies more than an order of magnitude outside the FSRQ parameter space in the CD sequence proposed by [475], indicating a shift in the sequence during flares. The high degree of optical polarization suggests that the emission

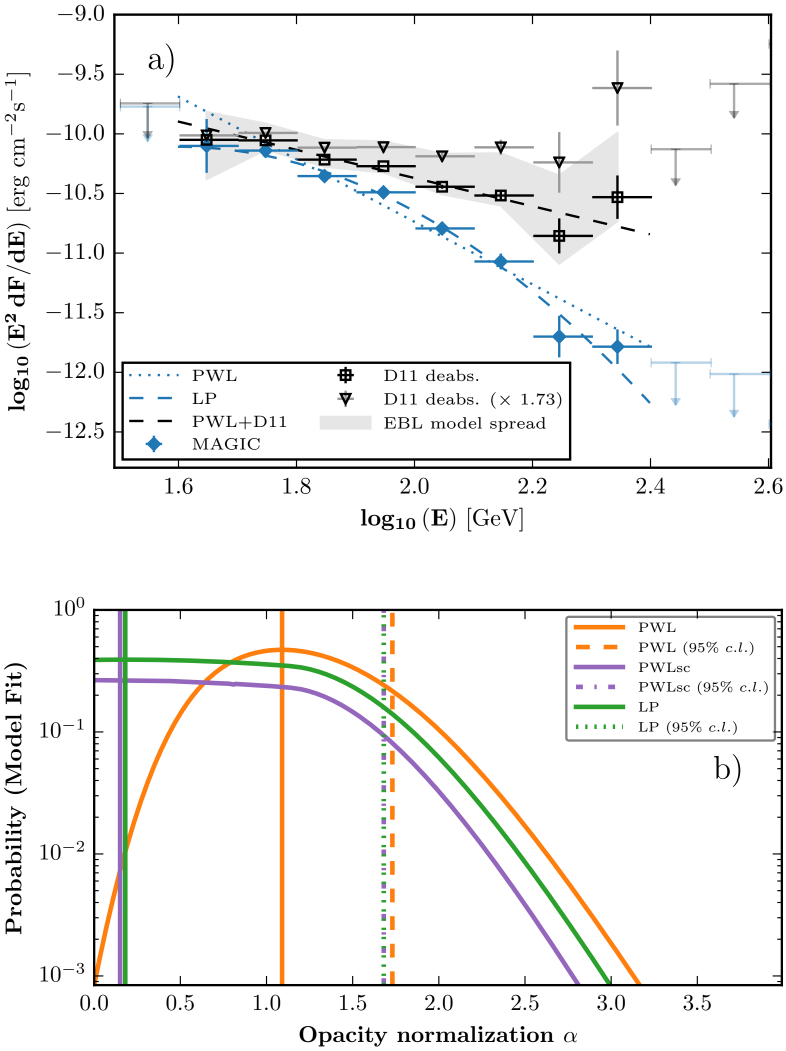

Figure 8.5: (a) Observed (blue diamonds) and EBL-corrected SED using [409] (black squares) for period B. The dotted and dashed lines show the best-fitting PWL, respectively. The gray shaded area accounts for the uncertainties derived by the use of different EBL models [409, 431, 433]. (b) The probability of fit as a function of EBL relative opacity [409, p. D11]. Only period *B* was considered (without upper limits). The best fit is marked with solid vertical lines and 95 % confidence level upper limits with dashed vertical lines.

may come from a compressed region in the jet like an internal shock, which is also an ideal site for electron acceleration/injection.

8.4 Constraints on EBL

Very high energy γ-ray photons coming from distant blazars such as PKS 1441+25 can interact with optical photons from the Extragalactic Background Light (EBL), resulting in an attenuation of the intrinsic VHE spectrum. The process is described in detail in chapter 11.

As B0218+357, PKS 1441+25 is a very good target for EBL studies because it

EBL model	Shape	$\alpha_{\text{best}}^{\text{nominal}}$	$\alpha_{\text{w/syst}}^{\text{UL}}$	Param. (best fit)				$p-$ value
				p_0	p_1	p_2	p_3	
PWL	No EBL	-	-	-11.9	-4.6			< 0.01
PWL	F08	$1.09^{+0.36}_{-0.31}$	1.72	-11.6	-3.1			0.50
PWL	D11	$1.09^{+0.37}_{-0.32}$	1.73	-11.5	-3.1			0.47
PWL	G12	$0.99^{+0.33}_{-0.28}$	1.55	-11.4	-2.7			0.51
PWL	S14 (max)	$1.09^{+0.37}_{-0.32}$	1.73	-11.5	-3.1			0.47
PWL	S14 (min)	$2.20^{+0.70}_{-0.61}$	3.41	-11.4	-2.7			0.54
LP	No EBL	-	-	-11.9	-4.7	3.2		0.39
LP	F08	$0.35^{+1.06}_{-1.58}$	1.69	-11.8	-4.2	2.2		0.40
LP	D11	$0.18^{+1.20}_{-1.42}$	1.68	-11.8	-4.4	2.7		0.39
LP	G12	$0.37^{+0.92}_{-1.63}$	1.53	-11.7	-3.9	2.0		0.40
LP	S14 (max)	$0.18^{+1.20}_{-1.42}$	1.68	-11.8	-4.4	2.7		0.39
LP	S14 (min)	$1.64^{+1.25}_{-3.56}$	3.40	-11.5	-3.2	0.83		0.42
SEPWL	No EBL	-	-	-6.2	1.4	-0.41	0.48	0.27
SEPWL	F08	$0.22^{+1.20}_{-3.21}$	1.70	-7.4	0.46	-0.13	0.47	0.27
SEPWL	D11	$0.15^{+1.23}_{-3.14}$	1.68	-2.7	2.7	-1.9	0.34	0.27
SEPWL	G12	$0.37^{+0.92}_{-3.36}$	1.54	-1.4	2.6	-3.0	0.27	0.27
SEPWL	S14 (max)	$0.15^{+1.23}_{-3.14}$	1.68	-2.7	2.7	-1.9	0.34	0.27
SEPWL	S14 (min)	$1.75^{+1.15}_{-4.74}$	3.40	-2.4	0.39	-5.8	0.17	0.29

Table 8.4: Upper limits at 95 % confidence level on the relative EBL opacity α. References: F08: Franceschini, Rodighiero, and Vaccari [431], D11: Domínguez et al. [409], G12: Gilmore et al. [433], S14: Scully, Malkan, and Stecker [476]. The normalization factor 10^{p_0} is given in units of erg cm^{-2} s^{-1}.

allows us to probe EBL models at a redshift poorly explored with ground-based γ-ray instruments. At the same time, the spectrum has very good photon statistics, which is a condition that B0218+357 did not met. However, KN effects together with an expected intrinsic γ-ray absorption in the VHE band (see section 8.3.3), can mimic the effect of EBL absorption, making it difficult to disentangle the two effects.

Following Abdo et al. [477], a LRT was used to compare a null hypothesis (no EBL absorption) with respect to the hypothesis of EBL absorption with a scaled opacity $\alpha\,\tau(z, E)$. Predicted opacities from [409] (τ_{D11}), [431] (τ_{F08}), [433] (τ_{G12}) and [476] (τ_{S14}) were considered, leaving α as a free scaling parameter. Different possible intrinsic spectral shapes were also accounted for:

- PWL $dF/dE = 10^{p_0}(E/E_0)^{p_1}$
- LP $dF/dE = 10^{p_0}(E/E_0)^{p_1 - p_2 \log_{10} E/E_0}$
- SEPWL $dF/dE = 10^{p_0}(E/E_0)^{p_1} \exp\left[(E/10^{p_2})^{p_3})\right]$

where E is measured in GeV and $E_0 = 100\,\text{GeV}$.

The resulting limits on the optical depth scaling are reported in Table 8.4. An example of such procedure is also given in Fig. 8.5. A possible overall systematic error of ±15 % in the absolute energy scale of the instrument was also considered by modifying the total light throughput of the instrument. Under the assumption that no curvature is present in the intrinsic VHE spectrum, the measured spectrum is compatible with the present generation of EBL models.

The 95 % confidence level limit obtained in this work for [431] is compatible with the statistical result from Ackermann et al. [425] for $0.5 \leq z \leq 1.6$, $\alpha = 1.3 \pm 0.4$, derived from multiple blazars at different redshifts.

The estimated scaling on the optical depth could in principle be translated into EBL density constraints following [409] and [428]. In order to determine which range of wavelengths are being constrained by MAGIC spectral measurements, a first order approximation as suggested in section 4 of Abramowski et al. [428] was adopted. In that work, the constraining range is given by $[(1+z)^2 E_{min}, E_{max}]$, where z is the redshift, E_{min} and E_{max} are the minimum and maximum energies of the VHE spectrum. The VHE energies can be translated then into $(\lambda_{EBL}/1\,\mu\mathrm{m}) = 1.187 \times (E/1\,\mathrm{TeV}) \times (1+z'^2)$ where $z' < z$. This method however fails to predict the correct range when the source has a very steep spectrum and high redshift. In order to deal with such cases (and particularly for PKS 1441+25, but also B0218+357), the following procedure was developed:

1. The EBL spectrum from [409] is divided in small bins (log-spaced in λ).
2. For each bin, the cross section for the $\gamma - \gamma$ pair creation and the total energy-dependent γ-ray opacity are computed. An example of this (with a rather coarse binning, giving several opacity components) can be seen in Figure 8.6a).
3. Each opacity component is scaled with a parameter α_k.
4. Fixing all the bins k to $\alpha_k = 1$ except for one (which is set at the upper limit for the general fit, $\alpha_k = \alpha_{UL} = 1.73$), a χ^2 is estimated and its difference with the one for the best fit χ^2_{best} is calculated ($\Delta\chi^2$).
5. The procedure is repeated for any individual EBL bin, obtaining an estimation of the relative contribution that each part of the EBL spectrum has to the total absorption in the PKS 1441+25 spectrum (Figure 8.6b).
6. A decision on whether a bin is significant or not is made by selecting those that produce a change of at least $\Delta\chi^2 = 1$.

With the aforementioned method, the observed VHE spectrum is able to give significant constrains to the EBL density between 0.21 and 1.13 μm, where the optical depth scaling $\alpha_{D11} < 1.73$ implies in the local Universe $\lambda f_{\lambda=0.5\mu m} < 8.7\,\mathrm{nW cm^{-2} sr^{-1}}$ for the model of Domínguez et al. [409].

8.5 Conclusions

MAGIC has detected for the first time VHE emission from the $z = 0.940$ blazar PKS 1441+25 during a MWL outburst in April 2015. PKS 1441+25 is, together

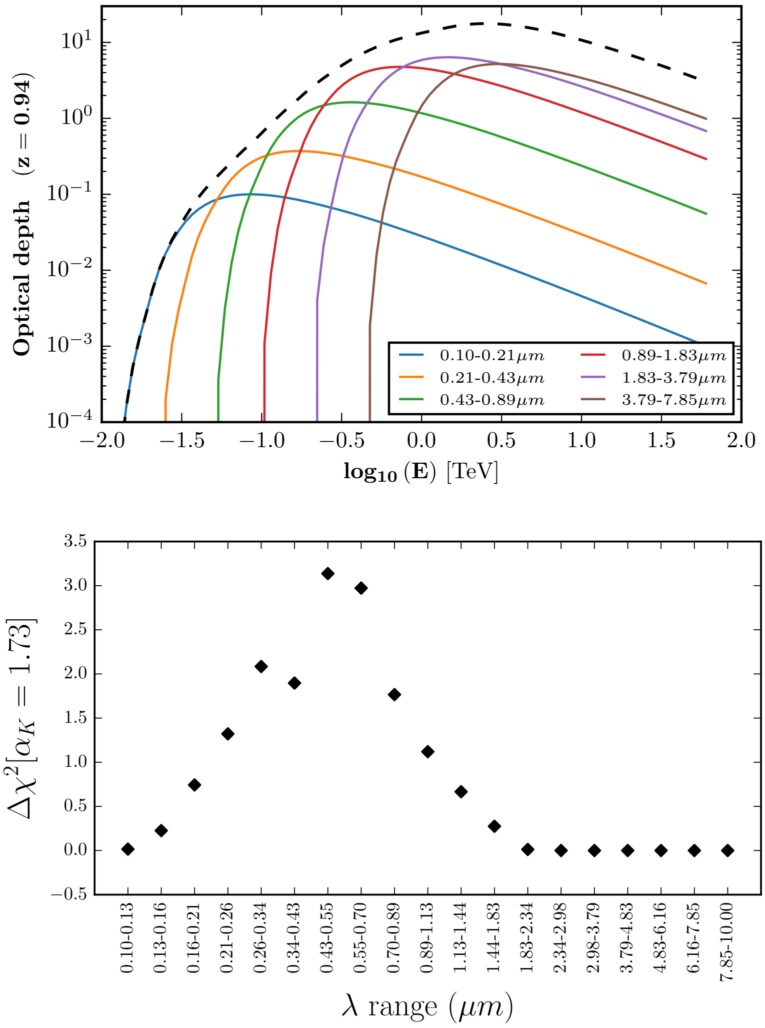

Figure 8.6: (a) Contribution from each EBL λ-bin in the total opacity of γ-rays. b) Worsening of the overall fit ($\Delta\chi^2$) when the optical depth scaling factor applied individually to each EBL bin is set to the upper limit value. Very low values mean little constraining power over that particular part of the EBL spectrum. Note that the binning is finer in the second panel to increase the resolution of our method.

with QSO B0218+357, the most distant VHE source detected so far. The data were used to infer properties about the emission from a VHE blazar which occurred when the Universe was only half of its current age.

The evolution of the MWL SED is studied in the framework of an external Compton emission model. The absence of intrinsic absorption features in the HE and the VHE regime constrains the localization of the emitting region to be just outside of the BLR during this period of high activity, while it is expected to be partially compatible with the BLR during the period of low activity. The SED evolution reveals changes in the electron distribution and the magnetic field.

For the first time, the VHE measurements are used to indirectly probe the EBL at redshifts out to z $\sim$ 1 with ground-based gamma-ray instruments. Although an internal cutoff cannot be excluded, the measured VHE spectrum is consistent with a steepening due to attenuation caused by the EBL. Employing state-of-the-art EBL models, upper limits to the EBL density are derived. The upper limits on the opacity calculated under the assumption of an intrinsic spectrum compatible with a PWL function for different EBL models result in $\tau(z,E) < 1.73\,\tau_{D11}$, $\tau(z,E) < 1.72\,\tau_{F08}$, $\tau(z,E) < 1.55\,\tau_{G12}$, $\tau(z,E) < 1.73\,\tau_{S12_{max}}$ and $\tau(z,E) < 3.41\,\tau_{S12_{min}}$ for EBL models from [409], [431], [433] and maximum and minimum from [476], respectively.

9
PKS 1424+240

Contents

In this chapter, we discuss the results of the MAGIC observational campaign of PKS 1424+240 during year 2014. The data was obtained after the major upgrade of the MAGIC system and was not included in the MAGIC multi-year campaign publication on the same source [478]. Although cross-checked and presented in MAGIC conference meetings, the analysis and interpretation should be considered preliminary. In section 9.1 PKS 1424+240 is presented together with its classification and redshift measurement. Section 9.2 covers the observations and analysis of multi-wavelength data obtained with MAGIC, *Fermi*-LAT, *Swift*-XRT and *Swift*-UVOT. Finally, sections 9.3, 9.4 and 9.5 summarize the results of this study.

9.1 Introduction

PKS 1424+240 is a distant BL Lac discovered in 1974 as a radio source [479] and classified as a blazar in 1988 [480]. It was first classified as an intermediate frequency peaked blazar (IBL) [481] and more recently reclassified as a high frequency peaked blazar (HBL) [482] based on refined estimations of the synchrotron peak position, found at $\nu_{\mathrm{Syn}} > 10^{15}\,\mathrm{Hz}$[1].

As seen in the previous chapters, the Compton dominance in FSRQs can be as high as $\sim 10^2$, which is interpreted as evidence of intense production of γ-rays from external inverse Compton scattering.

The lack of significant low energy emission in HBLs coming from the BLR and IR torus causes the Compton dominance to be typically $\lesssim 1$. In addition, the emitting blob can in principle be located anywhere along the jet. Positional information can still be extracted from causality considerations and the aperture angle of the jet. If the emitting region is very close to the central object, the blob is expected to be small and heavily compressed. This can explain the fast variability events sometimes exhibited by nearby HBLs, with time-scales of minutes in X-rays and γ-rays. Examples of this include Mrk 421 ([483, 484]) and Mrk 501 ([485–487]).

If a significant dusty torus structure is present in the BL Lac, then additional target photons for the inverse Compton scattering are available. In such case, the high energy component of the spectrum can be more prominent, resembling that of the FSRQs. This is thought to be the case of LBLs [488].

For HSPs, the lack of observable torus emission and the fact that the spectra in most cases can be well reproduced by simple SSC models is usually interpreted as an evidence that the torus is intrinsically weak. For these objects, if the emitting region is far away from the central object, variability is expected to be slow, but exceptions to this rule have been found. They are interpreted as small compressed emitting regions far away from the central object [489].

Several approaches have been followed to determine PKS 1424+240's redshift. Direct spectroscopic redshift measurements were initially unsuccessful due to the lack of strong optical features, which is one of the main properties of BL Lacs. Better results were achieved by looking into redshift ranges that were likely to host the source, being the most constraining ones a photometric upper limit of $z < 1.11$ obtained by observing the blazar from UV to NIR and modeling the SSC (excluding VHE energy data) [490]. Previous attempts that included also VHE data together with the HE data coming from *Fermi*-LAT provided a similar upper limit of $z < 1.19$ [491]. Finally, Furniss et al. [492] set a strict lower limit of $z \geq 0.6035$ based on observations of the Ly-α forest and Ly-β lines using HST/COS in the far UV ($1135 - 1795\,\text{Å}$). Such spectral features are caused by gas clouds which exist along the line of sight between the source and Earth. These results greatly differ from previous attempts to determine the redshift using empirical approaches such as Prandini et al. [493], which suggested a much lower distance of $z = 0.24 \pm 0.05$.

More recently, a very interesting approach was proposed by Rovero et al. [494]. They managed to identify a group of gravitationally bound objects close to the position of the blazar using the Gemini Multi-Object Spectrograph. They estimated a probability of 98% of PKS 1424+240 being a member of such group and set its most probable redshift to $z = 0.601 \pm 0.003$. Finally, Paiano et al. [376] claimed a detection of faint [O II] and [O III] features at 5981 Å and 8034 Å respectively,

---

[1] Note however that blazars are known to transition between these rigid classes during flares.

Date	$t\,(\mathrm{h})$	$S\,(\sigma)$	
03/24	0.49	3.59	
03/25	0.49	4.02	
03/27	1.00	3.79	
04/03	0.74	3.82	
04/05	0.86	6.92	
04/06	0.96	4.28	
04/07	0.97	4.42	
04/08	0.98	3.93	
04/09	0.93	2.85	
04/11	-	-	†
04/19	-	-	†
04/22	1.10	5.30	
04/23	1.10	5.23	
04/24	1.07	3.53	
04/25	0.95	2.46	
04/26	0.98	0.53	
04/27	0.98	2.79	
04/29	0.98	1.08	
04/30	0.93	3.01	
05/01	0.98	1.99	
05/02	0.98	3.15	
05/03	0.98	2.96	
05/04	0.97	2.40	
05/05	0.91	4.92	
05/06	0.98	4.39	
05/18	0.44	1.88	
05/19	0.64	3.51	
05/20	0.65	3.51	
05/21	0.65	3.76	
05/22	0.65	2.10	
05/23	0.48	3.35	
05/24	0.65	0.64	
05/25	0.65	2.87	
05/26	0.65	2.54	
05/27	0.65	2.66	
05/31	0.66	1.94	
06/02	0.65	0.97	
06/04	-	-	†
06/06	0.65	0.33	

Table 9.1: MAGIC observations of PKS 1424+240 during the campaign of 2014. The exposure is quoted after quality cuts. Third column denotes the statistical significance. † indicates bad weather.

providing the first firm spectroscopic redshift for the source $z = 0.6047(12)$.

PKS 1424+240 is a particularly interesting source because of its great distance (the largest among BL Lacs with VHE γ-ray emission) and the apparent hardening of the spectrum in the highest energies, which has triggered a long-lasting discussion and interpretations of its origin. Among other possible explanations for such unexpected spectral curvature, we note the existence of secondary γ-rays produced in the line-of-sight through interaction of cosmic rays with background photons and the effect of the hypothetical axion-like particles (ALPs) [495].

9.2 Observations and data analysis

PKS 1424+240 was first detected in HE γ-rays by *Fermi*-LAT in 2009 [182, 496] with a hard spectrum of $\Gamma = 1.85 \pm 0.07$. The discovery of VHE emission above 100 GeV by VERITAS [497] followed soon after. The source has also been observed multiple times with MAGIC [190, 204, 498] and is a regular target of the *Neil Gehrels Swift Observatory* (*Swift*).

9.2.1 VHE gamma rays

PKS 1424+240 has been one of the main targets of the MAGIC EBL key observation program (KOP), which provided time for regular monitoring of the source. MAGIC observed PKS 1424+240 between March 24th 2014 and June 6th 2014 for a total amount of 30 hours (see Table 9.1). The data analysis was done with the standard MAGIC Analysis and Reconstruction Software (MARS) [194]. The observations were carried out at low zenithal distances in order to minimize atmospheric extinction

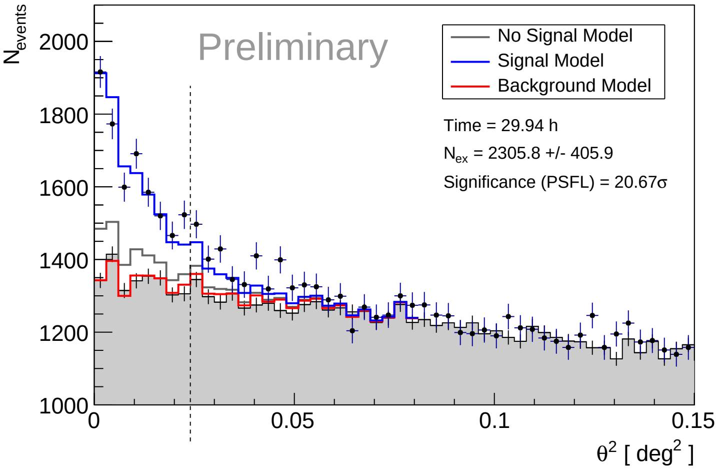

Figure 9.1: MAGIC θ^2 plot for PKS 1424+240 including data from the 2014 campaign. Statistical significance is computed using the method described in Appendix A.

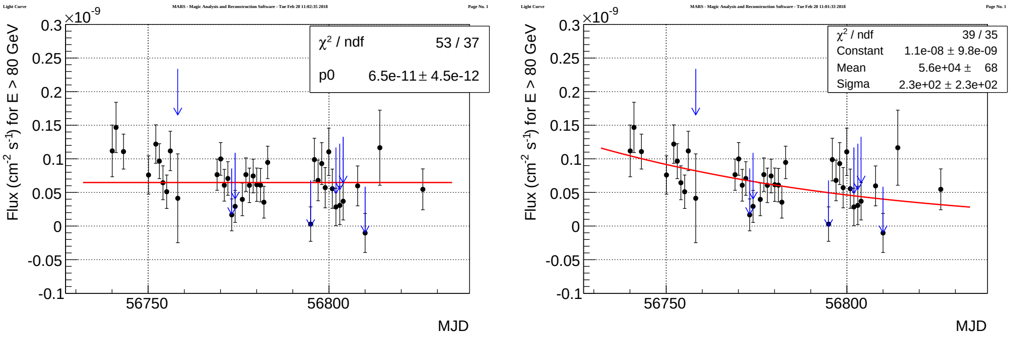

(a) Constant fit, $\chi^2/\mathrm{ndf} = 52.9/37$. **(b)** Gaussian decay, $\chi^2/\mathrm{ndf} = 39.3/35$.

Figure 9.2: MAGIC light curve for PKS 1424+240.

and provide the lowest energy threshold, which is estimated to be $\sim 60\,\mathrm{GeV}$ using the procedure described in Appendix C.2.1. A clear detection of $20.7\,\sigma$ ($17.9\,\sigma$ computed with the less sensitive Li&Ma formula 17) was made with an excess of $(2.34 \pm 0.11) \times 10^3$ γ-ray like events concentrated at the lowest energies of the MAGIC range $(50 - 300\,\mathrm{GeV})$.

The non-variability hypothesis was tested for PKS1424+240, which yields a low probability of $P = 0.044$ ($\chi^2/\mathrm{ndf} = 52.9/37$). Instead, a Gaussian-like flare decay model

$$F = F_0 + F_{amp}\, e^{-(t-t_0)^2/2\sigma^2} \tag{9.1}$$

provides a better description of the data ($P = 0.28$, $\chi^2/\mathrm{ndf} = 39.3/35$) and is preferred at $3.3\,\sigma$ over the constant flux model. Other possible decay profiles (exponential, linear) were also tested and resulted in similar values for the χ^2.

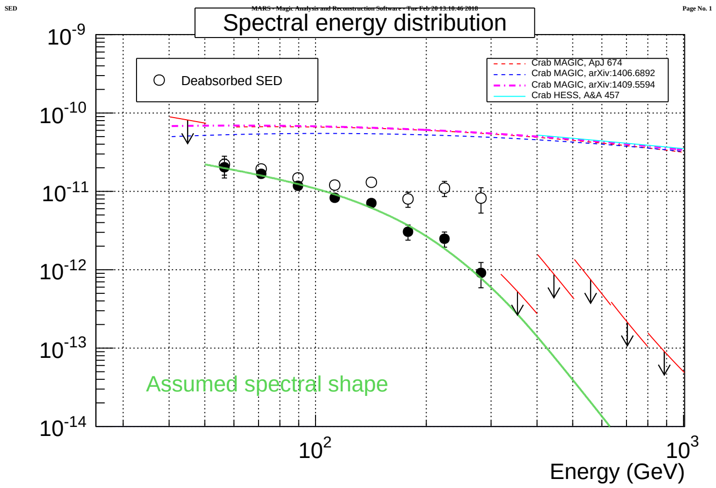

Figure 9.3: MAGIC spectral energy distribution for PKS 1424+240.

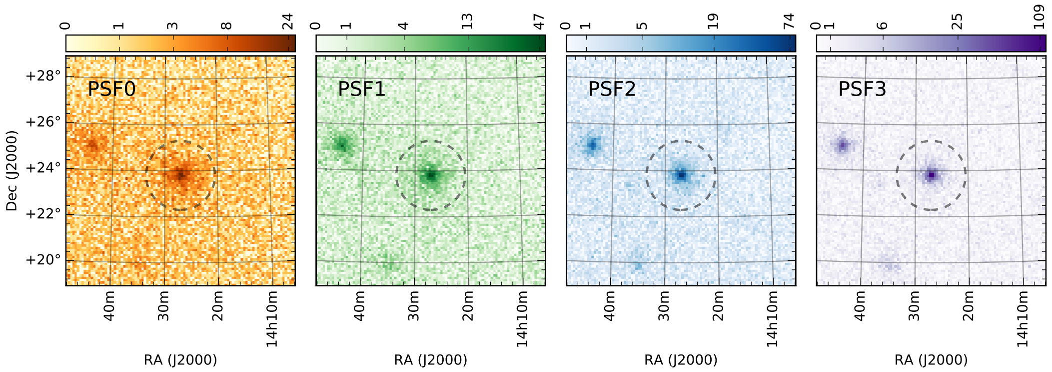

Figure 9.4: *Fermi*-LAT counts maps for PKS 1424+240 including data from the whole mission as a function of the PSF event type, with PSF0 including events with the worst reconstructed PSF and PSF3 those with a best positional reconstruction.

9.2.2 HE gamma rays

The constant monitoring of the sky by LAT allows to study the long-term and short-term HE γ-ray emission from PKS 1424+240.

The analysis of the PASS8 data coming from LAT was done using the standard Fermi `ScienceTools` (v10r0p5) through the `enrico` package [183] (see also section 4.5.7). Photons with energies between 300 MeV and 500 GeV were considered in the light curve generation. The lower limit was chosen instead of the usual 100 MeV to i) improve the SNR of the light curve; ii) remove the need for energy dispersion corrections; iii) to reduce the number of events affected by bad PSF and large background contamination. The upper bound was set to 500 GeV because at that energy the optical depth of the EBL becomes $\tau \sim 5$ in the model of Domínguez et al. [409] for $z \sim 0.6$, meaning that in practice no photons from the source were expected to arrive to the detector with larger energies.

The events were divided according to their PSF event type (see Figure 9.4), in

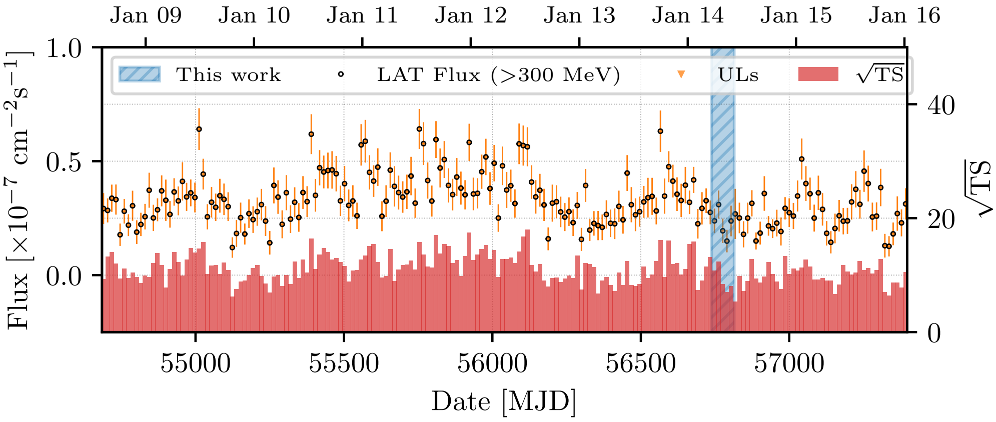

Figure 9.5: PKS 1424+240 emission above 300 MeV during the *Fermi*-LAT mission (up to January 2016). Shaded blue band highlights the observations of MAGIC during the campaign of 2014.

a scale from 0 (worst PSF) to 3 (best reconstructed PSF). Each event type was considered separately with its own IRFs and all of them were processed together in a joint Maximum Likelihood analysis. The assumed spectrum was a simple power-law absorbed by the EBL model from Domínguez et al. [409].

Wide bins of 2 weeks each were selected to simplify the analysis and improve statistics per bin. A light curve containing data from the whole *Fermi*-LAT mission up to January 2016 is shown in Figure 9.5. It is interesting to note that MAGIC observations in 2014 took place in a period or which the source was not particularly active in HE γ-rays.

9.2.3 X-rays and Optical

Soft X-rays (0.3 – 10 keV) and optical-UV photons were measured using the data from *Swift*-XRT (X-ray telescope) [397] and *Swift*-UVOT (UV-optical monitor) [399] on board the *Neil Gehrels Swift Observatory* (*Swift*).

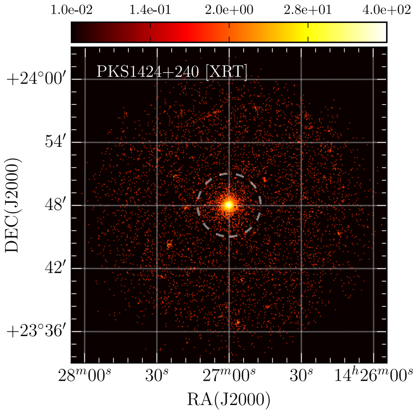

Figure 9.6: Counts map of PKS 1424+240 from the entire *Swift*-XRT mission.

Contemporaneous *Swift* data was taken in photon-counting mode during ten ∼ 1 ks observation windows. Standard event filtering and data analysis was done with HEASARC's tools: `xselect`, `ximage` and `xspec`. A binning was made so that every bin contains at least one event, as required by the *cstat* (Poissonian statistics) fitting routine. No pile-up corrections are needed because of the relatively low count rates. A Power Law spectral model can describe the intrinsic spectrum, but the predicted hydrogen column densities absorbing radiation below few keV exceed the Galactic measurements from Kalberla et al. [398] and Willingale et al. [499] ($n_{HI} = 3.10 \times 10^{20} cm^{-2}$ and $n_{H_2} = 4.42 \times 10^{192}$). Following [500], the additional absorption was interpreted as being due to a possible warm absorber in the host galaxy ($z = 0.604$) and close to the blazar structure. Once de-absorbed from dust, neutral and molecular hydrogen, the resulting pure Power Law had a photon index of 2.790 ± 0.075.

Optical and UV photometry was obtained with *Swift*-UVOT in 6 spectral bands. The analysis was done using standard tools included in the HEASOFT package (version 6.22): `uvotimsum` and `uvot2pha`. Fluxes were estimated using aperture photometry. Spectral points were then corrected assuming a reddening given by colour excess $E(B-V) = 0.0483$ [401] and $R_V = A_V/E(B-V) = 3.1$ [450] and converted into $\mathrm{erg\,cm^{-2}\,s^{-1}}$.

9.3 The multi-wavelength view of PKS 1424+240

One-zone leptonic models have traditionally failed to reproduce the Doppler factors measured from Radio observations of PKS 1424+240. This suggests that Radio and γ-rays, while possibly connected, are originated in different regions. The large Doppler factors derived from optical and X-ray data ($\delta \sim 100$) together with the large separation between the low energy and high energy components have been used as a criticism for such simple models. This contrasts with other BL Lacertae sources like Markarian 421 [501], where the comparatively higher frequency synchrotron peak allows one-zone SSC models to roughly reproduce the broadband spectrum. More complex leptonic models, such as multi-zone SSC or External Compton models on a ‘weak’ torus have been proposed to solve these issues.

The γ-ray emission of PKS 1424+240 has also been discussed multiple times in terms of p-γ interactions (hadronic emission). Such models could in principle solve the difficulties of one-zone pure leptonic models to describe the emission [44], justify the apparent spectral hardening at VHE[478, 482] and finally explain the relative stability in the γ-ray spectrum with respect to the much more variable optical and X-ray component[482]. By assuming that leptons and hadrons are co-accelerated (and thus share the same injection indices), some authors have obtained acceptable hadronic solutions with proton-synchrotron dominating the MeV-GeV emission and VHE emission arising from secondary (cascade) leptonic emission. Interestingly, hadronic models predict a significant hardening in the spectrum above $\sim 1\,\mathrm{TeV}$ [502, 503] which should be measurable with CTA.

In order to keep the interpretation simple and compare with previous results, in this work the broadband spectrum was modelled following [478]. The calculations were done using the SSC code from Saha and Bhattacharjee [504]. In this framework, the emission is explained as coming from two regions (blobs) that are expanding along the jet with bulk Lorentz factors $\Gamma_{in,out}$. They are filled relativistic leptons that have been injected with broken Power Law spectra. To simplify the calculations, we assume spherical shapes for the blobs in the rest frame of the plasma. For historical

---

[2] `http://www.swift.ac.uk/analysis/nhtot/`

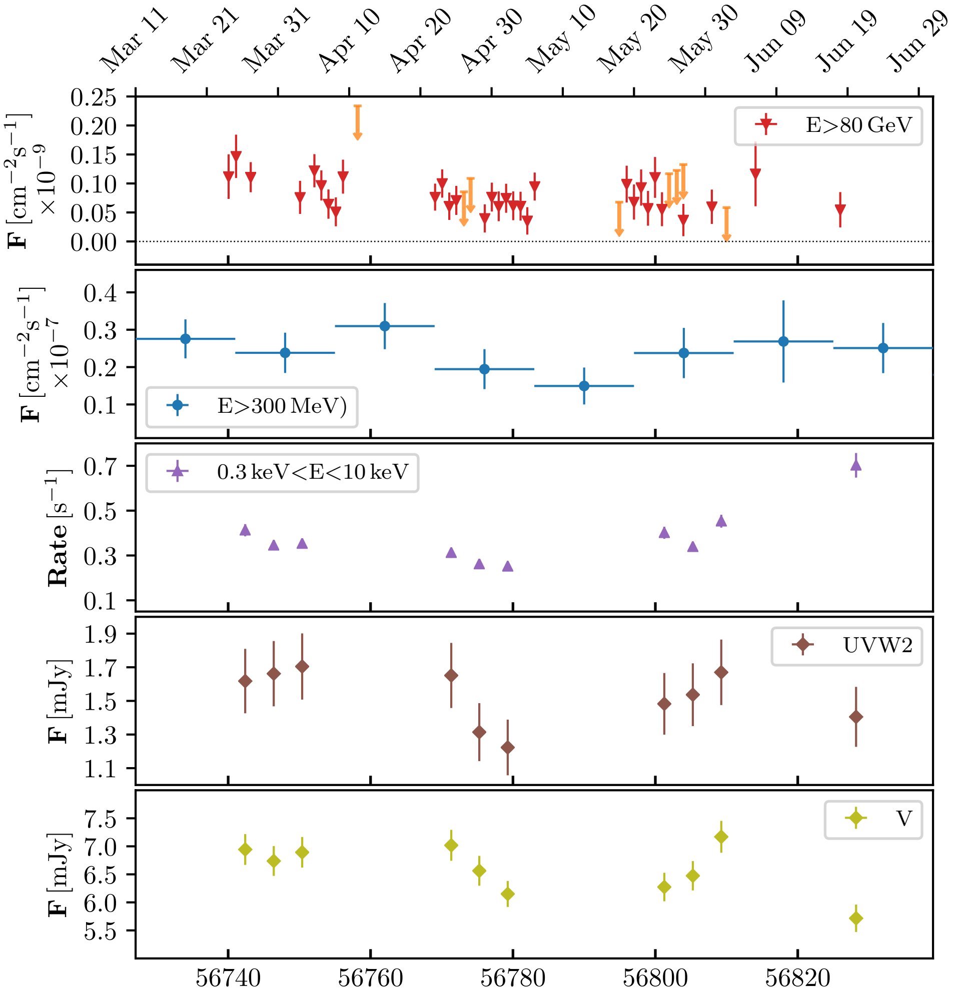

Figure 9.7: Broadband light curve of PKS 1424+240 during the campaign of 2014, including data from: MAGIC starting from 80 GeV (top panel), *Fermi*-LAT using photons from 300 MeV (second panel), *Swift*-XRT in the range $0.3 - 10$ keV (third panel) and finally two filters (W2 and V) from the *Swift*-UVOT in the two last panels.

reasons, we have dubbed these two components 'in' and 'out', even though they might be cospatial [505]. Additionally, the redshift of the source is set to $z = 0.6$ [376, 494]. The luminosity distance, needed to convert between luminosity and observed flux, is calculated assuming a flat Universe with $\Omega_M = 0.3$ and $\Omega_\Lambda = 0.7$ and following the prescriptions of [478] the angle between the line of sight and the jet is fixed for both regions to $\theta = 1.9°$.

The injected electron spectrum is assumed to be a broken power law

$$N_e(\gamma) = K\gamma^{-n_1}\left(1 + \frac{\gamma}{\gamma_{br}}\right)^{n_1-n_2} \tag{9.2}$$

where K is a normalization constant, γ is the Lorentz factor and $n_{1,2}$ are the spectral indices before and after the break. The results from this model are presented

	$\gamma_{\rm min}$ $[10^3]$	$\gamma_{\rm b}$ $[10^4]$	$\gamma_{\rm max}$ $[10^4]$	n_1	n_2	B [G]	ρ	R [cm]	δ	Γ
in	10	5.3	80	2.0	4.0	0.050	−1.5	16.7	30	30
out	1.0	2.0	3.5	2.1	4.0	0.033	−4.8	18.3	10	5.2

Table 9.2: Input parameters for the emission model shown in Fig. 9.8, where “in” and “out” denote the two populations of electrons along the jet that are responsible for the broadband emission. The parameters of the model are: the minimum ($\gamma_{\rm min}$), break ($\gamma_{\rm b}$) and maximum ($\gamma_{\rm max}$) Lorentz factors; the low energy (n_1) and the high energy (n_2) slopes of the broken power law used to model the electron energy distribution; the magnetic field B; the normalization of the electron energy distribution ρ in $\log_{10}$ scale and units of $\mathrm{erg\,cm^{-3}}$; the radius of the emission region in $\log_{10}$ scale, R; the Doppler factor δ; and the corresponding bulk Lorentz factor Γ. Doppler factors are calculated assuming that the observer lies at an angle $\theta_{\rm v} = 1.9^\circ$ from the jet axis. The parameters shown here were chosen to reproduce the observed spectrum.

in Figure 9.8 and the parameters of the model are summarized in Table 9.2.

Inner region

The first region, in expansion with bulk Lorentz factor $\Gamma \sim 1/\theta \approx 30$ is smaller in size ($R \sim 4.8 \times 10^{16}\,\mathrm{cm}^{-3}$ and is able to reproduce the variability seen in the *Swift*-XRT and MAGIC data without violating the causality relation $R < ct_{var}\delta/(1+z)$). Its contribution dominates the X-rays and GeV–TeV γ-rays spectral regions.

In this case, the spectral index of the electrons is assumed to be $n_1 = 2.0$ from the Lorentz factor $\gamma_{min} = 1.0 \times 10^4$ to $\gamma_{br} = 5.3 \times 10^4$ and then a softer $n_2 = 4.0$ from γ_{br} to $\gamma_{max} = 8.0 \times 10^5$. The relativistic Doppler factor is estimated to be $\delta = [\Gamma(1 - \beta\cos\theta)]^{-1} \sim 30$ and the magnetic field intensity $B \sim 5.0 \times 10^{-2}$ G. These values are similar to those derived by Aleksić et al. [478], but a small difference in the Lorentz factor distribution for the electrons, a softer spectral index above the break and slightly larger magnetic field intensities are found, all supported from the lower X-ray luminosity observed during the campaign of 2014, nearly one order of magnitude below the X-ray luminosity in 2009-2011.

Outer region

The outer emitting region contains a mildly relativistic ($\Gamma \approx 5$) electron plasma. It is described as a much larger ($R \sim 1.9 \times 10^{18}\,\mathrm{cm}^{-3}$) blob with variability only possible at large time scales ($t_{var} > 10^2$ days from the causality relation). It is mostly responsible for the optical part of the spectrum and the low energy γ-rays.

The electron energy distribution has roughly the same spectral indices as the inner blob but with $\gamma_{min} \approx 1.0 \times 10^3$, $\gamma_{br} \approx 2.0 \times 10^4$ and $\gamma_{max} \approx 3.5 \times 10^4$. The density of electrons is roughly 180 times lower in this case, the relativistic doppler factor is also lower ($\delta \sim 9$, very similar to the values of $\delta \sim 10$ derived from VLBA data for viewing angles of $1 - 5^\circ$) and the magnetic field strength drops to about $B \approx 3.3 \times 10^{-2}$ G. When compared to [478], the emission from this component in the current campaign

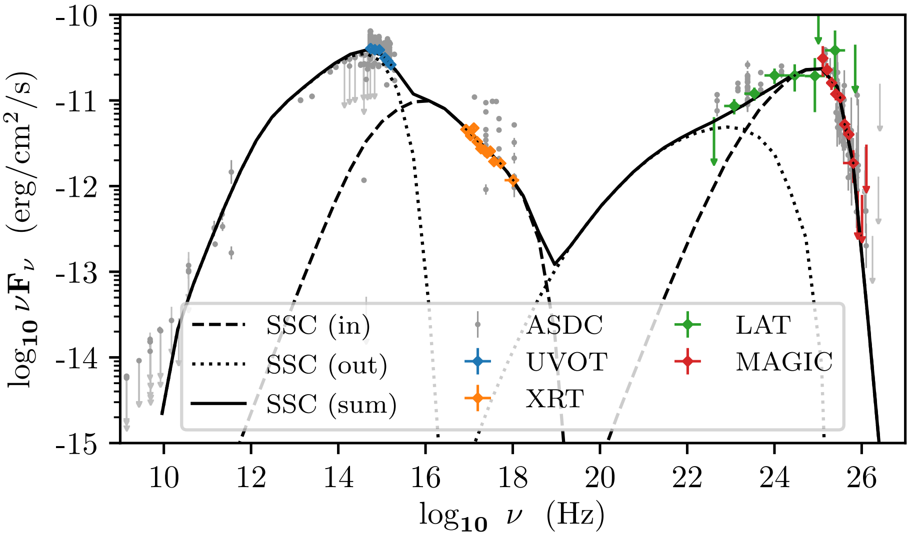

Figure 9.8: Broad band SED of PKS 1424+240 showing Optical and UV data from *Swift*-UVOT (blue points), soft X-rays from *Swift*-XRT (green points), HE γ-ray data from *Fermi*-LAT (green points), VHE γ-ray data from MAGIC, archival data compiled from ASDC (`http://tools.asdc.asi.it/SED`, gray points and upper limits). The inner emitting region with its SSC emission is represented in black dotted lines. The outer emitting region is plotted as dashed lines and the total emission of PKS 1424+240 according to this two-zone leptonic SSC model is presented in solid black lines.

does not exhibit significant changes with respect to the level of activity in 2009-2011, which is in the line with the suggested bigger emitting region size.

9.4 Constraints on EBL

PKS 1424+240 has traditionally drawn attention because of the apparent hardening of the spectrum above ~ 100 GeV, unexpected in pure leptonic models. One of the possible interpretations for it was the oscillation of γ-rays into hypothetical axion-like particles (ALPs), which would reduce the observed γ-ray opacity with respect to the predictions from EBL models. In order to investigate this scenario, we have included two observational campaigns of PKS 1424+240 (2014 and 2015) in the study of the EBL density presented in chapter 11.

9.5 Summary and conclusions

PKS 1424+240 is an intermediate BL Lac with significant and persistent VHE γ-ray emission. Its spectrum has been traditionally challenging to understand and its large redshift of $z = 0.6047(12)$ only recently measured, making it the most distant BL Lac observed in VHE γ-rays as of 2017.

In VHE energies, MAGIC has observed the source for at least 6 years. The campaigns of 2009, 2010 and 2011 were discussed in [478]. This chapter focuses on the MAGIC data from 2014, which has been analyzed together with contemporaneous HE

γ-ray data coming from *Fermi*-LAT and X-ray and optical data obtained with *Swift*.

The multi-wavelength evolution of the flux in the selected energy bands has been presented in Figure 9.7 and discussed in section 9.3. No clear correlation between the activity of the source in MAGIC with respect to *Fermi*-LAT *Swift*-XRT and *Swift*-UVOT is found. The data coming from the four instruments were compiled together to build an average broadband spectrum, shown in Figure 9.8.

Finally, the multi-wavelength SED is discussed in terms of a pure leptonic two-zone SSC model following Aleksić et al. [478]. The overall emission is found to be compatible with previous observations in all bands except X-rays, where significant variability is found between 2014 and previous campaigns. The proposed model can reproduce such evolution in X-rays by invoking subtle changes in the magnetic field strength and electron density of the inner emitting region.

Part IV

Extragalactic Background Light

> *Observing quasars is like observing the exhaust fumes of a car from a great distance and then trying to figure out what is going on under the hood.*
>
> —Carole Mundell, June 1998

10

Cosmic Optical and Infrared Backgrounds

Contents

10.1 Introduction

The study of galaxy formation and evolution is one of the main goals of astrophysics and cosmology. The accumulated emission from stars, nebulae, accretion and explosive phenomena and diffuse radiation through the Universe history remains encoded in a background radiation field known as extragalactic background light (EBL). It does not only carry information about the different population of stars (in particular the transition from the hypothetical population III to populations I-II) but is also an important proxy to study non-thermal phenomena such as AGN emission or starburst episodes.

While the cosmic background spectrum covers the whole spectrum from radio to gamma rays, EBL normally refers to the portion that goes from IR up to UV, which is thought to have mainly an astrophysical origin. It is common to leave out the Cosmic Gamma-ray and X-ray backgrounds (CGB, CXB) that are generated by non-thermal processes and the Cosmic Microwave Background (CMB), relic radiation emitted during the time of recombination in the Big Bang theory.

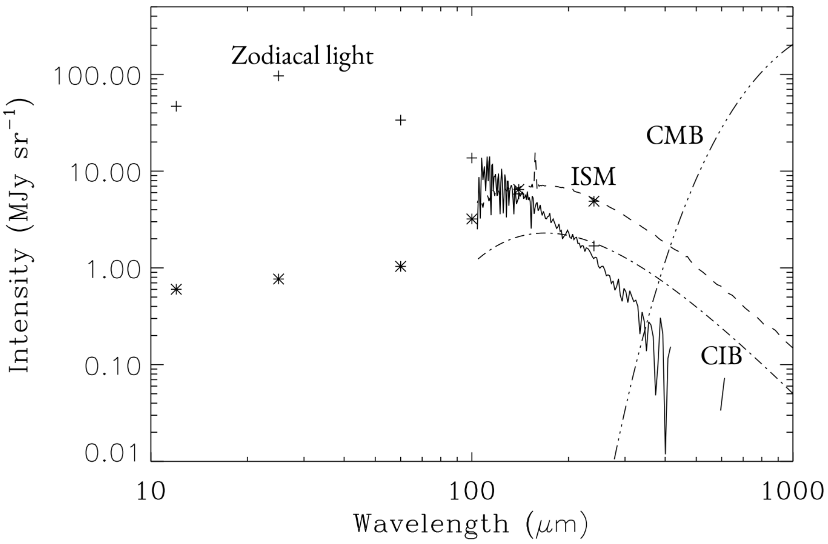

Figure 10.1: Foreground astrophysical sources that can be found on top of the EBL at IR and make its measurement a hardly known yet interesting topic nowadays. Adapted from [506]. The situation is not better at shorter wavelengths, where direct star and Galactic emission together with Zodiacal light dominates the total brightness of the sky.

The exact spectral shape of the EBL is, as of 2018, not perfectly understood. This is due to its low intensity compared to foregrounds, including diffuse emission from several astrophysical sources such as the Galactic diffuse emission and the reflected light by the cosmic dust (e.g. Zodiacal light). Moreover, ground based measurements are affected by additional contamination (e.g. Airglow).

Most models and measurements coincide in a double hump spectral shape.

The first hump, located in the optical and near IR ($0.1 - 10.0\,\mu$m) is the so called Cosmic Optical Background (COB). The bulk contribution to the COB comes from stellar nucleosynthesis in normal galaxies at redshifts $z < 10$ [508]. Second order contributions include light from gravitational collapse of stars, particle decay and mass accretion in AGNs. The accurate characterization of the COB emission is of fundamental importance, as its comparison with galaxy counts can give us information of the star formation history and the fraction of cosmic light whose origin is not well understood (more exotic physical phenomena).

The second hump is known as Cosmic Infrared Background (CIB). It is though to be originated when cosmic dust absorbs light from the COB and re-emits it at longer wavelengths. It is comparatively easier to measure it with missions such as DIRBE [509], FIRAS [510] (uncertainties of the level of 30%) and Planck [511]. CIB induces a strong suppression of γ-ray signals at very high energies ($\sim 100\,$TeV). Unfortunately, extragalactic sources tend to exhibit spectral cutoffs before reaching these energies. Even in the most favourable cases, their intrinsically weak emission at these energies require exceptionally large collection areas. In addition, current generation IACTs peak their sensitivity at lower energies (in MAGIC such “sweet point” is found at few hundred GeV [204]).

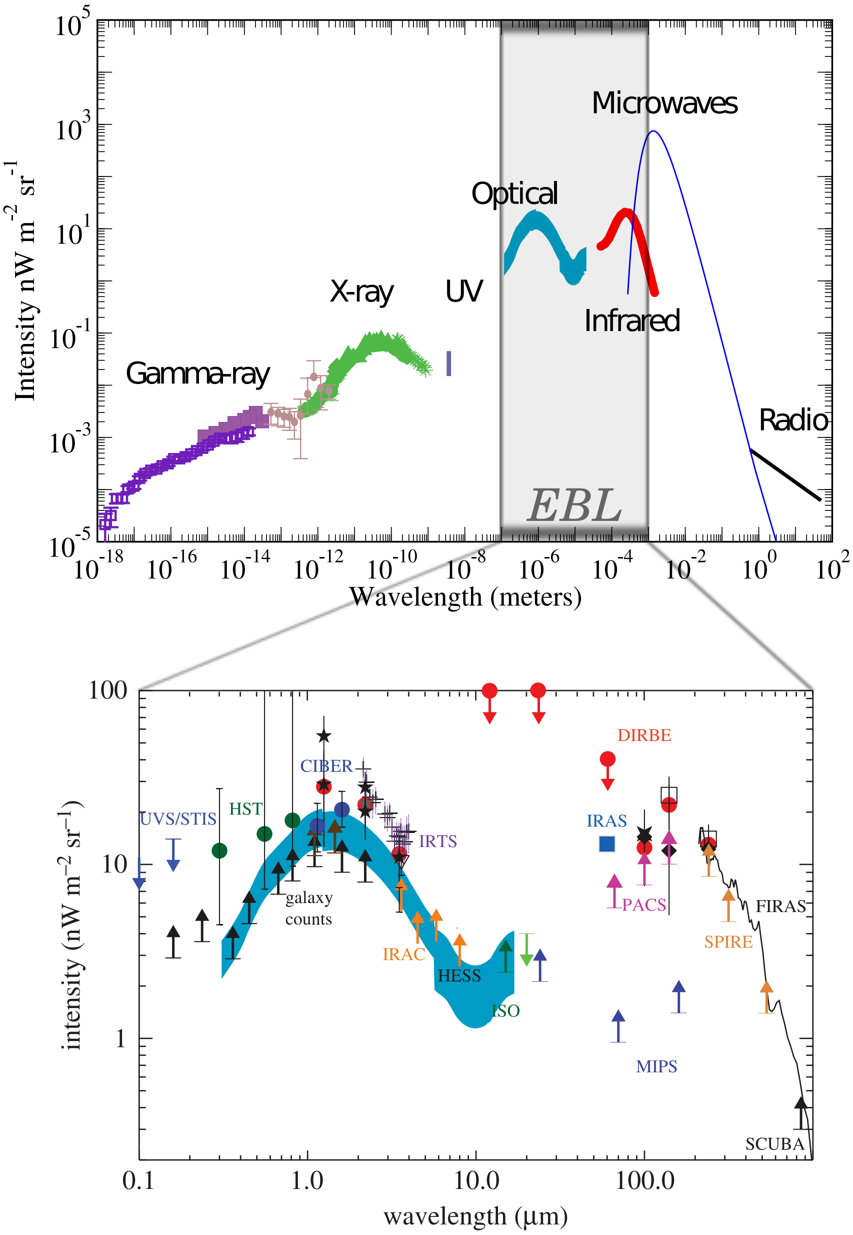

Figure 10.2: Top) Broadband spectrum of the background light. **Bottom)** Extragalactic Background Light spectrum as seen by several instruments. The shaded blue region was obtained from Abramowski et al. [428]. Adapted from [507].

10.2 Measurements

Extragalactic Background light measurements can be divided in direct and indirect measurements, but some authors tend to consider modeling predictions based in galaxy surveys as measurements as well. Direct measurements consist on those derived from galaxy counts (providing lower limits) and fluctuation measurements (model dependent), while indirect measurements are mainly derived from the absorption of γ-rays coming from distant sources through pair-production processes. Figure 10.5 summarizes the current status of EBL measurements.

10.2.1 Direct measurements

Direct measurements have the advantage of studying directly the object of interest, in this case the EBL, independently of models or assumptions. They are very challenging because EBL is actually a subdominant component of the total optical and infrared luminosity of the sky. The intensity is much lower (by a factor of ~ 100) than the corresponding one for foreground sources such as the Zodiacal Light (ZL hereafter) or the Diffuse Galactic Light (DGL). Any small systematic error in the estimation of their luminosity can thus spoil the EBL measurement by a large factor [512]. For instance, the measurements of the COB by DIRBE required a careful subtraction of stellar light (using data from 2MASS and Spitzer) [513–516].

Measurements from Earth

Some progress has been made recently to accurately characterize the atmosphere and ZL in order to measure the EBL density from Earth [517]. Bernstein, Freedman, and Madore [518–520] proposed a method to separate airglow from ZL by using the Fraunhofer lines, which are expected to be identical between the ZL and the solar spectrum (ZL is just scattered solar light) and different for the airglow, which involves other physical phenomena. There are however other complications that are also hard to deal with. Tropospheric scattered light, contrary to ON/OFF measurements of astrophysical objects, is hard to subtract as it needs to be actually estimated, taking special care in determining the fraction due to Rayleight and Mie (aerosol) scattering. The original problem of solving the expression

$$I_{\mathrm{EBL}} = I_{\mathrm{tot}} - I_{\mathrm{ZL}} - I_{\mathrm{DGL}} - I_{\mathrm{stellar}} \tag{10.1}$$

becomes, as discussed in [512, 517, 521], the more ambitious and complicated

$$\begin{aligned} I_{\mathrm{tot}}(\lambda, t, X) =& (I_{\mathrm{ZL}} + I_{\mathrm{stellar}} + I_{\mathrm{EBL}} + I_{\mathrm{DGL}})(\lambda) e^{-\tau_{\mathrm{atm}}(\lambda) X} + \\ & + I_{\mathrm{sca}}(\lambda, t, X) + I_{\mathrm{airglow}}(\lambda, t, X) \end{aligned} \tag{10.2}$$

where X is the air mass and τ_{atm} the atmospheric optical depth. The scattered component I_{sca} (Rayleight + Mie) has also 3 contributions, one from the integrated starlight, another from the ZL and the last one from the DGL.

Ground-based estimations of these components are plagued by uncertainties and biases. In the original works from Bernstein, Freedman, and Madore [518–520], results were spoiled as some components coming from the scattering of the DGL which contribute to the Fraunhofer lines were totally neglected. Mattila [512] spotted additional issues in the estimation of the different contributors to the I_{tot}, which were addressed in Bernstein [517] and Bernstein, Freedman, and Madore [522]. Among others, uncertainties in I_{ZL} were significantly larger in the revised analysis. After these corrections are taken into account, the hint of EBL discovered was about $1-2\,\sigma$, hampered by the lack of accurate estimations on I_{ZL} with the required $\lesssim 1\%$ uncertainties. The end result is that direct measurements from Earth based on surface photometry are still not competitive with the more constraining galaxy counts [518].

Measurements from space

The Imaging Photopolarimeter (IPP) on board the Pioneer 10/11 was probably the first one with adequate capacities for measuring the cosmic optical background from space [508]. When the atmosphere is removed from the equation, the airglow problem is immediately gone, as it is the atmospheric scattering. The ZL remains a critical issue up to heliocentric distances of $\sim 2\,\mathrm{AU}$ but reduces its intensity significantly further away. In the measurement available at $R = 2.41\,\mathrm{AU}$, ZL intensity went down to $\lesssim 10\%$ of the corresponding one at $R = 1\,\mathrm{AU}$. At $R = 3.26\,\mathrm{AU}$, it was no longer detectable from IPP [523]. The bulk of ZL is also confined at $< 30°$ of the ecliptic plane [524]. With this in mind, Eq. 10.1 then becomes

$$I_{\mathrm{EBL}} = I_{\mathrm{tot}} - I_{\mathrm{DGL}} - I_{\mathrm{stellar}} \tag{10.3}$$

With the help of star catalogs [525–527], which had a limiting magnitude of $R \sim 20\,\mathrm{mag}$ extrapolated to $R \sim 32\,\mathrm{mag}$ using models from [528], Matsuoka et al. [508] managed to subtract starlight from the IPP images. Following [517, 518], the contribution from the DGL could be estimated from its correlation with the diffuse far-IR emission from interestellar dust. The later was measured in [529] using data from IRAS and the Diffuse Infrared Background Experiment (DIRBE, on board COBE). The resulting calibration read

$$I^{\mathrm{optical}}_{\mathrm{diffuse}} = I_{\mathrm{DGL}} + I_{\mathrm{COB}} = a_d(I^{100\,\mu\mathrm{m}}_{\mathrm{diffuse}} - I^{100\,\mu\mathrm{m}}_{\mathrm{CIB}}) + I_{\mathrm{COB}} \tag{10.4}$$

where $I^{100\,\mu\mathrm{m}}_{\mathrm{CIB}} = 0.78 \pm 0.21\,\mathrm{MJy\,sr^{-1}}$ [530]. Note that these values were later revised by other authors without updating the $100\,\mu$m map that was extracted from Schlegel, Finkbeiner, and Davis [529], although as they had already pointed out, this map might include residual ZL, which in turn would spoil the estimation of I_{COB}.

Ignoring this caveat, Matsuoka et al. [508] obtained $I^{0.44\,\mu\mathrm{m}}_{\mathrm{COB}} = 7.9{\pm}4.0\,\mathrm{nW\,m^{-2}sr^{-1}}$ and $I^{0.64\,\mu\mathrm{m}}_{\mathrm{COB}} = 7.7 \pm 5.8\,\mathrm{nW\,m^{-2}sr^{-1}}$ after including systematic uncertainties. An interesting side result comes from the comparison of this result to the galaxy counts lower limits. In total, $60-90\%$ of the diffuse light at $0.44\,\mu$m of the flux is resolved in discrete galaxies in the Hubble Deep Field (HDF), while in the $0.64\,\mu$m band, the percentage goes up to about $80-100\%$. The main conclusions is that normal galaxies contribute to the bulk of the COB, and little room is left to other populations such as AGNs ($10-20\%$) [531].

Zemcov et al. [532] recently translated the method to NASA's New Horizons spacecraft using the Long Range Reconnaissance Imager (LORRI, [531]), imaging 4 fields (2 pointing to the minor planets Haumea and Chariklo at ecliptic angles of $\sim 30°$, while the other 2 had Neptune as a target). The main advantage of this camera over a scanning photometer such as the IPP on board the Pioneers is that due to its point source sensitivity and angular resolution, it can resolve many of the sources that needed to be modelled for IPP and therefore obtain a cleaner background. The total brightness measured in one of the LORRI images is the sum of:

$$I_{\rm meas} = I_{\rm IPD} + [I_{\rm stellar}^{\rm resolved} + I_{\rm stellar}^{\rm residual}] + I_{\rm DGL} + \epsilon I_{\rm COB} + I_{\rm inst} \tag{10.5}$$

In this formula $I_{\rm IPD}$ includes the effect of all interplanetary dust (not only zodiacal light, but beyond it), ϵ is an efficiency factor that makes up for the possibility of COB light being absorbed by Galactic dust and I_{inst} accounts for the instrument background. In general, stellar light can be split in resolved stars and unresolved/residual stellar light. Except for the resolved stellar light, the rest of the contributors can have an isotropic component, being this the main limitation of the technique. An important difference with respect to the Pioneer probes is that $I_{\rm IPD}$ could be neglected due to the careful pointing selection, concluding that any residual ZL had a negligible effect on the COB intensity estimation.

Zemcov et al. [532] concluded that $I_{\rm COB} = 4.7 \pm 7.3({\rm stat.})^{+10.3}_{-11.6}({\rm sys.})\,{\rm nW\,m^{-2}sr^{-1}}$ and a 2σ upper limit of $I_{\rm COB} < 19.3\,{\rm nW\,m^{-2}sr^{-1}}$, with a high likelihood of improving this result once LORRI is beyond the orbit of Pluto.

In reality, these measures can formally be considered only upper limits because clumps of circum-planetary dust around Neptune and around the minor planets may exist and reflect data which would be seen by the LORRI camera.

Anisotropy measurements

Extragalactic Background Light anisotropy measures have demonstrated to be a successful alternative to direct CIB measurements, which are plagued with uncertainties. In addition, the study of fluctuations of the intensity at large angular scales is interesting itself because they are thought to be caused by clustering of galaxies, which is a tracer of the underlying distribution of dark matter in the Universe. It can also probe the emission from the epoch of reionization (EOR) galaxies, direct-collapse black holes that formed during the EOR and finally stars stripped out from their original galaxies during tidal interactions (intra-halo light).

Using the specially designed *Cosmic Infrared Background Experiment* (CIBER), Zemcov et al. [533] managed to measure CIB anisotropy, which was found to be comparable to the integrated galaxy light derived from galaxy counts. The authors ruled out Zodiacal Light, Diffuse Galactic Light and fluctuations from faint stars as a possible source for such level of anisotropy. The first were discarded by observing

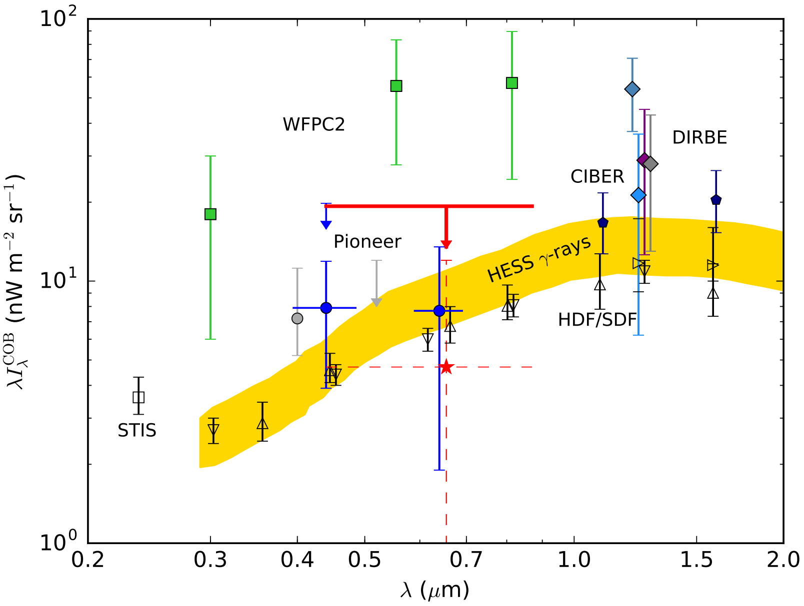

Figure 10.3: Cosmic Optical Background measurements from several experiments, including: Direct measurements from Pioneer 10/11 (blue filled circles, statistical errors only) and the New Horizons probe (red filled circles). Open points denote lower limits from galaxy counts, green squares measurements from HST-WFPC2, grey circles show estimations using the "dark cloud" method. DIRBE and 2MASS measurements are shown in diamonds and black pentagons are values inferred from CIBER. Finally, HESS indirect measurements is shown as a gold-colored region. Adapted from [532].

the same fields with 17 months time difference and through different lines of sight, yielding similar results. DGL, as measured by the IRAS satellite at 100 μm, was not bright enough to account for the level of anisotropy either. The effect from faint stars, not masked out using the 2MASS J- and H-band catalogs, was tested using the UKIDSS-UDS stellar catalog. This catalog is complete to $J = 24.9$ and $H = 24.2$ and accounts for $\gtrsim 99.9\%$ of the integrated light from stars. The results are also not consistent with linear galaxy clustering models, direct-collapse black hole models and first light galaxies. It could be easily explained however by tidally stripped stars (intra-halo light). If true, such wandering stars are responsible of a significant fraction of the total light in the Universe.

Dark cloud method

Differential photometry has been also applied successfully in [534, 535]. The method, shown schematically in Figure 10.4, was already explained in 1976 by Mattila [536] and exploits the idea of using a dark molecular cloud (an optically thick and relatively close galactic astrophysical object) that obscures and screens out the COB light, which has an extragalactic origin. Since comparing the brightness of the nebula with the surrounding optically thin neighbourhood is a relative measurement, it has the advantage that there is no need to model individually all the components (ZL,

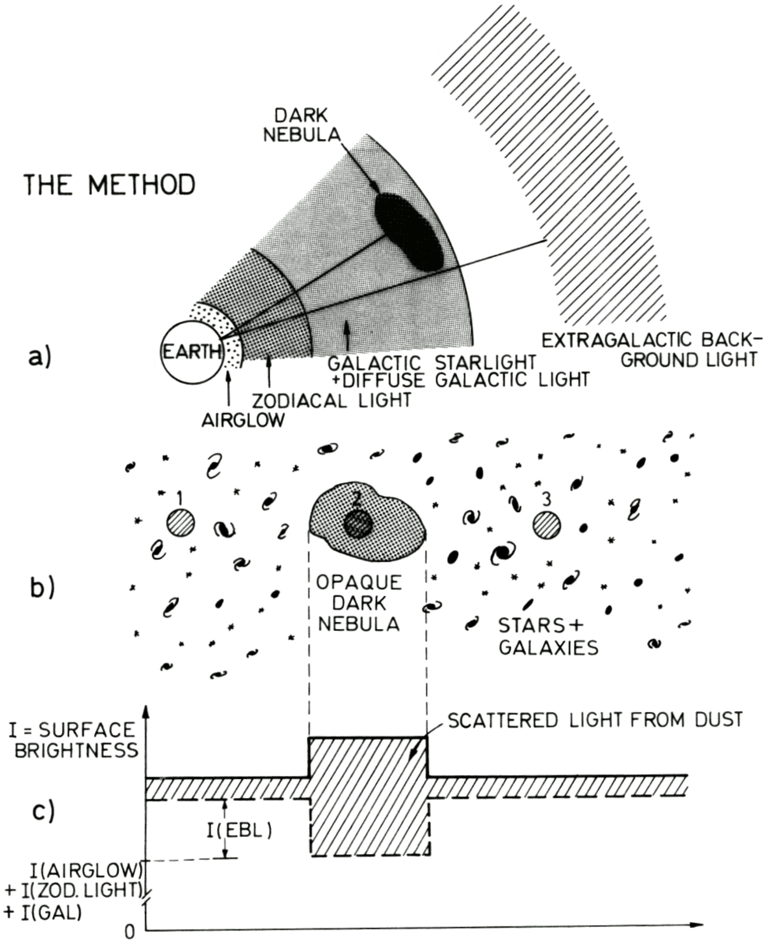

Figure 10.4: Adapted from [534]. Dark cloud method basic schema. **a)** schema showing two different lines of sight. The first is the direction of dark nebula, which blocks the background radiation (that is emitted from the EBL and part of the galactic star light). ***b and c)*** contributions to the total surface brightness from different components: airglow, zodiacal light, galactic and scattered light from dust.

airglow, part of the DGL). Using this robust technique, the difference in surface brightness between the obscured cloud and the unobscured surrounding sky is either due to the COB or the starlight that is diffused in the cloud by its dust content. To distinguish between COB and scattered starlight, spectroscopy is employed. One can expect not only Fraunhofer lines in the latter, but also a characteristic discontinuity at 400 nm. The EBL, on the other hand, is the sum of light from many different astrophysical objects at a variety of redshifts and should behave smoothly.

The resulting EBL intensity in the 381 − 432.5 nm band is $I_{\mathrm{EBL}} = 11.6 \pm 4.4\,\mathrm{nW\,m^{-2}sr^{-1}}$, while at $\sim 430\,\mathrm{nm}$ and $\sim 520\,\mathrm{nm}$ it is of $I_{\mathrm{EBL}} \leq 20.0\,\mathrm{nW\,m^{-2}sr^{-1}}$ and $I_{EBL} \leq 23.4\,\mathrm{nW\,m^{-2}sr^{-1}}$ respectively. Systematic uncertainties (multiplicative errors based on spectrophotometric calibration error, uncertainty in the blocking factor and wavelength dependence of I_{EBL}) are of $+20\%/-16\%$ in all cases.

Galaxy counts

Galaxy counts in very deep images can also be used to constraint the EBL density [531, 537–539]. The fluxes of these galaxies are measured in multiple wavelength bands to derive their total luminosity, which correspond to a strict lower bound on the integrated extragalactic background light.

Note however that there might be undetected sources that still give a non-negligible contribution to the EBL no matter how deep the survey is. This would be the case of low-surface-brightness Galaxies (whose contribution is expected to be of $< 20\%$), but also Intracluster and Intragroup light coming from tidally stripped material. Both would contribute to the optical component of the EBL with up to $\sim 50\%$ and 35% respectively [539]. Their contribution to the IR is negligible as the highly ionizing UV photon fields would evaporate any environmental dust. In addition, uncertainties due to extended galaxy tails with dim surface luminosities might be always present in these measurements.

Galaxy counts results have traditionally been in reasonably good agreement with other direct measurements in the CIB, with a 25% discrepancy that can be explained with extrapolations of the source counts plus contribution from lensed systems [540–543]. This can give additional constraints to the low-surface-brightness galaxies for instance if one assumes that their dust content is comparable to the one of normal spiral galaxies. Recent stacking analysis techniques [544] have revealed up to 90% of resolved sources, being the majority of them dusty Star Forming Galaxies (SFGs) at high redshifts ($z > 1$) [507].

This is not the case for the COB, were differences can be of a factor of $\gtrsim 5$ between galaxy counts and direct measurements, meaning that either Galaxy counts are missing a significant portion of the EBL radiation field or the foreground components of direct measurements are not correctly estimated. Agreement is better though with indirect measurements from blazar GeV–TeV spectra [425, 428], indicating that many direct measurements based on surface photometry are probably overestimating the EBL density by not accounting correctly for the foregrounds that exist in their measurements.

10.2.2 Indirect measurements

As opposed to the direct measurements, where the primary goal is to measure the EBL itself (or the directly detectable part of it using galaxy counts), indirect measurements exploit the fact that any particle traveling through the Universe can interact with background photon fields such as EBL.

One of the best examples of this is the observation of the γ-ray emission from blazars at cosmological distances. The phenomena was already described in the 60s by Nikishov [545] and Gould and Schréder [546] and basically consists on the interaction between two photons of energies ϵ and E which, if the product of their energies is above a certain threshold, creates a pair of particles (typically electron-positron). The total cross section of an interaction of the form $\gamma+\gamma' \to e^{+}+e^{-}$ can be written [545–547] as

$$\sigma_{\gamma\gamma}(\beta) = \frac{3\sigma_T}{16}(1-\beta^2)\left[(3-\beta^2)\ln\left(\frac{1+\beta}{1-\beta}\right) - 2\beta(2-\beta^2)\right] \tag{10.6}$$

where $\beta = (1-1/s)^{1/2}$, $s = (\epsilon E/2m^2c^4)(1-\cos\theta)$, $\sigma_T = \frac{8}{3}\pi r_0^2$ is the Thomson cross section and $r_0 = e^2/mc^2$ is the classical electron radius. For a head-on photon collision ($\theta = \pi$) the energy threshold (condition for which $s \geq 1$ or alternatively $\beta^2 \geq 0$) is $\epsilon E = m^2c^4$. The optical depth $\tau(E_0, z_0)$ that a γ-ray encounters is given by [548]

$$\tau(E_0, z_0) = \int_0^{z_0} dz \frac{\partial L}{\partial z}(z) \int_0^{\infty} d\epsilon \frac{\partial n}{\partial \epsilon}(\epsilon, z) \int_{-1}^{1} d\mu \frac{1-\mu}{2} \sigma_{\gamma\gamma}[\beta(E_0, z, \epsilon, \mu)] \tag{10.7}$$

where $\mu = cos\theta$ (θ being the angle between the two photons), $\partial n/\partial\epsilon$ is the density of EBL photons per energy interval and

$$\frac{\partial L}{\partial z} = \frac{c}{H_0}\frac{1}{(1+z)\sqrt{\Omega_\Lambda + \Omega_M(1+z)^3}} = \frac{c}{H_0}\frac{\partial l}{\partial z}$$

Following Biteau and Williams [548], The last integral of 10.7, referred to the integration of the angle between photons can be analytically calculated, simplifying the expression as

$$\tau(E_0, z_0) = \frac{3}{4}\frac{\sigma_T c}{H_0} \int_0^{z_0} dz \frac{\partial l}{\partial z}(z) \int_0^{\inf} d\epsilon \frac{\partial n}{\partial \epsilon}(\epsilon, z) \frac{1}{(1+z)^2} \left(\frac{m_e^2 c^4}{E_0 \epsilon}\right)^2 P(\beta_{max}) \tag{10.8}$$

where $\beta_{max}^2 = 1 - \frac{m_e^2c^4}{E_0\epsilon}\frac{1}{1+z}$ and $P(x)$ is a particle-physics kernel given by

$$\begin{aligned} P(x) = & \ln^2 2 - \frac{\pi^2}{6} + 2\mathrm{Li}_2\left(\frac{1-x}{2}\right) - \frac{x+x^3}{1-x^2} + \\ & + (\ln(1+x) - 2\ln 2)\ln(1-x) + \\ & + \frac{1}{2}(\ln^2(1-x) - \ln^2(1+x)) + \frac{1+x^4}{2(1-x^2)}\ln\frac{1+x}{1-x} \end{aligned} \tag{10.9}$$

This could be further simplified if one assumes approximations such as a decoupled evolution and spectrum of the EBL. With this in mind, the impact of the EBL on a given extragalactic source spectrum can be calculated if one assumes the cosmology (values of H_0, Ω_Λ and Ω_M), the EBL spectrum $\partial n/\partial\epsilon$ and if the redshift is known.

Indirect measurements based on γ-ray spectra can be subdivided in model-dependent estimations (the EBL spectral shape is fixed to a particular EBL model) and model-independent estimations (EBL spectral shape is left free or generated using grids, splines, etc).

The advantages of the first group is the robustness of the minimization. Typically only a global scaling factor of the EBL spectrum is left free, and the method exploits observational information (if the model is empirical). The main drawback is the lack of an easy way to test the spectral shape of the EBL.

Important works have been made around this idea. Probably one of the best known publications presented the discovery of VHE emission from FSRQ 3c 279 with MAGIC [549, 550]. The fact that a source at a distance of $z = 0.536$ could be detected with a VHE instrument directly ruled-out many models which predicted large γ-ray attenuations. Low density models, which were close to galaxy count measurements, were the only ones that could give a reasonable de-absorbed spectra. These measurements however were only useful to set upper limits on the EBL density. On one hand, the detection was not significant enough and gave large uncertainties in the spectrum. On the other hand, 3c 279 is an FSRQ and thus it is expected to exhibit intrinsic absorption (such as the one described for B0218+357 and PKS 1441+25. As a result, the usefulness of 3c 279 in EBL measurements is limited.

The *Fermi*-LAT collaboration was particularly successful in exploiting simultaneous multi-blazar modeling to constrain the EBL density [425]. Its value was estimated statistically from the overall absorption of γ-rays on the blazar sample above a certain energy. An assumption on the blazar spectrum was made by modeling these sources with Log Parabola spectral shapes from $1 - 500\,\mathrm{GeV}$. This could be validated in the first redshift bin ($z < 0.2$) where EBL absorption is thought to be nearly negligible in the most part of the *Fermi*-LAT energy band.

The second milestone regarding indirect measurements was done in [428] by the H.E.S.S collaboration. They followed the *Fermi*-LAT recipe of using not one but a collection of sources to be fitted and analyzed together, but in this case as the energy range is higher the sources were all closer ($z_{max} = 0.188$, 1ES 0347-121). Again, recent low-intensity models such as [431, 550] managed to reproduce the observed blazar spectra and the data disfavoured high-density EBL models.

The second group of measurements are more versatile and computationally easy in terms of directly estimating the EBL spectrum, as no model-based constraints are in place. The variables used to characterize the spectrum are however harder to interpret physically and the EBL evolution is under-constrained. An example of this approach is presented in [548, 551].

In this work, the results are obtained following a model-dependent analysis of the EBL inspired by Ahnen et al. [430]. In order to allow for possible EBL spectral discrepancies with the proposed models, the EBL spectrum is divided in wavelength bins and scaled with independent scaling factors, providing some of the advantages of the second group of measurements while maintaining the simple interpretation of the first group.

10.3 Models

The indirect EBL measurements described in chapter 11 are based on the assumption of an EBL spectrum, which is connected to the γ-ray opacity as a function of energy and blazar redshift. Several EBL models have been proposed in the last years, and some of them are shown in Figure 10.5. They are based on different schemes, which are summarized in what follows.

10.3.1 Forward evolution

Forward evolution models begin with cosmological initial conditions and model processes such as gas cooling, dark matter halo merging, hierarchical galaxy formation (including stars and AGNs), their SEDs, feedback processes, light absorption and re-emission by dust. From this, they estimate EBL density and its evolution with redshift [552]. An improved treatment of dust absorption and re-emission of starlight together with fine tuning of the cosmological input with new data from WMAP has been one of the main goals of this approach since the initial work by Primack et al. [552], resulting in recent models by Gilmore et al. [433], Inoue et al. [434], and Somerville et al. [553].

One of the advantages of this method is that their modeling of physical processes uses information of how the Universe evolves through key parameters such as the star formation history (SFH) and the initial mass function (IMF). They end up with observables that can be tested and validated, such as properties of galaxies in the known Universe ($0 \leq z \lesssim 6$) and the density of EBL, which can then be compared with direct measurements and checked with the observed high energy blazar spectra [552].

10.3.2 Backward evolution models

These models begin with the present day galaxy luminosity function (LF), a measurement of the number of galaxies per luminosity interval, and trace its time evolution by assuming a dependency on the redshift. One of the first estimations of the EBL density with this method was done by Malkan and Stecker [554], where IR luminosity functions from IRAS were extrapolated backwards in redshift using power law functions. The idea was improved by Stecker, Malkan, and Scully [555, 556]. One of the main issues that these models need to deal with is estimating the contribution from starburst galaxies, with greater impact in the total luminosity as the redshift increases. One of the most complete works that attempted to overcome this problem was given in Franceschini, Rodighiero, and Vaccari [431], where an extended set of data was used to account for galaxy morphology in their evolutionary schemes, including early and late-type galaxies with data available in the interval $0 \leq z \leq 1.4$. The starburst and irregular populations were introduced using only optical and local LFs, with extrapolations of all components to higher redshifts. The total emissivity was estimated using synthetic SEDs.

10.3.3 Galaxy evolution models

This family of models can be subdivided depending on how the evolution is considered. The first group infers it over a range of redshift from observations of quantities such as the SFR density of the universe, while the second directly observes it. They both have profited significantly from the advent of large-scale ground and space-based surveys at IR and UV.

The first steps of the inferred evolution family of models were done using HST and ISO data by Madau, Pozzetti, and Dickinson [557]. They used a simple stellar evolution model defined by a time-dependent SFR per unit comoving volume and an

IMF extending in the range $0.1 - 125 M_\odot$ was used to trace the evolution with cosmic time of the galaxy luminosity density. Pei, Fall, and Hauser [558] and Franceschini et al. [559] refined it by introducing chemical enrichment in Ly-α systems.

The idea was continued by Kneiske, Mannheim, and Hartmann [560], who parametrized the EBL and γ-ray attenuation in terms of the SFR density. Minimal background models were then introduced by Finke, Razzaque, and Dermer [432], Kneiske and Dole [561], and Razzaque, Dermer, and Finke [562] taking into account the SFR, IMF, dust extinction and modelling of stars and dust grains as a sequence of black bodies.

Finally, Domínguez et al. [409] was the first model of its class, studying directly the galaxy evolution up to redshift $z = 4$ using observations of the luminosity function in the K-band together with the distribution of 25 galaxy SED types with redshift. The idea was to use two galaxy catalogs. The first, AEGIS, has multiwavelength photometry available for 6000 galaxies in the redshift range $0.2 - 1.0$. The second, from Cirasuolo et al. [563] (C10) has K-band galaxy LF up to redshift 4 and is used to count galaxies (and its luminosity function) as a function of redshift.

The galaxy sample and LF were divided in 3 K-magnitude bins and a SED-type that depends on the redshift is statistically assigned to each galaxy in each bin. The statistical distribution of SED types and its dependency with redshift and K-band magnitude was obtained by fitting the AEGIS sample to a set of 25 types of galaxies from the SWIRE library. Since SWIRE has only LOCAL-type galaxies and AEGIS extends only up to $z = 1$, assumptions must be made to extend this galaxy-type composition further away. Two possibilities were proposed, being the first (fiducial) assuming that the composition is ‘frozen’ beyond $z = 1$. Alternatively, an upper bound based on the assumption that the number of starburst galaxies grows linearly with redshift was considered, accounting for up to 60% of galaxies at $z = 2$ and then freezing the composition beyond that distance.

The stellar population of a given galaxy, and its evolution with time, is then studied by fitting templates from Bruzual and Charlot [564], which also helps to estimate absolute magnitudes which are used together with Cirasuolo et al. [563] to calculate the absolute normalization of the light emitted by galaxies and thus the EBL.

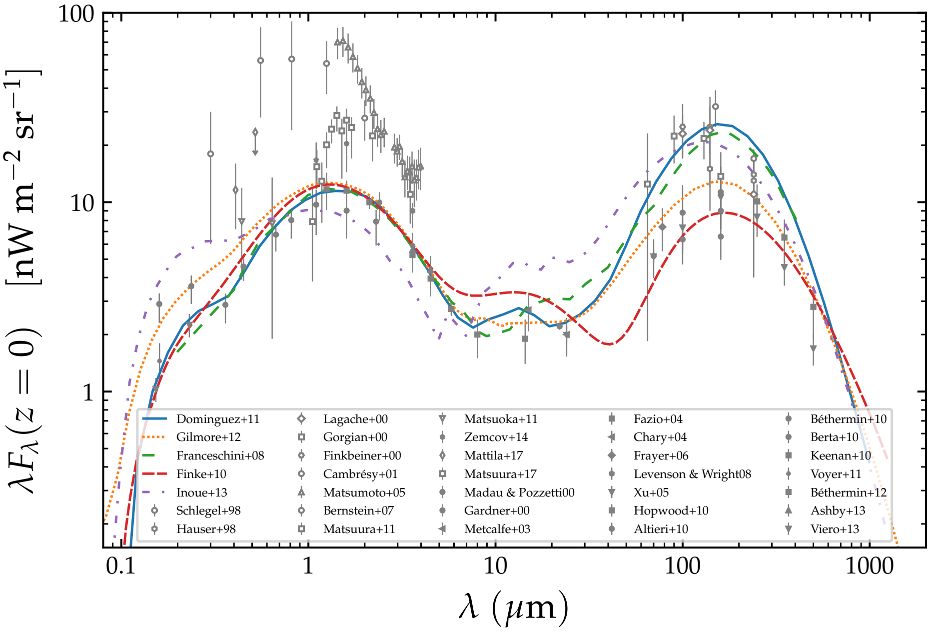

Figure 10.5: EBL models based different approaches. Direct EBL measurements (open gray symbols) and galaxy counts (filled gray symbols) covering the COB and CIB are shown for reference.

11

EBL studies with MAGIC and Fermi-LAT

Contents

In this work, a significant effort to collect and analyze promising MAGIC and *Fermi*-LAT data to constraint the EBL density in the optical wavelength range is presented. Assuming that simple analytical shapes can describe the intrinsic spectra and that the EBL can be written down in terms of models with one or more optical depth scaling factors α_i, constraints to the total absorption of the EBL are obtained and discussed.

11.1 Introduction

As explained in section 10.2.2, optical and infrared photons from the Extragalactic Background Light can interact with Very High Energy γ-rays through pair production processes. The observed spectra can then be written down as

$$\left(\frac{dF}{dE}\right)_{\text{obs}} = \left(\frac{dF}{dE}\right)_{\text{int}} \times e^{-\tau(E,z)} \tag{11.1}$$

where $\tau = \tau(E, z)$ is the energy and redshift-dependent optical depth of the process and $\left(\frac{dF}{dE}\right)_{\text{inst}}$ is the intrinsic spectrum of the source.

The problem to determine $\tau(E, z)$ with this approach is that the intrinsic spectrum of a given blazar is unknown, as the source emission is already absorbed by the EBL when it reaches us. Additionally, the observed spectrum is further distorted at the detection and reconstruction phase (instrument limitations, event reconstruction errors, atmospheric transmission and scattering). Furthermore, the redshift is unknown for some sources (often the case for HBL and their featureless optical spectra). For other sources like FSRQs, their spectra is expected to contain intrinsic absorption features which are hard to separate from EBL-induced absorption. Besides, VHE γ-ray spectra change from source-to-source and a compromise between freedom in the intrinsic spectral shapes and discrimination power for EBL absorption has to be reached. Finally, if more than one instrument is used to reconstruct the spectrum, the datasets are often not strictly simultaneous (source activity may have changed) and the instruments may lack proper cross-calibration.

The main ideas that have been employed so far to overcome these issues are:

- Extend the spectral shape observed at lower energies (typically with *Fermi*-LAT), believed to be unabsorbed. This requires a precise cross-instrument calibration, assumes that HE and VHE photons are generated by the same population of particles and completely ignores possible cutoffs and spectral breaks.
- Assume that the spectrum at VHE cannot be harder than in HE. This simple assumption, while robust, can only give us upper constraints on the EBL density and is only useful when there is little curvature in the intrinsic spectrum.
- Assume that the spectral index cannot be harder than a given value (for instance $\Gamma_{max} \sim 1.5$), based on the current understanding of particle acceleration mechanisms [424].
- Search for spectral features that are thought to be unnatural to blazar spectra, but explainable by EBL absorption. This approach, while shown powerful in some cases [430], can only be applied to very detailed spectra that extend well into the TeV energies in sources at intermediate redshifts ($0.1 \lesssim z \lesssim 0.4$).

The first two ideas are implemented by forcing the spectrum to be a concave function (i.e. spectrum becomes steeper with increasing energy). The third, to be effective, requires hard observed spectra. The last idea has been used in one case in MAGIC so far, but it is promising for more sensitive future facilities such as CTA.

11.2 Method

Up to now, EBL density constraints with MAGIC have been discussed for individual sources (see e.g. chapters 7 and 8). Nevertheless, from Ackermann et al. [425], Abramowski et al. [428], and Biteau and Williams [548] it is clear that the main strength of the indirect γ-ray method lies on the use of large blazar samples at different redshifts to counteract the uncertainties in the individual blazar intrinsic spectra. On one side, it provides statistics at different optical depths. On the other hand, it serves as a test for the intrinsic spectral shapes suggested for these blazars. At the same time, Ahnen et al. [430] shows that precise modeling of the instrument response functions (IRFs) is instrumental to avoid systematic effects. It also allows to exploit spectral features with a statistical accuracy which the unfolded (and correlated) HE and VHE γ-ray spectra simply cannot provide. In this chapter, a combination of both approaches is presented to derive robust and statistically significant measurements of the EBL density. Each blazar spectrum is assumed to be reproduced by an analytical shape, which depends on a number of parameters. Then, the spectrum is absorbed using the EBL spectrum. Contrary to Lorentz, Brun, and Sanchez [565], the assumed EBL shape used to absorb the spectra is adapted from a theoretical model and scaled with one or more optical depth scaling factors.

$$\left(\frac{dF}{dE}\right)_{\mathrm{obs}} = \left(\frac{dF}{dE}\right)_{\mathrm{int}} \times e^{-\sum_i \alpha_i \tau_i(\lambda_i, E, z)} \tag{11.2}$$

The resulting absorbed spectrum is compared with the observed data to derive the likelihood of the fit as a function of the EBL scaling factors (α_{λ_i}) and intrinsic shape parameters. This step is done using the full MAGIC IRFs to convert the absorbed spectrum into number of excess events per energy bin.

11.2.1 Profile Likelihood

Modeling multiple blazar spectra at the same time with different shape complexities requires dealing with many parameters that need to be optimized simultaneously. The Marginal Likelihood in such a case would be computationally challenging to calculate. Instead, this work uses the comparatively simpler Profile Likelihood [207]. The main advantage of the Profile Likelihood is that spectral parameters are treated as nuisance parameters. They are fit within the minimizing routine for each value of the EBL scaling, but the full parameter space does not need to be scanned.

The statistical hypotheses that are being tested are:

- Null hypothesis (H_0): the suggested spectral analytical shape provides an adecuate description of the observed spectrum, no improvement in the fit is achieved by including EBL attenuation.
- Alternative hypothesis (H_0): the suggested spectral analytical shape cannot give an acceptable description of the observed spectrum, but it reproduces the

spectrum once the EBL attenuation (with $\tau = \alpha \times \tau_{\mathrm{Model}}(E, z)$ derived from a given EBL model) is taken into account.

The actual likelihood value calculation is explained in section 11.2.2. The EBL density constraints are obtained with the following procedure:

1. For each source, and given an intrinsic spectral shape, a scan over reasonable values of α (from $\alpha_{min} = 0$ to $\alpha_{max} = 2.5$) is done by maximizing the likelihood over all the nuisance parameters (spectral shape) in each step of the scan.

2. The procedure is repeated for a variety of possible spectral shapes that may reproduce the observed data. The model that provides a better overall fit and most conservative discrimination power is preserved. The details of the best shape selection are described in section 11.2.4.

3. The Likelihood Ratio Test (LRT) profiles are computed by comparing the likelihood of the no-EBL ($\alpha = 0$) case with the likelihoods of the alternative ($\alpha \neq 0$) cases.

4. The LRT profiles of the different blazar spectra are stacked (summed).

5. The procedure is further repeated for different EBL models from the bibliography.

11.2.2 Software implementations

In order to automatize part of these steps, we have developed two independent software packages to statistically explore the agreement of EBL absorption models with observed γ-ray data.

Classical/blind approach: `eblfitter`

The first program is `eblfitter` and it was developed in `Python` by the author of this work. It was written to reproduce classical model-dependent EBL tests done in the VHE world, being compatible with basically any set of data that can be found in the bibliography. It uses SED points coming from a CSV file. By assuming gaussian errors, the likelihood maximization becomes a χ^2 minimization procedure. Furthermore, archival data could be added without difficulties [548]. The following drawbacks are however identified:

- Spill-over (energy migration) calculations are model-dependent (risk of introducing a bias) and can be difficult to compute for very steep spectra. Spectral points for such sources may have very large systematic uncertainties.
- Selection bias is almost unavoidable. Positive statistical fluctuations may create a point where otherwise there would be an upper limit. Negative statistical fluctuations may remove legit data points and show upper limits instead.

- Upper limits are difficult to correctly integrate in the likelihood calculation. Moreover, in MAGIC they are computed using the Rolke method [566], meaning that the quoted bounds no longer follow the simple Poissonian or Gaussian distributions that are used to build the rest of the error bars. If non-detections are ignored, the result might be strongly biased.

Correct 'full-IRFs' approach: `fitebl`

The second program is called `fitebl`. It was written in `ROOT/C++` by Dr. Abelardo Moralejo as part of the standard `MARS` package. Contrary to `eblfitter`, it fully includes the MAGIC-IRFs using a forward folding approach.

The code begins by assuming a given spectral shape for the intrinsic spectrum which depends on a number of nuisance parameters. The intrinsic spectrum is presented as a function of the true energy of the events. Then, `fitebl` absorbs the spectrum with a scaled γ-ray opacity ($\alpha_i \tau_i(E, z)$) derived from a model. The resulting absorbed spectrum (still as a function of the true energy) is convoluted with the MAGIC-IRFs, which consist on effective area estimations and an energy migration matrix. The effective area serves to calculate the number of excess events from a given flux, while the energy migration matrix connects the true energy of the events with the (estimated) energy reconstructed by MAGIC. Finally, the Poissonian likelihood is calculated for each energy bin using the previously computed excess events, a number of background events (nuisance parameters) and the given ON and OFF observations:

$$L(ebl, \theta_1, \theta_2, ..., \theta_{N_{\text{spectra}}}) = \prod_{i=1}^{N_{\text{spectra}}} \prod_{j=1}^{N_{\text{bins,i}}} L_{ij}(ebl, \theta_i) \tag{11.3}$$

where each θ_i is the list of parameters for the intrinsic spectrum i and ebl the parameters of the EBL model (scaling factors). Each factor L_{ij} has the form:

$$\begin{aligned} L_{ij}(ebl, \theta_i) = Poisson(g_{ij}(ebl, \theta_i) + b_{ij},\ N_{\text{on},ij}) \times \\ Poisson(b_{ij},\ N_{\text{off},ij}) \end{aligned} \tag{11.4}$$

Here $g_{ij}(ebl, \theta_i)$ denotes the γ-ray like excess predicted from the model and b_{ij} the background signal (nuisance parameters).

11.2.3 Fermi-LAT data

Fermi-LAT data can in principle be used to further constrain the spectral shapes that are being used to model the intrinsic blazar spectra. However, in many cases the simple functions that we have considered are no longer a good approximation of the true spectrum. In addition, *Fermi*-LAT spectral points are correlated and it is not statistically correct to use directly the data points coming from the instrument.

The most natural way to avoid the last problem is extending the forward folding to the *Fermi*-LAT band and using the full *Fermi*-LAT IRFs. This problem, while easy to define, is computationally expensive to solve as the resulting *Fermi*-LAT's source model needs to incorporate other components in the field of view (additional sources and diffuse Galactic and isotropic components). The large amount of free parameters to minimize makes the method too slow and the profile likelihood is no longer operative.

An alternative possibility is to simplify each *Fermi*-LAT spectrum to a Power Law, characterized by two variables: the flux and the spectral index at a given decorrelation energy. They are added to the total likelihood (Eq. 11.4) assuming Gaussian errors:

$$L_{ij} = L_{ij,\mathrm{MAGIC}} \times \exp\left\{-\frac{1}{2}\left(\frac{\Gamma-\Gamma_{\mathrm{LAT}}}{\Delta\Gamma_{\mathrm{LAT}}}\right)^2\right\} \times \exp\left\{-\frac{1}{2}\left(\frac{F-F_{\mathrm{LAT}}}{\Delta F_{\mathrm{LAT}}}\right)^2\right\} \tag{11.5}$$

where Γ and F are the model predicted spectral index and flux at the decorrelation energy of the *Fermi*-LAT 'spectral butterfly' and $\Gamma_{\mathrm{LAT}} \pm \Delta\Gamma_{\mathrm{LAT}}$ and $F_{\mathrm{LAT}} \pm \Delta F_{\mathrm{LAT}}$ the observed values of both parameters with their statistical errors.

Two remarks must be done here: i) If the pivot energy is set to the energy where the relative flux errors are minimized, then the correlation between the two parameters is minimized and the assumption of independent variables approximately holds; ii) Since the pivot energy is typically $\sim 0.1 - 10\,\mathrm{GeV}$, the EBL effect can be neglected. This simplifies the calculation of the normalization flux and spectral index from models with curvature terms (e.g. Log Parabola) or sub/super exponential cut-offs (see section 11.2.4).

11.2.4 Spectral shapes

This work assumes that the intrinsic emission of the blazar in GeV–TeV energies can be approximately described by simple analytical models such as:

- **Power Law** `[PWL]`: Power Laws are the usual products of particle acceleration mechanisms and can effectively describe the observed spectrum in some particular cases.

$$\frac{dF}{dE} = F_0\left(\frac{E}{E_0}\right)^{\Gamma} \tag{11.6}$$

  In this analysis, pure `PWLs` are only permitted to calculate systematic effects due to model selection, as by allowing it we are preferentially selecting simpler models that can reproduce any curvature in the intrinsic spectrum by just assuming that the EBL opacity is larger that what it would be measured otherwise.

- **Log Parabola** `[LP]`: Modification of a pure `PWL` that introduces a smooth curvature term:

$$\frac{dF}{dE} = F_0 \left(\frac{E}{E_0}\right)^{\Gamma - \beta \log(E/E_0)} \tag{11.7}$$

If E_0 is set to the decorrelation energy, Γ provides directly the spectral index of the equivalent `PWL`.

- **Power Law with a Super/Sub-exponential-cutoff** `[EPWL/SEPWL]`: Often used to model pulsar emission in γ-rays, it introduces a non-linear modification of the PowerLaw index, characterized by a cutoff energy E_c and the cutoff index Γ_2, which can be $0 < \Gamma_2 < 1$ for a sub-exponential cutoff or $\Gamma_2 > 1$ for the super-exponential cutoff case.

$$\frac{dF}{dE} = F_0 \left(\frac{E}{E_0}\right)^{\Gamma} \times \exp\left(-\left(\frac{E}{E_c}\right)^{\Gamma_2}\right) \tag{11.8}$$

The combination of a LogParabola with a (super/sub) exponential cutoff results in **LogParabola with Super/Sub-exponential-cutoff** models `[ELP, SELP]`:

$$\frac{dF}{dE} = F_0 \left(\frac{E}{E_0}\right)^{\Gamma - \beta \log(E/E_0)} \times \exp\left(-\left(\frac{E}{E_c}\right)^{\Gamma_2}\right) \tag{11.9}$$

In our case, we will always assume the particular case of $\Gamma_2 \equiv 1$ when reconstructing the *Fermi*-LAT spectrum with this model. It provides enough accuracy in reproducing the observed data and simplifies the calculation of the equivalent `PWL` flux and spectral index at the decorrelation energy. The later is given by:

$$\Gamma' = \Gamma - \frac{E_0}{E_c} \tag{11.10}$$

where E_0 is the normalization or decorrelation energy and E_c the cut-off energy.

For the EBL analysis, super and sub-exponential cutoffs are also allowed.

Selection criteria

The selection of the best-fit model is a complicated task that often requires deciding between models of different complexity levels (number of degrees of freedom) which normally would give different likelihood scores. In this work, (astro)physical and statistical considerations are simultaneously taken into account.

Astrophysical considerations imply that pure `PWL` spectra should be discarded, as it is known that blazar spectra exhibit sooner or later spectral curvature and/or breaks. In fact, even if `PWL` plus a given scaled EBL absorption provides a good description to the observed spectrum, its sole consideration introduces a bias in the EBL density determination, as all curvature is attributed to the EBL attenuation. For "curved" spectral shapes, curvature terms are assumed to be always positive (i.e. spectra becomes steeper with energy).

Statistical considerations are mainly taken into account to avoid over-fitting the data and to provide a conservative selection of the spectral shapes. Initially, the model providing best-fit probability is selected. Given two spectral shapes with similar best-fit probability, the one predicting a flatter profile likelihood is chosen. This corresponds to selecting the model that predicts more conservative limits on EBL. Alternative selection criteria are discussed in section C.3 of the appendix.

11.2.5 Redshift uncertainties

The total γ-ray attenuation induced by the EBL depends on the redshift. This is however not always known (e.g. for PG 1553+113), but fortunately the proposed method accepts introducing it as an additional nuisance parameter. The only drawback of this approach is that there is normally an important degeneracy between redshift and the scaling factor of the EBL optical depth. In `fitebl`, any unknown redshift is scanned in the provided range and the value corresponding to the highest likelihood is selected.

11.3 Observations

The selection and analysis of a large data sample such as the one presented in this work needs extensive and careful planification. The instantaneous performances of the telescopes change over time and the IRFs depend on each particular dataset.

The sources are also intrinsically different. Some of them require very long integration times (for instance 1ES 0229+200) to achieve good statistics in both MAGIC+*Fermi*-LAT. Others have remarkable variability (e.g. Markarian 421) in the selected periods and their data needed to be divided and studied separately in very small samples. In this case, a careful selection of the corresponding *Fermi*-LAT periods is needed to achieve an equilibrium between statistics and a larger compatibility between the MAGIC and *Fermi*-LAT samples. A longer integration time would provide larger statistics and therefore a more detailed spectrum, but a too large *Fermi*-LAT integration window may also led to different average levels of activity in both bands and biased results.

Table 11.1 summarizes the observations that were used to perform the study. It includes the classification of the sources, their redshift, dates of the data acquisition and the total exposure invested in generating the MAGIC spectra. The distribution of energies covered by the spectra and redshifts for the different sources is represented in 11.1. Details of individual sources and references can be seen in appendix B.

The MAGIC observations were performed in all cases in wobble mode with a 0.4°

offset and four symmetric positions with respect to the camera center [195]. The VHE data were collected under dark conditions to minimize systematic effects and reduce the energy thresholds. The analysis was done using the standard MAGIC analysis framework `MARS` [204, 446].

The *Fermi*-LAT data were extracted from the weekly LAT data files available in the FSSC data center. For each data sample, we consider only Pass 8 source-class photons detected within 15° of the nominal position of the source. Only events whose reconstructed energy lies between 100 MeV and 500 GeV were selected. Following the event selection recommendations from Cicerone[1], we only included good data (`(DATA_QUAL>0)&&(LAT_CONFIG==1)`) with zenith distance lower than 90°. As commented before, the time-based filtering of the data was done to balance out photon statistics and systematic uncertainties due to the lack of true simultaneity with respect to the MAGIC observations.

The data were reduced and analyzed using the open-source software package `enrico` (see section 4.5.7) as a wrapper for the *Fermi* `ScienceTools` (version v10r0p5)[2]. We followed a summed binned likelihood analysis approach split in PSF event types (0, 1, 2 and 3) with 10 bins per energy decade and using the instrument response functions (IRFs) P8R2_SOURCE_V6. All the 3FGL (third *Fermi* Large Area Telescope source catalog) sources within the ROI are included in the model, along with Galactic and isotropic models using `gll_iem_v06.fits` and `iso_P8R2_SOURCE_V6_v06.txt` files respectively. The spectrum of the sources was selected in order to maximize L_{max} for $\alpha \neq 0$ (alternative hypothesis, H1) while being physically sound. Curvature terms were used in all datasets. In the simplest cases, we used a Power Law attenuated using the EBL model of Franceschini, Rodighiero, and Vaccari [431] (F08). In others, we employed functions with intrinsic curvature terms (Log Parabola or Power Law with exponential cutoffs). The spectral parameters of all sources that are significantly detected ($TS > 4$) within a radius of 3° from the source position were left free in the fit. The parameters of the rest of the sources within 10° are fixed to the published 3FGL values. We also left free the normalization of the diffuse components. Finally, the data was divided in energy bins so that the obtained spectral points in *Fermi*-LAT could be effectively compared with the corresponding spectrum in MAGIC in order to ensure a smooth transition between the spectra of both instruments. A summary of the selected *Fermi*-LAT data, including the total exposure, redshift used in the attenuated model (if applicable) and spectral shapes used can be found in Table 11.2.

11.4 Results

The main product of the Likelihood Ratio Test scan done by both `fitebl` and `eblfitter` is the a curve presenting the total χ^2 of the fit with respect to the scanning variable(s), in the simplest case the global optical depth scaling α for the

---

[1] `https://fermi.gsfc.nasa.gov/ssc/data/analysis/documentation/Cicerone/`

[2] `http://fermi.gsfc.nasa.gov/ssc/data/analysis/scitools`

Source [samples]	class	redshift	period	observation time (h)
Mrk 421 [15]	HBL	0.030	201304[10-19], 20140426	43.8
1ES 1959+650	HBL	0.048	201511[06-18]	4.8
1ES 1727+502	HBL	0.055	2015[1012-1102]	6.4
BL Lacertae	IBL	0.069	20150615	1.0
1ES 0229+200	HBL	0.14	2012-2015	105.2
1ES 1011+496	HBL	0.212	2014[0206-0307]	11.8
PKS 1510-089 [2]	FSRQ	0.361	201505[18-19], 20160531	5.0
PKS 1222+216	FSRQ	0.432	20100618	0.5
PG 1553+113 [5]	HBL	$0.43 - 0.58$	2012-2016	66.4
PKS 1424+240 [2]	HBL	0.604	2014-2015	49.1
PKS 1441+25	FSRQ	0.939	20150418-20150423	20.1
QSO B0218+35	FSRQ	0.944	201407[25-26]	2.1

Table 11.1: List of spectra used to estimate the EBL density. In brackets (first column) the number of spectra that are available for each source.

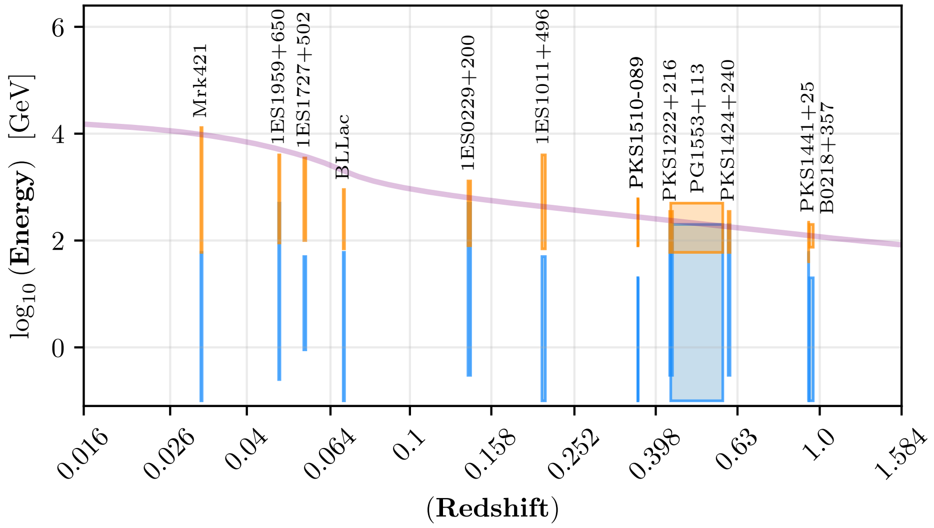

Figure 11.1: Energies covered for each source in the MAGIC (orange) and *Fermi*-LAT (blue) bands as a function of source redshift. The γ-ray horizon, defined as $\tau = 1$ in the D11 model, is plotted in purple.

Source [date]	z	TSTART	TSTOP	Exp (d)	spec.	TS
1ES0229+200 [all]	0.14	2009-11-01T00:00	2017-01-01T12:00	2200	PWL	113
1ES1011+496 [2014]	$0.0^\ddagger$	2014-02-05T12:00	2014-03-07T12:00	17.7	EPWL	425
1ES1727+502 [2015]	0.055	2015-03-29T12:00	2015-11-02T12:00	57.3	PWL	98
1ES1959+650 [2015]	0.047	2015-11-05T12:00	2015-11-18T12:00	11	LP	405
B0218+357 [2014]	0.944	2014-07-24T21:00	2014-07-26T12:00	1.37	PWL	179
BLLac [20150615]	0.069	2015-06-14T15:00	2015-06-15T03:00	0.376	PWL	26
BLLac [2015]	0.069	2015-06-14T12:00	2015-06-28T12:00	11.8	PWL	1079
Mrk421 [20130410]	0.03	2013-04-09T12:00	2013-04-10T12:00	0.845	PWL	179
Mrk421 [20130411]	0.03	2013-04-10T18:00	2013-04-11T06:00	0.389	PWL	44
Mrk421 [20130412]	0.03	2013-04-11T18:00	2013-04-12T06:00	0.388	PWL	120
Mrk421 [20130413a]	0.03	2013-04-12T12:00	2013-04-13T12:00	0.848	PWL	158
Mrk421 [20130413b]	0.03	2013-04-12T12:00	2013-04-13T12:00	0.848	PWL	158
Mrk421 [20130413c]	0.03	2013-04-12T12:00	2013-04-13T12:00	0.848	PWL	158
Mrk421 [20130414]	0.03	2013-04-13T12:00	2013-04-14T12:00	0.844	PWL	122
Mrk421 [20130415a]	0.03	2013-04-14T21:17	2013-04-15T04:13	0.209	PWL	81
Mrk421 [20130415b]	0.03	2013-04-14T21:17	2013-04-15T04:13	0.209	PWL	81
Mrk421 [20130415c]	0.03	2013-04-14T21:17	2013-04-15T04:13	0.209	PWL	81
Mrk421 [20130416]	0.03	2013-04-15T12:00	2013-04-16T09:00	0.723	PWL	110
Mrk421 [20130417]	0.03	2013-04-16T18:00	2013-04-17T06:00	0.359	PWL	23
Mrk421 [20130418]	0.03	2013-04-17T12:00	2013-04-18T12:00	0.845	PWL	87
Mrk421 [20130419]	0.03	2013-04-18T12:00	2013-04-19T12:00	0.844	PWL	104
Mrk421 [2014]	0.03	2014-04-25T18:00	2014-04-26T06:00	0.365	PWL	69
PG1553+113 [ST0202]	0.45	2012-02-28T12:00	2012-03-04T12:00	4.22	PWL	71
PG1553+113 [ST0203]	0.45	2012-03-13T12:00	2012-05-02T12:00	41.9	PWL	457
PG1553+113 [ST0302]	0.45	2013-04-07T12:00	2013-06-12T12:00	55.7	LP	475
PG1553+113 [ST0303]	0.45	2014-03-11T12:00	2014-03-25T12:00	11.8	PWL	207
PG1553+113 [ST0306]	0.45	2015-01-25T12:00	2015-08-07T12:00	164	EPWL	2606
PG1553+113 [ST0307]	0.45	2016-05-25T12:00	2017-04-25T12:00	282	EPWL	4306
PKS1222+216 [2010]	0.432	2010-06-17T20:00	2010-06-18T00:00	0.152	LP	224
PKS1424+240 [2014]	0.6	2014-03-23T12:00	2014-06-18T12:00	73.3	PWL	453
PKS1424+240 [2015]	0.6	2015-01-22T12:00	2015-06-13T12:00	120	PWL	945
PKS1441+25 [2015]	0.94	2015-04-17T12:00	2015-04-23T12:00	5.06	PWL	621
PKS1510-089 [2015]	$0^\ddagger$	2015-05-17T22:48	2015-05-19T02:10	0.299	EPWL	353
PKS1510-089 [2016]	$0^\ddagger$	2016-05-30T12:00	2016-05-31T12:00	0.843	EPWL	205
S50716+714 [2015]	$0^\ddagger$	2015-01-21T12:00	2015-02-15T12:00	21.1	EPWL	2002

Table 11.2: List of observations selected in *Fermi*-LAT. ‡: these sources were modeled with an intrinsic curved spectrum assuming redshift $z = 0$.

EBL density based on a given model. The results presented in the next sections were obtained from `fitebl` unless otherwise specified.

11.4.1 Optical depth scaling factor α

The method was first applied on the three different EBL models considered in this work: Franceschini, Rodighiero, and Vaccari [431] [F08], Domínguez et al. [409] [D11] and the fiducial model of Gilmore et al. [433] [G12]. Only a global scaling parameter was used.

Table 11.3 summarizes the best-fit optical depth scaling factors obtained for each of these EBL models together with the $1\,\sigma$ statistical uncertainties and the

	MAGIC only		**MAGIC+*Fermi*-LAT**	
	best fit	extreme	best fit	extreme
F08	$0.974\ (-0.113, +0.105)$ $P = 1.4 \times 10^{-2}$	$[0.657, 1.195]$	$1.024\ (-0.087, +0.075)$ $P = 4.9 \times 10^{-4}$	$[0.791, 1.205]$
D11	$0.918\ (-0.105, +0.105)$ $P = 1.3 \times 10^{-2}$	$[0.655, 1.143]$	$0.972\ (-0.071, +0.069)$ $P = 4.0 \times 10^{-4}$	$[0.734, 1.167]$
G12	$0.944\ (-0.107, +0.104)$ $P = 1.5 \times 10^{-2}$	$[0.656, 1.251]$	$1.012\ (-0.078, +0.079)$ $P = 9.9 \times 10^{-4}$	$[0.800, 1.144]$

Table 11.3: Estimations for the best-fit optical depth scaling factors in the MAGIC and MAGIC+*Fermi*-LAT cases using 3 different EBL models (F08: [431], D11: [409], G12: [433]). Statistical uncertainties are written in parentheses. Brackets (extremes) are obtained from the most conservative lower and upper limits (including $1\,\sigma$ uncertainties) among runs with ±15% scaled light throughput and systematics due to spectral model selection.

total fit probability (P-value). The first group (columns 2-3) includes MAGIC only data. Columns 3 and 4 show the same results when *Fermi*-LAT flux and spectral index parameters (hereafter 'bow-tie') is included in the analysis. The extreme case limits quoted in columns 3 and 5 provide an estimation of the systematic uncertainty band of this method. They were obtained from repeated test runs using a modified light throughput assumption for the telescope (up to ±15%). Additionally, alternative model selections were tested at: i) the predicted minimum EBL densities from galaxy counts[3] from Madau and Pozzetti [531]; ii) accepting also the power law as a legitimate spectral shape.

The MAGIC data itself do not favor any particular tested model, being all the results compatible at $1\,\sigma$ level with model predictions ($\alpha = 1$) for F08, D11 and G12. In all cases, the obtained probabilities are low ($P \sim 10^{-2}$ for MAGIC only, $P \sim 10^{-4}$ for MAGIC+*Fermi*-LAT), which we interpret as an oversimplification of the analytical spectra used to model the intrinsic blazar spectra together with systematic errors in the reconstruction of the broadband γ-ray spectra and uncertainties in the EBL models themselves. Better statistical constraints are obtained if the *Fermi*-LAT bow-tie is included. In this case the statistical errors roughly halve, at the cost of significantly lower fit probabilities ($\sim 10^{-4}$ vs $\sim 10^{-2}$), being this a symptom of over-simplification in the intrinsic model spectral shape selection, particularly for the broadband γ-ray spectral case. In both cases, the systematic uncertainties obtained through this method are similar and do not exclude any of the considered models.

The most constraining sources in the sample are Mrk 421 (15 high-significant spectra), 1ES1011+496 (showing a $4.6\,\sigma$ inflection point at $\sim 1\,$TeV, expected from most EBL models) and PG1553+113 (which, despite the badly constrained redshift, introduces sharp constraints in the upper bound on the scaling factors).

An example of the procedure applied to our data can be seen in figures 11.3a). The EBL density is extracted from Domínguez et al. [409] and only MAGIC data is considered, including just statistical uncertainties. The contribution from each

---

[3] Measured at $1.1\,\mu$m and taking into account statistical uncertainties.

individual spectra to the final result obtained with this method can be seen in Figure 11.3b). Note that the resulting TS profile cannot be directly interpreted as a 'detection plot', as such claim would require to know in advance the intrinsic spectral shapes or at least select those which provide a better description of the observed data. The best-fit models for the resulting α has been plotted with the corresponding spectral points in Figure 11.2.

11.4.2 Systematic uncertainties

Systematic effects are hard to determine and are out of the scope of this chapter, but three major components have been identified so far, they have been included in the results and are described below.

Selection of intrinsic spectral shape

In all cases, the predicted optical depth scaling factors are larger if the simple `PWL` shape is considered among the possible spectral models, which is interpreted in terms of forcing the EBL attenuation to explain any intrinsic curvature term in the data itself and biasing the scaling factor toward higher values. The inclusion of `PWL` hence marks an upper bound on the systematic effect due to the model selection. The corresponding lower bound can be estimated for instance by using the spectral shapes that provide the best description of the observed data assuming that the EBL density is the one predicted from galaxy counts [531]. In this way, the chosen models are more complex and can partially or totally reproduce the EBL-induced spectral curvature, hence resulting in lower values of the best-fit EBL photon density.

Uncertainties in the total light throughput

Systematic uncertainties in the energy scale are mainly due to our limited knowledge of the absolute atmospheric transmission and telescope efficiency. In order to estimate the contribution of this source of errors we adopted a ±15% systematic uncertainty, globally applied to the full dataset, in the energy scale following Aleksić et al. [204]. It is equivalent to modify the calibration constants used to convert pixel-wise digitized signals into photoelectrons, which not only changes the estimated energy of the events, but also the derived IRFs of the instrument. The profile likelihood method was then repeated with the artificially distorted MAGIC spectra.

EBL model selection

This work assumes a given EBL spectral shape to compute the total γ-ray attenuation as a function of energy and redshift. For each EBL model, a best-fit value of the global optical depth scaling factor α was obtained. However, the individual EBL models have different spectral shapes and evolution. These differences can be particularly large in some parts of the spectrum, which can be interpreted as an additional component to the total systematic uncertainty of the method.

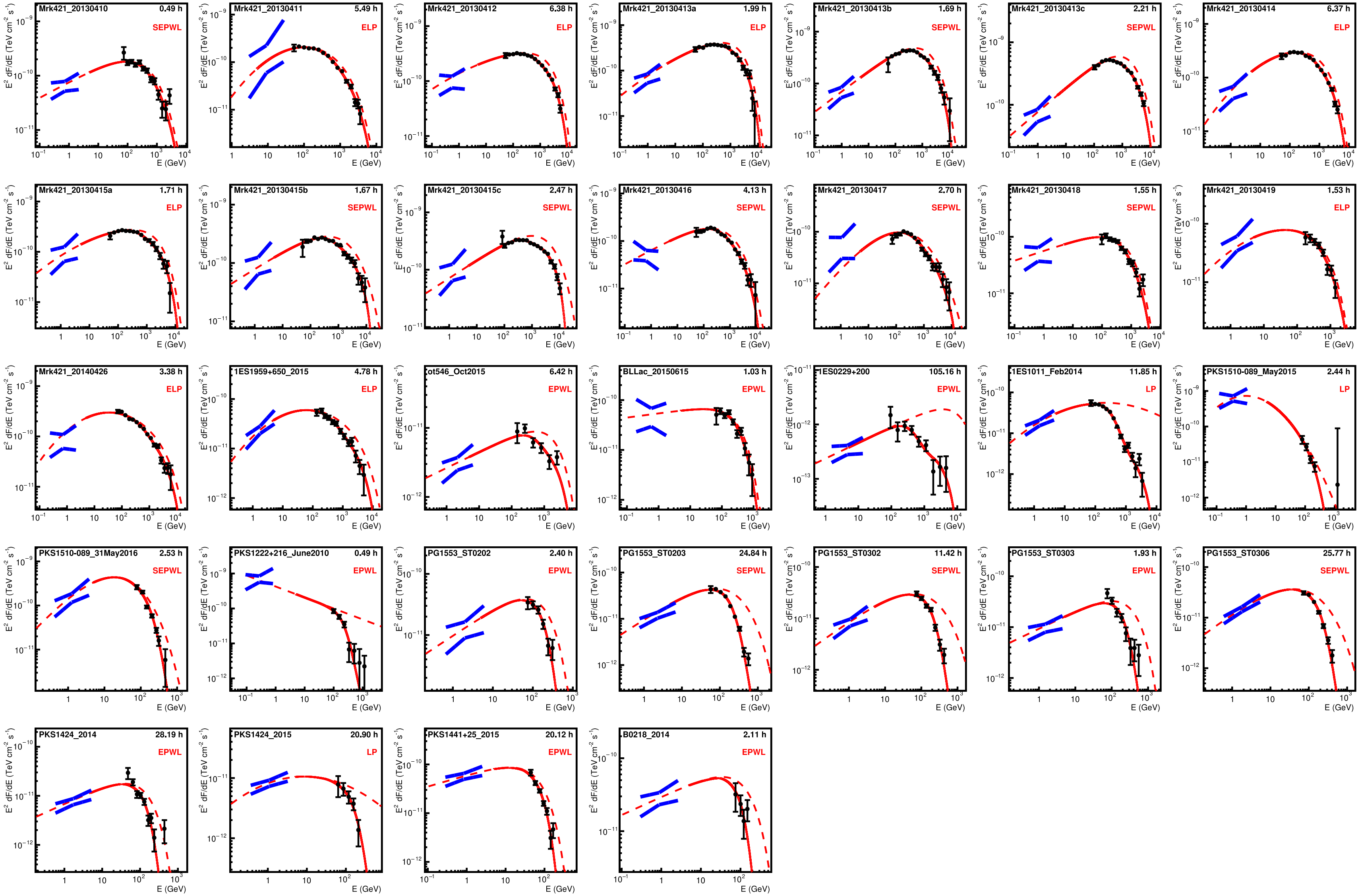

Figure 11.2: VHE SEDs for the 32 spectra considered in our study including MAGIC points (black), *Fermi*-LAT best-fit model in blue (considered as a pure PWL around the decorrelation energy of the *Fermi*-LAT data) and the best-fit models with the resulting α scaling factor in red (dashed red line represents the de-absorbed data).

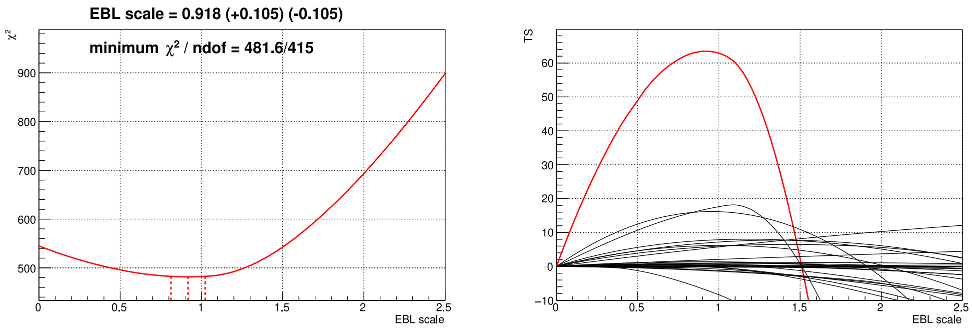

Figure 11.3: a) log *Likelihood* (χ^2) profile vs the optical depth scaling factor using the model from Domínguez et al. [409]. Only MAGIC data were used. **b)** LRT scan, as defined by the difference between χ^2 at the null hypothesis (no EBL, $\alpha = 0$) and the χ^2 at a given scaling factor. In black, the contribution from individual samples. In red, the combined LRT profile from all sources.

Instrument cross-correlation

The consideration of light throughput and intrinsic shape selection uncertainties yields the extreme values given in Table 11.3 (third column) for the upper and lower bounds in the MAGIC-only case. For MAGIC+*Fermi*-LAT it is actually harder to quote a realistic estimation of systematic uncertainties as *Fermi*-LAT contributes with its own systematics in both the spectral index and flux normalization. Furthermore, the differences in exposures in the *Fermi*-LAT and MAGIC samples adds uncertainties that are hard to gauge. This is particularly true for variable sources such as blazars. A somewhat extreme (but incomplete) case could be explored if the *Fermi*-LAT is left unmodified (but with an overall 10% uncertainties in flux normalization added in quadrature to the statistical uncertainty in the flux normalization) and the MAGIC results are modified with the aforementioned methods. Again, Table 11.3 (last column) shows the worst (extreme) constraints (including their statistical uncertainties) obtained with the above described systematic error components.

11.4.3 The EBL density

Results including both statistic uncertainties and statistic+systematic uncertainties are shown in figures 11.4 (MAGIC only) and 11.5 (MAGIC+*Fermi*-LAT). In the figures, the scaling factors derived from the study have already been applied to the EBL density profiles for the different EBL models considered to obtain the estimated EBL spectral energy distribution (energy density as a function of wavelength). The best-fit and statistical uncertainties are calculated with respect to the model of Domínguez et al. [409]. The systematic uncertainties are calculated to cover, at all wavelengths, the most conservative limits for Domínguez et al. [409] (D11), Gilmore et al. [433] (G12) and Franceschini, Rodighiero, and Vaccari [431] (F08). In Figure 11.4a the confidence bands obtained in this work are compared with direct measurements and galaxy counts (strict lower limits). In Figure 11.4b), indirect measurements coming from γ-ray attenuation in blazars are shown for comparison. In both cases, some selected EBL models from the literature are provided as a reference.

From the figures, it is obvious that γ-ray indirect measurements lie close to the galaxy counts results. The upper uncertainty band limit is only about $\sim 60\%$ larger than the lowest prediction from galaxy counts at $1\,\mu$m from Madau, Pozzetti, and Dickinson [557], leaving little room for undetected components of EBL and being compatible with an scenario of a galaxy-dominated COB. The resulting EBL density is very close to the nominal values from D11, G12 and F08. All these models, despite having been built in a completely different manner and under different assumptions, have their differences concentrated mostly in the CIB and near-UV. They are nearly indistinguishable in the optical and near-IR bands. The only exceptions are Finke, Razzaque, and Dermer [432] (FI10) (predicting larger opacities in the mid IR) and G12 predicting higher intensity in the UV. When compared with γ-ray attenuation based measurements, our results perfectly overlap in the optical-UV with the measurements from Ackermann et al. [425] and are in good agreement with [428] and the wavelength-resolved multi-source and multi-experiment measurement from Biteau and Williams [548], except a hint of deviation in the optical and near-UV which could be attributed to the fact that they allow power laws as legit intrinsic spectral shapes, the calculation of statistical errors is overly simplified and the points do not include systematic uncertainties.

Finally, we can compare our result with searches of EBL imprint on GRBs [567]. GRBs are different sources than blazars, their typical redshift is large ($z \gtrsim 1$) and their spectra are modeled differently. They are thus sampling the near UV part of the COB. A comparison of the results from both experiments can serve as a crosscheck of the method, the robustness of the EBL models across a broad spectral range and potentially the galaxy evolution models themselves. Despite the agreement with their value of $\alpha_{D11}^{GRB} = 2.21^{+1.48}_{-1.83}$, it is clear that the large error bars leave room for improvement.

11.4.4 Alternative γ-ray propagation models

Modifications to the standard model of energetic photon propagation have been proposed several times in the past. The idea got renewed interest among researchers with the increasing amount of high redshift sources detected at HE and VHE, whose emission, according to the EBL opacity models existing at the time, was difficult to explain. In Horns and Meyer [568], a collection of spectra measured with WHIPPLE, HEGRA, H.E.S.S. and MAGIC was stacked and the evolution of γ-ray residuals (using the analytical spectra that gives the best fit to the observed spectra) with respect to their τ optical depths was built (assuming the lower limits to the EBL from Kneiske and Dole [561]). A shift towards larger residuals (i.e. larger transparencies) was observed as τ increased, with a significance of $4.2\,\sigma$ (or even $5.6\,\sigma$ if Gaussianity of the residuals is assumed, which is reduced to $2.6\,\sigma$ if the last point (largest τ) of each spectra is dropped to account for possible observational biases due to statistical fluctuations in the last energy bin).

We tried to repeat this experiment in a more systematic way in Figure 11.6.

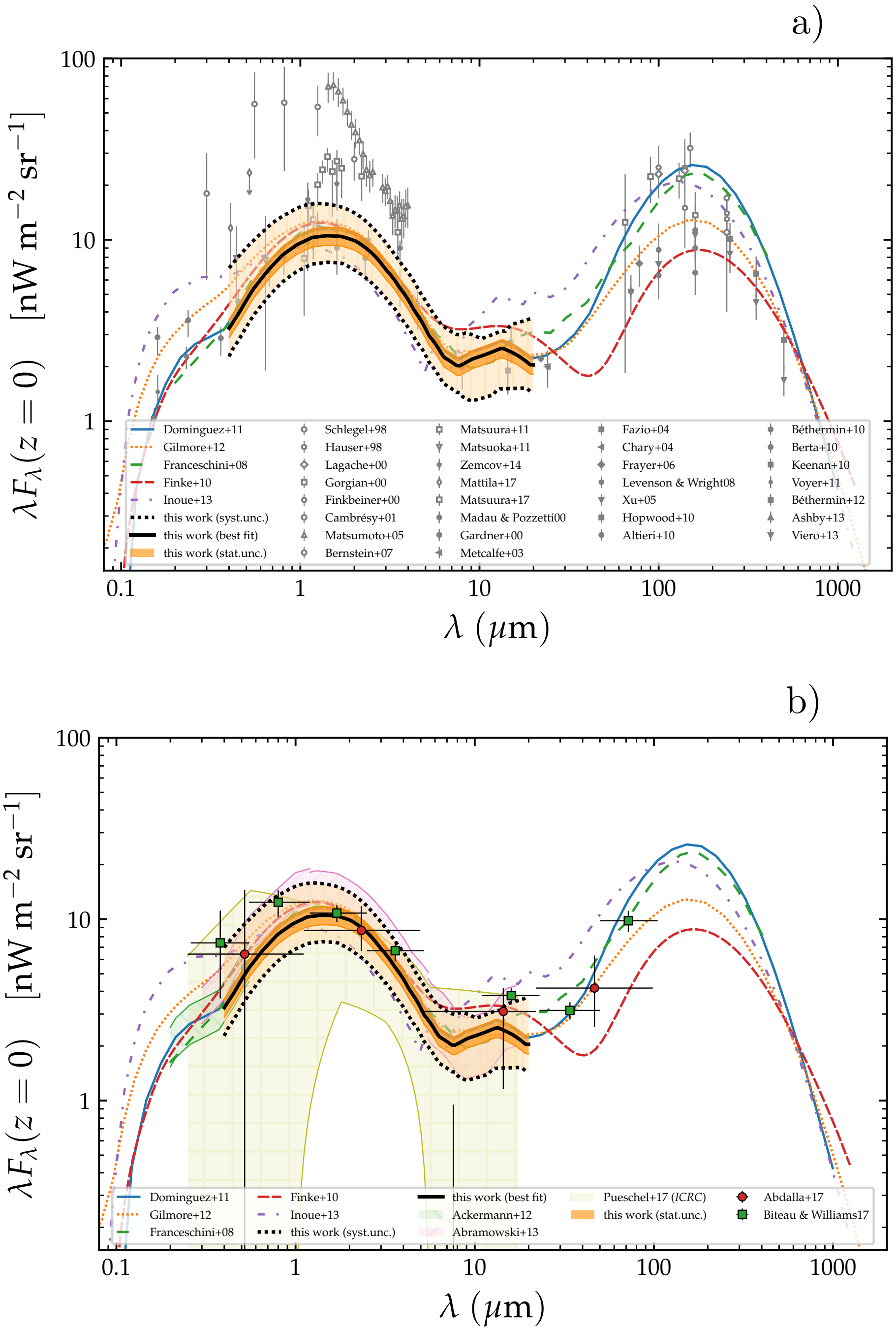

Figure 11.4: Spectral energy distribution of the EBL including statistic (orange filled) and statistic+systematic (wide black dotted curve) confidence bands with MAGIC. Only one global scaling factor was scanned with respect to the model of D11 (solid black line) at $z = 0$. Systematics curves comprise the worst lower and upper bounds for D11, G12 and F08 models. Panel a) comparison with several bibliography direct EBL measurements and EBL models compared to the results derived in this work; b) comparison with other indirect measurements coming from γ-rays.

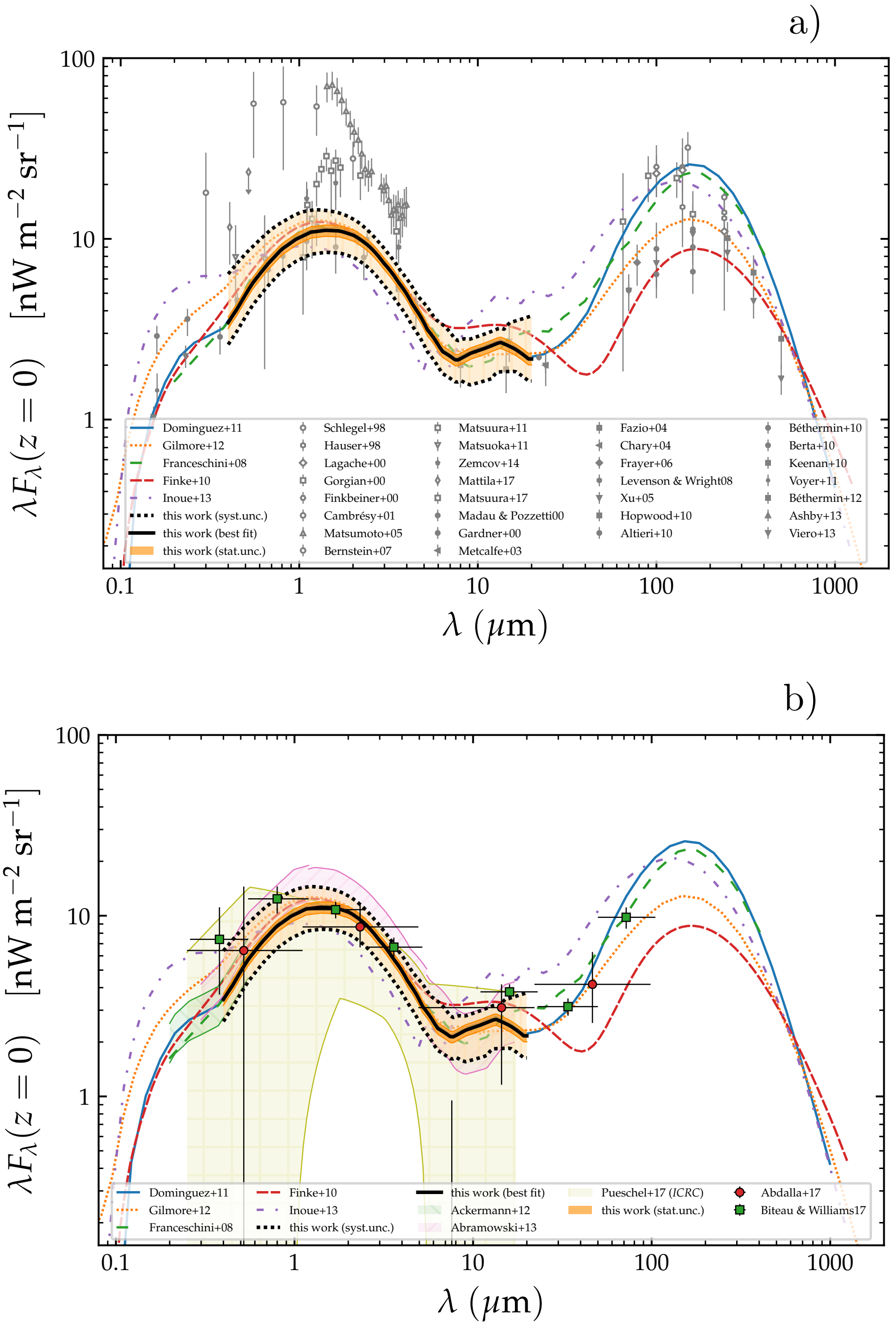

Figure 11.5: Spectral energy distribution of the EBL including statistic (orange filled) and statistic+systematic (wide black dotted curve) confidence bands with MAGIC+*Fermi*-LAT. Only one global scaling factor was scanned with respect to the model of D11 (solid black line) at $z = 0$. Systematics curves comprise the worst lower and upper bounds for D11, G12 and F08 models. Panel a) comparison with several bibliography direct EBL measurements and EBL models compared to the results derived in this work; b) comparison with other indirect measurements coming from γ-rays.

Instead of using the spread of the spectral points with respect to the assumed spectral shapes, we calculated the relative excesses in the number of events for each particular energy bin with respect to the predicted number of events from the spectral shape. This is in principle more robust since negative excesses (which would led to an upper limit and hence omitted from an study like [568]) can be taken into account.

The results, seen in Figure 11.6a for the MAGIC-only analysis show no significant trend like the one claimed in [568]. The same conclusions are derived from the MAGIC+*Fermi*-LAT analysis (Figure 11.6b). In both cases, a fit to a linear model is compatible with a 0 slope model within $1\,\sigma$ level. The data are hence compatible with current generation EBL models and no exotic γ-ray propagation models are needed to explain the large-τ γ-ray photons.

11.4.5 EBL scaling factor evolution with redshift

Star formation history (SFH) measurements are consistent with a strong peak in the star formation rate around $z \sim 2$, decreasing in ~ 1 order of magnitude towards $z = 0$ [569]. EBL should correlate with the star formation history, so any evolution in the star formation rate (SFR) should be reproduced by the EBL models. The ideal instrument to test the imprint of SFR evolution in γ-ray blazar spectra is *Fermi*-LAT, which can measure the EBL density at $z > 1$. Still, the samples presented here at $z \gtrsim 0.5$ are good candidates to test if there is any departure in the optical depth predicted by EBL models.

The sample was further divided in four redshift bins ($0.0-0.1$, $0.1-0.3$, $0.3-0.6$ and $0.6-1.0$) in order to check for deviations of the optical depth scaling factor α as a function of redshift. Results for the z-resolved analysis for the model of [409] are presented in Figure 11.7. The first two bins are dominated by Mrk 421 and 1ES 1011+496 respectively. The 3rd and 4th bins collect mostly contributions from PG1553+113 (strong upper bounds), PKS 1424+240 and PKS 1441+25. The results are, in all cases, compatible with the model predictions ($\alpha = 1$) once systematic uncertainties are taken into account. Only one bin shows a very slight deviation, $0.3 < z < 0.6$. There, the EBL attenuation and intrinsic spectral curvature are totally degenerated and the effect of the EBL attenuation can be simply reproduced with an exponential or super-exponential cut-off.

11.4.6 The wavelength-resolved EBL density

For the model of Domínguez et al. [409] (D11), the spectral energy distribution of the EBL was divided in six wavelength bins ($\lambda_1 = [0.1, 0.18]\,\mu$m, $\lambda_2 = [0.18, 0.62]\,\mu$m, $\lambda_3 = [0.62, 2.24]\,\mu$m, $\lambda_4 = [2.27, 7.94]\,\mu$m, $\lambda_5 = [7.94, 28.17]\,\mu$m) and the predicted γ-ray opacities due to the EBL at $z = 0$ for such bins were calculated as a function of γ-ray energy. By doing so, λ-resolved EBL density values could be obtained. The procedure in this case changes, as the results for each source cannot be stacked "a posteriori" using the profile likelihood approach. Instead, the χ^2 minimization needs to incorporate all the spectral parameters for each source together with the 6 α scaling factors. The problem becomes computationally challenging because of the a)

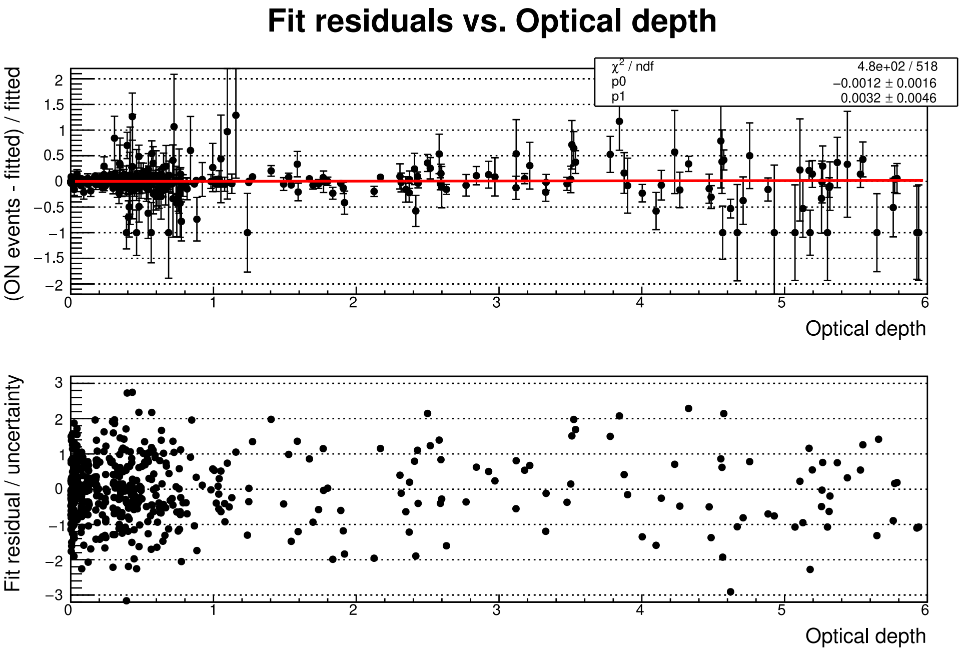

b)

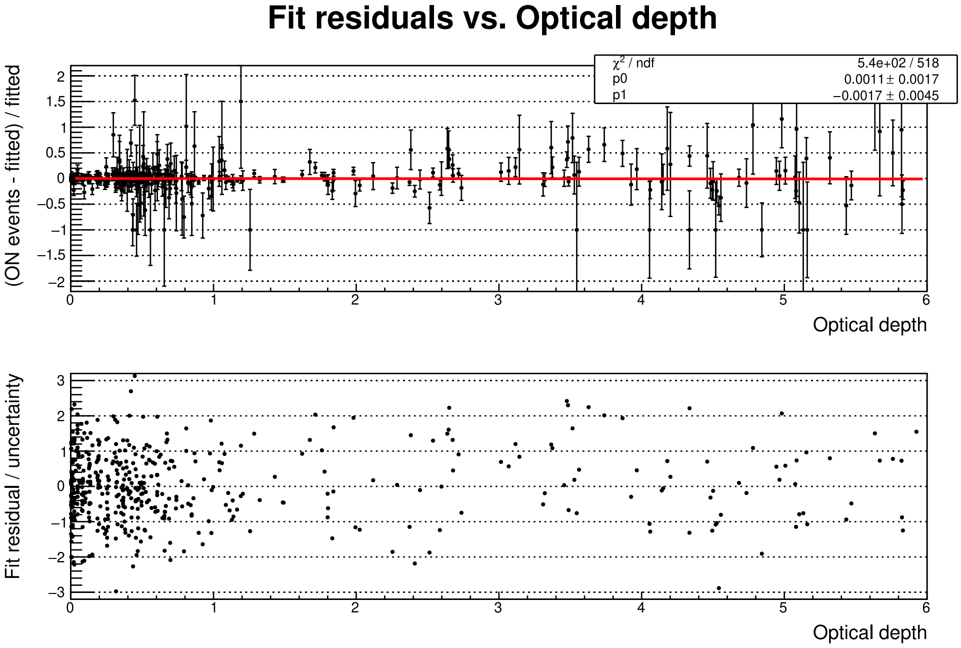

Figure 11.6: Relative event excess as a function of the optical depth for the collection of 32 blazars considered in our study. a) using only MAGIC data, b) Including also *Fermi*-LAT bow-tie. Relative excesses of −1 are set wherever the number of ON events is the selected energy bin is 0.

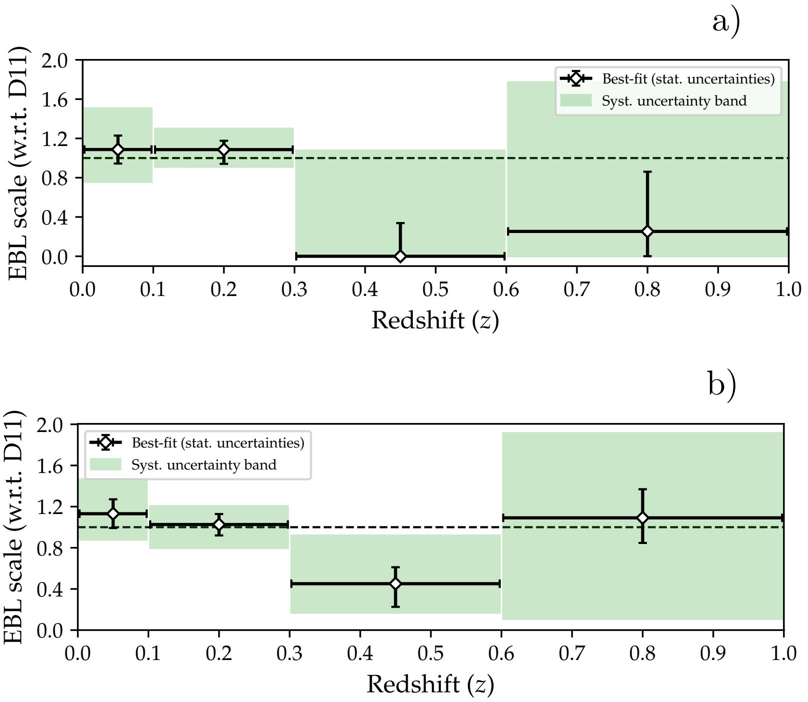

Figure 11.7: EBL scaling factors when the sources are grouped by redshift. a) Using MAGIC-only data, b) Including *Fermi*-LAT bow-tie.

significant parameter degeneracy. Without *Fermi*, such degeneracy is so large that in most cases the minimization becomes computationally unstable.

The results for the λ-resolved measurements are summarized in Figure 11.8. The figure shows the scaling parameters and confidence bands for all but the first EBL bin ($\lambda_1 = [0.1, 0.18]\,\mu$m), where our dataset has little to no constraining power. Systematic uncertainties quoted are purely based on MAGIC instrumental uncertainties and should be considered with caution. For *Fermi*-LAT systematic errors were assumed to be only a 10% systematic uncertainty in the flux normalization added in quadrature its statistical uncertainty. The confidence bands are in all cases compatible with predictions from F08, D11 and G12. They are also in good agreement with classical measurements from Abramowski et al. [428] and Ackermann et al. [425] and with the more recent values from Biteau and Williams [548], Pueschel [570] and Abdalla et al. [571]. The obtained upper bounds in the range $\lesssim \lambda \lesssim 30\,\mu$m are close to values from galaxy counts, meaning that most of the EBL in that wavelength range is already resolved in individual galaxies.

11.4.7 Crosscheck with eblfitter

In addition to the results from `fitebl`, a limited crosscheck was done with `eblfitter`. The method is known to be affected by the same selection bias affecting Horns and Meyer [568] (only significant points with $> 2\,\sigma$ excesses were considered). Additionally, it was not possible to easily modify the light throughput of the telescope by ±15%,

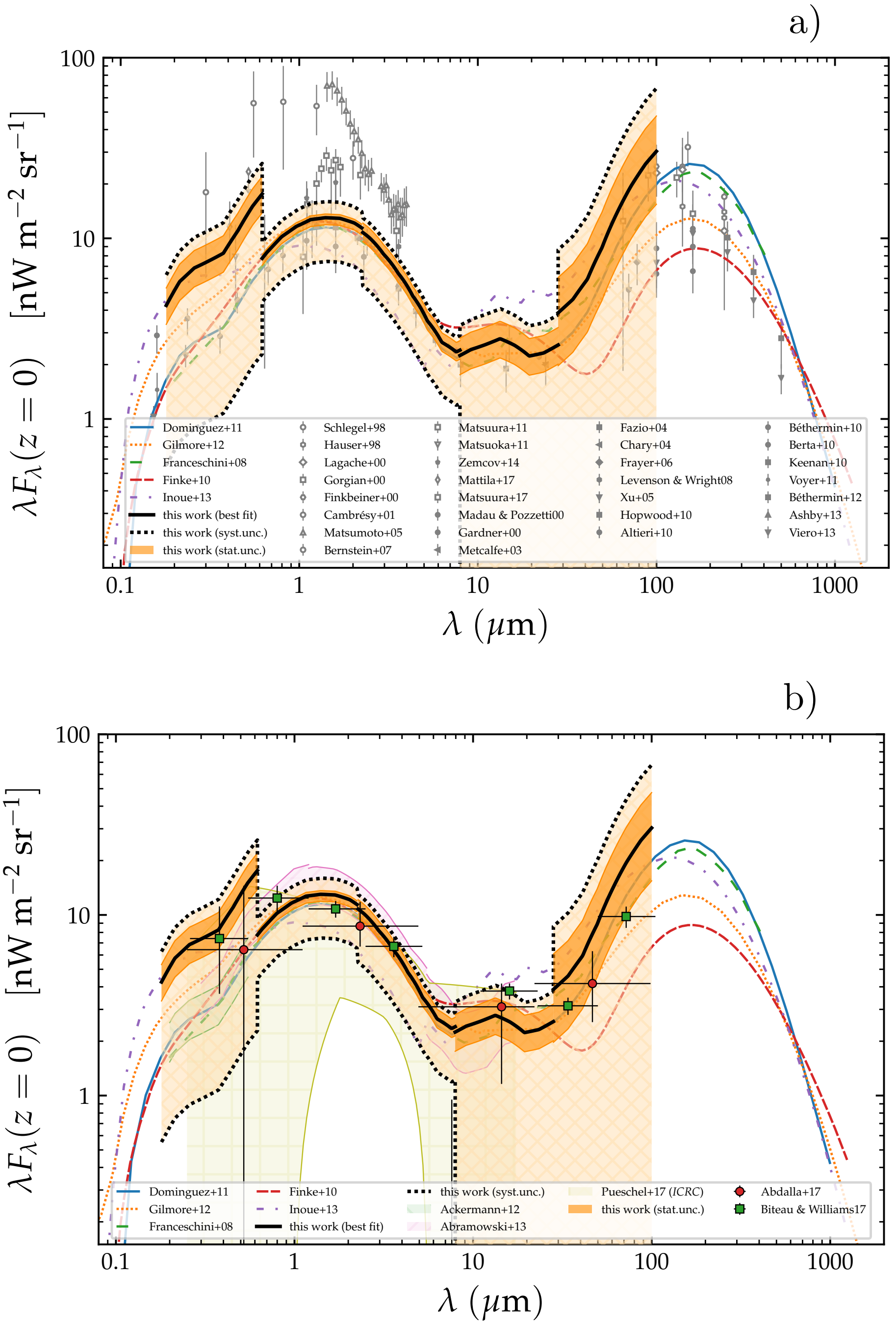

Figure 11.8: Spectral energy distribution of the EBL including statistic (orange filled) and statistic+systematic (wide black dotted curve) confidence bands with MAGIC and *Fermi*-LAT. Six (the first not shown in the figure) wavelength bins between 0.10 μm and 100 μm were defined with respect to the model of D11 (solid black line) at $z = 0$ and one scaling value were left free for each. Systematics curves comprise the worst lower and upper bounds for D11. Panel a) comparison with several bibliography direct EBL measurements and EBL models compared to the results derived in this work; b) comparison with other indirect measurements coming from γ-rays.

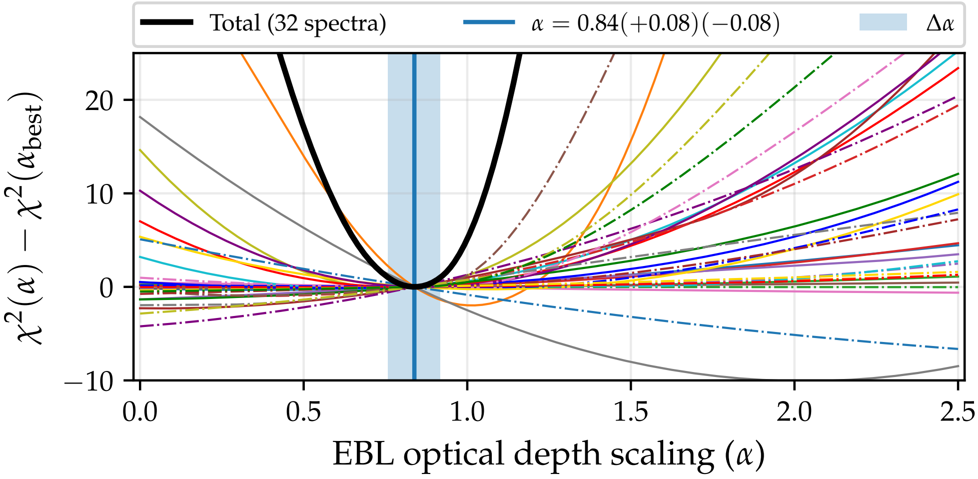

Figure 11.9: Optical depth α scan obtained with `eblfitter`. Only MAGIC data were used. The contributions of each source in $(\chi^2(\alpha) - \chi^2(\alpha_{\text{best-fit}}))$ are shown as a function of the optical depth scaling factor. The black solid line shows the combined result and the vertical blue solid line and lighter blue band shows the best-fit scaling α and its $1\,\sigma$ statistical confidence band.

meaning that no systematic uncertainty estimation was performed.

The results are referred to the EBL model from Domínguez et al. [409]. The EBL scan was done by leaving the redshift as a free parameter (in the range $0.43 < z < 0.58$) during the minimization for the different PG 1553+113 spectra. Since `eblfitter` works on each spectrum individually, the redshift for each PG 1553+113 sample is considered as an individual nuisance parameter.

The profile likelihood results are presented in Figure 11.9. The obtained optical depths (e.g. $\alpha = 0.84(+0.08)(-0.08)_{stat}$ for the model of D11), are in general compatible with the ones from `fitebl`, both in value and statistical uncertainty.

11.5 Discussion

The first and most immediate conclusion we can extract from the results presented before is that the current state-of-art models for the Extragalactic Background Light, based on galaxy population studies seem to correctly reproduce our HE and VHE γ-ray observations. These models nearly predict the same EBL densities that are measured in the so called galaxy count measurements, meaning that normal galaxies are expected to be responsible for most of the emission we see in the COB, leaving little room for more exotic components such as hypothetical Population III stars at high redshift, which could have contributed to the reionization of the Universe.

Based on the MAGIC dataset, it is currently not possible to reject any of the considered state-of-the-art models: Franceschini, Rodighiero, and Vaccari [431] (F08), Domínguez et al. [409] (D11) or Gilmore et al. [433] (G12). Obtained densities are overall comparable with D11, but discrepancies are found in the near-UV (D11 predicting a somewhat lower opacity) and at mid-IR (where G12 predicts significantly more light than D11). With this in mind, we can not statistically reject any of the 3 models with our current data. This is somewhat expected since our EBL determination is dominated by sources like 1ES 1011+496 that are mostly affected by the optical and near-IR parts of the COB, where all models basically agree.

No significant deviation is found in any of the spectra and no hints of EBL density being lower or higher than the values predicted from the models are found in any of the considered redshift bins. This result contradicts the hints of anomalies pointed out by Horns and Meyer [568]. They invoked several possible physical processes to explain discrepancies with EBL models by modifying the standard behavior of light propagation models such as Lorentz-invariance violation (LIV) and the conversion and re-conversion into and from axion-like particles (ALPS). Our result points into the direction that standard models can successfully explain the observed data even in the optically thick regime.

Systematic uncertainties are discussed by their origin and some of its components considered in the study (those due to the energy scale, to spectral shape selection and to EBL model selection). However, it is not fully clear how a mismatch in the instrument cross-calibration or a significant difference in the exposures between the measurements on different instruments shows up in the final EBL determination. There are some ideas that can be employed to try to estimate this effects that we are not developing here but leave instead for future work. Perhaps one of the easiest tests that can be done is studying how the spectra of the sources change in different bands and if the spectral shape significantly changes by including more or less data in the sample. Similarly, studying the broadband γ-ray emission from Crab Nebula simultaneously with *Fermi*-LAT and MAGIC could help us to improve the cross-instrument calibration and to gauge its evolution with time. Systematic errors in the energy scale of the spectra reconstructed by MAGIC can in principle be reduced if LIDAR measurements and background event rates are considered as well. The first can provide corrections to the collection area estimation due to non-optimal atmospheric conditions. The latter should depend only on instrumental parameters (trigger, pointing), with most unexpected deviations being attributed to changes in the atmospheric transmission.

In section 11.4.6, λ-resolved EBL estimations were discussed. The problem in this case was that the procedure becomes computationally more challenging since the individual log-likelihoods cannot be summed. Instead, a full estimation with the spectral parameters for all the sources need to be fitted simultaneously. Still, the obtained results were compatible with the current generation of EBL models and are close, in all wavelengths to the densities obtained from galaxy counts.

12

Conclusions

The work presented in this document has been divided in four parts. The first was mostly introductory and its goal was to bring an updated review of γ-ray astronomy. It covers particle acceleration mechanisms, γ-ray emission channels and finally the most important families of sources that are known to emit γ-rays in the Universe.

The three other parts have all the same structure. First, an introductory chapter details the current knowledge of the topic of interest. Then, the subsequent chapters describe my work in the field. Here, I present some of the conclusions extracted during my thesis project and a brief outlook of what we will hopefully be able to do with the next-generation instruments in that regard.

12.1 Instrumentation

The main goal of this thesis was to study the γ-ray emission from blazars, for which we have used MAGIC and *Fermi*-LAT (see II). In both cases, my contributions are centered in improving the existing analysis pipelines.

12.1.1 Fermi-LAT

In chapter 4 we described the Large Area Telescope (LAT), which is the primary instrument on board *Fermi* and the current most sensitive γ-ray astronomy detector working in the energy range which spawns from $0.1 - 100\,\mathrm{GeV}$. In that chapter, I described my contributions to the `enrico` software package, an abstraction layer working on top of the Fermi `ScienceTools` that significantly simplifies the analysis of *Fermi*-LAT data and helps to generate high level products. In particular, I have successfully implemented a summed likelihood analysis scheme that takes advantage of the event classification introduced in PASS8. Events are now divided in types according to their position and energy reconstruction accuracy and IRFs are available for each type. The summed likelihood analysis results in a statistical improvement of the instrument sensitivity. I have extensively used this feature both in this work and in a recent paper submitted by MAGIC to Science [1]. In addition, I have introduced different energy binning schemes (apart from the default equally log-energy spaced) for the spectral energy distribution. Finally, the implementation of EBL-attenuated spectral models in `enrico` was essential to analyze the selected *Fermi*-LAT samples that were used to derive constraints on the EBL photon density in chapter 11.

12.1.2 MAGIC

The MAGIC telescopes, described in chapter 5, are optimized to provide a low energy threshold and good sensitivity at low energies. Both goals are achieved through a combination of hardware (large mirrors, efficient triggering system) and software developments. In that sense, we briefly described a method to exploit the imaging capabilities of IACTs to improve their sensitivity (see appendix A, [206]). Similarly, in section 5.3.1 we introduced the MAGIC *On Site Analysis* (OSA).

The goal of the OSA is to quickly analyze the data coming from the telescopes and deliver high level products to the MAGIC data center. MAGIC produces a very high rate of raw data, which requires some time to be transferred and processed. OSA analyzes the data in parallel with the raw data transfer. It produces high level products with a reduction of a factor of ~ 200 in data volume which are delivered together with the raw data, cutting down the waiting time for scientist. One of my most significant technical contributions in MAGIC has been maintaining the system and making it more efficient. In particular, I redesigned the tool (`nightsummary`), which now identifies automatically the optimal configuration to analyze the data. I also wrote a high level analysis tool for OSA, in charge of automatically producing θ^2-plots, skymaps, spectra, light curves and a quick data quality check. In addition, I also collaborated in the development of the `autocloser`, which completely automatizes the generation of analysis logs, manages the 'closing' of the data runs and triggers the transfer of resulting high level products to the science data server at PIC. The mentioned interventions had the effect of boosting the processing speed in OSA. By the end of the day following the MAGIC observations, 94% of the nights were fully analyzed in 2017, as opposed to 69% of the nights in 2013 (the year I entered the collaboration). As a result, analyzers can normally download already reduced and cleaned data from PIC the day right after the data was acquired. This has been essential to provide a fast reply to alerts about flaring blazars.

12.2 Blazars

Blazars, described in 6, make up a large fraction of the number of sources detected by the *Fermi*-LAT. Approximately two thirds of them are flat spectrum radio quasars (FSRQs), while the rest are of the BL Lac type. In VHE, the number of sources not only is greatly reduced, but the fraction of radio quasars and BL Lacs is completely

---

[1] The manuscript describes the MAGIC observations of the blazar TXS 0506+056, spatially coincident with IceCube neutrino event EHE 170922A.

different, with only 8 FSRQs detected with IACTs.

In part III we considered the case of three of the most distant blazars that are known to emit VHE γ-rays. The first two, B0218+357 (chapter 7, [325]) and PKS 1441+25 (chapter 8, [426]) are the most distant FSRQs detected until now in VHE. We learned how these sources, for which we do not expect significant γ-ray emission above 100 GeV, can emit photons of such energies under very special circumstances. According to the models presented in this work, the VHE γ-ray emission from FSRQs is highly dependent on the precise location of the γ-ray emitting region with respect to the broad line region (BLR). We also used these far beacons to probe the attenuation from current generation of EBL models, finding good agreement between their predictions and our measurements. For B0218+357, we could probe for the first time in VHE some interesting properties of gravitational lensed systems. The delayed emission components cannot be only predicted, but also provide useful information about distribution of matter in the lens and the sizes and location of the emitting region in different wavelengths. The third source, PKS 1424+240, was briefly described in chapter 9. It is the most distant BL Lac detected in the VHE band and its hard spectrum has been traditionally challenging to interpret. We could also reproduce the modeling proposed in Aleksić et al. [478] , which can successfully explain the broadband emission of PKS 1424+240 in 2014 as being produced in two regions filled with plasmas of slightly different properties.

12.3 EBL

Part IV describes our studies of the Extragalactic Background Light (EBL). This cosmic background radiation field of energies ranging from far IR to UV is the result of the accumulated starlight, AGN and diffuse radiation emitted through the history of the Universe. In chapter 11 we studied the interaction of γ-rays coming from blazars with the EBL. Such interaction leaves a distinctive attenuation in blazar spectra. Using a multiple-source stacking, we could study this effect in detail and measure indirectly the EBL photon density as a function of wavelength and redshift. Results were then compared with predictions from theoretical and empirical models and measurements, finding that: i) The density of EBL photons nowadays is very close to galaxy count measurements, which means that normal galaxies are the most important sources of low energy cosmic photons; ii) The current VHE data is not sufficiently good to discriminate between models.

12.4 Outlook

The future Cherenkov Telescope Array (CTA)[2] is ran by more than 1400 project participants from 32 countries. It will provide a nearly full-sky coverage with its two sites and greatly outperform the capabilities of current generation of IACTs. The northern site will be compose of 4 LSTs and 15 MSTs, while the southern site will increase the number of MSTs to 25 and it will feature around 70 SSTs

---

[2] `https://www.cta-observatory.org`

covering the highest energies. CTA will offer the chance to improve the results of many of the topics covered in this thesis.

The new instrumentation will give us an excellent opportunity to study AGNs, particularly blazars and radio-galaxies. The proposed blind survey of one-fourth of the extragalactic sky will provide a nearly unbiased VHE extragalactic source catalog. At the same time, the lowest energies covered by the LSTs will greatly extend the number of detections of distant γ-ray blazars (particularly FSRQs) and the much better sensitivity will allow to study their spectra in detail and probe the possible link between high redshift BL Lacs and FSRQs.

Finally, with CTA, we will have the ideal tool to study not only the EBL photon density, but also its evolution with look-back time and make EBL anisotropy studies. This will be instrumental to indirectly probe the star formation history, the galaxy formation and clustering, the existence of cosmic voids and alternative γ-ray propagation models involving hypothetical particles, such as axion-like particles. The strategy is similar to that one outlined in this work: obtaining high quality spectra from sources with spectra entering deeply into the $\tau_{EBL} > 1$ space, from which the imprint from the EBL is measured. The main differences are that:

- CTA will hopefully allow to measure spectra from GRBs[572], which will provide excellent targets for studying the EBL at relatively high redshifts.
- It will greatly extend the amount of extreme HBLs within the reach of ground-based instruments[573], which are also excellent targets because of their relatively simple and featureless intrinsic spectra.
- The improved energy resolution will help to measure the inflection point in the AGN spectra at $\sim 1\,\text{TeV}$ caused by EBL even on challenging targets (IBLs, LBLs and FSRQs), allowing to confidently use them to measure the EBL imprint for the first time.
- In all cases, the lower energy threshold provided by the LSTs will give us a handle on the truly simultaneous intrinsic spectrum for the first time, vastly reducing the systematic uncertainties in the EBL measurements coming from the instrument cross-calibration.

Appendices

A

Source detection with PSF templates

Contents

The so called Li&Ma formula is still the most frequently used method for estimating the significance of observations carried out by Imaging Atmospheric Cherenkov Telescopes. This work, published in Nievas-Rosillo and Contreras [206], presents a straightforward extension of the method for point sources that profits from the good imaging capabilities of current instruments. It is based on a likelihood ratio under the assumption of a well-known PSF and a smooth background. Its performance is tested with Monte Carlo simulations based on real observations and its sensitivity is compared to standard methods which do not incorporate PSF information. The gain of significance that can be attributed to the inclusion of the PSF is around 10% and can be boosted if a background model is assumed or a finer binning is used.

A.1 Introduction

The statistical significance of an observation is a key issue in *signal starved* fields such as Imaging Atmospheric Cherenkov Telescopes (IACTs) Astronomy, and in general

Very High Energy (VHE) Astronomy. It determines whether a given astronomical source has been detected or not, providing a probability for the excess being due to background fluctuations. It also limits how much detail can be recovered in spectra and light curves, because a minimum significance is usually required for each spectral or light curve point to be accepted. Finally, it also plays an important role when the goal is to set upper limits for non-detected sources. In this case, the sensitivity of the method determines how constraining the upper limit is.

Until the publication of the classical article by Li&Ma [408], several approaches to define the significance of astronomical observations had been used in VHE observations. As shown in that article, most of them were based on incorrect statistical hypotheses, and thus yielded unexpected widths of the significance distributions when they were tested with Monte Carlo (MC) simulations. In their article, Li&Ma proposed a robust and reliable method for estimating that significance. Since at that time VHE instrumentation had very limited angular resolution, the method was designed as an event counting technique which makes very little use of the instrument resolution, given by its Point Spread Function (PSF), and background distribution. Therefore, the sensitivity achieved should be worse than the one of methods that incorporate that information.

The *Li&Ma* method, which shall be known as just *Li&Ma* in the rest of this work, is a particular case of a more general family of techniques based on maximum likelihood principles. Generalized maximum likelihood methods such as that implemented in [574] and [437] are sometimes difficult to implement. There have been general proposals such as [575] to extend the *Li&Ma* formula or include the effect of systematic errors (e.g. [576] and [577]). Still, the use of general likelihood methods in IACT Astronomy is restricted in practice to special analyses such as sky maps [578] or spectral line studies in Dark Matter searches, as seen in [579] and [580]. Nevertheless, even if they risk losing robustness and stability, they are usually more sensitive than event counting methods.

In this article, a simple technique that takes into account the a priori knowledge of the instrumental PSF is presented and characterized in detail, under the assumption of a smooth background for which dedicated measures are available. Although the method is applicable to a wide range of situations, it has been tested in our field of interest: VHE observations. It can be understood as a generalization of the *Li&Ma* method or a particular application of that proposed in [575] to a specially relevant case: the search for one isolated point source in the field of view (FoV), which is the common case in extragalactic observations with the current sensitivity of IACT experiments. A point source is defined as one whose angular size is smaller than the PSF of the instrument. Known as the *PSF-Likelihood* method it can recover more information from the source of interest while keeping, at the same time, the simplicity of the standard *Li&Ma* method. In order to check whether the statistical foundations of the technique are correct, and estimate its rejection power, it is tested with a set of *toy Monte Carlo* samples generated using real background and data from observations of the Crab Nebula performed by the MAGIC experiment [498]. The comparison allows what can be gained from this kind of approach in a real situation to be gauged.

A.1.1 Maximum likelihood with background estimation

IACTs operate in harsh environments and their performance is highly dependent on the atmospheric and instrumental observing conditions. As a consequence the background affecting an observation is highly variable and is usually estimated jointly with the signal. In the past, the observation time was divided between ON observations, in which the telescope was pointed towards the source, and OFF observations, in which the telescope was pointed to an equivalent region with no source present. Nowadays it is customary to use alternative methods that do not require dedicated OFF observations. This is the case of the *Wobble* method, in which the telescope is pointed to different positions at a small fixed distance from the source. The size of the IACTs Field of View (FoV) makes it possible to take simultaneous ON and OFF data, as described in [195, 498, 581]. Sometimes it is possible to define several OFF regions within the same field, but additional care should be taken to avoid counting events twice.

All the significance estimators tested in this article are based on a binned Maximum Likelihood Ratio approach, which tests an assumed null hypothesis against an alternative one, formulated as:

Null hypothesis, H0 ON and OFF regions contain no sources, only background.

Alternative hypothesis, H1 While the OFF region only contains background, in the ON region there is, in addition, a source.

A simple case, in which the result of an observation is a one-dimensional histogram showing the number of events detected as a function of the squared distance to the source, will be assumed. The number of events per bin will follow Poisson statistics, leading to the Likelihood function:

$$\mathcal{L}(X|\Theta) = \prod_{i}^{N} \frac{f_i^{n_i}(\Theta) e^{-f_i(\Theta)}}{n_i!} \tag{A.1}$$

where Θ is the parameter space for our model, i is the bin index (for a total of N bins), n_i the number of events in bin i and f_i the value of the test model in the given bin.

It is often convenient to work with the negative logarithm of this function,

$$\begin{aligned} \mathbf{L}(X|\Theta) &\equiv -\log \mathcal{L}(X|\Theta) = \\ &= -\sum_{i}^{N} n_i \log f_i(\Theta) - f_i(\Theta) - \log n_i! \end{aligned} \tag{A.2}$$

Since the last term of the summation is only a normalization factor, which does not depend on the parameters of the likelihood (Θ), it can be safely removed and the expression simplified to:

$$\mathbf{L}'(X|\Theta) = -\sum_{i}^{N} n_i \log f_i(\Theta) - f_i(\Theta) \tag{A.3}$$

Now the likelihood ratio λ and its logarithm can be computed, giving:

$$\begin{aligned} -2\log\lambda &\equiv -2\log\left[\frac{\mathcal{L}_{H0}(X|\Theta)}{\mathcal{L}_{H1}(X|\Theta)}\right] = \\ &= 2\{\mathbf{L}'_{H0}(X|\Theta) - \mathbf{L}'_{H1}(X|\Theta)\} \end{aligned} \tag{A.4}$$

From Wilks [582] it is known that, when the null hypothesis is true, $-2\log\lambda$ asymptotically follows a χ^2_r distribution for large event counts, where r is the difference in the number of degrees of freedom between both hypotheses. This can be used to compute the probability of the observed excess being due to a background fluctuation. It can also be translated into a test statistics $TS = \chi^2_1$, where χ^2_1 is the value of the χ^2 with one degree of freedom corresponding to the same probability as the original χ^2_r. The accurate approximation proposed by Wallace [583] can be used to compute the corresponding value in the limit of high TS, while its sign can be set from the sign of the event excess.

The *Li&Ma* method In the *Li&Ma* method, where $r = 1$, only one bin is defined in each, ON and OFF regions. Then TS has an analytical expression, which is normally known as the Li&Ma formula (see [408], formula 17). It depends on $n_{\rm on}$ and $n_{\rm off}$, the number of ON and OFF events respectively and α, the ratio between the effective ON and OFF observation times. A source region must be selected *a priori* to count ON and OFF events, which must be done carefully to avoid losing sensitivity. It is usually chosen as the one giving the maximum significance in a test sample (typically a Crab Nebula test sample) taking into account the PSF of the instrument and the expected background statistics.

The *Li&Ma with fit background* method The number of OFF events can also be obtained by incorporating information from a region larger than that considered in *Li&Ma*, by fitting a background model against the data and integrating the model in the selected signal region. This method usually gives smaller statistical uncertainties, as it is in principle equivalent to having better OFF statistics. In order to use this model, one must be aware of any existing inhomogeneity in the camera or other gamma-ray sources which would introduce additional components in the background shape. An additional constrain exists if Wobble-mode observations are performed, as the wobble offset (distance between the source position and the actual pointing position) limits the maximum range of the fit that can be used

	Number of OFF positions					
	1	3	5	9	15	∞
$S(\sigma)$	4.2	5.2	5.5	5.8	5.9	6.1
		+24%	+31%	+36%	+39%	+44%

Table A.1: Expected improvements from Li&Ma Formula 17 with the number of OFF positions ($1/\alpha$) for the particular case $n_{\rm off} = 640/\alpha$ and $n_{\rm on} = 160 + 640$.

without double-counting events.

We will call this variant hereafter the *Li&Ma with fit background* method. It can be implemented by calculating modified $\alpha' \equiv \alpha\sqrt{\frac{(\delta n_{\rm off})^2}{n_{\rm off}}}$ and $n'_{\rm off} \equiv n_{\rm off}\frac{\alpha}{\alpha'}$ values, where $\delta n_{\rm off}$ is the estimated $n_{\rm off}$ uncertainty. In this case, $\delta n_{\rm off}$ is no longer the Poisson based $\sqrt{n_{\rm off}}$, but the total uncertainty estimated using the fit covariance matrix. α is the actual ratio between the effective ON and OFF time. These new α' and $n'_{\rm off}$ values can be inserted into the *Li&Ma* formula to get the significance.

Other background estimation methods There are other ways of increasing the effective statistics in the background region and thus to potentially improve the sensitivity. One clear example is to increase the number of OFF regions as discussed in section 2.3 of [584]. An example of the gain that can be obtained with this approach is shown in Table A.1. The main advantage of this method is that all the positions remain symmetric with respect to the center of the camera and the relative radial response is the same as in the ON region, which means that the only assumptions that are needed are a radially symmetric camera response, no significant sky changes among the different OFF regions and no additional sources present in the selected OFF positions. These requirements are different from those required in *Li&Ma with fit background* formula and the best solution would thus depend on the particularities of the given instrument.

Another example is the so called *Ring method* [584]. The main advantages of this method is that its symmetry properties make it less prone to systematic errors due to sky gradients. In principle it can be applied to any point of the FoV and it is conceptually similar to other aperture photometry methods widely used in Astronomy. The main drawback is that the response of the OFF region is no longer the same as in the ON region because each position inside the ring lies at a different distance from the center of the camera. It thus becomes necessary to model the camera response carefully, which complicates the evaluation of the observation significance. The comparison of *Li&Ma with fit background* with this method, while possible, is out of the scope of this paper.

The *PSF-Likelihood* method The method proposed in this work has been known as the *PSF-Likelihood* method. It considers not only the number of ON and OFF events, but also the differences between the shapes of the signal and background model, that is, how the ON and OFF events are distributed. Any existing excess produced by a point source should follow the shape of the PSF to be considered as a signal. The statistical hypothesis can be rewritten as:

Null hypothesis, H0 The ON and OFF observations have the same origin, and therefore the same functional shape. Both can be explained with the same background model.

Alternative hypothesis, H1 The ON and OFF samples have a different origin. OFF contains only background events, while ON also contains signal events. An additional PSF-like component is needed to explain the ON data.

In this method, both histograms are fitted at the same time with the models derived from the aforementioned hypotheses, using common parameters, taking into account the different observation times. The Likelihood in each hypothesis is then defined as the product of the Likelihoods for ON and OFF, obtaining a total $\mathbf{L}'(X|\Theta)$ as the sum of the $\mathbf{L}'(X|\Theta)$ for the ON histogram plus that for the OFF data. The probabilities are calculated from $-2\log\lambda$ and translated into significances. The approach is similar to that used in the *Li&Ma* method, but the implementation is slightly different.

A.1.2 Analytic expressions in the limit of perfect background knowledge

Based on common principles, the *PSF-Likelihood* method and the *Li&Ma*'s one converge to similar mathematical expressions at certain limits. This is the case when the background is perfectly known (infinite statistics and precise modelling). In that limit the contributions to the likelihood ratio from the OFF region fit with the two models used in the *PSF-Likelihood* approach cancel approximately, and it can be written as

$$-2\log\lambda = 2\sum_{i}^{N}\left[n_{i,\text{on}}\log\frac{f_{i,\text{on}}}{f_{i,b}} - (f_{i,\text{on}} - f_{i,b})\right] \tag{A.5}$$

where $f_{i,\text{on}/b}$ denotes the value of the background+signal and background models evaluated in bin i and $n_{i,\text{on}/\text{off}}$ the contents of the bin in the real observations.

A similar expression can be derived from Li&Ma formula 17 if we take $n_{\text{off}} = n_b/\alpha$ and calculate the limit of $-2\log\lambda$ when α is very small (perfect background knowledge).

$$\lim_{\alpha\to 0^+}[-2\log\lambda] = 2\left[n_{\text{on}}\log\frac{n_{\text{on}}}{n_b} - (n_{\text{on}} - n_b)\right] \tag{A.6}$$

While the formula are similar, the *PSF-Likelihood* expression is more restrictive on what is called a *signal.* It does not simply require differences between the ON and OFF histograms, but also that the excess behaves like the PSF of the instrument in each bin. In addition the *PSF-Likelihood* method naturally incorporates the information contained in a wider region, removing also the need for a tight cut in the extension of the signal region which, once optimized, may significantly decrease the signal statistics.

As an alternative to using one single bin, the *Li&Ma* could be applied to several bins of the θ^2 histogram individually. In this case, the whole excess would be incorporated, but with a significant drawback. Since no particular PSF shape is assumed, $-2\log\lambda$ would asymptotically behave like a χ^2 with N degrees of freedom, where N is the number of used bins. It would then lead to a low TS once this χ^2_N is translated into χ^2_1. This is not the situation in the *PSF-Likelihood* where the use of a predefined PSF shape that can predict several bin contents does not increase the number of degrees of freedom.

A.2 Method

The methods described above were compared for the case of the search for a point-like source using simulated ON and OFF θ^2 samples. These samples, plotted as histograms, show the number of events recorded as a function of θ^2, where θ is the angular distance to the assumed source position. An automatic pipeline worked on them taking two histograms as input, one used as a source template, the other as the background template, and a template for the PSF. Several samples are then simulated with different amounts of excess events (signal) and computed the significance obtained from each method.

For the source template, a background subtracted signal from MAGIC observations of the Crab Nebula (the standard candle in VHE astronomy) were selected (see Figure A.1).

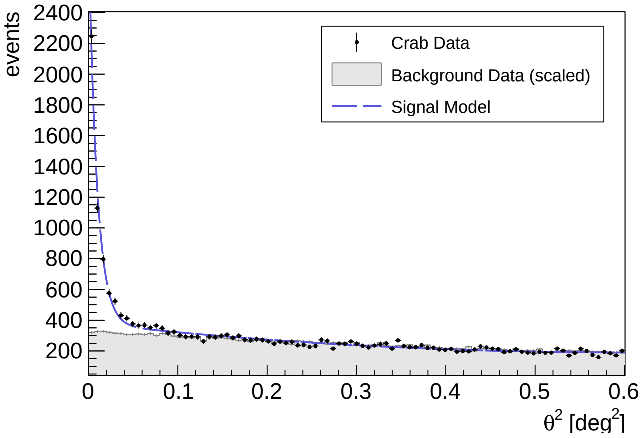

Figure A.1: Experimental θ^2 distribution measured over a Crab Nebula sample with the MAGIC telescopes and scaled OFF data to be subtracted from the Crab Nebula data. The resulting distribution is used to generate the Monte Carlo simulated source samples on which we applied the methods.

A different background sample was generated for each simulation, based on a background template with Poisson fluctuations in each bin. The number of simulated events was the same as in the real background scaled to the observation time. The template itself was obtained by fitting a second order polynomial to the histogram of a high statistics OFF sample. As seen in Figure A.2 it reproduces the data used correctly. If, instead of a smooth template, a real background observation had been used directly as the model, it would have carried with it spurious fluctuations arising from the finite sample statistics, which the simulations would have propagated too, artificially increasing the total spread.

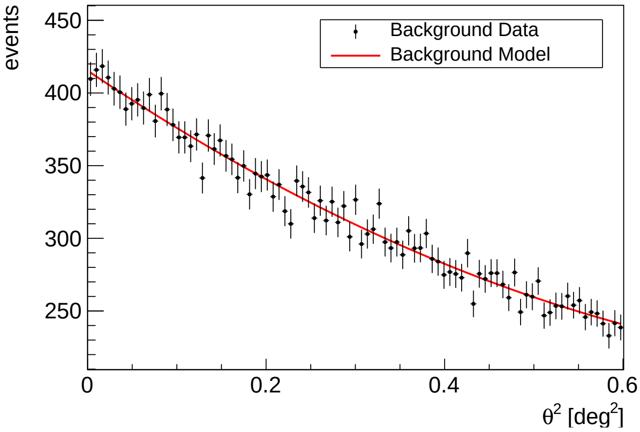

Figure A.2: Experimental θ^2 distribution measured for a background region with the MAGIC telescopes using 3 simultaneous OFF regions. It was found that a 2nd order polynom was complex enough to reproduce the observed data, with a total $\chi^2 = 63.4$ for 88 *d.o.f.*. (In the $\theta^2 < 0.2$ range, using the same parameter values the result was $\chi^2 = 16.3$ for 28 *d.o.f.*).

In order to build the PSF model two possibilities were explored, inspired in the study presented by [585], the King function described in [586] and a simpler Gaussian PSF. Both gave good results, with a minor improvement in the reproduction of the tails in the King function, at the cost of adding one more parameter to be optimized. Since the differences are rather small as regards the significance, the 1D Gaussian in θ, with fixed width σ was finally selected.

The values of σ and the θ^2 cut were optimized for the original Crab sample, so as to be in the best case scenario for all the methods. Using the isolated Crab signal and the background template, $3 \cdot 10^6$ simulated ON and OFF samples were generated for 10 different signal fractions (0%, 0.2%, 0.5%, 1%, 2%, 3%, 5%, 8%, 15% and 50%), covering a wide range of signal strengths.

In each simulation, the *H0* and *H1* statistical hypotheses were tested with the ON and OFF samples for the proposed methods and the significances were calculated. For the *PSF-Likelihood* method this implied fitting the histograms to the models using a binned likelihood minimization with Poissonian errors, using the prescriptions from Section A.1.1. An example of the intermediate results can be seen in Figure A.3.

A.3 Results

The main concern when testing a new detection technique is its statistical correctness. The distribution of significance provided by the method on pure background samples must follow the expected probability distribution. In our case, where the PSF model only adds one degree of freedom to those of the background model, the

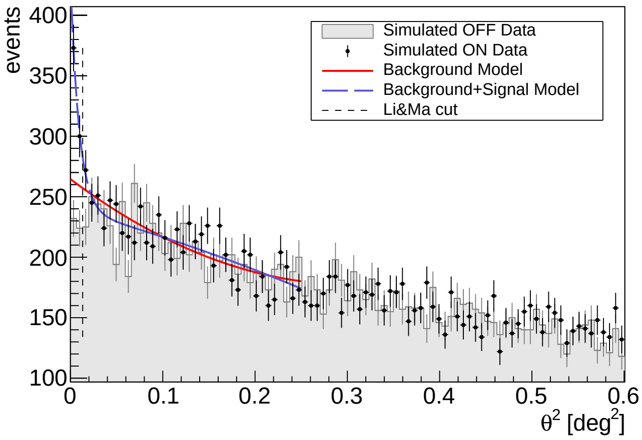

Figure A.3: Testing the method with simulated samples for an ON region with 8% of excess events (black points and error bars) and a single OFF region (shaded region). The background-only model (red line) and background+signal model (blue line) are shown as reference. The dashed vertical line shows the region used by the *Li&Ma* method to count events and calculate the significance.

statistical distribution for background samples according to [582] should be a χ^2_1 just like in *Li&Ma*.

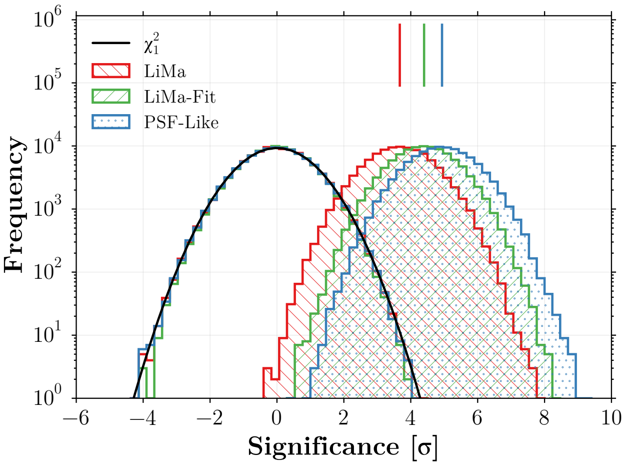

Figure A.4: Significance calculated on background-only Monte Carlo simulations and on a sample with 5% signal with a single OFF region. The expected χ^2_1 distribution for the background-only case is plotted as reference.

From the left-hand curve of Figure A.4, it is seen that the three methods give statistically correct results when tested against background samples with random statistical fluctuations.

After validating the method statistically, it can be checked whether the method is competitive against existing ones. If this is the case, the mean significance provided by the method for samples containing signal should be higher. An example can be seen in the filled curves of Figure A.4, where the different methods are compared for a sample containing a 3% of signal events. A drift towards higher significance values can be clearly seen for the proposed method.

A more complete comparison that covers all the different fractions of excess events simulated is presented in Figure A.5. From the figure, it seems evident that increasing the background statistics (using for instance *Li&Ma with fit background* to extend the region used to calculate the background) helps to improve the sensitivity over the *Li&Ma* method. In the same test, *PSF-Likelihood* outperforms *Li&Ma* and *Li&Ma with fit background* for every step in the signal fraction, proving that taking into account the PSF also contributes to improving the sensitivity of the method.

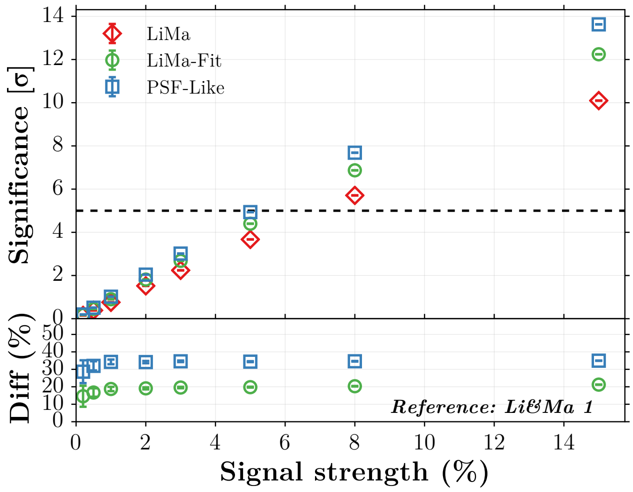

Figure A.5: Significance of different methods on Monte Carlo simulations. The 5σ limit (the usual detection threshold) is drawn as a horizontal dashed line. The differences (%) always refer to *Li&Ma*.

It must be noted that the method allows, at the same time, the number of events detected from the source to be computed, which is simply related to the normalization factor of the fit PSF, and its uncertainty. In that case, the improved sensitivity of the method is translated into smaller uncertainties for the number of excess events, and therefore the fluxes that can be computed from them.

This procedure could also be translated to data with finer energy bins, i.e. the source spectrum. The PSF to be used should then be optimized for each energy bin, as angular resolution usually depends strongly on energy.

In order to estimate how much the uncertainty in the fluxes can be reduced with this method, one may consider the extremely simplified case in which the background is perfectly known, so that $\sqrt{TS} \sim \frac{S}{\sigma(S)}$. Thus, a 35% improvement in $\sqrt{TS}$ would translate into a 35% decrease in the estimated uncertainty. Being more conservative and removing the part of the gain which comes from the improved background statistics, the remaining improvement would be of the order of 10%, as will be seen in section A.3.4.

A.3.1 The method in the limit of low statistics

Li and Ma [408] made an extensive study using MC simulations to detect the practical limits of the Likelihood Ratio approach, since the Wilks theorem [582] only assures that the result is valid for high statistics. They found that the method is fairly robust, giving statistically accurate results with as few as 10 events in the ON and OFF samples.

It should be kept in mind that *PSF-Likelihood* has additional technical complications, which are not genuinely due to the method, but to the implementation. Instead of counting events, it tries to minimize a function, which is not always trivial and the algorithm might fail to converge due to local minima or wrong calculation of gradients, especially in the very low statistics regime. In order to check whether this technical problem could be a potential drawback of the method or not, MC simulations with the same parameters as before were carried out, using a reduced equivalent exposure, which would give rise to very low counts in the ON and OFF samples.

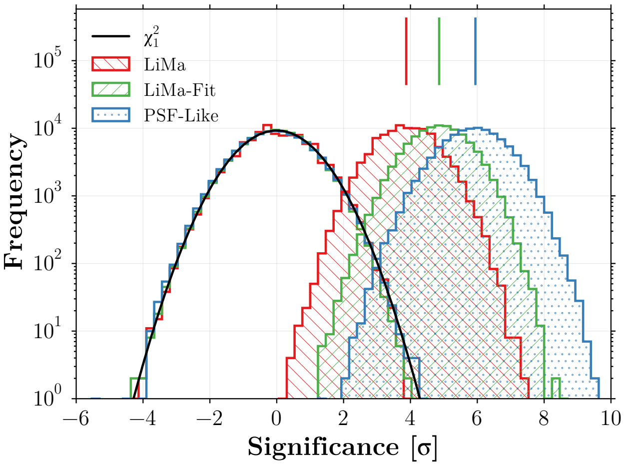

Figure A.6: Significance calculated on background-only Monte Carlo simulations and on a sample with 50% signal with very low statistics per bin.

It was found that, even if the statistics are scarce (of the order of 10 events in the *Li&Ma*-equivalent ON region), the method still works fairly well in most of the cases, with essentially no degradation in the estimated values and with only a minor fraction (of the order of 0.5%) of non-classifiable histograms. Figure A.6 shows the effect of event quantization around $TS = 0$ in the *Li&Ma* distribution.

A.3.2 Non-optimal PSF model

An accurate knowledge of the PSF is not only important in *PSF-Likelihood* but also in *Li&Ma* when optimized cuts are used. In fact, in the latter, the estimation of the optimal cut to select the ON zone is usually done by evaluating both the PSF width and the number of background events. This should be done very carefully and blindly, otherwise it would bias the estimated significance. For *PSF-Likelihood*, a realistic PSF model is desirable to improve the sensitivity when a signal exists in the data, which has a significant impact on the discriminating power of the technique. Nevertheless the correctness of the PSF does not affect the statistical validity of the method, which depends mainly on the accuracy of the background model.

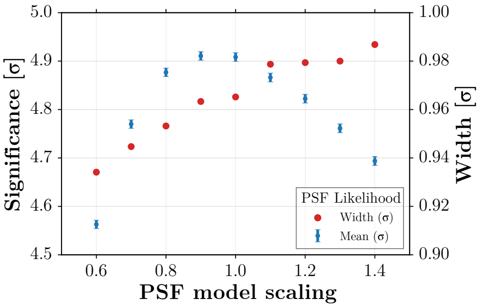

Figure A.7: Significance of PSF-Likelihood with a signal strength of 5% with a systematically wrong PSF model.

Signal	PSF model scaling				
(%)	0.7	0.9	1.0	1.1	1.3
0.0	0.0	0.0	0.0	0.0	0.0
2.0	2.0	2.0	2.0	2.0	2.0
5.0	4.8	4.9	4.9	4.9	4.8
15.0	13.2	13.6	13.5	13.4	13.1
50.0	36.8	37.5	37.3	37.0	36.0

Table A.2: Mean significance (in σ) when a suboptimal PSF shape is used. Errors are of the order of ~ 0.0090, with spread of less than 10%.

In order to study the importance of a good PSF model, additional signal samples were generated and analyzed using a PSF template with a systematically wrong width (scaling from 0.6 to 1.4 times the nominal value). The resulting performance, shown in Figure A.7 and Table A.2, can be compared with that from the standard analysis, represented by the case of a nominal PSF value. There is an obvious shift towards lower significance values of the distributions of $\sqrt{TS}$ with non-zero signal. Despite this, the degradation is never larger than 10% even if the PSF width is wrong by a 40%.

A.3.3 Effects of binning

Since the *Li&Ma* formula uses one single bin in both the ON and OFF regions, the only discrimination power optimization that can be considered comes from the selection of their widths. It is limited by the statistics of events per bin when a tight bin is considered and the amount of background events when the bin is broader. On the other hand, in the *PSF-Likelihood* method the ON region size is limited only by technical limitations of the instrument such as systematic uncertainties which may exist far from the center of the field of view. It seems therefore logical to think that the sensitivity of the method should improve as the bin width decreases due to a better description of the PSF. Although a detailed study of this effect would exceed the scope of this work, some checks were carried out.

Bins	Significance (σ)
1	4.50 ± 0.96
2	4.93 ± 0.97
4	5.07 ± 0.97
8	5.18 ± 0.97

Table A.3: $\sqrt{TS}$ distribution mean and width for 5% signal strength and different binning configurations for the *PSF-Likelihood* method.

Four different bin widths have been simulated and the resulting performance compared in Table A.3, where it was found that the significance improves systematically with decreasing bin width. For a binning four times finer than the standard value (2 bins in $\theta < \theta^2_{cut}$), an additional improvement in *PSF-Likelihood* of $\sim 5\%$ in $\sqrt{TS}$ would have been reached in all the simulations. It can be assumed that the performance could be improved even further with an unbinned likelihood approach, but its treatment is out of the scope of this paper as it would require knowing the precise position information for each event.

A.3.4 Using real background data

The study presented so far was centered in how to proceed when the background and signal behaviour can be described by smooth and simple models, with a few degrees of freedom. Figures A.4-A.7 are generated under this assumption. This is not always the case, and it can be argued that for some experiments the observed background cannot be easily predicted due to systematic effects and changing conditions in the instrument.

For these cases, the method can still be used with good performance. The idea is to replace the analytic function that provides the background shape (so far a polynomial) by a discrete function for which the value of each bin is totally independent, thus turning the bin values into uncorrelated variables. The Likelihood Ratio still behaves like a χ^2_1 because the number of background parameters are the same in the null and alternative hypothesis and there is only one extra parameter to describe the signal. The sensitivity is slightly degraded as the background model is allowed to mimic the signal excess partially, as seen in Figure A.8.

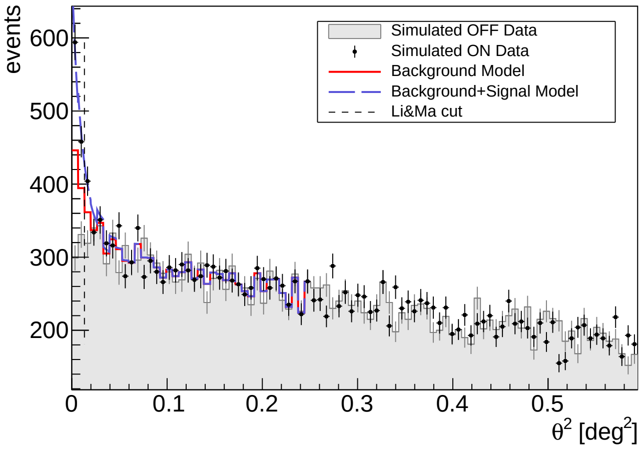

Figure A.8: Testing the method with simulated samples for an ON region with 15% of excess events (black points and error bars) and a single OFF region (shaded region) using an analytic PSF and an empirical background shape (uncorrelated bin values).

Additional care should be taken during the implementation of this variant because the number of parameters for the background function is greatly increased, thus making the whole minimization more complicated for standard algorithms such as `Minuit` [587]. Once implemented, it can be seen that the method behaves correctly when tested against background only data (Figure A.9) and still performs better than the standard Li&Ma (Figure A.10).

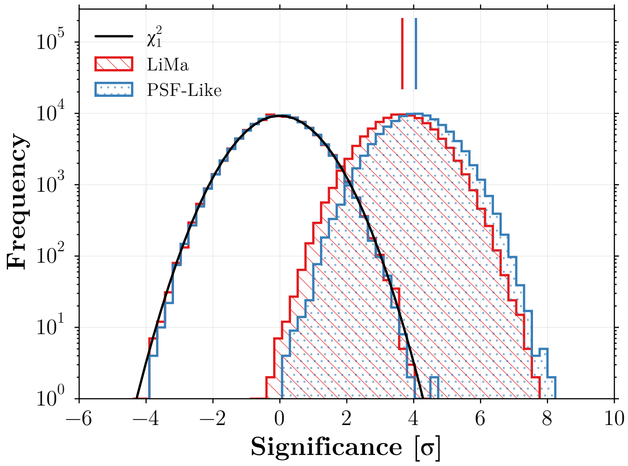

Figure A.9: Significance calculated on background-only Monte Carlo simulations and on a sample with 5% signal.

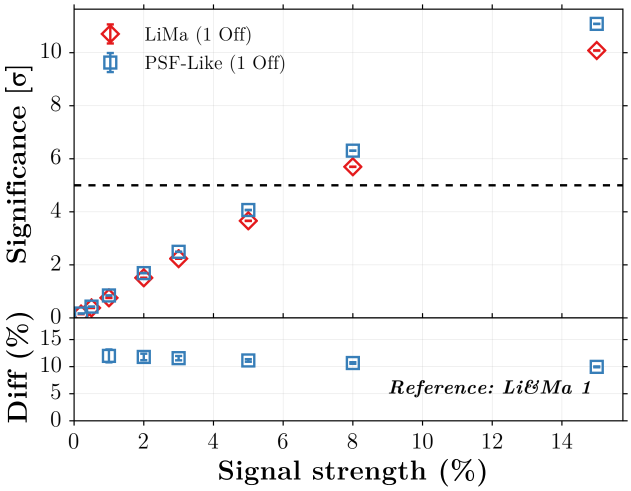

Figure A.10: Evolution of significance against signal strength and improvements on *Li&Ma* with a single OFF region for the background model-less variant of *PSF-Likelihood*.

A.4 Conclusions

A possible implementation of the binned Likelihood Ratio method to estimate the significance of IACT observations of point-like sources, *PSF-Likelihood*, has been described. The method considers measured θ^2 distributions for an ON and OFF region and compares the likelihood that both of them are explained by the same background only model with that including also a source in the ON region.

When the method is tested on Monte Carlo simulations containing only background, it reproduces the expected χ^2_1 significance distribution, proving that the chance probability of a false detection is correctly estimated.

If a certain amount of signal is included in the simulations, an improvement in sensitivity is found over other methods. Part of the gain can be attributed to the increased effective background statistics, but a significant fraction of it stems from the inclusion of the PSF in the method, as was shown in section A.3.4.

The method has been tested in different scenarios, comparing its sensitivity with the different techniques usually employed in the field. An alternative implementation, which does not need a careful modelling of the background, has been proposed and tested in section A.3.4 for those cases in which the background behaviour is not predictable. At the cost of a more complex minimization process, it represents a possible very general worst case alternative implementation.

An additional test was carried out to check whether the performance of the method holds even if the PSF shape is not perfectly known or the reconstructed position of the events does not follow the expected θ^2 distribution. It was found that even in this case, *PSF-Likelihood* still outperforms *Li&Ma*.

Finally it must be highlighted that the procedure proposed can be easily generalized to include additional information. As an example, two dimensional distributions of the events in the sky could be used incorporating the corresponding two dimensional PSF while maintaining the simplicity of the method. It is reasonable to assume, although it has not been tested, that this additional information would increase the discriminating power. The proposed method could also be used for any other imaging observation of point-like sources that incorporates an independent background observation. Also non-positional information such as the tagging variables usually employed in the IACT field to discriminate gamma rays from hadronic cosmic rays would be amenable to this kind of treatment.

B

The MAGIC EBL blazar dataset

In this section of the appendix we compile information about the MAGIC and *Fermi*-LAT observations used to derive the limits on the Extragalactic Background Light density (chapter 11). Some details about each source and the MAGIC analysis are provided as a reference. The selected datasets were found to be ideal to study the imprint of the EBL on the γ-ray blazar spectra. In general, they were selected because of their high quality *Fermi*-LAT and MAGIC data, hard spectra and their moderate or high redshifts.

B.1 1ES 0229+200

1ES 0229+200 is an extragalactic γ-ray source discovered in VHE in December 2006, with a hard spectrum of ~ 2.5 [588]. Its intermediate redshift of $z \sim 0.14$ together with its classification as BL Lac and a spectrum reaching TeV energies make it an ideal candidate for EBL studies. MAGIC observed the source as part of the EBL key science program starting from 2012 with a deep exposure covering several years: 2012-[11,12], 2013-[01,02,09,10], 2014-[08,09,10], 2015-[01,09,10,11,12] and 2016-[10,11]. Its low flux makes it a challenging source to analyze, but no long and short-term variability was detected with current generation of γ-ray instruments, making stacking an option to achieve good statistics.

B.2 1ES 1011+496

An optical outburst occurred in the direction of 1ES 1011+496 ($z = 0.212 \pm 0.002$) in March 2007, triggering MAGIC observations (back then with a single telescope), detecting for the first time this source with a significance of about $6.2\,\sigma$ [589] and an integrated flux of $F_{E>200\,\mathrm{GeV}} = (1.58 \pm 0.32) \times 10^{-11}\,\mathrm{cm}^{-2}\,\mathrm{s}^{-1}$. At the same time, optical observations confirmed the lack of strong spectral features typically seen in HBL sources.

Name	1ES 0229+200
Src. Type	HBL
R.A. [hms]	02 32 53.2
Dec. [dms]	+20 16 21
Redshift	$z = 0.1396 \pm 0.001$
Dataset	>1 year

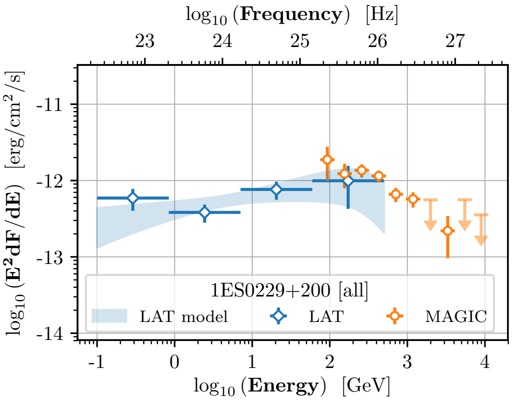

Table B.1: 1ES 0229+200 data from TeVCat [49] and MAGIC + *Fermi*-LAT spectra.

Name	1ES 1011+496
Src. Type	HBL
R.A. [hms]	10 15 04.1
Dec. [dms]	+49 26 01
Redshift	$z = 0.212 \pm 0.002$
Dataset	>1 month

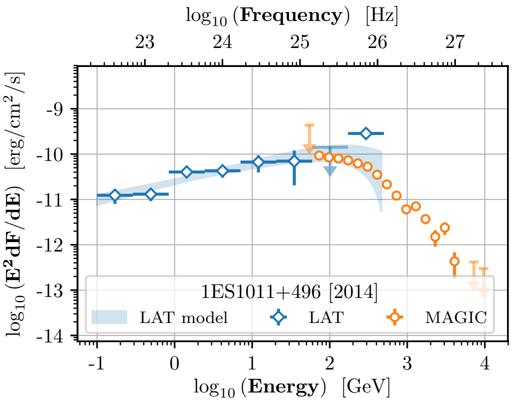

Table B.2: 1ES 1011+496 data from TeVCat [49] and MAGIC + *Fermi*-LAT spectra.

In February-March 2014, the source went again to a very high state [430]. MAGIC observations pointed out to an exceptionally high flux of $F_{E>200\,\mathrm{GeV}} = (2.3 \pm 0.1) \times 10^{-10}\,\mathrm{cm}^{-2}\,\mathrm{s}^{-1}$ (29 times higher than in 2007 observations) and a very hard and stable spectral shape, with an intrinsic spectral index of $\Gamma = 2.0 \pm 0.1$. These characteristics made 1ES 1011+496 one of the best candidates EBL-wise ever observed with an IACT, leading to a statistical significance for the EBL imprint detection with this source alone of $\sim 4.6\,\sigma$ [430].

B.3 1ES 1727+502

Also known as OT 546, this HBL was detected in May-June 2011 as a VHE emitter with MAGIC [590] after an optical outburst and a detection attempt in 2010, which was not conclusive due to bad weather conditions. Its detection in *Fermi*-LAT with a hard spectrum, together with the high quality data obtained in MAGIC for the 2015 campaign (covering about 10 days of IACT observations, yet to be published) motivated its inclusion in the MAGIC EBL dataset. The MAGIC spectral points extend up to several TeV as seen in Figure B.3.

Name	1ES 1727+502
Src. Type	HBL
R.A. [hms]	17 28 18.6
Dec. [dms]	+50 13 10
Redshift	$z = 0.0554 \pm 0.0003$
Dataset	$\sim$ 10 days

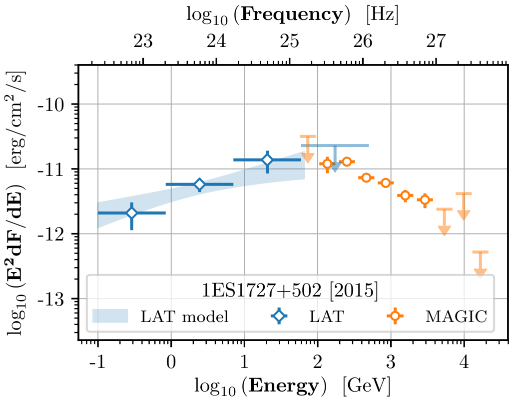

Table B.3: 1ES 1727+502 data from TeVCat [49] and MAGIC + *Fermi*-LAT spectra.

Name	1ES 1959+650
Src. Type	HBL
R.A. [hms]	19 59 59.8
Dec. [dms]	+65 08 55
Redshift	$z \sim 0.048$
Dataset	$\sim$ 10 days

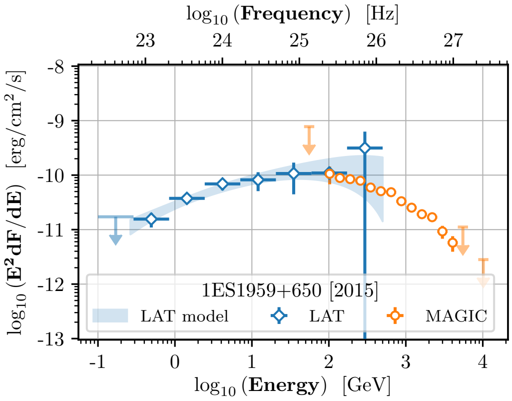

Table B.4: 1ES 1959+650 data from TeVCat [49] and MAGIC + *Fermi*-LAT spectra.

B.4 1ES 1959+650

With a redshift similar to 1ES 1727+502 [591, 592] and a much higher flux that can be as high as several times the flux of the Crab Nebula in this range of energies [593, 594], 1ES 1959+650 is a good target for EBL studies when the source during high states. Under the assumption that the inter-night variability observed in the source affects only the absolute flux normalization but not the shape of the spectrum, stacking can improve the signal-to-noise ratio of the spectrum both in *Fermi*-LAT and MAGIC. In this work we focus on a flare that lasted 1̃0 days in November 2015.

B.5 B0218+357

Also known as S3 0218+35, the gravitationally lensed blazar B0218+357 is the farthest object ever detected with an IACT. The redshift from this object is still controversial, ranging from $z = 0.944 \pm 0.002$ [592] to $z \sim 0.954$ [376]. The source was detected in the VHE band during a very short outburst of two days in 2014 [325] thanks to an alert from LAT for the leading component.

Name	B0218+357
Src. Type	FSRQ
R.A. [hms]	02 21 05.5
Dec. [dms]	+35 56 14
Redshift	$z \sim 0.954$
Dataset	2 days

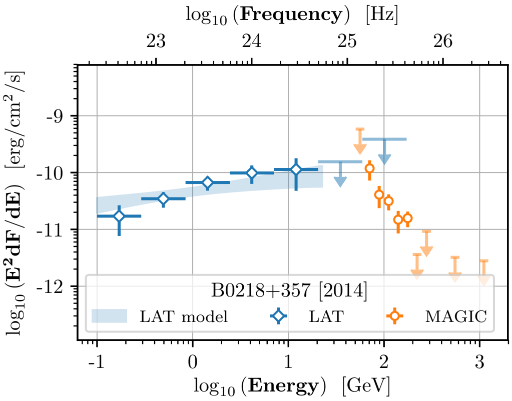

Table B.5: B0218+357 data from TeVCat [49] and MAGIC + *Fermi*-LAT spectra.

Name	BL Lacertae
Src. Type	IBL
R.A. [hms]	22 02 43.3
Dec. [dms]	+42 16 40
Redshift	$z \sim 0.069$
Dataset	1 day

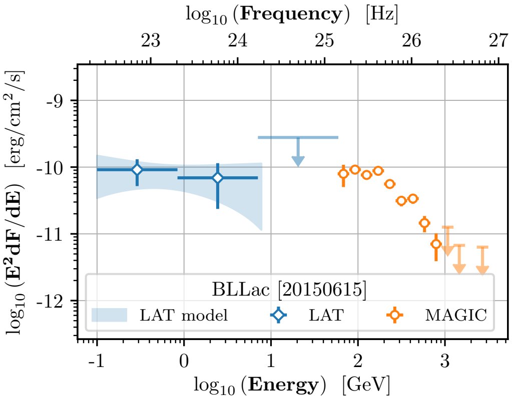

Table B.6: BLLac data from TeVCat [49] and MAGIC + *Fermi*-LAT spectra.

B.6 BL Lac

Classified as an IBL [373] and discovered as a VHE emitter by the Crimean Astrophysical Observatory's GT-48 Cherenkov Detector [595], BL Lac is a strong *Fermi*-LAT source whose emission extends up to $\sim 1\,TeV$ in our MAGIC sample. At a redshift of $z \sim 0.069$, some EBL absorption is expected. The dataset included in this section corresponds to the high state that was observed in June 15th [596].

B.7 Markarian 421

Markarian 421 was the first extragalactic source discovered as a VHE γ-ray emitter. Also known as Mrk 421 or Mkn 421, it was first detected by the Whipple observatory in August 1992 [308] with a flux that was found to be around 30% of those of the Crab Nebula from 0.5 TeV (typical activity from this source). It was later seen by HEGRA, CAT, H.E.S.S, MAGIC, Milagro, Telescope Array, CANGAROO, TACTIC, ARGO-YBJ, HAGAR, FACT, VERITAS and HAWC [49] with outbursts reaching a TeV brightness level of several times those of the Crab Nebula [597]. It is also a rapidly variable source with doubling times of minutes [598].

Mrk 421 is one of the most widely studied sources of the γ-ray sky and its

Name	Markarian 421
Src. Type	HBL
R.A. [hms]	11 04 19
Dec. [dms]	+38 11 41
Redshift	$z \sim 0.031$
Dataset	$\sim$ 10 days (2013) 1 day (2014)

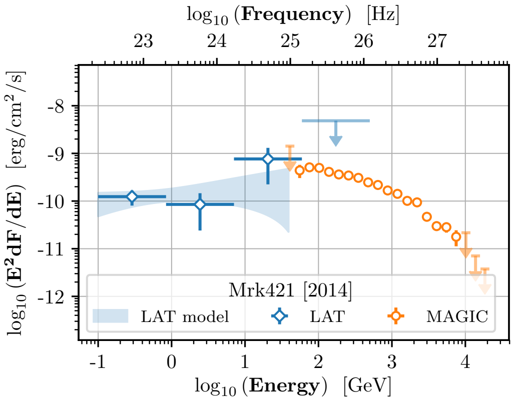

Table B.7: Mrk421 data from TeVCat [49] and MAGIC + *Fermi*-LAT spectra from 2014.

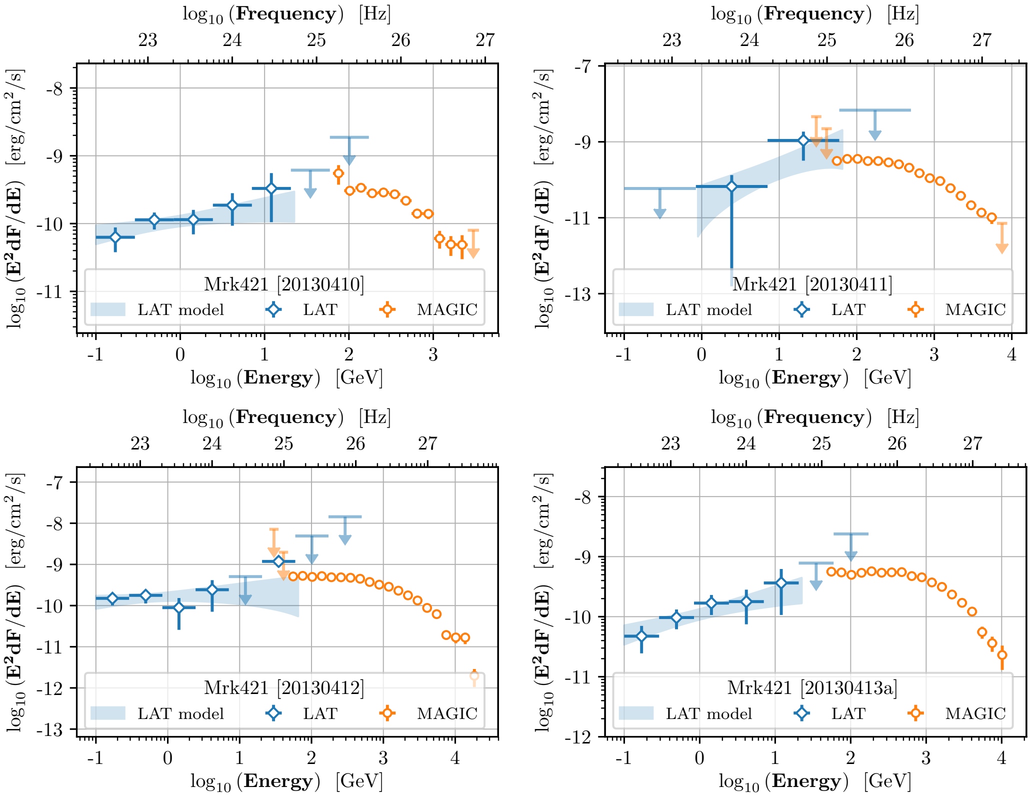

Figure B.1: Mrk421: April 10th and April 11th 2013 (first row), April 12th and April 13th (A) 2013 (second row).

data has been extensively used to test blazar emission models [599–603] and to try to link the emission in different wavelengths [604–610]. Its hard spectrum of $\Gamma \sim 2.2$ and the lack of cutoffs up to several TeV has turned Mrk 421 into a common target for EBL studies [428].

MAGIC has recently observed two big flares coming from this source. The first, in April 2013, exhibited intra-night and day-to-day variability and was hence divided in several sub-samples. The second, shorter, occurred in April 26th 2014. The corresponding contemporaneous *Fermi*-LAT data had enough signal to be split in

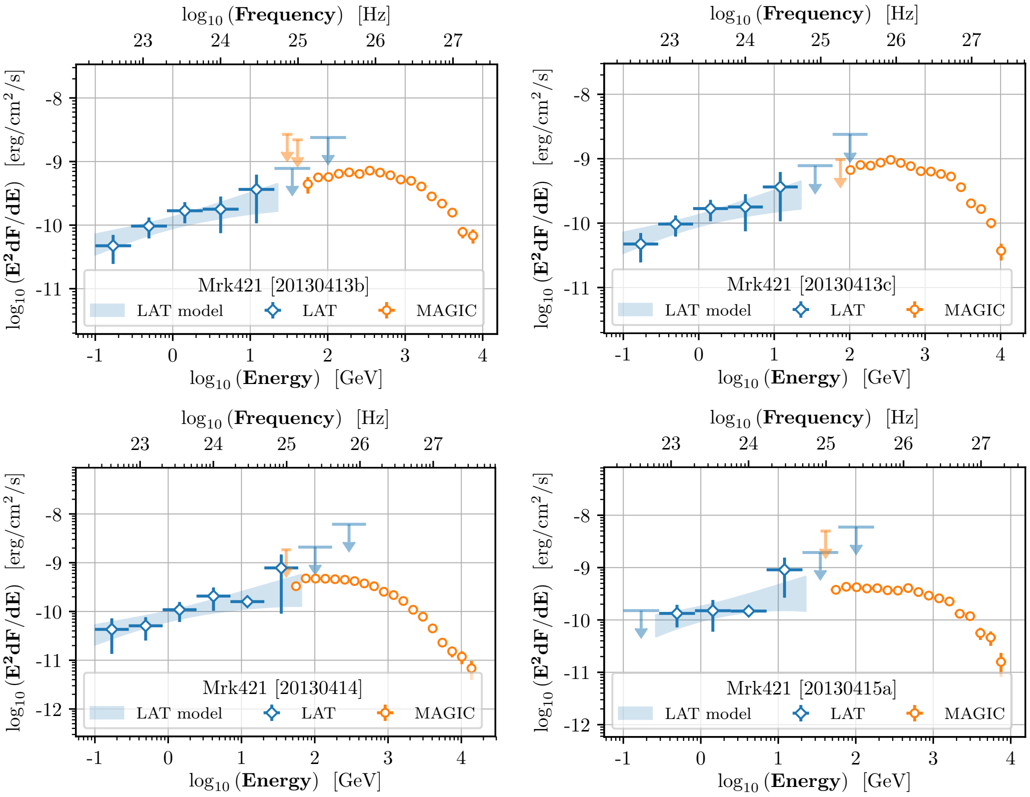

Figure B.2: Mrk421: April 13th (B) and April 13th (C) 2013 (first row), April 14th and April 15th (A) 2013 (second row).

daily bins, but its coverage and signal was not enough to differentiate intra-night variability. In some cases, where significant variability was seen in the *Fermi*-LAT band, the integration window was reduced in order to improve the simultaneity between the MAGIC and *Fermi*-LAT datasets.

B.8 PG 1553+113

Name	PG 1553+113
Src. Type	HBL
R.A. [hms]	15 55 44.7
Dec. [dms]	+11 11 41
Redshift	$0.395 < z < 0.62$
Dataset	Several samples

Table B.8: PG1553+113 data from TeVCat [49].

Discovered by the Palomar-Green survey [611] as a BL-Lac with a featureless spectrum, PG 1553+113 was detected as a VHE emitter by the H.E.S.S telescopes in 2005 [612] and later on confirmed by MAGIC [613]. This object drew astronomers' attention because of the apparent periodicity in its multi-wavelength emission [614]. This is often interpreted as being produced by pulsational-accretional flow instabilities, jet precession, accretion-outflow coupling or even the evidence of a binary supermassive black hole (SMBH) [615].

Periodicity studies together with the strong signal observed for such a distant source has motivated an extended observation program with the MAGIC telescopes [616] which is still on-going as of 2018. Until now, no claim of periodic variability has

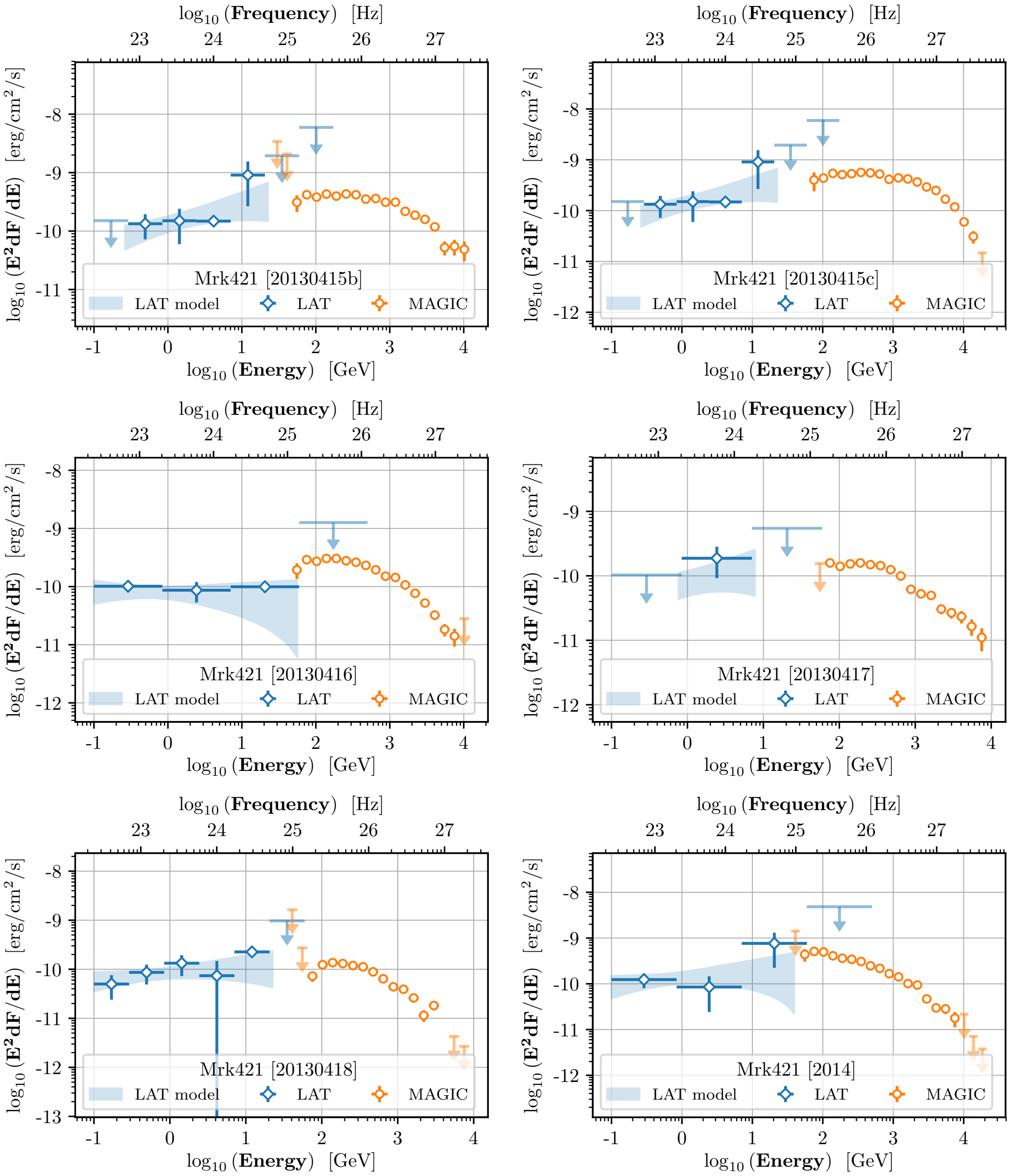

Figure B.3: Mrk421: April 15th (B) and April 15th (C) 2013 (first row), April 16th and April 17th 2013 (second row), April 18th and April 19th 2013 (third row).

been done in VHE. The reason for this is twofold: i) the poor temporal coverage that can be made on such a source (only a few months per year and always in competition with other observational programs); ii) the unpredictable intrinsic variability.

The source is a very interesting candidate for EBL studies for several reasons. First, it is a very strong source with a relative luminous quiescent state. Second, it appears to be reasonably stable in scales of about a month [616]. The lack of strong and fast flares allows us to stack the data (at least in scales of several months) as needed to improve the signal both in MAGIC and *Fermi*-LAT, yielding a very highly detailed γ-rays spectrum.

The main drawback, EBL-wise, is the lack of a firm redshift measurement.

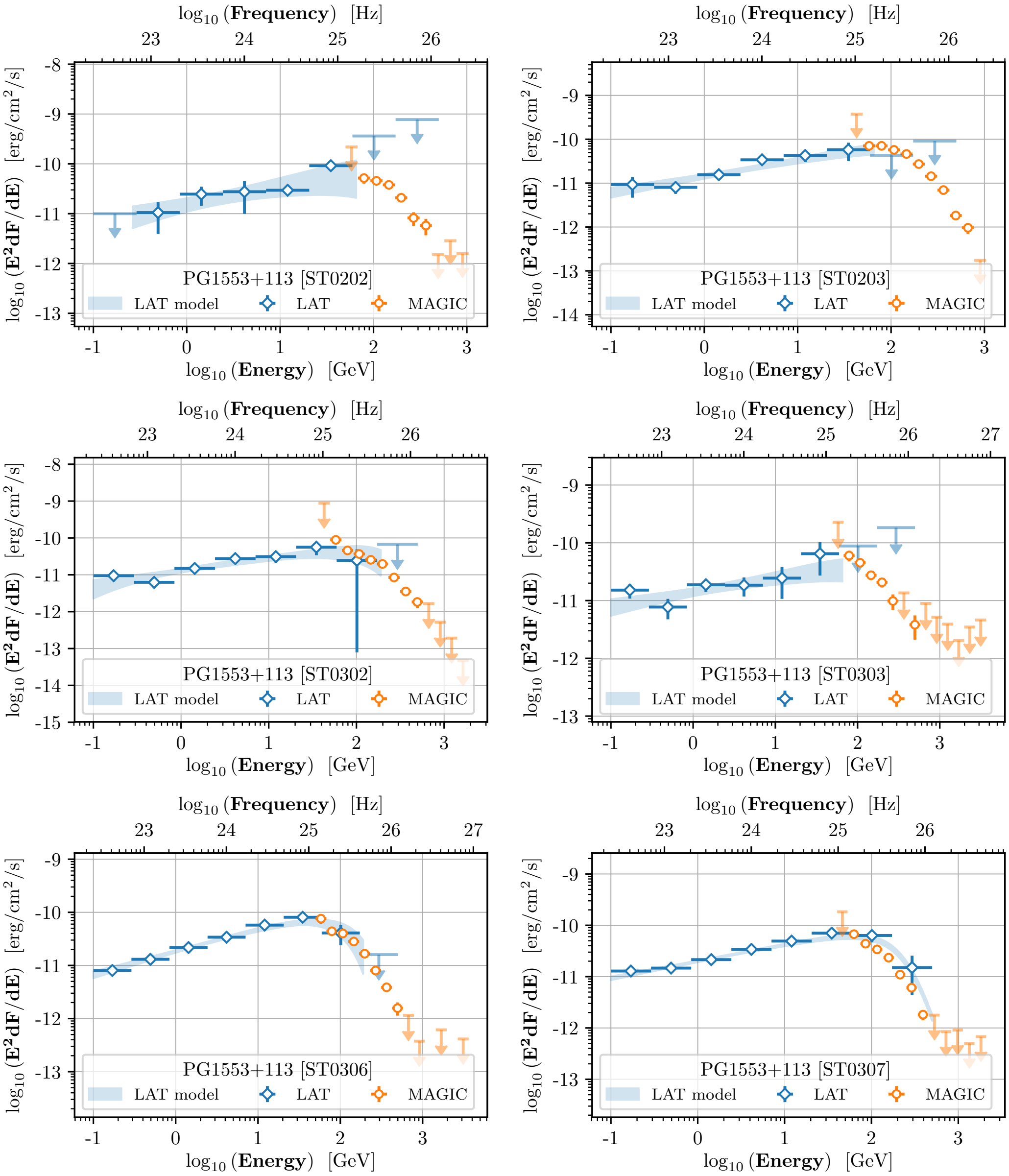

Figure B.4: PG 1553+113: MAGIC periods a) ST0202, b) ST0203, c) ST0302, d) ST0303, e) ST0306, f) ST0307.

Yang and Wang [491] set an upper limit on the redshift of $z < 0.78$ through extrapolation of *Fermi*-LAT data to the VHE range. A similar study, based on VERITAS data [617] lowered this limit to $z \leq 0.62$ and similarly H.E.S.S managed to constraint the redshift with a Bayesian statistic method [618] to 0.49 ± 0.04. These redshifts tend however to be bound in one of another way to EBL models or intrinsic spectral shape assumptions in VHE.

If we restrict the redshift assumptions to the ones not based on VHE observations, the lower limit of $z_{em} > 0.395$ based on confirmed Ly-α + O IV absorbers of $z_{em} > 0.433$, based on single-line detection of Ly-α, and the upper limit of $z_{em} <\sim 0.58$ based on the non-detection of any Ly-β absorbers at $z > 0.4$ are the most constraining measurements available.

In MAGIC, the data taken in stereo mode has been divided in periods based on the differences in IRFs:

- ST0202: ST02XX data covers the comissioning period of the upgrades [185, 190] that took place in both telescopes. DRS4 was installed in both telescopes, but the MAGIC-1 camera was still the original one (576 PMTs, two sizes), while MAGIC-2 had roughly twice that. ST0202 covers data from 2012-02-26 to 2012-03-09 and only 11 runs (4 days) of PG1553+113 were analyzed for that short period of time.
- ST0203: Post-comissioning repairs are finished. This period, of about 2.5 months duration contains 116 runs of PG 1553+113.
- ST0302: ST03XX data was acquired after the commissioning of the upgraded MAGIC-1 camera (similat to MAGIC-2 camera), with improved design and quantum efficiency. Both cameras have now about 1039 pixels all of the same type and size. New MC and IRFs were needed for the upgraded system. In total, during period ST0302 (2013-01-18 to 2013-07-26) 52 runs of PG 1553+113 were taken, covering just above 2 months.
- ST0303: This period covers data from 2013-07-27 until 2014-06-18, and then again 2014-07-05 to 2014-08-05. The gap in between (ST0304) corresponds to Mono observations due to a hardware failure in MAGIC-1. Only 11 runs of the source are available in ST0303.
- ST0306: ST0305 was a transitional period that took place between the maintenance of the heavily damaged mirrors in both telescopes and before the down-sampling of the readout system from 2 GHz to 1.64 GHz that was done to get rid of the deadzone of the stereo trigger systems (a region for which the stereo trigger system was blind because of the delay of arrival times was too large for the trigger buffers to retain the events). After the down-sampling, ST0306 (2014-11-24 to 2016-04-28) started and about 110 runs were taken from January 2015 to August of the same year and a few additional runs from January to April 2016 (most of it of bad quality data).
- ST0307: Newest data available in MAGIC, starting from 2016-04-29 and still running as of 2018 (with the exception of a temporal degradation of the optical PSF which defined ST0308 in fall 2017). This dataset has not been included yet in the EBL sample.

B.9 PKS 1222+216

Also known as 4C+21.35, PKS 1222+216 [619] is a FSRQ discovered in VHE by *Fermi*-LAT and MAGIC in May-June 2010 [620, 621]. Its redshift of $z = 0.4335 \pm 0.0033$ is ideal for EBL studies with IACTs, but its blazar type is non-optimal as FSRQs are known to have intrinsic absorption and exhibit rapid outbursts.

Name	PKS1222+216
Src. Type	FSRQ
R.A. [hms]	12 24 54.4
Dec. [dms]	+21 22 46
Redshift	$z \sim 0.43$
Dataset	$\sim$ 1 hour

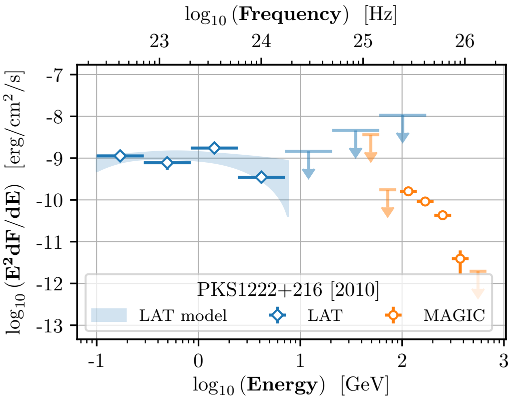

Table B.9: PKS 1222+216 data from TeVCat [49] and MAGIC + *Fermi*-LAT spectra.

In our case, only 2 runs are available for the source in 2010 (before the upgrade of the MAGIC system), which means that less than 1 hour of data is available. This is clearly not enough for *Fermi*-LAT to gather enough photons to make a decent spectrum, so that small period needed to be expanded to include about 4 hours of data, centered at the MAGIC observations.

B.10 PKS 1424+240

Name	PKS 1424+240
Src. Type	HBL
R.A. [hms]	14 27 00.0
Dec. [dms]	+23 47 40
Redshift	$z \sim 0.601(3)$
Dataset	$\sim$ 3 mo. (2014) $\sim$ 5 mo. (2015)

Table B.10: PKS 1424+240 data from TeVCat [49].

Discovered in 1970s as a radio source [479] and first detected in HE γ-rays by *Fermi*-LAT [182] with a relatively hard spectrum ($\Gamma \sim 1.7 - 1.8$), the source was finally seen in VHE γ-rays by the VERITAS experiment [622, 623]. Observations during the campaign of 2014 for this source were described in detail in chapter 9. The data used in this project was taken in two distinct periods, each with its own set of IRFs. 2014 (MAGIC's ST0303) has 119 runs taken in 3 months, while 2015 data (ST0306) is a sparser collection of 74 runs covering 5 months.

B.11 PKS 1441+25

PKS 1441+25 observations were described in chapter 8. The source is a known high-energy (HE, 0.1 GeV < E < 100 GeV) γ-ray flat spectrum radio quasar (FSRQ) [436–438] located at $z = 0.9397 \pm 0.0003_{stat}$[1], which entered a very pronounced high state in multiple wavelength bands in the end of 2014 and peaked in April 2015 with a very hard γ-ray spectrum which made it observable with the MAGIC telescopes.

---

[1] SDSS: `http://skyserver.sdss.org/dr10/en/get/SpecById.ashx?id=6780257851631206400`, see also [439]

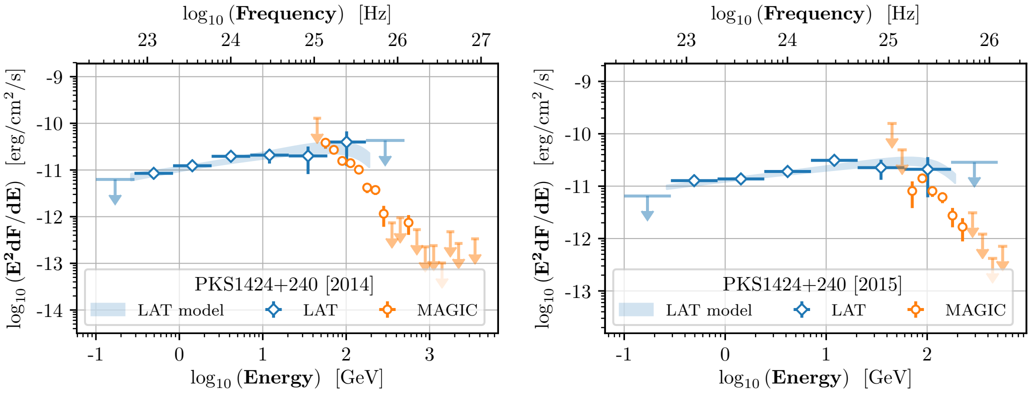

Figure B.5: PKS 1424+240: MAGIC periods ST0303 and ST0306.

Name	PKS1441+25
Src. Type	FSRQ
R.A. [hms]	14 43 56.9
Dec. [dms]	+25 01 44
Redshift	$z \sim 0.939$
Dataset	$\sim$ 5 days

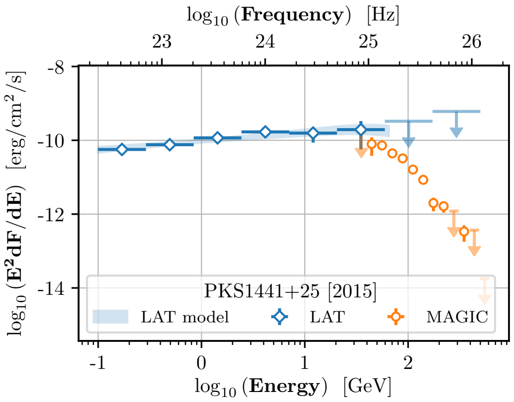

Table B.11: PKS 1441+25 data from TeVCat [49] and MAGIC + *Fermi*-LAT spectra.

B.12 PKS 1510-089

Name	PKS 1510-089
Src. Type	FSRQ
R.A. [hms]	15 12 52.2
Dec. [dms]	−09 06 21.6
Redshift	$z \sim 0.36$
Dataset	$\sim$ 2 nights (2015)
	$\sim$ 3 hours (2016)

Figure B.6: PKS 1510-089 data from TeVCat [49].

The FSRQ PKS 1510-089 was discovered in March-April 2009 by the H.E.S.S. collaboration [624]. With a very soft spectral index of $\Gamma = 5.4 \pm 0.7_{stat} \pm 0.3_{sys}$ and a intermediate redshift of $z = 0.359999(63)$ [625], the source could only be detected during a bright flare in the HE γ-rays, accompanied by a high state in other wavelengths. As with other FSRQs, violent variability was observed and the origin of VHE γ-rays was assumed to be in a region somewhere along the jet far away from the Broad Line Region [419, 626].

The source entered again two significant high states in May 2015 (observed by MAGIC in two nights, with a similar level of activity, [627, 628]) and in May 2016, with an impressive flare that lasted only a few hours [629, 630]. In both cases, we tried to obtain the corresponding spectrum in *Fermi*-LAT by centering LAT exposures at the MAGIC observations. For 2015, we included about 8 hours around the MAGIC observations, while for the the flare in 2016 we integrated one day of *Fermi*-LAT data.

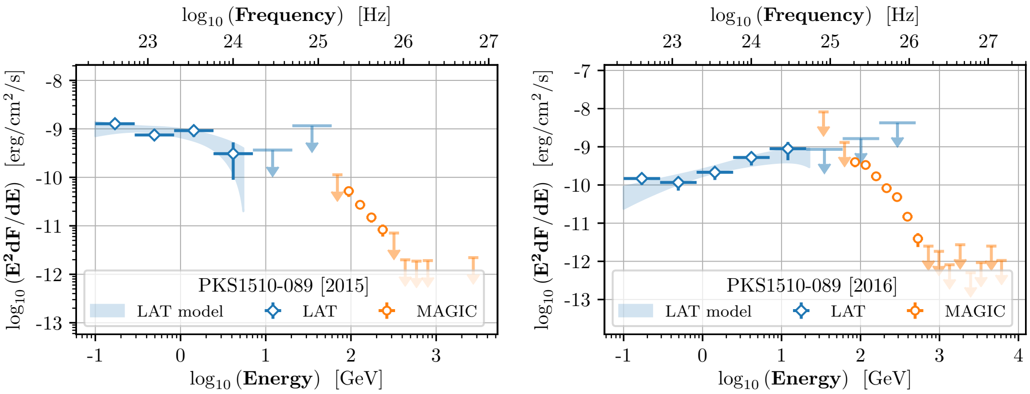

Figure B.7: PKS 1510-089: MAGIC and *Fermi*-LAT observations during the flares in May 2015 and May 2016.

C
Analysis details

In this section of the appendix we give some details of the analyses presented in parts III and IV, which were left out from the main text due to space constraints.

C.1 B0218+357

This section provides additional information about the results described in chapter 7.

C.1.1 *Fermi-LAT PASS8 re-analysis*

B0218+357 data published in Ahnen et al. [325] was analyzed at the time when the *Fermi*-LAT collaboration was working on the PASS8 Data release. It not only included a new reconstruction of the events, but a whole new set of IRFs and diffuse response maps. After the publication, the analysis of the source was redone with the new data. The results obtained from the reanalysis were used in the EBL study presented in chapter 11. The comparison of the PASS7 and PASS8 analyses is shown in Figure C.1.

The differences with the current PASS8 data release are mainly concentrated at the extremes (both low and high) of the LAT spectrum, where the effective area is increased due to improved reconstruction of each event. For B0218+357, the resulting spectrum is not significantly different from the one published by MAGIC[325].

C.1.2 *Swift-XRT cross-check*

The analysis of B0218+357 in *Swift*-XRT with the prescriptions from section 7.4.3 is shown in Figure C.2. A cross-check between the analysis that was finally released in Ahnen et al. [325] and the second analysis done by the author of this lines is provided in the right panel.

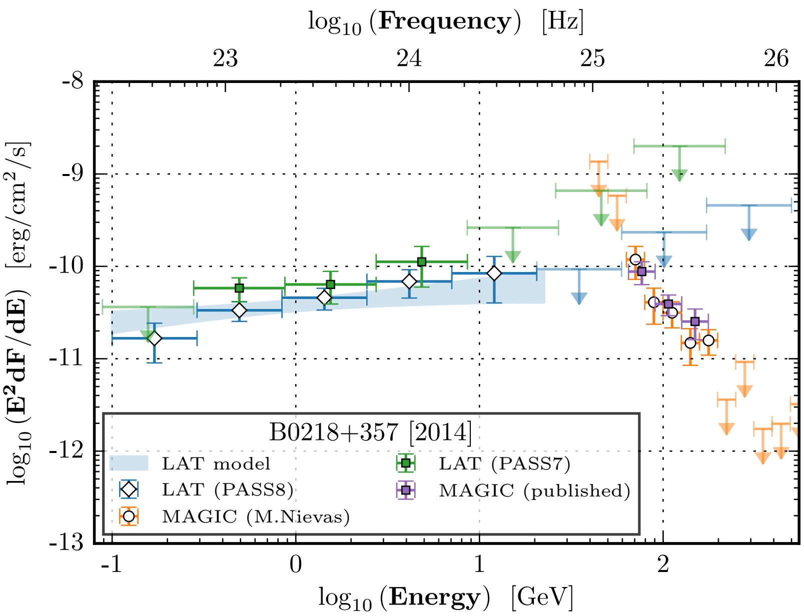

Figure C.1: Broadband γ-ray SED of B0218+357 as observed during the two flaring nights, 25 and 26 of July. Two independent analyses are compared: i) MAGIC and *Fermi*-LAT with PASS7 as published in [325] with filled green and purple squares; ii) an independent reanalysis with different binning in MAGIC and *Fermi*-LAT using a slightly different data selection and PASS8 in *Fermi*-LAT (empty blue and orange markers).

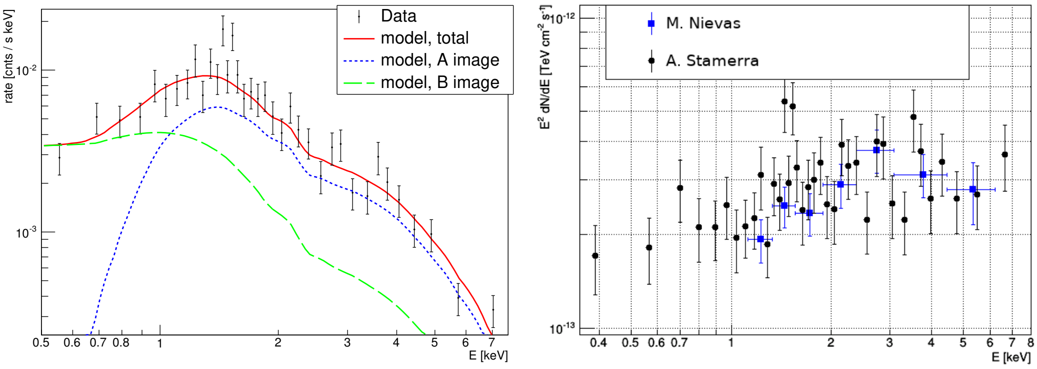

Figure C.2: Left Panel. Energy-binned counts observed by *Swift* from the direction of B0218+357 (data points). The emission is modeled as a sum (solid red line) of two power-law components with the same spectral index. The first component (image A) is magnified by a factor 2.7 with an additional strong hydrogen absorption at the lens (dotted blue line). The second component (image B) is intrinsically weaker (magnification factor 0.7), but not absorbed at the lens (dashed green line). **Right Panel**. Comparison of the analysis which was used in the modeling before re-binning (with contemporaneous but not simultaneous data, black circles) with an independent analysis performed over strictly simultaneous data (blue circles). From the plot, it is clear that the source did not only remain roughly constant in integrated emitted flux, but the shape also was sufficiently stable over the extended period used in the analysis. Credits: Julian Sitarek (private communication).

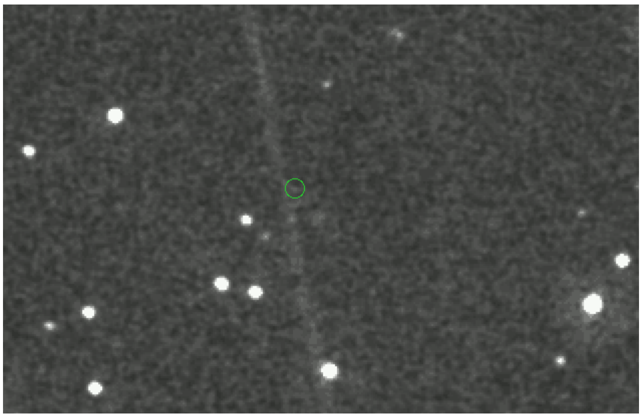

Figure C.3: B0218+357 region as seen by the *Swift*-UVOT in the B band with the expected position of the source marked in green.

C.1.3 Swift-UVOT analysis

As pointed out in Section 7.2.3, the observations of B0218+357 with the optical and UV monitor on board of *Swift* did not result in a significant detection. The integrated exposure was not enough to account for the low flux of the source in this energy band (see Figure C.3). Additionally, the spider that holds the secondary mirror of the telescope in place created a significant diffraction feature coming from a bright star at the border of the field, contaminating the region where the source was supposed to be. This instrument was therefore excluded from the analysis.

C.2 PKS 1424+240

This section contains analysis details which were only mention briefly in chapter 9. First, we describe a method to estimate the energy threshold of a MAGIC data analysis. The second subsection describes in detail the procedure we developed to analyze *Swift*-XRT data.

C.2.1 Energy threshold calculation

The energy threshold of the reconstruction and analysis of the data with IACT instruments heavily depends on the zenith distance (ZD) of the observations and the source itself. When the observations are done at high zenithal angles, the collection area becomes larger at higher energies, but at the same time low energy events (which leave few Cherenkov photons in the atmosphere) are extincted by the thicker atmosphere. This is excellent for sources whose signal is expected to be mainly at energies of several TeVs.

For PKS 1424+240 most of the γ-rays are expected at low energies. This is partly caused by the soft spectrum, but also due to the EBL extinction, which at redshift $z \sim 0.6$ becomes apparent already at $\sim 100\,\mathrm{GeV}$. For such reasons, observations were planned carefully so that the data was acquired when the source was high in the sky and the atmospheric extinction was low. With those constraints, an

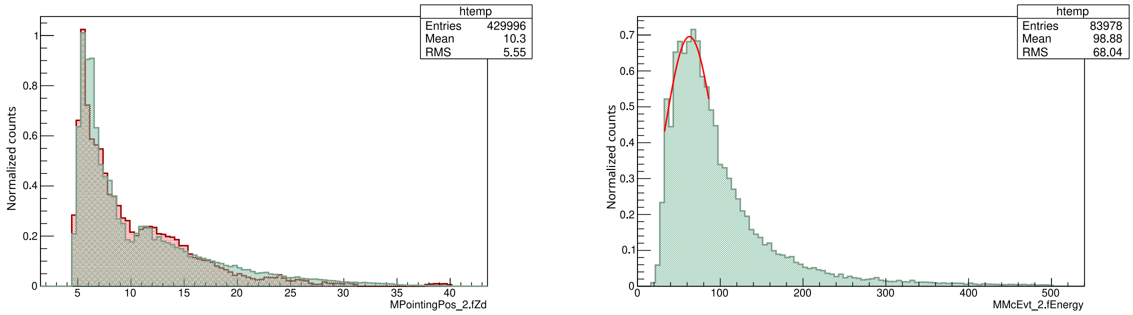

(a) ZD distribution (arbitrary event number scaling) for PKS 1424+240 MAGIC data (red) and MC data (in green, reweighting the events to roughly match the ZD and E_{true} distribution of the data.

(b) True energy distribution (arbitrary event number scaling) of the Monte Carlo simulated events after weighting to match an observed spectrum with $\Gamma \sim 3.6$ and a ZD (similar to PKS 1424+240 data).

Figure C.4: Example of energy threshold calculation. The Gaussian fit to the MC E_{true} distribution yields a mean of $63 \pm 28\,\mathrm{GeV}$.

energy threshold of $E_{th} \sim 60\,\mathrm{GeV}$ is reachable.

The procedure to estimate the energy threshold could be as follows:

1. A histogram containing the pointings of the telescope (or alternatively the event reconstructed ZD) during the observations is drawn using `_Q_` files (reconstructed events, after selection cuts, see Section 5.2.9).

2. A similar set of cuts as those used in the analysis are applied on a pure γ-ray sample of simulated Monte Carlo events analyzed with MARS (using MC `_Q_` files).

3. Events from the previous histogram are weighted by ZD and energy to roughtly match the observed data (see Figure C.4a).

4. The distribution of simulated (true) energies of the MC events are drawn with such cuts and the maximum of the histogram is calculated, which we define as the energy threshold (see Figure C.4b).

Note that the energy threshold, as we have defined it, does not strictly correspond to the minimum possible reconstructed energy of the events.

C.2.2 Swift-XRT analysis

Data preparation

In order to make the analysis of Swift-XRT data for all the sources as systematic as possible, we have prepared a set of tools and uploaded them to `https://github.com/mireianievas/Swift`.

The first step in the XRT analysis is to collect all the available events and exposure maps and generate with them source and background images, spectra and light curves. These steps can be done with `xselect` and the corresponding extraction orders are already implemented in the macro `xrtprepare.py`. It needs as input parameter the full path where the *Swift* data are stored. In addition, the macro looks for the `source.reg` and `background.reg` region files (generated for instance with `ds9`) inside the `XRT` sub-directory. Depending on the rates and if it is needed to correct for pile-up effects, these files should include an annular region instead of a circular one so that the central pixels are excluded (in case they are piled-up). Details about how to deal with piled-up analysis in XRT can be checked here: `http://www.swift.ac.uk/analysis/xrt/pileup.php`.

Then, `xrtprepare.py` creates the `XRT/events` and `XRT/exposure` sub-directories which are populated with symbolic links with all the files containing XRT data that were found in the previous step. The analysis results, including not only the light curves, spectra and events for the source and background region, but also a summed exposure map (`sw_sum_exposures_po_ex.img`) are also stored in `XRT/events`.

Generate ARFs and determine the RMF file

The ancillary response file (ARF) can be generated using the tool `xrtmkarf`. This step needs to be done for every extracted spectrum (in the example we propose, it should be done for the summed source and summed background spectra). `xrtmkarf` receives as input the spectrum file (PHA file), the exposure map, the output file name, two flags (one for PSF correction, needed for non-circular shapes, the other to overwrite any files that previously existed) and finally the position of the source in the image. Note that while `xrtmkarf` can estimate it for the source file (given that it is significantly detected), one should provide the same coordinates for the background ARF generation.

The response matrix files (RMFs) are included as part of the HEASARC calibration database (caldb) for all the instruments of *Swift* and do not need to be generated again. Note however that RMFs are time-dependent (the XRT CCD spectral resolution degrades with time) and it is needed to use an appropriate RMF for the sample that is being analyzed. The correct RMF file can be determined with `xrtmkarf` or `quzcif`.

Data grouping and quality flags

`grppha` is an interactive program distributed with HEASARC/FTOOLS that is in charge of grouping (binning) the data, setting up the quality flags and the fractional systematic errors with channels in the PHA file. For XRT, the basic processing with `grppha` includes setting the first 30 channels as bad data (below 0.3 keV, where the spectral reconstruction is not reliable), binning the data (a minimum of 1 event per bin is needed for Poissonian statistics, while for χ^2 statistics this number is ~ 20) and including the name of the background spectral file, ARF and RMFs inside the header of the source PHA file.

Spectral analysis and unfolding

The spectral analysis in *Swift*-XRT is usually done with `xspec`, which admits the use of macros containing the orders to execute and the model parameters. An example is provided in the github repository: `https://github.com/mireianievas/Swift/blob/master/macro_pwl.xcm`. The procedure it follows is simple:

1. Load the data file (`grppha` output, containing all the information about the RMFs, ARFs, background), open a graphical window, setting the spectral range to plot, setting some physical and cosmological parameters (abundances, photoelectric cross-sections, values for H_0, the deceleration parameter q_0 and Ω_Λ), etc.

2. Define the model. In this step, we have found to be good practice to include all the absorption and multiplicative components (reddening, neutral hydrogen, molecular hydrogen, dust) before the intrinsic model so that after fitting, we can remove the multiplicative components and recover the original spectrum. It is sometimes useful to calculate in this step the integrated flux of the intrinsic model, for which we can use the `cflux` component preceding the intrinsic model (e.g. `powerlaw`).

3. Set the statistics to `cstat` (Poissonian statistics), renormalize, fit the data and plot both the data, fit and residuals of the fit.

4. Recover the intrinsic spectrum by exporting the *unfolded (absorbed) spectrum* (`ufspec`, model dependent), the *ratio* between the data and the folded model (`ratio`) and finally remove the absorbing components by setting their values to zero and export again *unfolded (de-absorbed) spectrum* (`ufspec`). The three files that we generate in this step are called `ObsData_UnfAbsModel`, `ObsData_FoldedModel_ratio` and the de-absorbed `UnfData_UnfDeAbsModel`.

We are mainly interested in the unfolded and de-absorbed spectrum, which is obtained by extracting the intrinsic (de-absorbed) model from the fifth column of the `UnfData_UnfDeAbsModel` file. The model is then multiplied by the ratio between the observed data and the folded model (3rd and 4th columns of `ObsData_FoldedModel_ratio` for the ratio itself and its error). A similar procedure can be done with `ObsData_UnfAbsModel` and `ObsData_FoldedModel_ratio` to obtain the unfolded and absorbed (observed) spectrum.

C.3 Selection based on information criteria

As seen in chapter 11, there is in many cases an ambiguity in the functions used to model the intrinsic spectral shape. In fact, several functions with different number of degrees of freedom may yield similar χ^2 when fitted to the real data. However, the selection of one or another shape may have a significant impact on the measurement of the EBL scaling factor(s). In section 11.2.4, we proposed a simple selection

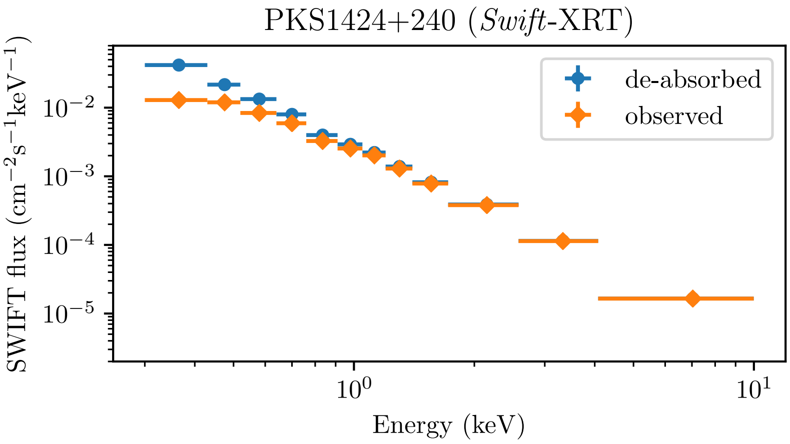

Figure C.5: Unfolded (model dependent) absorbed and de-absorbed spectra of PKS 1424+240

criterion based on the best-fit probability. While statistically more meaningful than the minimum reduced χ^2 of the fit, it still does not properly account for over-fitting. The following example illustrates this:

Example C.3.1. *Suppose we have 10 spectral points that we want to fit with one of the following models. Model A has 3 parameters and gives us* $\chi^2 = 2$. *Model B has 4 parameters and gives us a* $\chi^2 = 1$. *Which model is more appropriate?*

The rule of thumb is to select the model with the smallest reduced χ^2 (A gives $\chi^2_{red} \sim 0.29$, B $\chi^2_{red} \sim 0.17$), and this possibility is further justified if we calculate their probabilities (A giving $P(X, \Theta) \sim 0.96$, B leading with $P(X, \Theta) \sim 0.99$). These simple criteria are however failing to take something into account: we are clearly over-fitting the data.

Both models (particularly B) are complex enough to reproduce not only the data, but also the statistical noise. If new data are introduced, they may fail to reproduce it.

In statistical model selection we are looking for the proper balance (following the so called Principle of Parsimony, also known as Occam's razor) between over-fitting and under-fitting, choosing between simplicity and complexity, balancing bias-variance. A simpler model with fewer parameters means lower variability (more stability), but also larger modeling bias. Complex models reduce bias at the cost of a larger variability and higher risk of over-fitting the data.

Simple likelihood maximization (and χ^2) approaches try to minimize the bias, but they fail to take into account variance. This is clear when one compares nested models, where the more general one (containing the simpler one) will score better (or in the worst case, the same) in $\mathcal{L}(X|\Theta)$ (or χ^2).

The classic way to overcome ill-posed problems (those with no exact solution or multiple solutions) is by means of regularization [631] (e.g. [632–634], also known as Ridge Regression) where the variance of the estimator is reduced at the cost of increasing its bias component by penalizing part of the parameter space. This is somewhat equivalent to introducing additional constraints on the parameters to select among possible solutions for a given problem.

In some cases similar scores are obtained with models of different complexities. In those situations, one can avoid regularization by using criteria such as the Akaike's criterion AIC [635] (based on the minimizing the information lost using the Kullback-Leibler divergence [636]) or its Bayesian counterpart BIC [637].

One of the limitations of the AIC criterion is its validity on small samples (it is bias-corrected only to order $\mathcal{O}^{-1}$). The AICc criterion [638] was developed on top of the AIC as a correction for small samples. Both are modifications of the χ^2 and thus very easy to compute once the sample size (N) and number of parameters in the model including the residual variance (k) are known.

$$AICc = \underbrace{-2\log L_{max} + 2k}_{\text{AIC}} + \underbrace{\frac{2k(k+1)}{N-k-1}}_{\text{small samples}} \tag{C.1}$$

which, in the χ^2 case, reduces to

$$AICc = \chi^2 + 2k + \frac{2k(k+1)}{N-k-1} \tag{C.2}$$

Note that the bias-correction for small samples presented here is in principle valid only when the errors are Gaussian. A bias-corrected ($\mathcal{O}^{-2}$) for the Poissonian distribution of errors was recently developed [639], but it is a common practice to use the Gaussian version when the distributions are not extremely skewed [640].

The best model would be the one that minimizes the $AICc$. In the example described in the beginning of this section, $AICc$ gives 14 for the simpler model (best, selected) and 17 for the more complex one.

The original Akaike Information Criterion is currently implemented in both `fitebl` (part of the `MARS` analysis framework) and `eblfitter` and can be used as a replacement for the probability criterion used to select among source intrinsic spectral shapes.

List of Figures

List of Tables

Bibliography

[1] Victor Franz Hess. “Observations of the penetrating radiation on seven balloon flights”. In: *Physikalische Zeitschrift* 13.1084 (1912).

[2] Victor Franz Hess and translated by Codd, L. W. “The Electrical Conductivity of the Atmosphere and its Causes. By V. F. Hess. Translated from the German by L. W. Codd. London (Constable & Co.), 1928. 8vo. Pp. xviii. and 204. 12s”. In: *Quarterly Journal of the Royal Meteorological Society* 55.231 (1929), pp. 320–322.

[3] J. Clay. “Penetrating Radiation”. In: *Proceedings of the Section of Sciences, Koninklijke Akademie van Wetenschappen te Amsterdam* 30.9-10 (1927), pp. 1115–1127.

[4] W. Bothe and W. Kolhörster. “Das Wesen der Höhenstrahlung”. In: *Zeitschrift für Physik* 56.11 (Nov. 1929), pp. 751–777.

[5] Bruno Rossi. “On the Magnetic Deflection of Cosmic Rays”. In: *Phys. Rev.* 36 (3 Aug. 1930), pp. 606–606.

[6] Thomas H. Johnson. “The Azimuthal Asymmetry of the Cosmic Radiation”. In: *Phys. Rev.* 43 (10 May 1933), pp. 834–835.

[7] Luis Alvarez and Arthur H. Compton. “A Positively Charged Component of Cosmic Rays”. In: *Phys. Rev.* 43 (10 May 1933), pp. 835–836.

[8] Bruno Rossi. “Directional Measurements on the Cosmic Rays Near the Geomagnetic Equator”. In: *Phys. Rev.* 45 (3 Feb. 1934), pp. 212–214.

[9] Bruno Rossi. “Misure sulla distribuzione angolare di intensita della radiazione penetrante all’Asmara”. In: *Ricerca Scientifica* 5 (1 1934), pp. 579–589.

[10] Pierre Auger et al. “Extensive Cosmic-Ray Showers”. In: *Rev. Mod. Phys.* 11 (3-4 July 1939), pp. 288–291.

[11] G. Contopoulos. *Cosmology: The Structure and Evolution of the Universe.* Springer-Verlag, 1987.

[12] H. Hu. “Status of the EAS studies of cosmic rays with energy below 10**16 eV”. In: *ArXiv e-prints* (Nov. 2009).

[13] P. Blasi. “The origin of galactic cosmic rays”. In: A&A Rev. 21, 70 (Nov. 2013), p. 70.

[14] K. Brecher and G. R. Burbidge. “Extragalactic Cosmic Rays”. In: ApJ 174 (June 1972), p. 253.

[15] R. Aloisio, V. Berezinsky, and A. Gazizov. “Transition from galactic to extragalactic cosmic rays”. In: *Astroparticle Physics* 39 (Dec. 2012), pp. 129–143.

[16] G. Brunetti and T. W. Jones. “Cosmic Rays in Galaxy Clusters and Their Nonthermal Emission”. In: *International Journal of Modern Physics D* 23, 1430007-98 (Mar. 2014), pp. 1430007–98.

[17] J. Abraham et al. “Correlation of the highest-energy cosmic rays with the positions of nearby active galactic nuclei”. In: *Astroparticle Physics* 29 (Apr. 2008), pp. 188–204.

[18] N. Mirabal and I. Oya. “Correlating Fermi gamma-ray sources with ultra-high-energy cosmic rays”. In: MNRAS 405 (June 2010), pp. L99–L101.

[19] E. Álvarez et al. “Searches for correlation between UHECR events and high-energy gamma-ray Fermi-LAT data”. In: J. Cosmology Astropart. Phys. 12, 023 (Dec. 2016), p. 023.

[20] V. Petrosian and A. M. Bykov. “Particle Acceleration Mechanisms”. In: Space Sci. Rev. 134 (Feb. 2008), pp. 207–227.

[21] D. B. Melrose. “Acceleration Mechanisms”. In: *ArXiv e-prints* (Feb. 2009).

[22] H. Dreicer. “Electron and Ion Runaway in a Fully Ionized Gas. I”. In: *Physical Review* 115 (July 1959), pp. 238–249.

[23] M. Aschwanden. *Particle Acceleration and Kinematics in Solar Flares*. Springer Netherlands, 2013.

[24] J. Kaastra. *Clusters of Galaxies: Beyond the Thermal View*. Springer New York, 2008.

[25] K. Hirotani. “Particle Accelerator in Pulsar Magnetospheres: Super-Goldreich-Julian Current with Ion Emission from the Neutron Star Surface”. In: ApJ 652 (Dec. 2006), pp. 1475–1493.

[26] E. Fermi. “On the Origin of the Cosmic Radiation”. In: *Phys. Rev.* 75 (8 Apr. 1949), pp. 1169–1174.

[27] M.S. Longair. *High Energy Astrophysics*. Cambridge University Press, 2011.

[28] F. M. Rieger, V. Bosch-Ramon, and P. Duffy. “Fermi acceleration in astrophysical jets”. In: Ap&SS 309 (June 2007), pp. 119–125.

[29] E. Fermi. “Galactic Magnetic Fields and the Origin of Cosmic Radiation.” In: ApJ 119 (Jan. 1954), p. 1.

[30] J. R. Jokipii. “a Model of Fermi Acceleration at Shock Fronts with an Application to the Earth’s Bow Shock”. In: ApJ 143 (Mar. 1966), p. 961.

[31] Igor Oya Vallejo. “Observation of active galatic [sic] nuclei with the Magic telescope”. PhD thesis. Madrid, Oct. 2010.

[32] Abelardo Morelejo Olaizola. “Búsqueda de fuentes cósmicas de radiación gamma de muy alta energía con el detector AIROBICC”. PhD thesis. Madrid, Nov. 2000.

[33] P.V.R. Murthy and A.W. Wolfendale. *Gamma-ray Astronomy*. Cambridge Astrophysics. Cambridge University Press, 1993.

[34] T.C. Weekes. *Very High Energy Gamma-Ray Astronomy*. Series in Astronomy and Astrophysics. CRC Press, 2003.

[35] D. Maoz. *Astrophysics in a Nutshell*. In a Nutshell. Princeton University Press, 2007.

[36] J.D. Jackson. *Classical electrodynamics*. Wiley, 1975.

[37] M. A. Ruderman and P. G. Sutherland. “Theory of pulsars - Polar caps, sparks, and coherent microwave radiation”. In: ApJ 196 (Feb. 1975), pp. 51–72.

[38] W. Heitler. *The Quantum Theory of Radiation*. Dover Books on Physics. Dover Publications, 1954.

[39] F. W. Stecker. “Gamma Ray Astrophysics”. In: *Origin of Cosmic Rays: Proceedings of the NATO Advanced Study Institute held in Durham, England, August 26–September 6, 1974*. Ed. by J. L. Osborne and A. W. Wolfendale. Dordrecht: Springer Netherlands, 1975, pp. 267–334.

[40] F.A. Aharonian. *Very High Energy Cosmic Gamma Radiation: A Crucial Window on the Extreme Universe*. EBSCO ebook academic collection. World Scientific, 2004.

[41] G.E. Romero and G.S. Vila. *Introduction to Black Hole Astrophysics.* Lecture Notes in Physics. Springer Berlin Heidelberg, 2013.

[42] A. Abramowski et al. “Acceleration of petaelectronvolt protons in the Galactic Centre”. In: Nature 531 (Mar. 2016), pp. 476–479.

[43] D. Yan and L. Zhang. “Understanding the TeV emission from a distant blazar PKS 1424+240 in a lepto-hadronic jet model”. In: MNRAS 447 (Mar. 2015), pp. 2810–2816.

[44] M. Cerruti et al. “Luminous and high-frequency peaked blazars: the origin of the γ-ray emission from PKS 1424+240”. In: A&A 606, A68 (Oct. 2017), A68.

[45] J. A. Goodman. “Study of galactic gamma ray sources with Milagro”. In: *Journal of Physics: Conference Series* 60.1 (2007), p. 123.

[46] F. W. Stecker. “Diffuse Cosmic Gamma rays: Present Status of Theory and Observations”. In: *Nature Physical Science* 241 (Jan. 1973), pp. 74–77.

[47] T. M. Kneiske. “Gamma-Ray Background: A Review”. In: *Chinese Journal of Astronomy and Astrophysics Supplement* 8 (Oct. 2008), pp. 219–225.

[48] A. G. Cohen, A. De Rújula, and S. L. Glashow. “A Matter-Antimatter Universe?” In: ApJ 495 (Mar. 1998), pp. 539–549.

[49] S. P. Wakely and D. Horan. “TeVCat: An online catalog for Very High Energy Gamma-Ray Astronomy”. In: *International Cosmic Ray Conference* 3 (2008), pp. 1341–1344.

[50] M. Ackermann et al. “High-energy Gamma-Ray Emission from Solar Flares: Summary of Fermi Large Area Telescope Detections and Analysis of Two M-class Flares”. In: ApJ 787, 15 (May 2014), p. 15.

[51] E. Aliu et al. “Observation of Pulsed γ-Rays Above 25 GeV from the Crab Pulsar with MAGIC”. In: *Science* 322 (Nov. 2008), p. 1221.

[52] I. A. Grenier and A. K. Harding. “Gamma-ray pulsars: A gold mine”. In: *Comptes Rendus Physique* 16 (Aug. 2015), pp. 641–660.

[53] F. A. Aharonian, S. V. Bogovalov, and D. Khangulyan. “Abrupt acceleration of a ‘cold’ ultrarelativistic wind from the Crab pulsar”. In: Nature 482 (Feb. 2012), pp. 507–509.

[54] J. Aleksić et al. “Detection of bridge emission above 50 GeV from the Crab pulsar with the MAGIC telescopes”. In: A&A 565, L12 (May 2014), p. L12.

[55] Michael Gajdus. “The Vela pulsar in very high energy gamma-rays with H.E.S.S. II”. PhD thesis. Humboldt-Universität zu Berlin, Mathematisch-Naturwissenschaftliche Fakultät, 2016.

[56] A. Djannati-Ataï et al. “Probing Vela pulsar down to 20 GeV with H.E.S.S. II observations”. In: *AIP Conference Proceedings* 1792.1 (2017), p. 040028.

[57] G. Dubus. “Gamma-ray binaries and related systems”. In: A&A Rev. 21, 64 (Aug. 2013), p. 64.

[58] P. C. Gregory and A. R. Taylor. “New highly variable radio source, possible counterpart of gamma-ray source CG135+1”. In: Nature 272 (Apr. 1978), pp. 704–706.

[59] P. C. Gregory et al. “The radio, optical, X-ray, gamma-ray star LSI +61 deg 303”. In: AJ 84 (July 1979), pp. 1030–1036.

[60] M. Chernyakova, A. Neronov, and R. Walter. “INTEGRAL and XMM-Newton observations of LSI +61° 303”. In: MNRAS 372 (Nov. 2006), pp. 1585–1592.

[61] J. Albert et al. “Variable Very-High-Energy Gamma-Ray Emission from the Microquasar LS I +61 303”. In: *Science* 312 (June 2006), pp. 1771–1773.

[62] J. Albert et al. “Periodic Very High Energy γ-Ray Emission from LS I +61°303 Observed with the MAGIC Telescope”. In: ApJ 693 (Mar. 2009), pp. 303–310.

[63] M. F. Cawley et al. “Variability in the light curve of very high energy gamma rays from Cygnus X-3”. In: ApJ 296 (Sept. 1985), pp. 185–189.

[64] P. M. Chadwick et al. “Further Evidence for the Emission of 1000 GeV Gamma Rays with 12 ms Periodicity from Cygnus X-3”. In: *NATO Advanced Science Institutes (ASI) Series C*. Ed. by K. E. Turver. Vol. 199. NATO Advanced Science Institutes (ASI) Series C. 1987, p. 115.

[65] C. C. G. Bowden et al. “Recent Observations of VHE Gamma Rays from Cygnus X-3”. In: *International Cosmic Ray Conference* 1 (Aug. 1991), p. 253.

[66] R. Giacconi et al. “An X-Ray Survey of the Cygnus Region”. In: ApJ 148 (June 1967), p. L119.

[67] L. L. E. Braes and G. K. Miley. “Radio Detection of Cygnus X-3”. In: Nature 237 (June 1972), p. 506.

[68] P. C. Gregory and P. P. Kronberg. “Discovery of Giant Radio Outburst from Cygnus X-3”. In: Nature 239 (Oct. 1972), pp. 440–443.

[69] J. M. Bonnet-Bidaud and G. Chardin. “Cygnus X-3, a critical review.” In: Phys. Rep. 170 (Dec. 1988), pp. 325–404.

[70] G. Chardin and G. Gerbier. “Cygnus X-3 at high energies - A critical analysis of observational results”. In: A&A 210 (Feb. 1989), pp. 52–65.

[71] M. H. van Kerkwijk et al. “Infrared helium emission lines from Cygnus X-3 suggesting a Wolf-Rayet star companion”. In: Nature 355 (Feb. 1992), pp. 703–705.

[72] F. Aharonian et al. “An unidentified TeV source in the vicinity of Cygnus OB2”. In: A&A 393 (Oct. 2002), pp. L37–L40.

[73] W. Bednarek. “Gamma-rays and cosmic rays from a pulsar in Cygnus OB2”. In: MNRAS 345 (Nov. 2003), pp. 847–853.

[74] F. Camilo et al. “Radio Detection of LAT PSRs J1741-2054 and J2032+4127: No Longer Just Gamma-ray Pulsars”. In: ApJ 705 (Nov. 2009), pp. 1–13.

[75] A. G. Lyne et al. “The binary nature of PSR J2032+4127”. In: MNRAS 451 (July 2015), pp. 581–587.

[76] J. Marti, J. M. Paredes, and M. Ribo. “The system LS 5039: a new massive radio emitting X-ray binary”. In: A&A 338 (Oct. 1998), pp. L71–L74.

[77] M. Ribó et al. “<ASTROBJ>LS 5039</ASTROBJ>: A runaway microquasar ejected from the galactic plane”. In: A&A 384 (Mar. 2002), pp. 954–964.

[78] F. Aharonian et al. “Discovery of Very High Energy Gamma Rays Associated with an X-ray Binary”. In: *Science* 309 (July 2005), pp. 746–749.

[79] M. F. Bode and A. Evans. *Classical Novae*. Apr. 2008.

[80] A. A. Abdo et al. “Gamma-Ray Emission Concurrent with the Nova in the Symbiotic Binary V407 Cygni”. In: *Science* 329 (Aug. 2010), pp. 817–821.

[81] M. Ackermann et al. “Fermi establishes classical novae as a distinct class of gamma-ray sources”. In: *Science* 345 (Aug. 2014), pp. 554–558.

[82] C. C. Cheung et al. “Fermi-LAT Gamma-Ray Detections of Classical Novae V1369 Centauri 2013 and V5668 Sagittarii 2015”. In: ApJ 826, 142 (Aug. 2016), p. 142.

[83] M. Hernanz. “Gamma-ray Emission from Nova Outbursts”. In: *Stellar Novae: Past and Future Decades*. Ed. by P. A. Woudt and V. A. R. M. Ribeiro. Vol. 490. Astronomical Society of the Pacific Conference Series. Dec. 2014, p. 319.

[84] E. Aliu et al. “VERITAS Observations of the Nova in V407 Cygni”. In: ApJ 754, 77 (July 2012), p. 77.

[85] M. L. Ahnen et al. “Very high-energy γ-ray observations of novae and dwarf novae with the MAGIC telescopes”. In: A&A 582, A67 (Oct. 2015), A67.

[86] J. Becker Tjus et al. “Gamma-ray emitting supernova remnants as the origin of Galactic cosmic rays?” In: *Astroparticle Physics* 81 (Aug. 2016), pp. 1–11.

[87] H. Abdalla et al. “H.E.S.S. observations of RX J1713.7-3946 with improved angular and spectral resolution; evidence for gamma-ray emission extending beyond the X-ray emitting shell”. In: *ArXiv e-prints* (Sept. 2016).

[88] D.F. Torres and O. Reimer. *Cosmic Rays in Star-Forming Environments: Proceedings of the Second Session of the Sant Cugat Forum on Astrophysics*. Astrophysics and Space Science Proceedings. Springer Berlin Heidelberg, 2013.

[89] J. W. Hewitt and M. Lemoine-Goumard. “Observations of supernova remnants and pulsar wind nebulae at gamma-ray energies”. In: *Comptes Rendus Physique* 16 (Aug. 2015), pp. 674–685.

[90] F. A. Aharonian. “Gamma rays from supernova remnants”. In: *Astroparticle Physics* 43 (Mar. 2013), pp. 71–80.

[91] S. Archambault et al. “Gamma-Ray Observations of Tycho’s Supernova Remnant with VERITAS and Fermi”. In: ApJ 836, 23 (Feb. 2017), p. 23.

[92] M. L. Ahnen et al. “A cut-off in the TeV gamma-ray spectrum of the SNR Cassiopeia A”. In: *ArXiv e-prints* (July 2017).

[93] E. G. Berezhko and H. J. Völk. “Hadronic versus leptonic origin of the gamma-ray emission from supernova remnant RX J1713.7-3946”. In: A&A 492 (Dec. 2008), pp. 695–701.

[94] A. R. Bell et al. “Cosmic-ray acceleration and escape from supernova remnants”. In: MNRAS 431 (May 2013), pp. 415–429.

[95] F. Acero et al. “Prospects for Cherenkov Telescope Array Observations of the Young Supernova Remnant RX J1713.7-3946”. In: ApJ 840, 74 (May 2017), p. 74.

[96] S. Giacchè and J. G. Kirk. “Electron Acceleration at Pulsar Wind Termination Shocks”. In: ApJ 835, 235 (Feb. 2017), p. 235.

[97] S. J. Tanaka and F. Takahara. “A Model of the Spectral Evolution of Pulsar Wind Nebulae”. In: ApJ 715 (June 2010), pp. 1248–1257.

[98] D. F. Torres et al. “Time-dependent modeling of TeV-detected, young pulsar wind nebulae”. In: *Journal of High Energy Astrophysics* 1 (May 2014), pp. 31–62.

[99] M. Meyer, D. Horns, and H.-S. Zechlin. “The Crab Nebula as a standard candle in very high-energy astrophysics”. In: A&A 523, A2 (Nov. 2010), A2.

[100] J. Aleksić et al. “Measurement of the Crab Nebula spectrum over three decades in energy with the MAGIC telescopes”. In: *Journal of High Energy Astrophysics* 5 (Mar. 2015), pp. 30–38.

[101] H. Abdalla et al. “The population of TeV pulsar wind nebulae in the H.E.S.S. Galactic Plane Survey”. In: *ArXiv e-prints* (Feb. 2017).

[102] M. Ackermann et al. “The Spectrum and Morphology of the Fermi Bubbles”. In: ApJ 793, 64 (Sept. 2014), p. 64.

[103] G. Dobler et al. “The Fermi Haze: A Gamma-ray Counterpart to the Microwave Haze”. In: ApJ 717 (July 2010), pp. 825–842.

[104] D. P. Finkbeiner. “WMAP Microwave Emission Interpreted as Dark Matter Annihilation in the Inner Galaxy”. In: *ArXiv Astrophysics e-prints* (Sept. 2004).

[105] F. Guo and W. G. Mathews. “The Fermi Bubbles. I. Possible Evidence for Recent AGN Jet Activity in the Galaxy”. In: ApJ 756, 181 (Sept. 2012), p. 181.

[106] J. Bland-Hawthorn et al. “Fossil Imprint of a Powerful Flare at the Galactic Center along the Magellanic Stream”. In: ApJ 778, 58 (Nov. 2013), p. 58.

[107] K. Zubovas, A. R. King, and S. Nayakshin. “The Milky Way’s Fermi bubbles: echoes of the last quasar outburst?” In: MNRAS 415 (July 2011), pp. L21–L25.

[108] K.-S. Cheng et al. “Origin of the Fermi Bubble”. In: ApJ 731, L17 (Apr. 2011), p. L17.

[109] R. M. Crocker and F. Aharonian. “Fermi Bubbles: Giant, Multibillion-Year-Old Reservoirs of Galactic Center Cosmic Rays”. In: *Physical Review Letters* 106.10, 101102 (Mar. 2011), p. 101102.

[110] M. Su, T. R. Slatyer, and D. P. Finkbeiner. “Giant Gamma-ray Bubbles from Fermi-LAT: Active Galactic Nucleus Activity or Bipolar Galactic Wind?” In: ApJ 724 (Dec. 2010), pp. 1044–1082.

[111] J. Kataoka et al. “Suzaku Observations of the Diffuse X-Ray Emission across the Fermi Bubbles’ Edges”. In: ApJ 779, 57 (Dec. 2013), p. 57.

[112] E. Carretti et al. “Giant magnetized outflows from the centre of the Milky Way”. In: Nature 493 (Jan. 2013), pp. 66–69.

[113] D. Malyshev. “Fermi Bubbles: an elephant in the gamma-ray sky”. In: *European Physical Journal Web of Conferences*. Vol. 136. European Physical Journal Web of Conferences. Mar. 2017, p. 03011.

[114] V. L. Ginzburg. “Gamma Radiation of Magellanic Clouds and Metagalactic Origin of Cosmic Rays”. In: *Nature Physical Science* 239 (Sept. 1972), pp. 8–9.

[115] F. W. Stecker. “Gamma rays from the magellanic clouds”. In: *NASA STI/Recon Technical Report N* 78 (Aug. 1977).

[116] X. Chi and A. W. Wolfendale. “Gamma Rays from the Magellanic Clouds and the Origin of Cosmic Rays”. In: *International Cosmic Ray Conference* 1 (1993), p. 144.

[117] A. A. Petrukhin and S. Yu. Matveev. “Gamma-Rays from magellanic clouds and origin of cosmic rays”. In: *Bulletin of the Russian Academy of Sciences: Physics* 73.5 (May 2009), pp. 584–587.

[118] M. Ackermann et al. “Deep view of the Large Magellanic Cloud with six years of Fermi-LAT observations”. In: A&A 586, A71 (Feb. 2016), A71.

[119] M. Ackermann et al. “An extremely bright gamma-ray pulsar in the Large Magellanic Cloud”. In: *Science* 350.6262 (2015), pp. 801–805.

[120] A. Abramowski et al. “The exceptionally powerful TeV γ-ray emitters in the Large Magellanic Cloud”. In: *Science* 347 (Jan. 2015), pp. 406–412.

[121] M. Ackermann et al. “Observations of M31 and M33 with the Fermi Large Area Telescope: A Galactic Center Excess in Andromeda?” In: ApJ 836, 208 (Feb. 2017), p. 208.

[122] A. A. Abdo et al. “Detection of Gamma-Ray Emission from the Starburst Galaxies M82 and NGC 253 with the Large Area Telescope on Fermi”. In: ApJ 709 (Feb. 2010), pp. L152–L157.

[123] T. Piran. “The physics of gamma-ray bursts”. In: *Reviews of Modern Physics* 76 (Oct. 2004), pp. 1143–1210.

[124] M. Ackermann et al. “Fermi Observations of GRB 090510: A Short-Hard Gamma-ray Burst with an Additional, Hard Power-law Component from 10 keV TO GeV Energies”. In: ApJ 716 (June 2010), pp. 1178–1190.

[125] F. Piron. “Gamma-ray bursts at high and very high energies”. In: *Comptes Rendus Physique* 17 (June 2016), pp. 617–631.

[126] T. Piran. “Gamma-ray bursts and the fireball model”. In: Phys. Rep. 314 (June 1999), pp. 575–667.

[127] F. G. Schröder. “Radio detection of Extensive Air Showers (ECRS 2016)”. In: *ArXiv e-prints* (Jan. 2017).

[128] and. “On the stopping of fast particles and on the creation of positive electrons”. In: *Proceedings of the Royal Society of London A: Mathematical, Physical and Engineering Sciences* 146.856 (1934), pp. 83–112.

[129] K. Schmeiser and W. Bothe. “Die harten Ultrastrahlschauer”. In: *Annalen der Physik* 424.1-2 (1938), pp. 161–177.

[130] W. Kolhörster, I. Matthes, and E. Weber. “Gekoppelte Höhenstrahlen”. In: *Naturwissenschaften* 26 (Sept. 1938), pp. 576–576.

[131] P. Auger et al. “Extensive Cosmic-Ray Showers”. In: *Reviews of Modern Physics* 11 (July 1939), pp. 288–291.

[132] and. “The passage of fast electrons and the theory of cosmic showers”. In: *Proceedings of the Royal Society of London A: Mathematical, Physical and Engineering Sciences* 159.898 (1937), pp. 432–458.

[133] Bruno Rossi and Kenneth Greisen. “Cosmic-Ray Theory”. In: *Rev. Mod. Phys.* 13 (4 Oct. 1941), pp. 240–309.

[134] G. Puppi, H.S. Bridge, and K. Greisen. *Progress in Cosmic Ray Physics. Vol. 3. Edited by J.G. Wilson, ... Contributors: K. Greisen, H.S. Bridge, R.W. Thompson, G. Puppi.* North-Holland Publishing C°, 1956.

[135] T.K. Gaisser. *Cosmic Rays and Particle Physics.* Cambridge University Press, 1990.

[136] J. F. Carlson and J. R. Oppenheimer. “On Multiplicative Showers”. In: *Physical Review* 51 (Feb. 1937), pp. 220–231.

[137] A. L. Connolly and A. G. Vieregg. “Radio Detection of High Energy Neutrinos”. In: *ArXiv e-prints* (July 2016).

[138] A. Zuñiga Reyes, A. Hernández Almada, and A. Sandoval Espinosa. “Muon study for gamma/hadron air-shower discrimination in the HAWC observatory”. In: *Journal of Physics Conference Series.* Vol. 876. Journal of Physics Conference Series. July 2017, p. 012023.

[139] A. Borione et al. “High statistics search for ultrahigh energy γ-ray emission from Cygnus X-3 and Hercules X-1”. In: Phys. Rev. D 55 (Feb. 1997), pp. 1714–1731.

[140] Z. Zhang et al. “Study on the performance of electromagnetic particle detectors of LHAASO-KM2A”. In: *Nuclear Instruments and Methods in Physics Research A* 845 (Feb. 2017), pp. 429–433.

[141] F. A. Aharonian and G. Heinzelmann. “The HEGRA Experiment Status and Recent Results”. In: *Nuclear Physics B Proceedings Supplements* 60 (Jan. 1998), pp. 193–198.

[142] M. Amenomori et al. In: ().

[143] R. Atkins et al. “Observation of TeV Gamma Rays from the Crab Nebula with Milagro Using a New Background Rejection Technique”. In: ApJ 595 (Oct. 2003), pp. 803–811.

[144] G. di Sciascio and E. Rossi. “Measurement of the angular resolution of the ARGO-YBJ detector”. In: *International Cosmic Ray Conference* 4 (2008), pp. 123–126.

[145] A. U. Abeysekara et al. “Sensitivity of the high altitude water Cherenkov detector to sources of multi-TeV gamma rays”. In: *Astroparticle Physics* 50 (Dec. 2013), pp. 26–32.

[146] The Pierre Auger Collaboration et al. “The Fluorescence Detector of the Pierre Auger Observatory”. In: *ArXiv e-prints* (July 2009).

[147] D. Morcuende et al. “A Monte Carlo study of the relevance of fluorescence radiation in VHE gamma ray observations with Cherenkov telescopes”. In: *ArXiv e-prints* (Aug. 2017).

[148] R. M. Baltrusaitis et al. “The Utah Fly’s Eye detector”. In: *Nuclear Instruments and Methods in Physics Research A* 240 (Oct. 1985), pp. 410–428.

[149] D. J. Bird et al. “The cosmic-ray energy spectrum observed by the Fly’s Eye”. In: ApJ 424 (Mar. 1994), pp. 491–502.

[150] T. Abu-Zayyad. “The Cosmic Ray Energy Spectrum as measured in Monocular Mode by the High Resolution Fly’s Eye Experiment”. In: *International Cosmic Ray Conference* 3 (Aug. 1999), p. 264.

[151] J. Rosado, F. Blanco, and F. Arqueros. “On the absolute value of the air-fluorescence yield”. In: *Astroparticle Physics* 55 (Mar. 2014), pp. 51–62.

[152] H. Tokuno et al. “New air fluorescence detectors employed in the Telescope Array experiment”. In: *Nuclear Instruments and Methods in Physics Research A* 676 (June 2012), pp. 54–65.

[153] J. L. Contreras et al. “Feasibility of VHE gamma ray detection by an array of imaging atmospheric Cherenkov telescopes using the fluorescence technique”. In: *ArXiv e-prints* (Aug. 2015).

[154] T. K. Gaisser and A. M. Hillas. “Reliability of the method of constant intensity cuts for reconstructing the average development of vertical showers”. In: *International Cosmic Ray Conference* 8 (1977), pp. 353–357.

[155] M. de Naurois and D. Mazin. “Ground-based detectors in very-high-energy gamma-ray astronomy”. In: *Comptes Rendus Physique* 16 (Aug. 2015), pp. 610–627.

[156] J V Jelley. “Cerenkov radiation and its applications”. In: *British Journal of Applied Physics* 6.7 (1955), p. 227.

[157] P. A. Čerenkov. “Visible emission of clean liquids by action of γ radiation”. In: *Doklady Akademii Nauk SSSR* 2 (1934), pp. 451+.

[158] P. A. Čerenkov. “Visible Radiation Produced by Electrons Moving in a Medium with Velocities Exceeding that of Light”. In: *Physical Review* 52 (Aug. 1937), pp. 378–379.

[159] I. M. Frank and I. E. Tamm. “Coherent visible radiation of fast electrons passing through matter”. In: *Compt. Rend. Acad. Sci. URSS* 14.3 (1937), pp. 109–114.

[160] P.M.S. Blackett. “Neue Berufsorganisation für Wissenschaftler”. In: *Physik Journal* 3.10 (1947), pp. 329–331.

[161] W. Galbraith and J. V. Jelley. “Light Pulses from the Night Sky associated with Cosmic Rays”. In: Nature 171 (Feb. 1953), pp. 349–350.

[162] A. Karle et al. “Design and performance of the angle integrating Čerenkov array AIROBICC”. In: *Astroparticle Physics* 3 (Aug. 1995), pp. 321–347.

[163] D. S. Hanna et al. “The STACEE-32 ground based gamma-ray detector”. In: *Nuclear Instruments and Methods in Physics Research A* 491 (Sept. 2002), pp. 126–151.

[164] A. M. Hillas. “Cerenkov light images of EAS produced by primary gamma”. In: *International Cosmic Ray Conference* 3 (Aug. 1985).

[165] T. C. Weekes et al. “Observation of TeV gamma rays from the Crab nebula using the atmospheric Cerenkov imaging technique”. In: ApJ 342 (July 1989), pp. 379–395.

[166] M. Santander. “The Dawn of Multi-Messenger Astronomy”. In: *ArXiv e-prints* (June 2016).

[167] A. De Angelis et al. “The e-ASTROGAM mission. Exploring the extreme Universe with gamma rays in the MeV - GeV range”. In: *Experimental Astronomy* 44 (Oct. 2017), pp. 25–82.

[168] R. Rando. “The all-sky medium energy gamma-ray observatory”. In: *Journal of Instrumentation* 12 (Nov. 2017), p. C11024.

[169] J. Chang et al. “The DArk Matter Particle Explorer mission”. In: *Astroparticle Physics* 95 (Oct. 2017), pp. 6–24.

[170] N. P. Topchiev et al. “GAMMA-400 gamma-ray observatory”. In: *ArXiv e-prints* (July 2015).

[171] A. V. Bakaldin et al. “The high-performance data acquisition system for the GAMMA-400 satellite-borne gamma-ray telescope”. In: *ArXiv e-prints* (July 2017).

[172] M. Fiorini et al. “The ASTRI SST-2M prototype for the next generation of Cherenkov telescopes: a single framework approach from requirement analysis to integration and verification strategy definition”. In: *Modeling, Systems Engineering, and Project Management for Astronomy VI.* Vol. 9150. Proc. SPIE. Aug. 2014, p. 915024.

[173] M. Actis et al. “Design concepts for the Cherenkov Telescope Array CTA: an advanced facility for ground-based high-energy gamma-ray astronomy”. In: *Experimental Astronomy* 32 (Dec. 2011), pp. 193–316.

[174] B. S. Acharya et al. “Introducing the CTA concept”. In: *Astroparticle Physics* 43 (Mar. 2013), pp. 3–18.

[175] T. Cherenkov Telescope Array Consortium et al. “Science with the Cherenkov Telescope Array”. In: *ArXiv e-prints* (Sept. 2017).

[176] K. Bernlöhr. “Simulation of imaging atmospheric Cherenkov telescopes with CORSIKA and sim_ telarray”. In: *Astroparticle Physics* 30 (Oct. 2008), pp. 149–158.

[177] G. W. Clark, G. P. Garmire, and W. L. Kraushaar. “Observation of High-Energy Cosmic Gamma Rays”. In: ApJ 153 (Sept. 1968), p. L203.

[178] S. M. Derdeyn et al. “SAS-B digitized spark chamber gamma ray telescope.” In: *Nuclear Instruments and Methods* 98 (1972), pp. 557–566.

[179] C. E. Fichtel et al. “High-energy gamma-ray results from the second small astronomy satellite”. In: ApJ 198 (May 1975), pp. 163–182.

[180] G. F. Bignami et al. “The COS-B experiment for gamma-ray astronomy”. In: *Space Science Instrumentation* 1 (Aug. 1975), pp. 245–268.

[181] B. N. Swanenburg et al. “Second COS B catalog of high-energy gamma-ray sources”. In: ApJ 243 (Jan. 1981), pp. L69–L73.

[182] W. B. Atwood et al. “The Large Area Telescope on the Fermi Gamma-Ray Space Telescope Mission”. In: ApJ 697 (June 2009), pp. 1071–1102.

[183] D. A. Sanchez and C. Deil. “Enrico : a Python package to simplify Fermi-LAT analysis”. In: *ArXiv e-prints* (July 2013).

[184] F. Acero et al. “Fermi Large Area Telescope Third Source Catalog”. In: ApJS 218, 23 (June 2015), p. 23.

[185] D. Mazin et al. “Upgrade of the MAGIC telescopes”. In: *ArXiv e-prints* (Oct. 2014).

[186] F. Aharonian et al. “Observations of the Crab nebula with HESS”. In: A&A 457 (Oct. 2006), pp. 899–915.

[187] J. Holder et al. “Status of the VERITAS Observatory”. In: *American Institute of Physics Conference Series*. Ed. by F. A. Aharonian, W. Hofmann, and F. Rieger. Vol. 1085. American Institute of Physics Conference Series. Dec. 2008, pp. 657–660.

[188] D. Bastieri et al. “The Mirrors for the MAGIC Telescopes”. In: *International Cosmic Ray Conference* 5 (2005), p. 283.

[189] G. Pareschi et al. “Glass mirrors by cold slumping to cover 100 m^2 of the MAGIC II Cherenkov telescope reflecting surface”. In: *Advanced Optical and Mechanical Technologies in Telescopes and Instrumentation*. Vol. 7018. Proc. SPIE. July 2008, 70180W.

[190] J. Aleksić et al. “The major upgrade of the MAGIC telescopes, Part I: The hardware improvements and the commissioning of the system”. In: *Astroparticle Physics* 72 (Jan. 2016), pp. 61–75.

[191] J. R. García et al. “Status of the new Sum-Trigger system for the MAGIC telescopes”. In: *ArXiv e-prints* (Apr. 2014).

[192] R. López-Coto et al. “The Topo-trigger: a new concept of stereo trigger system for imaging atmospheric Cherenkov telescopes”. In: *Journal of Instrumentation* 11 (Apr. 2016), P04005.

[193] C. Fruck et al. “A novel LIDAR-based Atmospheric Calibration Method for Improving the Data Analysis of MAGIC”. In: *ArXiv e-prints* (Mar. 2014).

[194] Roberta Zanin. “MARS, the MAGIC analysis and reconstruction software”. In: *Proceedings, 33rd International Cosmic Ray Conference (ICRC2013): Rio de Janeiro, Brazil, July 2-9, 2013*, p. 0773.

[195] V. P. Fomin et al. “New methods of atmospheric Cherenkov imaging for gamma-ray astronomy. I. The false source method”. In: *Astroparticle Physics* 2 (May 1994), pp. 137–150.

[196] I. Antcheva et al. “ROOT – A C++ framework for petabyte data storage, statistical analysis and visualization”. In: *Computer Physics Communications* 180 (Dec. 2009), pp. 2499–2512.

[197] R. Mirzoyan. “On the Calibration Accuracy of Light Sensors in Atmospheric Cherenkov Fluorescence and Neutrino Experiments”. In: *International Cosmic Ray Conference* 7 (1997), p. 265.

[198] T. Schweizer et al. “The optical calibration of the MAGIC telescope camera”. In: *IEEE Transactions on Nuclear Science* 49 (Oct. 2002), pp. 2497–2503.

[199] J. Albert et al. “Implementation of the Random Forest method for the Imaging Atmospheric Cherenkov Telescope MAGIC”. In: *Nuclear Instruments and Methods in Physics Research A* 588 (Apr. 2008), pp. 424–432.

[200] D. Heck et al. *CORSIKA: a Monte Carlo code to simulate extensive air showers.* Feb. 1998.

[201] P. Majumdar et al. “Monte Carlo simulation for the MAGIC telescope”. In: *International Cosmic Ray Conference* 5 (2005), p. 203.

[202] E. Carmona et al. “Monte Carlo Simulation for the MAGIC-II System”. In: *International Cosmic Ray Conference* 3 (2008), pp. 1373–1376.

[203] E. Domingo-Santamaria et al. “The DISP analysis method for point-like or extended gamma source searches/studies with the MAGIC Telescope”. In: *International Cosmic Ray Conference* 5 (2005), p. 363.

[204] J. Aleksić et al. “The major upgrade of the MAGIC telescopes, Part II: A performance study using observations of the Crab Nebula”. In: *Astroparticle Physics* 72 (Jan. 2016), pp. 76–94.

[205] Ti-pei Li and Yu-qian Ma. “Analysis methods for results in gamma-ray astronomy”. In: *The Astrophysical Journal* 272 (1983), pp. 317–324.

[206] M. Nievas-Rosillo and J. L. Contreras. “Extending the Li&Ma method to include PSF information”. In: *Astroparticle Physics* 74 (Feb. 2016), pp. 51–57.

[207] W. A. Rolke, A. M. López, and J. Conrad. “Limits and confidence intervals in the presence of nuisance parameters”. In: *Nuclear Instruments and Methods in Physics Research A* 551 (Oct. 2005), pp. 493–503.

[208] E. P. Hubble. “Extragalactic nebulae.” In: ApJ 64 (Dec. 1926).

[209] E. A. Fath. “The Spectra of Some Spiral Nebulæ and Globular Star Clusters”. In: PASP 21 (June 1909), pp. 138–143.

[210] C. K. Seyfert. “Nuclear Emission in Spiral Nebulae.” In: ApJ 97 (Jan. 1943), p. 28.

[211] K. G. Jansky. “Electrical disturbances apparently of extra-terrestrial origin”. In: *Proc. Inst. Radio Engrs., N. Y.* 21 (1933), p. 1387.

[212] G Jansky K. “A note on the source of interstellar interference.” In: *Proc. Inst. Radio Engrs., N. Y.* 23 (1935), p. 1158.

[213] J. S. Hey, S. J. Parsons, and J. W. Phillips. “Fluctuations in Cosmic Radiation at Radio-Frequencies”. In: Nature 158 (Aug. 1946), p. 234.

[214] J. G. Bolton and G. J. Stanley. “The Position and Probable Identification of the Source of the Galactic Radio-Frequency Radiation Taurus-A”. In: *Australian Journal of Scientific Research A Physical Sciences* 2 (June 1949), p. 139.

[215] J. G. Bolton, G. J. Stanley, and O. B. Slee. “Positions of Three Discrete Sources of Galactic Radio-Frequency Radiation”. In: Nature 164 (July 1949), pp. 101–102.

[216] R. Hanbury Brown, R. C. Jennison, and M. K. D. Gupta. “Apparent Angular Sizes of Discrete Radio Sources: Observations at Jodrell Bank, Manchester”. In: Nature 170 (Dec. 1952), pp. 1061–1063.

[217] R. C. Jennison and M. K. Das Gupta. “Fine Structure of the Extra-terrestrial Radio Source Cygnus I”. In: Nature 172 (Nov. 1953), pp. 996–997.

[218] C. Wildy, M. R. Goad, and J. T. Allen. “Quasar broad absorption line variability measurements using reconstructions of unabsorbed spectra”. In: MNRAS 437 (Jan. 2014), pp. 1976–1995.

[219] G. Reber. “Notes: Cosmic Static.” In: ApJ 91 (June 1940), pp. 621–624.

[220] H. Alfvén and N. Herlofson. “Cosmic Radiation and Radio Stars”. In: *Physical Review* 78 (June 1950), pp. 616–616.

[221] K. O. Kiepenheuer. “Cosmic Rays as the Source of General Galactic Radio Emission”. In: *Physical Review* 79 (Aug. 1950), pp. 738–739.

[222] W. L. Ginsburg and H. Vogel. “Der Ursprung der kosmischen Strahlung und die Radioastronomie”. In: *Fortschritte der Physik* 1 (1953), pp. 659–706.

[223] V. L. Ginzburg and S. I. Syrovatskii. “Cosmic Magnetobremsstrahlung (synchrotron Radiation)”. In: ARA&A 3 (1965), p. 297.

[224] D. O. Edge et al. “A survey of radio sources at a frequency of 159 Mc/s.” In: MmRAS 68 (1959), pp. 37–60.

[225] A. S. Bennett. "The preparation of the revised 3C catalogue of radio sources". In: MNRAS 125 (1962), p. 75.

[226] I. F. Zwicky. "Compact Galaxies and Compact Parts of Galaxies." In: ApJ 140 (Nov. 1964), p. 1467.

[227] F. Zwicky. "Compact Galaxies and Compact Parts of Galaxies. II". In: ApJ 143 (Jan. 1966), p. 192.

[228] B. E. Markarian. "Galaxies with an Ultraviolet Continuum". In: *Astrofizika* 3 (1967).

[229] R. Minkowski. "A New Distant Cluster of Galaxies." In: ApJ 132 (Nov. 1960), pp. 908–910.

[230] T. A. Matthews and A. R. Sandage. "Optical Identification of 3C 48, 3C 196, and 3C 286 with Stellar Objects." In: ApJ 138 (July 1963), p. 30.

[231] M. Schmidt. "3C 273 : A Star-Like Object with Large Red-Shift". In: Nature 197 (Mar. 1963), p. 1040.

[232] C. Hazard, M. B. Mackey, and A. J. Shimmins. "Investigation of the Radio Source 3C 273 By The Method of Lunar Occultations". In: Nature 197 (Mar. 1963), pp. 1037–1039.

[233] J. B. Oke. "Absolute Energy Distribution in the Optical Spectrum of 3C 273". In: Nature 197 (Mar. 1963), pp. 1040–1041.

[234] J. L. Greenstein. "Red-Shift of the Unusual Radio Source: 3C 48". In: Nature 197 (Mar. 1963), pp. 1041–1042.

[235] H. J. Smith and D. Hoffleit. "Light Variations in the Superluminous Radio Galaxy 3C273". In: Nature 198 (May 1963), pp. 650–651.

[236] B. J. Robinson, K. J. van Damme, and J. A. Koehler. "21-cm Absorption of the Radiation from 3C273". In: Nature 199 (Sept. 1963), pp. 990–991.

[237] G. R. Burbidge, E. M. Burbidge, and A. R. Sandage. "Evidence for the Occurrence of Violent Events in the Nuclei of Galaxies". In: *Reviews of Modern Physics* 35 (1963), pp. 947–972.

[238] J. L. Greenstein and M. Schmidt. "The Quasi-Stellar Radio Sources 3C 48 and 3C 273." In: ApJ 140 (July 1964), p. 1.

[239] A. Sandage. "The Existence of a Major New Constituent of the Universe: the Quasistellar Galaxies." In: ApJ 141 (May 1965), p. 1560.

[240] A. Sandage and P. Véron. "Photometric Results of a Special Survey for Interlopers." In: ApJ 142 (July 1965), pp. 412–414.

[241] M. Schmidt. "Large Redshifts of Five Quasi-Stellar Sources." In: ApJ 141 (Apr. 1965), p. 1295.

[242] C. R. Lynds and A. N. Stockton. "The Large Redshift of the Quasi-Stellar Source 1116+12". In: ApJ 144 (Apr. 1966), p. 446.

[243] M. Schmidt and E. T. Olsen. "Sectrum of the Large Redshift Quasi-Stellar Source 4c 25.5". In: *The Astronomical Journal Supplement* 73 (Mar. 1968), p. 117.

[244] J. L. Greenstein and M. Schmidt. "The Two Absorption-Line Redshifts in Parkes 0237-23". In: ApJ 148 (Apr. 1967), p. L13.

[245] T. D. Kinman and E. M. Burbidge. "Spectroscopic Observations of Nineteen Quasi-Stellar Radio Sources". In: ApJ 148 (May 1967), p. L59.

[246] C. R. Lynds. "A Quasi-Stellar Source with a Rapidly Expanding Envelope". In: ApJ 147 (Jan. 1967), p. 396.

[247] E. Y. Khachikian and D. W. Weedman. “An atlas of Seyfert galaxies”. In: ApJ 192 (Sept. 1974), pp. 581–589.

[248] L. Woltjer. “Emission Nuclei in Galaxies.” In: ApJ 130 (July 1959), p. 38.

[249] G. R. Burbidge et al. “On the Interpretation of the Line Spectra of Quasi-Stellar Objects”. In: Nature 210 (May 1966), pp. 774–778.

[250] G. A. Shields. “Composition gradients across spiral galaxies”. In: ApJ 193 (Oct. 1974), pp. 335–341.

[251] E. E. Salpeter. “Accretion of Interstellar Matter by Massive Objects.” In: ApJ 140 (Aug. 1964), pp. 796–800.

[252] Y. B. Zel’dovich. “The Fate of a Star and the Evolution of Gravitational Energy upon Accretion”. In: *Dokl. Akad. Nauk SSSR* 155 (1964), p. 67.

[253] D. Lynden-Bell and J. E. Pringle. “The evolution of viscous discs and the origin of the nebular variables.” In: MNRAS 168 (Sept. 1974), pp. 603–637.

[254] D. Lynden-Bell. “Galactic Nuclei as Collapsed Old Quasars”. In: Nature 223 (Aug. 1969), pp. 690–694.

[255] C.M. Harrison. *Observational Constraints on the Influence of Active Galactic Nuclei on the Evolution of Galaxies.* Springer Theses. Springer International Publishing, 2016.

[256] J. B. Oke. “Spectrophotometric Observations of Rapid Variability in 3c 279 and 3c 446”. In: ApJ 147 (Mar. 1967), p. 901.

[257] G. H. Rieke and F. J. Low. “Infrared Photometry of Extragalactic Sources”. In: ApJ 176 (Sept. 1972), p. L95.

[258] G. H. Rieke and F. J. Low. “Variability of Extragalactic Sources at 10 Microns”. In: ApJ 177 (Nov. 1972), p. L115.

[259] G. H. Rieke and F. J. Low. “The nucleus of NGC 253”. In: ApJ 197 (Apr. 1975), pp. 17–23.

[260] N. Visvanathan and J. B. Oke. “Non-Thermal Component in the Continuum of NGC 1068”. In: ApJ 152 (June 1968), p. L165.

[261] I. S. Shklovskii. “Quasistellar Objects and Seyfert Galaxies”. In: Soviet Ast. 9 (Apr. 1966), p. 683.

[262] F. Hoyle. “On the Nature of the Quasi-stellar Sources”. In: Nature 209 (Feb. 1966), pp. 751–753.

[263] L. Woltjer. “Inverse Compton Radiation in Quasi-Stellar Objects”. In: ApJ 146 (Nov. 1966), p. 597.

[264] U. Giveon et al. “Long-term optical variability properties of the Palomar-Green quasars”. In: MNRAS 306 (July 1999), pp. 637–654.

[265] D. Trèvese and F. Vagnetti. “Spectral variability of QSOs in the optical band”. In: Mem. Soc. Astron. Italiana 72 (2001), pp. 33–35.

[266] B. C. Kelly, J. Bechtold, and A. Siemiginowska. “Are the Variations in Quasar Optical Flux Driven by Thermal Fluctuations?” In: ApJ 698, 895-910 (June 2009), pp. 895–910.

[267] A. G. Pacholczyk and W. Z. Wisniewski. “Infrared Radiation from the Seyfert Galaxy NGC 1068”. In: ApJ 147 (Jan. 1967), p. 394.

[268] M. J. Rees et al. “Infrared Radiation from Dust in Seyfert Galaxies”. In: Nature 223 (Aug. 1969), pp. 788–791.

[269] R. A. Edelson. “Far-infrared properties of optically selected quasars”. In: ApJ 309 (Oct. 1986), pp. L69–L72.

[270] W. A. Stein and D. W. Weedman. “The origin of ultraviolet and infrared continuum radiation from Seyfert galaxies”. In: ApJ 205 (Apr. 1976), pp. 44–51.

[271] G. Neugebauer. “Infrared observations of Seyfert galaxies and quasars”. In: Phys. Scr 17 (Mar. 1978), pp. 149–157.

[272] R. A. Edelson, M. A. Malkan, and G. H. Rieke. “Broad-band properties of the CfA Seyfert Galaxies. II - Infrared to millimeter properties”. In: ApJ 321 (Oct. 1987), pp. 233–250.

[273] M. H. Cohen et al. “Radio Interferometry at One-Thousandth Second of Arc”. In: *Science* 162 (Oct. 1968), pp. 88–94.

[274] B. G. Clark et al. “Radio Interferometry Using a Base Line of 20 Million Wavelengths”. In: ApJ 153 (July 1968), p. L67.

[275] M. J. Rees. “Appearance of Relativistically Expanding Radio Sources”. In: Nature 211 (July 1966), pp. 468–470.

[276] C. A. Knight et al. “Quasars: Millisecond-of-Arc Structure Revealed by Very-Long-Baseline Interferometry”. In: *Science* 172 (Apr. 1971), pp. 52–54.

[277] M. H. Cohen et al. “The Small-Scale Structure of Radio Galaxies and Quasi-Stellar Sources at 3.8 Centimeters”. In: ApJ 170 (Dec. 1971), p. 207.

[278] R. D. Blandford and A. Königl. “Relativistic jets as compact radio sources”. In: ApJ 232 (Aug. 1979), pp. 34–48.

[279] B. L. Fanaroff and J. M. Riley. “The morphology of extragalactic radio sources of high and low luminosity”. In: MNRAS 167 (May 1974), 31P–36P.

[280] M. S. Longair. “Evolution of a Radio Source Population”. In: *Nature Physical Science* 232 (July 1971), pp. 59–60.

[281] R. Giacconi et al. “Evidence for x Rays From Sources Outside the Solar System”. In: *Physical Review Letters* 9 (Dec. 1962), pp. 439–443.

[282] W. L. Kraushaar and G. W. Clark. “Search for Primary Cosmic Gamma Rays with the Satellite Explorer XI”. In: *Physical Review Letters* 8 (Feb. 1962), pp. 106–109.

[283] R. J. Gould and G. R. Burbidge. “X-Rays from the Galactic Center, External Galaxies, and the Intergalactic Medium.” In: ApJ 138 (Nov. 1963), p. 969.

[284] H. Friedman, E. T. Byram, and T. A. Chubb. “Distribution and Variability of Cosmic X-Ray Sources”. In: *Science* 156 (Apr. 1967), pp. 374–378.

[285] C. S. Bowyer et al. “Detection of X-Ray Emission from 3c 273 and NGC 5128”. In: ApJ 161 (July 1970), p. L1.

[286] W. Tucker et al. “X-Ray Observations of NGC 5128 (centaurus a) from UHURU”. In: ApJ 180 (Mar. 1973), pp. 715–724.

[287] W. Forman et al. “The fourth Uhuru catalog of X-ray sources.” In: ApJS 38 (Dec. 1978), pp. 357–412.

[288] H. Gursky et al. “Detection of X-Rays from the Seyfert Galaxies NGC 1275 and NGC 4151 by the UHURU Satellite”. In: ApJ 165 (Apr. 1971), p. L43.

[289] H. Tananbaum et al. “UHURU observations of X-ray emission from Seyfert galaxies”. In: ApJ 223 (July 1978), pp. 74–81.

[290] M. Elvis et al. “Seyfert galaxies as X-ray sources”. In: MNRAS 183 (Apr. 1978), pp. 129–157.

[291] R. E. Griffiths et al. “Observations of Type 1 Seyfert galaxies with the HEAO-1 scanning modulation collimator”. In: MNRAS 188 (Sept. 1979), pp. 813–817.

[292] P. J. N. Davison et al. “An increase in the X-ray flux from Centaurus A”. In: ApJ 196 (Feb. 1975), pp. L23–L25.

[293] P. F. Winkler Jr. and A. E. White. “A sudden increase in the X-ray flux from Centaurus A”. In: ApJ 199 (Aug. 1975), pp. L139–L142.

[294] N. Marshall, R. S. Warwick, and K. A. Pounds. “The variability of X-ray emission from active galaxies”. In: MNRAS 194 (Mar. 1981), pp. 987–1002.

[295] H. Tananbaum et al. “X-ray studies of quasars with the Einstein Observatory”. In: ApJ 234 (Nov. 1979), pp. L9–L13.

[296] G. Zamorani et al. “X-ray studies of quasars with the Einstein Observatory. II”. In: ApJ 245 (Apr. 1981), pp. 357–374.

[297] D. M. Worrall et al. “X-ray studies of quasars with the Einstein Observatory. IV - X-ray dependence on radio emission”. In: ApJ 313 (Feb. 1987), pp. 596–606.

[298] K. Nandra. “Reprocessing and the Origin of the Blue Bump in AGN”. In: *Reverberation Mapping of the Broad-Line Region in Active Galactic Nuclei*. Ed. by P. M. Gondhalekar, K. Horne, and B. M. Peterson. Vol. 69. Astronomical Society of the Pacific Conference Series. 1994, p. 273.

[299] A. C. Fabian. “A short introduction to broad and variable iron lines around black holes”. In: *Astronomische Nachrichten* 327 (Dec. 2006), p. 943.

[300] C. D. Dermer and B. Giebels. “Active galactic nuclei at gamma-ray energies”. In: *Comptes Rendus Physique* 17 (June 2016), pp. 594–616.

[301] D. J. Thompson et al. “The Second EGRET Catalog of High-Energy Gamma-Ray Sources”. In: ApJS 101 (Dec. 1995), p. 259.

[302] P. Sreekumar et al. “EGRET Observations of the Extragalactic Gamma-Ray Emission”. In: ApJ 494 (Feb. 1998), pp. 523–534.

[303] F. W. Stecker and M. H. Salamon. “The Gamma-Ray Background from Blazars: A New Look”. In: ApJ 464 (June 1996), p. 600.

[304] G. Ghisellini, L. Maraschi, and A. Treves. “Inhomogeneous synchrotron-self-Compton models and the problem of relativistic beaming of BL Lac objects”. In: A&A 146 (May 1985), pp. 204–212.

[305] S. D. Bloom and A. P. Marscher. “Examining the synchrotron self-Compton model for blazars.” In: *American Institute of Physics Conference Series*. Ed. by M. Friedlander, N. Gehrels, and D. J. Macomb. Vol. 280. American Institute of Physics Conference Series. 1993, pp. 578–582.

[306] M. Sikora, M. C. Begelman, and M. J. Rees. “Comptonization of diffuse ambient radiation by a relativistic jet: The source of gamma rays from blazars?” In: ApJ 421 (Jan. 1994), pp. 153–162.

[307] S. Funk. “The status of gamma-ray astronomy”. In: *ArXiv e-prints* (Apr. 2012).

[308] M. Punch et al. “Detection of TeV photons from the active galaxy Markarian 421”. In: Nature 358 (Aug. 1992), p. 477.

[309] J. Quinn et al. “Detection of Gamma Rays with E > 300 GeV from Markarian 501”. In: ApJ 456 (Jan. 1996), p. L83.

[310] K. I. Kellermann et al. “VLA observations of objects in the Palomar Bright Quasar Survey”. In: AJ 98 (Oct. 1989), pp. 1195–1207.

[311] C. M. Urry and P. Padovani. “Unified Schemes for Radio-Loud Active Galactic Nuclei”. In: PASP 107 (Sept. 1995), p. 803.

[312] J.-H. Woo and C. M. Urry. “Active Galactic Nucleus Black Hole Masses and Bolometric Luminosities”. In: ApJ 579 (Nov. 2002), pp. 530–544.

[313] L. C. Ho. “Nuclear Activity in Nearby Galaxies”. In: ARA&A 46 (Sept. 2008), pp. 475–539.

[314] T. M. Heckman and P. N. Best. “The Coevolution of Galaxies and Supermassive Black Holes: Insights from Surveys of the Contemporary Universe”. In: ARA&A 52 (Aug. 2014), pp. 589–660.

[315] C. Hoffmeister. “354 neue Veränderliche”. In: *Astronomische Nachrichten* 236 (Sept. 1929), p. 233.

[316] J. L. Schmitt. “BL Lac identified as a Radio Source”. In: Nature 218 (May 1968), p. 663.

[317] N. Visvanathan. “The Continuum of BL Lac”. In: ApJ 155 (Mar. 1969), p. L133.

[318] D. G. MacDonell and A. H. Bridle. “Opaque Radio Sources near the Galactic Equator”. In: Nature 227 (Aug. 1970), pp. 582–583.

[319] G. D. Nicolson. “Radio Sources similar to BL Lac”. In: *Nature Physical Science* 233 (Oct. 1971), p. 155.

[320] J. B. Oke and J. E. Gunn. “The Distance of BL Lacertae”. In: ApJ 189 (Apr. 1974), p. L5.

[321] G. M. Blake. “Observations of Extragalactic Radio Sources Having Unusual Spectra”. In: Astrophys. Lett. 6 (July 1970), p. 201.

[322] L. Maraschi, G. Ghisellini, and A. Celotti. “A jet model for the gamma-ray emitting blazar 3C 279”. In: ApJ 397 (Sept. 1992), pp. L5–L9.

[323] F. Melia and A. Konigl. “The radiative deceleration of ultrarelativistic jets in active galactic nuclei”. In: ApJ 340 (May 1989), pp. 162–180.

[324] J. Aleksić et al. “MAGIC Discovery of Very High Energy Emission from the FSRQ PKS 1222+21”. In: ApJ 730, L8 (Mar. 2011), p. L8.

[325] M. L. Ahnen et al. “Detection of very high energy gamma-ray emission from the gravitationally lensed blazar QSO B0218+357 with the MAGIC telescopes”. In: A&A 595, A98 (Nov. 2016), A98.

[326] F. Tavecchio and G. Ghisellini. “Spine-sheath layer radiative interplay in subparsec-scale jets and the TeV emission from M87”. In: MNRAS 385 (Mar. 2008), pp. L98–L102.

[327] A. P. Marscher and W. K. Gear. “Models for high-frequency radio outbursts in extragalactic sources, with application to the early 1983 millimeter-to-infrared flare of 3C 273”. In: ApJ 298 (Nov. 1985), pp. 114–127.

[328] A. Mücke et al. “Monte Carlo simulations of photohadronic processes in astrophysics”. In: *Computer Physics Communications* 124 (Feb. 2000), pp. 290–314.

[329] Y. T. Tanaka, S. Buson, and D. Kocevski. “Fermi-LAT detection of increased gamma-ray activity of TXS 0506+056, located inside the IceCube-170922A error region.” In: *The Astronomer’s Telegram* 10791 (Sept. 2017).

[330] R. Mirzoyan. “First-time detection of VHE gamma rays by MAGIC from a direction consistent with the recent EHE neutrino event IceCube-170922A”. In: *The Astronomer’s Telegram* 10817 (Oct. 2017).

[331] M. Böttcher et al. “Leptonic and Hadronic Modeling of Fermi-detected Blazars”. In: ApJ 768, 54 (May 2013), p. 54.

[332] C. Ramos Almeida and C. Ricci. “Nuclear obscuration in active galactic nuclei”. In: *Nature Astronomy* 1 (Oct. 2017), pp. 679–689.

[333] H. Netzer. “Revisiting the Unified Model of Active Galactic Nuclei”. In: ARA&A 53 (Aug. 2015), pp. 365–408.

[334] E. A. Pier and J. H. Krolik. “Radiation-pressure-supported obscuring tori around active galactic nuclei”. In: ApJ 399 (Nov. 1992), pp. L23–L26.

[335] D. B. Sanders et al. “Continuum energy distribution of quasars - Shapes and origins”. In: ApJ 347 (Dec. 1989), pp. 29–51.

[336] J. H. Krolik and M. C. Begelman. “Molecular tori in Seyfert galaxies - Feeding the monster and hiding it”. In: ApJ 329 (June 1988), pp. 702–711.

[337] C. P. Dullemond and I. M. van Bemmel. “Clumpy tori around active galactic nuclei”. In: A&A 436 (June 2005), pp. 47–56.

[338] R. Antonucci. “Unified models for active galactic nuclei and quasars”. In: ARA&A 31 (1993), pp. 473–521.

[339] C. Urry. “AGN Unification: An Update”. In: *AGN Physics with the Sloan Digital Sky Survey.* Ed. by G. T. Richards and P. B. Hall. Vol. 311. Astronomical Society of the Pacific Conference Series. June 2004, p. 49.

[340] J. S. Miller, R. W. Goodrich, and W. G. Mathews. “Multidirectional views of the active nucleus of NGC 1068”. In: ApJ 378 (Sept. 1991), pp. 47–64.

[341] C. A. Heisler, S. L. Lumsden, and J. A. Bailey. “Visibility of scattered broad-line emission in Seyfert 2 galaxies”. In: Nature 385 (Feb. 1997), pp. 700–702.

[342] G. Fabbiano et al. “The highly obscured nucleus of 3C 219”. In: ApJ 304 (May 1986), pp. L37–L40.

[343] R. W. Pogge. “Extended ionized gas in the Seyfert 2 galaxy NGC 4388”. In: ApJ 332 (Sept. 1988), pp. 702–710.

[344] T. Storchi-Bergmann, A. S. Wilson, and J. A. Baldwin. “The ionization cone, obscured nucleus, and gaseous outflow in NGC 3281 - A prototypical Seyfert 2 galaxy?” In: ApJ 396 (Sept. 1992), pp. 45–61.

[345] H. Spinrad et al. “A third update of the status of the 3CR sources - Further new redshifts and new identifications of distant galaxies”. In: PASP 97 (Oct. 1985), pp. 932–961.

[346] M. Stickel, K. Meisenheimer, and H. Kuehr. “The optical identification status of the 1 Jy radio source catalogue”. In: A&AS 105 (June 1994), pp. 211–234.

[347] S. A. Baum and T. Heckman. “Extended optical line emitting gas in powerful radio galaxies - Statistical properties and physical conditions”. In: ApJ 336 (Jan. 1989), pp. 681–701.

[348] S. di Serego Alighieri et al. “Anisotropic [OIII] emission in radio loud AGN”. In: A&A 328 (Dec. 1997), pp. 510–516.

[349] J. C. Baker. “Origin of the viewing-angle dependence of the optical continuum emission in quasars”. In: MNRAS 286 (Mar. 1997), pp. 23–37.

[350] P. Giommi and P. Padovani. “BL Lac Reunification”. In: MNRAS 268 (May 1994), p. L51.

[351] P. Padovani and P. Giommi. “The connection between x-ray- and radio-selected BL Lacertae objects”. In: ApJ 444 (May 1995), pp. 567–581.

[352] P. Padovani and C. M. Urry. “Fanaroff-Riley I galaxies as the parent population of BL Lacertae objects. I - X-ray constraints”. In: ApJ 356 (June 1990), pp. 75–82.

[353] P. Padovani and C. M. Urry. “Fanaroff-Riley I galaxies as the parent population of BL Lacertae objects. II - Optical constraints”. In: ApJ 368 (Feb. 1991), pp. 373–379.

[354] C. M. Urry, P. Padovani, and M. Stickel. “Fanaroff-Riley I galaxies as the parent populations of BL Lacertae objects. III - Radio constraints”. In: ApJ 382 (Dec. 1991), pp. 501–507.

[355] P. Padovani. “Is there a relationship between BL Lacertae objects and flat-spectrum radio quasars?” In: MNRAS 257 (Aug. 1992), pp. 404–414.

[356] P. Padovani. “A statistical analysis of complete samples of BL Lacertae objects”. In: A&A 256 (Mar. 1992), pp. 399–407.

[357] L. Maraschi and F. Rovetti. “A unified relativistic beaming model for BL Lacertae objects and flat spectrum radio quasars”. In: ApJ 436 (Nov. 1994), pp. 79–88.

[358] R. I. Kollgaard et al. “Radio constraints on the nature of BL Lacertae objects and their parent population”. In: AJ 104 (Nov. 1992), pp. 1687–1705.

[359] R. A. Laing et al. “Spectrophotometry of a Complete Sample of 3CR Radio Sources: Implications for Unified Models”. In: *The Physics of Active Galaxies*. Ed. by G. V. Bicknell, M. A. Dopita, and P. J. Quinn. Vol. 54. Astronomical Society of the Pacific Conference Series. 1994, p. 201.

[360] H. Landt and H. E. Bignall. “On the relationship between BL Lacertae objects and radio galaxies”. In: MNRAS 391 (Dec. 2008), pp. 967–985.

[361] Y.-D. Xu, X. Cao, and Q. Wu. “On the BL Lacertae Objects/Radio Quasars and the FR I/II Dichotomy”. In: ApJ 694 (Apr. 2009), pp. L107–L110.

[362] G. Ghisellini et al. “The Fermi blazar sequence”. In: MNRAS 469 (July 2017), pp. 255–266.

[363] G. Ghisellini et al. “The transition between BL Lac objects and flat spectrum radio quasars”. In: MNRAS 414 (July 2011), pp. 2674–2689.

[364] T. Sbarrato, P. Padovani, and G. Ghisellini. “The jet-disc connection in AGN”. In: MNRAS 445 (Nov. 2014), pp. 81–92.

[365] S. L. Morris et al. “The luminosity function and cosmological evolution of X-ray-selected BL Lacertae objects”. In: ApJ 380 (Oct. 1991), pp. 49–65.

[366] F. Vagnetti, A. Cavaliere, and E. Giallongo. “BL Lacertae objects and radio-loud quasars within an evolutionary unified scheme”. In: ApJ 368 (Feb. 1991), pp. 366–372.

[367] P. Giommi et al. “A simplified view of blazars: clearing the fog around long-standing selection effects”. In: MNRAS 420 (Mar. 2012), pp. 2899–2911.

[368] G. Fossati et al. “A unifying view of the spectral energy distributions of blazars”. In: MNRAS 299 (Sept. 1998), pp. 433–448.

[369] G. Ghisellini et al. “A theoretical unifying scheme for gamma-ray bright blazars”. In: MNRAS 301 (Dec. 1998), pp. 451–468.

[370] S. G. Jorstad et al. “Multiepoch Very Long Baseline Array Observations of EGRET-detected Quasars and BL Lacertae Objects: Superluminal Motion of Gamma-Ray Bright Blazars”. In: ApJS 134 (June 2001), pp. 181–240.

[371] M. L. Lister et al. “MOJAVE. X. Parsec-scale Jet Orientation Variations and Superluminal Motion in Active Galactic Nuclei”. In: AJ 146, 120 (Nov. 2013), p. 120.

[372] G. Ghisellini and F. Tavecchio. “Fermi/LAT broad emission line blazars”. In: MNRAS 448 (Apr. 2015), pp. 1060–1077.

[373] M. Ackermann et al. “The Second Catalog of Active Galactic Nuclei Detected by the Fermi Large Area Telescope”. In: ApJ 743, 171 (Dec. 2011), p. 171.

[374] J. G. Cohen, C. R. Lawrence, and R. D. Blandford. “The Redshift of the Lensed Object in the Einstein Ring B0218+357”. In: ApJ 583 (Jan. 2003), pp. 67–69.

[375] R. Falomo et al. “On the lensed blazar B0218+357”. In: MNRAS 470 (Sept. 2017), pp. 2814–2821.

[376] S. Paiano et al. “On the Redshift of TeV BL Lac Objects”. In: ApJ 837, 144 (Mar. 2017), p. 144.

[377] C. L. Carilli, M. P. Rupen, and B. Yanny. “Neutral hydrogen 21 centimeter absorption at Z = 0.6847 toward the 'smallest Einstein ring'”. In: ApJ 412 (Aug. 1993), pp. L59–L62.

[378] A. D. Biggs et al. “MERLIN/VLA imaging of the gravitational lens system B0218+357”. In: MNRAS 322 (Apr. 2001), pp. 821–826.

[379] C.S. Kochanek, P. Schneider, and J. Wambsganss. “Part 2 of Gravitational Lensing: Strong, Weak & Micro”. In: Proceedings of the 33rd Saas-Fee Advanced Course. Ed. by G. Meylan, P. Jetzer, and P. North. Berlin, Germany: Springer-Verlag, 2004.

[380] C. S. Kochanek et al. “Turning AGN Microlensing from a Curiosity into a Tool”. In: *Statistical Challenges in Modern Astronomy IV*. Ed. by G. J. Babu and E. D. Feigelson. Vol. 371. Astronomical Society of the Pacific Conference Series. Nov. 2007, p. 43.

[381] C. P. O'Dea et al. “Radio and optical observations of 0218+357 - The smallest Einstein ring?” In: AJ 104 (Oct. 1992), pp. 1320–1330.

[382] E. A. Corbett et al. “Radio Measurement of the Time Delay in 0218+357”. In: *Astrophysical Applications of Gravitational Lensing*. Ed. by C. S. Kochanek and J. N. Hewitt. Vol. 173. IAU Symposium. 1996, p. 37.

[383] A. D. Biggs et al. “Time delay for the gravitational lens system B0218+357”. In: MNRAS 304 (Apr. 1999), pp. 349–358.

[384] A. S. Cohen et al. “Further Investigation of the Time Delay, Magnification Ratios, and Variability in the Gravitational Lens 0218+357”. In: ApJ 545 (Dec. 2000), pp. 578–590.

[385] E. Eulaers and P. Magain. “Time delays for eleven gravitationally lensed quasars revisited”. In: A&A 536, A44 (Dec. 2011), A44.

[386] R. Mittal et al. “VLBI phase-reference observations of the gravitational lens JVAS B0218+357”. In: A&A 447 (Feb. 2006), pp. 515–524.

[387] R. Mittal, R. Porcas, and O. Wucknitz. “Free-free absorption in the gravitational lens JVAS B0218+357”. In: A&A 465 (Apr. 2007), pp. 405–415.

[388] E. E. Falco et al. “Dust and Extinction Curves in Galaxies with z>0: The Interstellar Medium of Gravitational Lens Galaxies”. In: ApJ 523 (Oct. 1999), pp. 617–632.

[389] C. C. Cheung et al. “Fermi Large Area Telescope Detection of Gravitational Lens Delayed γ-Ray Flares from Blazar B0218+357”. In: ApJ 782, L14 (Feb. 2014), p. L14.

[390] I. Vovk and A. Neronov. “Microlensing constraints on the size of the gamma-ray emission region in blazar B0218+357”. In: A&A 586, A150 (Feb. 2016), A150.

[391] J. Sitarek and W. Bednarek. “Variability of GeV gamma-ray emission in QSO B0218+357 due to microlensing on intermediate size structures”. In: MNRAS 459 (June 2016), pp. 1959–1967.

[392] C. Spingola et al. “Radio follow-up of the γ-ray flaring gravitational lens JVAS B0218+357”. In: MNRAS 457 (Apr. 2016), pp. 2263–2271.

[393] R. Mirzoyan. “Discovery of Very High Energy Gamma-Ray Emission From Gravitationally Lensed Blazar S3 0218+357 With the MAGIC Telescopes”. In: *The Astronomer's Telegram* 6349 (July 2014).

[394] M. L. Ahnen et al. “Performance of the MAGIC telescopes under moonlight”. In: *ArXiv e-prints* (Apr. 2017).

[395] A. R. Patnaik et al. “Interferometer phase calibration sources. I - The region 35-75 deg”. In: MNRAS 254 (Feb. 1992), pp. 655–676.

[396] J. R. Mattox et al. “The Likelihood Analysis of EGRET Data”. In: ApJ 461 (Apr. 1996), p. 396.

[397] D. N. Burrows et al. “The Swift X-Ray Telescope”. In: Space Sci. Rev. 120 (Oct. 2005), pp. 165–195.

[398] P. M. W. Kalberla et al. “The Leiden/Argentine/Bonn (LAB) Survey of Galactic HI. Final data release of the combined LDS and IAR surveys with improved stray-radiation corrections”. In: A&A 440 (Sept. 2005), pp. 775–782.

[399] P. W. A. Roming et al. “The Swift Ultra-Violet/Optical Telescope”. In: Space Sci. Rev. 120 (Oct. 2005), pp. 95–142.

[400] K. Nilsson et al. “Host galaxy subtraction of TeV candidate BL Lacertae objects”. In: A&A 475 (Nov. 2007), pp. 199–207.

[401] E. F. Schlafly and D. P. Finkbeiner. “Measuring Reddening with Sloan Digital Sky Survey Stellar Spectra and Recalibrating SFD”. In: ApJ 737, 103 (Aug. 2011), p. 103.

[402] A. Barnacka et al. “The Structure of the Strongly Lensed Gamma-Ray Source B2 0218+35”. In: ApJ 821, 58 (Apr. 2016), p. 58.

[403] T. York et al. “The Hubble constant from the gravitational lens CLASS B0218+357 using the Advanced Camera for Surveys”. In: MNRAS 357 (Feb. 2005), pp. 124–134.

[404] A. Neronov, I. Vovk, and D. Malyshev. “Central engine of a gamma-ray blazar resolved through the magnifying glass of gravitational microlensing”. In: *Nature Physics* 11 (Aug. 2015), pp. 664–667.

[405] K. M. Menten and M. J. Reid. “Formaldehyde Absorption at z=0.685 toward the ”Einstein Ring” B0218+357”. In: ApJ 465 (July 1996), p. L99.

[406] I. Sushch and M. Böttcher. “Probing cluster environments of blazars through $\gamma\gamma$ absorption”. In: A&A 573, A47 (Jan. 2015), A47.

[407] A. Barnacka, M. Böttcher, and I. Sushch. “How Gravitational Lensing Helps γ-Ray Photons Avoid γ - γ Absorption”. In: ApJ 790, 147 (Aug. 2014), p. 147.

[408] T.-P. Li and Y.-Q. Ma. “Analysis methods for results in gamma-ray astronomy”. In: ApJ 272 (Sept. 1983), pp. 317–324.

[409] A. Domínguez et al. “Extragalactic background light inferred from AEGIS galaxy-SED-type fractions”. In: MNRAS 410 (Feb. 2011), pp. 2556–2578.

[410] M. Bertero. “Linear inverse and ill-posed problems”. In: ed. by P. W. Hawkes. Vol. 75. Academic Press, New York, 1989, pp. 1–120.

[411] J. Albert et al. “Unfolding of differential energy spectra in the MAGIC experiment”. In: *Nuclear Instruments and Methods in Physics Research A* 583 (Dec. 2007), pp. 494–506.

[412] D. Donato, C. C. Cheung, and S. Ciprini. “Swift XRT/UVOT follow-up of the gravitationally lensed blazar S3 0218+35 after a gamma-ray flare”. In: *The Astronomer’s Telegram* 4351 (Sept. 2012).

[413] J. Lehár et al. “Hubble Space Telescope Observations of 10 Two-Image Gravitational Lenses”. In: ApJ 536 (June 2000), pp. 584–605.

[414] M. Xue et al. “A Precise Determination of the Mid-infrared Interstellar Extinction Law Based on the APOGEE Spectroscopic Survey”. In: ApJS 224, 23 (June 2016), p. 23.

[415] J. Aleksić et al. “MAGIC gamma-ray and multi-frequency observations of flat spectrum radio quasar PKS 1510-089 in early 2012”. In: A&A 569, A46 (Sept. 2014), A46.

[416] L. Pacciani et al. “Exploring the Blazar Zone in High-energy Flares of FSRQs”. In: ApJ 790, 45 (Aug. 2014), p. 45.

[417] F. Tavecchio and G. Ghisellini. “On the spine-layer scenario for the very high-energy emission of NGC 1275”. In: MNRAS 443 (Sept. 2014), pp. 1224–1230.

[418] M. Sikora. “High-energy radiation from active galactic nuclei”. In: ApJS 90 (Feb. 1994), pp. 923–928.

[419] F. Tavecchio et al. “On the origin of the γ-ray emission from the flaring blazar PKS 1222+216”. In: A&A 534, A86 (Oct. 2011), A86.

[420] G. Ghisellini et al. “General physical properties of bright Fermi blazars”. In: MNRAS 402 (Feb. 2010), pp. 497–518.

[421] G. Ghisellini and F. Tavecchio. “Canonical high-power blazars”. In: MNRAS 397 (Aug. 2009), pp. 985–1002.

[422] L. Sironi, M. Petropoulou, and D. Giannios. “Relativistic jets shine through shocks or magnetic reconnection?” In: MNRAS 450 (June 2015), pp. 183–191.

[423] E. Dwek and J. Slavin. “On the determination of the cosmic infrared background radiation from the high-energy spectrum of extragalactic gamma-ray sources”. In: ApJ 436 (Dec. 1994), pp. 696–704.

[424] D. Mazin and M. Raue. “New limits on the density of the extragalactic background light in the optical to the far infrared from the spectra of all known TeV blazars”. In: A&A 471 (Aug. 2007), pp. 439–452.

[425] M. Ackermann et al. “The Imprint of the Extragalactic Background Light in the Gamma-Ray Spectra of Blazars”. In: *Science* 338 (Nov. 2012), p. 1190.

[426] M. L. Ahnen et al. “Very High Energy γ-Rays from the Universe’s Middle Age: Detection of the z = 0.940 Blazar PKS 1441+25 with MAGIC”. In: ApJ 815, L23 (Dec. 2015), p. L23.

[427] A. U. Abeysekara et al. “Gamma-Rays from the Quasar PKS 1441+25: Story of an Escape”. In: ApJ 815, L22 (Dec. 2015), p. L22.

[428] A. Abramowski et al. “Measurement of the extragalactic background light imprint on the spectra of the brightest blazars observed with H.E.S.S.” In: A&A 550, A4 (Feb. 2013), A4.

[429] M. Ackermann et al. “In-flight measurement of the absolute energy scale of the Fermi Large Area Telescope”. In: *Astroparticle Physics* 35 (Jan. 2012), pp. 346–353.

[430] M. L. Ahnen et al. “MAGIC observations of the February 2014 flare of 1ES 1011+496 and ensuing constraint of the EBL density”. In: A&A 590, A24 (May 2016), A24.

[431] A. Franceschini, G. Rodighiero, and M. Vaccari. “Extragalactic optical-infrared background radiation, its time evolution and the cosmic photon-photon opacity”. In: A&A 487 (Sept. 2008), pp. 837–852.

[432] J. D. Finke, S. Razzaque, and C. D. Dermer. “Modeling the Extragalactic Background Light from Stars and Dust”. In: ApJ 712 (Mar. 2010), pp. 238–249.

[433] R. C. Gilmore et al. “Semi-analytic modelling of the extragalactic background light and consequences for extragalactic gamma-ray spectra”. In: MNRAS 422 (June 2012), pp. 3189–3207.

[434] Y. Inoue et al. “Extragalactic Background Light from Hierarchical Galaxy Formation: Gamma-Ray Attenuation up to the Epoch of Cosmic Reionization and the First Stars”. In: ApJ 768, 197 (May 2013), p. 197.

[435] E. B. Fomalont et al. “The Second VLBA Calibrator Survey: VCS2”. In: AJ 126 (Nov. 2003), pp. 2562–2566.

[436] A. A. Abdo et al. “Fermi Large Area Telescope First Source Catalog”. In: ApJS 188 (June 2010), pp. 405–436.

[437] P. L. Nolan et al. “Fermi Large Area Telescope Second Source Catalog”. In: ApJS 199, 31 (Apr. 2012), p. 31.

[438] M. Ackermann et al. “The First Fermi-LAT Catalog of Sources above 10 GeV”. In: ApJS 209, 34 (Dec. 2013), p. 34.

[439] M. S. Shaw et al. “Spectroscopy of Broad-line Blazars from 1LAC”. In: ApJ 748, 49 (Mar. 2012), p. 49.

[440] R. Ojha. “Fermi LAT Detection of a Bright GeV Flare from the FSRQ PKS 1441+25”. In: *The Astronomer’s Telegram* 6878 (Jan. 2015).

[441] L. Carrasco et al. “NIR Photometry of the FRQS PKD1441+25”. In: *The Astronomer’s Telegram* 6895 (Jan. 2015).

[442] T. Pursimo and R. Ojha. “Optical Activity of the Flaring Gamma-ray Blazar PKS 1441+25”. In: *The Astronomer’s Telegram* 6923 (Jan. 2015).

[443] L. Pacciani. “Optical, X-, Gamma-ray flare of the FSRQ PKS 1441+25”. In: *The Astronomer’s Telegram* 7402 (Apr. 2015).

[444] R. Mirzoyan. “Discovery of Very High Energy Gamma-Ray Emission from the distant FSRQ PKS 1441+25 with the MAGIC telescopes”. In: *The Astronomer’s Telegram* 7416 (Apr. 2015).

[445] R. Mukherjee. “Very-high-energy gamma-ray emission from PKS 1441+25 detected with VERITAS”. In: *The Astronomer’s Telegram* 7433 (Apr. 2015).

[446] Roberta Zanin. “MARS, the MAGIC analysis and reconstruction software”. In: *Proceedings, 33rd International Cosmic Ray Conference (ICRC2013): Rio de Janeiro, Brazil, July 2-9, 2013*, p. 0773.

[447] F. A. Harrison et al. “The Nuclear Spectroscopic Telescope Array (NuSTAR) High-energy X-Ray Mission”. In: ApJ 770, 103 (June 2013), p. 103.

[448] M. Perri, S. Puccetti, N Spagnuolo, et al. *The NuSTAR Data Analysis Software Guide*. 2014.

[449] N. Gehrels et al. “The Swift Gamma-Ray Burst Mission”. In: ApJ 611 (Aug. 2004), pp. 1005–1020.

[450] G. V. Schultz and W. Wiemer. “Interstellar reddening and IR-excess of O and B stars”. In: A&A 43 (Sept. 1975), pp. 133–139.

[451] P. S. Smith and D. T. Ozdarcan. “High Optical Polarization Detected in PKS 1441+25”. In: *The Astronomer’s Telegram* 7417 (Apr. 2015).

[452] A. A. Abdo et al. “A change in the optical polarization associated with a γ-ray flare in the blazar 3C279”. In: Nature 463 (Feb. 2010), pp. 919–923.

[453] S. Kiehlmann et al. “Polarization angle swings in blazars: The case of <ASTROBJ>3C 279</ASTROBJ>”. In: A&A 590, A10 (May 2016), A10.

[454] H. Zhang, M. Boettcher, and H. Li. “Constraining blazar physics with polarization signatures”. In: *American Astronomical Society Meeting Abstracts*. Vol. 227. American Astronomical Society Meeting Abstracts. Jan. 2016, p. 318.01.

[455] G. D. Schmidt, H. S. Stockman, and P. S. Smith. “Discovery of a sub-megagauss magnetic white dwarf through spectropolarimetry”. In: ApJ 398 (Oct. 1992), pp. L57–L60.

[456] I. A. Steele et al. “The Liverpool Telescope: performance and first results”. In: *Ground-based Telescopes*. Ed. by J. M. Oschmann Jr. Vol. 5489. Proc. SPIE. Oct. 2004, pp. 679–692.

[457] J. Masegosa et al. “Guaranteed Time Programs with the ALFOSC”. In: *The NOT in the 2000’s*. Ed. by N. Bergvall, L. O. Takalo, and V. Piirola. 2000, p. 112.

[458] M. F. Skrutskie et al. “The Two Micron All Sky Survey (2MASS)”. In: AJ 131 (Feb. 2006), pp. 1163–1183.

[459] H. Teraesranta et al. “Fifteen years monitoring of extragalactic radio sources at 22, 37 and 87 GHz”. In: A&AS 132 (Nov. 1998), pp. 305–331.

[460] J. L. Richards et al. “Blazars in the Fermi Era: The OVRO 40 m Telescope Monitoring Program”. In: ApJS 194, 29 (June 2011), p. 29.

[461] M. Wood et al. “Dark Matter Searches with the Fermi-LAT in the Direction of Dwarf Spheroidals”. In: *ArXiv e-prints* (July 2015).

[462] P. S. Smith et al. “Coordinated Fermi/Optical Monitoring of Blazars and the Great 2009 September Gamma-ray Flare of 3C 454.3”. In: *ArXiv e-prints* (Dec. 2009).

[463] B. M. Peterson. “Variability of Active Galactic Nuclei”. In: *Advanced Lectures on the Starburst-AGN*. Ed. by I. Aretxaga, D. Kunth, and R. Mújica. 2001, p. 3.

[464] E. Angelakis et al. “RoboPol: the optical polarization of gamma-ray-loud and gamma-ray-quiet blazars”. In: MNRAS 463 (Dec. 2016), pp. 3365–3380.

[465] H. Zhang et al. “Polarization Swings Reveal Magnetic Energy Dissipation in Blazars”. In: ApJ 804, 58 (May 2015), p. 58.

[466] G. Ghisellini et al. “The red blazar PMN J2345-1555 becomes blue”. In: MNRAS 432 (May 2013), pp. 66–70.

[467] G. Ghisellini, L. Maraschi, and F. Tavecchio. “The Fermi blazars’ divide”. In: MNRAS 396 (June 2009), pp. L105–L109.

[468] R. J. Protheroe and P. L. Biermann. “Photon-photon absorption above a molecular cloud torus in blazars”. In: *Astroparticle Physics* 6 (Mar. 1997), pp. 293–300.

[469] A.-C. Donea and R. J. Protheroe. “Radiation fields of disk, BLR and torus in quasars and blazars: implications for /γ-ray absorption”. In: *Astroparticle Physics* 18 (Jan. 2003), pp. 377–393.

[470] H. T. Liu and J. M. Bai. “Absorption of 10-200 GeV Gamma Rays by Radiation from Broad-Line Regions in Blazars”. In: ApJ 653 (Dec. 2006), pp. 1089–1097.

[471] L. Maraschi and F. Tavecchio. “The Jet-Disk Connection and Blazar Unification”. In: ApJ 593 (Aug. 2003), pp. 667–675.

[472] G. R. Blumenthal and R. J. Gould. “Bremsstrahlung, Synchrotron Radiation, and Compton Scattering of High-Energy Electrons Traversing Dilute Gases”. In: *Reviews of Modern Physics* 42 (1970), pp. 237–271.

[473] A. A. Zdziarski and J. H. Krolik. “Compton scattering and the gamma-ray power-law spectrum in Markarian 421”. In: ApJ 409 (June 1993), pp. L33–L36.

[474] R. Moderski et al. “Klein-Nishina effects in the spectra of non-thermal sources immersed in external radiation fields”. In: MNRAS 363 (Nov. 2005), pp. 954–966.

[475] J. D. Finke. “Compton Dominance and the Blazar Sequence”. In: ApJ 763, 134 (Feb. 2013), p. 134.

[476] S. T. Scully, M. A. Malkan, and F. W. Stecker. “An Empirical Determination of the Intergalactic Background Light Using Near-infrared Deep Galaxy Survey Data out to 5 μm and the Gamma-Ray Opacity of the Universe”. In: ApJ 784, 138 (Apr. 2014), p. 138.

[477] A. A. Abdo et al. “Fermi Large Area Telescope Constraints on the Gamma-ray Opacity of the Universe”. In: ApJ 723 (Nov. 2010), pp. 1082–1096.

[478] J. Aleksić et al. “MAGIC long-term study of the distant TeV blazar PKS 1424+240 in a multiwavelength context”. In: A&A 567, A135 (July 2014), A135.

[479] C. Fanti et al. “The B2 catalogue of radio sources - fourth part.” In: A&AS 18 (1974), pp. 147–156.

[480] C. D. Impey and S. Tapia. “New blazars discovered by polarimetry”. In: ApJ 333 (Oct. 1988), pp. 666–672.

[481] P. Majumdar. “Observations of selected IBLs and LBLs with VERITAS”. In: *International Cosmic Ray Conference* 8 (2011), p. 43.

[482] S. Archambault et al. “Deep Broadband Observations of the Distant Gamma-Ray Blazar PKS 1424+240”. In: ApJ 785, L16 (Apr. 2014), p. L16.

[483] A. Celotti, A. C. Fabian, and M. J. Rees. “Limits from rapid TeV variability of MRK 421”. In: MNRAS 293 (Jan. 1998), p. 239.

[484] V. S. Paliya et al. “The Violent Hard X-Ray Variability of Mrk 421 Observed by NuSTAR in 2013 April”. In: ApJ 811, 143 (Oct. 2015), p. 143.

[485] I. Vovk and A. Neronov. “Variability of Gamma-Ray Emission from Blazars on Black Hole Timescales”. In: ApJ 767, 103 (Apr. 2013), p. 103.

[486] D. Giannios, D. A. Uzdensky, and M. C. Begelman. “Fast TeV variability in blazars: jets in a jet”. In: MNRAS 395 (May 2009), pp. L29–L33.

[487] E. Aliu et al. “Very high energy outburst of Markarian 501 in May 2009”. In: A&A 594, A76 (Oct. 2016), A76.

[488] MAGIC Collaboration et al. “The detection of the blazar S4 0954+65 at very-high-energy with the MAGIC telescopes during an exceptionally high optical state”. In: *ArXiv e-prints* (Jan. 2018).

[489] L. Costamante. “Blazar Properties:. AN Update from Recent Results”. In: *International Journal of Modern Physics D* 18 (2009), pp. 1483–1488.

[490] A. Rau et al. “BL Lacertae objects beyond redshift 1.3 - UV-to-NIR photometry and photometric redshift for Fermi/LAT blazars”. In: A&A 538, A26 (Feb. 2012), A26.

[491] J. Yang and J. Wang. “Redshifts of Distant Blazars Limited by Fermi and VHE γ-Ray Observations”. In: PASJ 62 (Aug. 2010), pp. L23–L26.

[492] A. Furniss et al. “The Solid Redshift Lower Limit of the Most Distant TeV-Emitting Blazar PKS 1424+240”. In: *AAS/High Energy Astrophysics Division*. Vol. 13. AAS/High Energy Astrophysics Division. Apr. 2013, p. 101.09.

[493] E. Prandini et al. “Blazars distance indications from Fermi and TeV data”. In: *ArXiv e-prints* (Jan. 2011).

[494] A. C. Rovero et al. “The BL-Lacertae gamma-ray blazar PKS 1424+240 associated with a group of galaxies at z = 0.6010”. In: A&A 589, A92 (May 2016), A92.

[495] M. Meyer and D. Horns. “Impact of oscillations of photons into axion-like particles on the very-high energy gamma-ray spectrum of the blazar PKS1424+240”. In: *ArXiv e-prints* (Oct. 2013).

[496] A. A. Abdo et al. “Fermi Observations of TeV-Selected Active Galactic Nuclei”. In: ApJ 707 (Dec. 2009), pp. 1310–1333.

[497] V. A. Acciari et al. “Discovery of Very High Energy Gamma Rays from PKS 1424+240 and Multiwavelength Constraints on Its Redshift”. In: ApJ 708 (Jan. 2010), pp. L100–L106.

[498] J. Aleksić et al. “Performance of the MAGIC stereo system obtained with Crab Nebula data”. In: *Astroparticle Physics* 35 (Feb. 2012), pp. 435–448.

[499] R. Willingale et al. “Calibration of X-ray absorption in our Galaxy”. In: MNRAS 431 (May 2013), pp. 394–404.

[500] A. C. Fabian et al. “PMN J0525-3343: soft X-ray spectral flattening in a blazar at z=4.4”. In: MNRAS 323 (May 2001), pp. 373–379.

[501] J. Aleksić et al. “Mrk 421 active state in 2008: the MAGIC view, simultaneous multi-wavelength observations and SSC model constrained”. In: A&A 542, A100 (June 2012), A100.

[502] M. Cerruti et al. “A hadronic origin for ultra-high-frequency-peaked BL Lac objects”. In: MNRAS 448 (Mar. 2015), pp. 910–927.

[503] W. Essey and A. Kusenko. “Understanding the spectrum of a distant blazar PKS 1424 + 240 and its implications”. In: *Astroparticle Physics* 57 (May 2014), pp. 30–32.

[504] Lab Saha and Pijushpani Bhattacharjee. “Constraints on the synchrotron self-Compton mechanism of TeV gamma ray emission from the Milagro TeV source MGRO J2019+37 within the pulsar wind nebula scenario”. In: *Journal of High Energy Astrophysics* 5-6 (2015), pp. 9–14.

[505] G. Ghisellini, F. Tavecchio, and M. Chiaberge. “Structured jets in TeV BL Lac objects and radiogalaxies. Implications for the observed properties”. In: A&A 432 (Mar. 2005), pp. 401–410.

[506] D. J. Fixsen and E. Dwek. “The Zodiacal Emission Spectrum as Determined by COBE and Its Implications”. In: ApJ 578 (Oct. 2002), pp. 1009–1014.

[507] A. Cooray. “Extragalactic background light measurements and applications”. In: *Royal Society Open Science* 3 (Mar. 2016), p. 150555.

[508] Y. Matsuoka et al. “Cosmic Optical Background: The View from Pioneer 10/11”. In: ApJ 736, 119 (Aug. 2011), p. 119.

[509] M. G. Hauser et al. “The COBE Diffuse Infrared Background Experiment Search for the Cosmic Infrared Background. I. Limits and Detections”. In: ApJ 508 (Nov. 1998), pp. 25–43.

[510] D. J. Fixsen et al. “The Spectrum of the Extragalactic Far-Infrared Background from the COBE FIRAS Observations”. In: ApJ 508 (Nov. 1998), pp. 123–128.

[511] D. S. Y. Mak et al. “Measurement of CIB power spectra over large sky areas from Planck HFI maps”. In: MNRAS 466 (Apr. 2017), pp. 286–319.

[512] K. Mattila. “Has the Optical Extragalactic Background Light Been Detected?” In: ApJ 591 (July 2003), pp. 119–124.

[513] E. L. Wright. “DIRBE minus 2MASS: Confirming the Cosmic Infrared Background at 2.2 Microns”. In: ApJ 553 (June 2001), pp. 538–544.

[514] L. Cambrésy et al. “The Cosmic Infrared Background at 1.25 and 2.2 Microns Using DIRBE and 2MASS: A Contribution Not Due to Galaxies?” In: ApJ 555 (July 2001), pp. 563–571.

[515] L. R. Levenson, E. L. Wright, and B. D. Johnson. “DIRBE Minus 2MASS: Confirming the CIRB in 40 New Regions at 2.2 and 3.5 μm”. In: ApJ 666 (Sept. 2007), pp. 34–44.

[516] L. R. Levenson and E. L. Wright. “Probing the 3.6 μm CIRB with Spitzer in Three DIRBE Dark Spots”. In: ApJ 683, 585-596 (Aug. 2008), pp. 585–596.

[517] R. A. Bernstein. "The Optical Extragalactic Background Light: Revisions and Further Comments". In: ApJ 666 (Sept. 2007), pp. 663–673.

[518] R. A. Bernstein, W. L. Freedman, and B. F. Madore. "The First Detections of the Extragalactic Background Light at 3000, 5500, and 8000 Å. I. Results". In: ApJ 571 (May 2002), pp. 56–84.

[519] R. A. Bernstein, W. L. Freedman, and B. F. Madore. "The First Detections of the Extragalactic Background Light at 3000, 5500, and 8000 Å. II. Measurement of Foreground Zodiacal Light". In: ApJ 571 (May 2002), pp. 85–106.

[520] R. A. Bernstein, W. L. Freedman, and B. F. Madore. "The First Detections of the Extragalactic Background Light at 3000, 5500, and 8000 Å. III. Cosmological Implications". In: ApJ 571 (May 2002), pp. 107–128.

[521] K. Mattila. "The 1-μm discontinuity in the extragalactic background light spectrum: an artefact of foreground subtraction". In: MNRAS 372 (Nov. 2006), pp. 1253–1258.

[522] R. A. Bernstein, W. L. Freedman, and B. F. Madore. "Corrections of Errors in "The First Detections of the Extragalactic Background Light at 3000, 5500, and 8000 Å. I, II, and III" (ApJ, 571; 56, 85, 107 [2002])". In: ApJ 632 (Oct. 2005), pp. 713–717.

[523] J. M. Hahn et al. "Clementine Observations of the Zodiacal Light and the Dust Content of the Inner Solar System". In: Icarus 158 (Aug. 2002), pp. 360–378.

[524] E. Grün et al. *Interplanetary Dust*. 2001.

[525] D. Hoffleit. *Catalogue of bright stars*. 1964.

[526] E. Høg et al. "The Tycho-2 catalogue of the 2.5 million brightest stars". In: A&A 355 (Mar. 2000), pp. L27–L30.

[527] B. M. Lasker et al. "The Second-Generation Guide Star Catalog: Description and Properties". In: AJ 136 (Aug. 2008), pp. 735–766.

[528] L. Girardi et al. "Star counts in the Galaxy. Simulating from very deep to very shallow photometric surveys with the TRILEGAL code". In: A&A 436 (June 2005), pp. 895–915.

[529] D. J. Schlegel, D. P. Finkbeiner, and M. Davis. "Maps of Dust Infrared Emission for Use in Estimation of Reddening and Cosmic Microwave Background Radiation Foregrounds". In: ApJ 500 (June 1998), pp. 525–553.

[530] G. Lagache et al. "Evidence for dust emission in the Warm Ionised Medium sing WHAM data". In: A&A 354 (Feb. 2000), pp. 247–252.

[531] P. Madau and L. Pozzetti. "Deep galaxy counts, extragalactic background light and the stellar baryon budget". In: MNRAS 312 (Feb. 2000), pp. L9–L15.

[532] M. Zemcov et al. "Measurement of the cosmic optical background using the long range reconnaissance imager on New Horizons". In: *Nature Communications* 8, 15003 (Apr. 2017), p. 15003.

[533] M. Zemcov et al. "On the origin of near-infrared extragalactic background light anisotropy". In: *Science* 346 (Nov. 2014), pp. 732–735.

[534] K. Mattila et al. "Extragalactic Background Light: a measurement at 400 nm using dark cloud shadow I. Low surface brightness spectrophotometry in the area of Lynds 1642". In: *ArXiv e-prints* (May 2017).

[535] K. Mattila et al. "Extragalactic background Light: a measurement at 400 nm using dark cloud shadow II. Spectroscopic separation of dark cloud's light, and results". In: *ArXiv e-prints* (May 2017).

[536] K. Mattila. "On the measurement of the extragalactic background brightness at 4000 A". In: A&A 47 (Feb. 1976), pp. 77–95.

[537] G. G. Fazio et al. “Number Counts at 3 um < lambda < 10 um from the Spitzer Space Telescope”. In: ApJS 154 (Sept. 2004), pp. 39–43.

[538] R. C. Keenan et al. “The Resolved Near-infrared Extragalactic Background”. In: ApJ 723 (Nov. 2010), pp. 40–46.

[539] S. P. Driver et al. “Measurements of Extragalactic Background Light from the Far UV to the Far IR from Deep Ground- and Space-based Galaxy Counts”. In: ApJ 827, 108 (Aug. 2016), p. 108.

[540] M. Béthermin et al. “HerMES: deep number counts at 250 μm, 350 μm and 500 μm in the COSMOS and GOODS-N fields and the build-up of the cosmic infrared background”. In: A&A 542, A58 (June 2012), A58.

[541] M. Béthermin et al. “A Unified Empirical Model for Infrared Galaxy Counts Based on the Observed Physical Evolution of Distant Galaxies”. In: ApJ 757, L23 (Oct. 2012), p. L23.

[542] B. Magnelli et al. “The deepest Herschel-PACS far-infrared survey: number counts and infrared luminosity functions from combined PEP/GOODS-H observations”. In: A&A 553, A132 (May 2013), A132.

[543] J. L. Wardlow et al. “HerMES: Candidate Gravitationally Lensed Galaxies and Lensing Statistics at Submillimeter Wavelengths”. In: ApJ 762, 59 (Jan. 2013), p. 59.

[544] A. Cooray and R. Sheth. “Halo models of large scale structure”. In: Phys. Rep. 372 (Dec. 2002), pp. 1–129.

[545] A.I. Nikishov. “Absorption of High Energy Photons in the Universe”. In: *Zhur. Eksptl’. i Teoret. Fiz.* Vol: 41 (Aug. 1961).

[546] R. J. Gould and G. P. Schréder. “Opacity of the Universe to High-Energy Photons”. In: *Physical Review* 155 (Mar. 1967), pp. 1408–1411.

[547] R. J. Gould and G. P. Schréder. “Pair Production in Photon-Photon Collisions”. In: *Physical Review* 155 (Mar. 1967), pp. 1404–1407.

[548] J. Biteau and D. A. Williams. “The Extragalactic Background Light, the Hubble Constant, and Anomalies: Conclusions from 20 Years of TeV Gamma-ray Observations”. In: ApJ 812, 60 (Oct. 2015), p. 60.

[549] J. Albert et al. “Very-High-Energy gamma rays from a Distant Quasar: How Transparent Is the Universe?” In: *Science* 320 (June 2008), p. 1752.

[550] F. Tavecchio and D. Mazin. “Intrinsic absorption in 3C 279 at GeV-TeV energies and consequences for estimates of the extragalactic background light”. In: MNRAS 392 (Jan. 2009), pp. L40–L44.

[551] M. Lorentz, P. Brun, and D. Sanchez. “Update on the determination of the extragalactic background light spectral energy distribution with H.E.S.S.” In: *34th International Cosmic Ray Conference (ICRC2015).* Vol. 34. International Cosmic Ray Conference. July 2015, p. 777.

[552] J. R. Primack et al. “Probing galaxy formation with TeV gamma ray absorption”. In: *Astroparticle Physics* 11 (June 1999), pp. 93–102.

[553] R. S. Somerville et al. “Galaxy properties from the ultraviolet to the far-infrared: Lambda cold dark matter models confront observations”. In: MNRAS 423 (July 2012), pp. 1992–2015.

[554] M. A. Malkan and F. W. Stecker. “An Empirically Based Calculation of the Extragalactic Infrared Background”. In: ApJ 496 (Mar. 1998), pp. 13–16.

[555] F. W. Stecker, M. A. Malkan, and S. T. Scully. “Intergalactic Photon Spectra from the Far-IR to the UV Lyman Limit for 0<z<6 and the Optical Depth of the Universe to High-Energy Gamma Rays”. In: ApJ 648 (Sept. 2006), pp. 774–783.

[556] F. W. Stecker, M. A. Malkan, and S. T. Scully. "Erratum: "Intergalactic Photon Spectra from the Far-IR to the UV Lyman Limit for 0<z <6 and the Optical Depth of the Universe to High-Energy Gamma Rays"". In: ApJ 658 (Apr. 2007), pp. 1392–1392.

[557] P. Madau, L. Pozzetti, and M. Dickinson. "The Star Formation History of Field Galaxies". In: ApJ 498 (May 1998), pp. 106–116.

[558] Y. C. Pei, S. M. Fall, and M. G. Hauser. "Cosmic Histories of Stars, Gas, Heavy Elements, and Dust in Galaxies". In: ApJ 522 (Sept. 1999), pp. 604–626.

[559] A. Franceschini et al. "A long-wavelength view on galaxy evolution from deep surveys by the Infrared Space Observatory". In: A&A 378 (Oct. 2001), pp. 1–29.

[560] T. M. Kneiske, K. Mannheim, and D. H. Hartmann. "Implications of cosmological gamma-ray absorption. I. Evolution of the metagalactic radiation field". In: A&A 386 (Apr. 2002), pp. 1–11.

[561] T. M. Kneiske and H. Dole. "A lower-limit flux for the extragalactic background light". In: A&A 515, A19 (June 2010), A19.

[562] S. Razzaque, C. D. Dermer, and J. D. Finke. "The Stellar Contribution to the Extragalactic Background Light and Absorption of High-Energy Gamma Rays". In: ApJ 697 (May 2009), pp. 483–492.

[563] M. Cirasuolo et al. "A new measurement of the evolving near-infrared galaxy luminosity function out to z ˜= 4: a continuing challenge to theoretical models of galaxy formation". In: MNRAS 401 (Jan. 2010), pp. 1166–1176.

[564] G. Bruzual and S. Charlot. "Stellar population synthesis at the resolution of 2003". In: MNRAS 344 (Oct. 2003), pp. 1000–1028.

[565] Matthias Lorentz, Pierre Brun, and David Sanchez. "Update on the determination of the extragalactic background light spectral energy distribution with H.E.S.S." In: *PoS* ICRC2015 (2016), p. 777.

[566] W. A. Rolke and A. M. López. "Confidence intervals and upper bounds for small signals in the presence of background noise". In: *Nuclear Instruments and Methods in Physics Research A* 458 (Feb. 2001), pp. 745–758.

[567] A. Desai et al. "Probing the EBL Evolution at High Redshift Using GRBs Detected with the Fermi-LAT". In: ApJ 850, 73 (Nov. 2017), p. 73.

[568] D. Horns and M. Meyer. "Indications for a pair-production anomaly from the propagation of VHE gamma-rays". In: J. Cosmology Astropart. Phys. 2, 033 (Feb. 2012), p. 033.

[569] P. Madau and M. Dickinson. "Cosmic Star-Formation History". In: ARA&A 52 (Aug. 2014), pp. 415–486.

[570] E. Pueschel. "The Extragalactic Background Light: Constraints from TeV Blazar Observations". In: *35th International Cosmic Ray Conference (ICRC2017)*. Vol. 35. International Cosmic Ray Conference. Oct. 2017.

[571] H. Abdalla et al. "Measurement of the EBL spectral energy distribution using the VHE γ-ray spectra of H.E.S.S. blazars". In: A&A 606, A59 (Oct. 2017), A59.

[572] D. Mazin et al. "Potential of EBL and cosmology studies with the Cherenkov Telescope Array". In: *Astroparticle Physics* 43 (Mar. 2013), pp. 241–251.

[573] T. Hassan et al. "Extragalactic source population studies at very high energies in the Cherenkov Telescope Array era". In: *ArXiv e-prints* (Aug. 2017).

[574] M. Kerr. "Likelihood methods for the detection and characterization of gamma-ray pulsars with the Fermi large area telescope". PhD thesis. University of Washington, 2010.

[575] S. Klepser. “A generalized likelihood ratio test statistic for Cherenkov telescope data”. In: *Astroparticle Physics* 36 (Aug. 2012), pp. 64–76.

[576] H. Dickinson and J. Conrad. “Handling systematic uncertainties and combined source analyses for Atmospheric Cherenkov Telescopes”. In: *Astroparticle Physics* 41 (Jan. 2013), pp. 17–30.

[577] G. Spengler. “Significance in gamma ray astronomy with systematic errors”. In: *Astroparticle Physics* 67 (July 2015), pp. 70–74.

[578] S. Klepser, J. Krause, and J. Sitarek. “Application of a generalized likelihood ratio test statistic to MAGIC data”. In: *American Institute of Physics Conference Series*. Ed. by F. A. Aharonian, W. Hofmann, and F. M. Rieger. Vol. 1505. American Institute of Physics Conference Series. Dec. 2012, pp. 713–716.

[579] J. Aleksić et al. “Optimized dark matter searches in deep observations of Segue 1 with MAGIC”. In: J. Cosmology Astropart. Phys. 2, 008 (Feb. 2014), p. 008.

[580] Jelena Aleksić. “Optimized Dark Matter Searches in Deep Observations of Segue 1 with MAGIC”. PhD thesis. Barcelona: IFAE/Universitat Autònoma de Barcelona, May 2013.

[581] T. Bretz et al. “Comparison of On-Off and Wobble mode observations for MAGIC”. In: *International Cosmic Ray Conference* 4 (2005), p. 311.

[582] S. S. Wilks. “The Large-Sample Distribution of the Likelihood Ratio for Testing Composite Hypotheses”. In: *Annals Math. Statist.* 9.1 (1938), pp. 60–62.

[583] David L. Wallace. “Bounds on Normal Approximations to Student’s and the Chi-Square Distributions”. In: *The Annals of Mathematical Statistics* 30:4 (1959), pp. 1121–1130.

[584] D. Berge, S. Funk, and J. Hinton. “Background modelling in very-high-energy γ-ray astronomy”. In: A&A 466 (May 2007), pp. 1219–1229.

[585] P. Da Vela et al. “Study of the IACT angular acceptance and Point Spread Function”. In: *Astroparticle Physics* 98 (Mar. 2018), pp. 1–8.

[586] M. G. F. Kirsch et al. “XMM-Newton (cross)-calibration”. In: *UV and Gamma-Ray Space Telescope Systems*. Ed. by G. Hasinger and M. J. L. Turner. Vol. 5488. Proc. SPIE. Oct. 2004, pp. 103–114.

[587] F. James and M. Roos. “Minuit - a system for function minimization and analysis of the parameter errors and correlations”. In: *Computer Physics Communications* 10 (Dec. 1975), pp. 343–367.

[588] F. Aharonian et al. “New constraints on the mid-IR EBL from the HESS discovery of VHE γ-rays from 1ES 0229+200”. In: A&A 475 (Nov. 2007), pp. L9–L13.

[589] J. Albert et al. “Discovery of Very High Energy γ-Rays from 1ES 1011+496 at z = 0.212”. In: ApJ 667 (Sept. 2007), pp. L21–L24.

[590] J. Aleksić et al. “Discovery of very high energy gamma-ray emission from the blazar 1ES 1727+502 with the MAGIC Telescopes”. In: A&A 563, A90 (Mar. 2014), A90.

[591] L. S. Mao. “2MASS observation of BL Lac objects II”. In: New A 16 (Dec. 2011), pp. 503–529.

[592] E. Aliu et al. “Multiwavelength Observations and Modeling of 1ES 1959+650 in a Low Flux State”. In: ApJ 775, 3 (Sept. 2013), p. 3.

[593] A. Biland and R. Mirzoyan. “FACT and MAGIC measure an increased gamma-ray flux from the HBL 1ES 1959+650”. In: *The Astronomer’s Telegram* 9203 (July 2016).

[594] A. Biland. “FACT measures new maximum flux from the HBL 1ES 1959+650 at TeV energies”. In: *The Astronomer’s Telegram* 9239 (July 2016).

[595] Y. I. Neshpor et al. "BL Lac: A New Ultrahigh-Energy Gamma-Ray Source". In: *Astronomy Reports* 45 (Apr. 2001), pp. 249–254.

[596] R. Mirzoyan. "MAGIC detects an increased activity from BL Lacertae at very high energy gamma-rays". In: *The Astronomer's Telegram* 7660 (June 2015).

[597] J. Cortina and J. Holder. "MAGIC and VERITAS detect an unprecedented flaring activity from Mrk 421 in very high energy gamma-rays". In: *The Astronomer's Telegram* 4976 (Apr. 2013).

[598] J. A. Gaidos et al. "Extremely rapid bursts of TeV photons from the active galaxy Markarian 421". In: Nature 383 (Sept. 1996), pp. 319–320.

[599] A. Mastichiadis, M. Petropoulou, and S. Dimitrakoudis. "Mrk 421 as a case study for TeV and X-ray variability in leptohadronic models". In: MNRAS 434 (Sept. 2013), pp. 2684–2695.

[600] J. Kakuwa et al. "Synchrotron self-Compton emission by relativistic electrons under stochastic acceleration: application to Mrk 421 and Mrk 501". In: MNRAS 449 (May 2015), pp. 551–558.

[601] A. Marinelli, B. Patricelli, and N. Fraija. "Hadronic flares and associated neutrinos for Markarian 421". In: *Extragalactic Jets from Every Angle*. Ed. by F. Massaro et al. Vol. 313. IAU Symposium. Mar. 2015, pp. 177–178.

[602] Q. Zhu et al. "Testing one-zone synchrotron-self-Compton models with spectral energy distributions of Mrk 421". In: MNRAS 463 (Dec. 2016), pp. 4481–4489.

[603] K. K. Singh et al. "A time dependent approach to model X-ray and γ-ray light curves of Mrk 421 observed during the flare in February 2010". In: New A 54 (July 2017), pp. 24–29.

[604] M. Błażejowski et al. "A Multiwavelength View of the TeV Blazar Markarian 421: Correlated Variability, Flaring, and Spectral Evolution". In: ApJ 630 (Sept. 2005), pp. 130–141.

[605] G. Fossati et al. "Multiwavelength Observations of Markarian 421 in 2001 March: An Unprecedented View on the X-Ray/TeV Correlated Variability". In: ApJ 677, 906-925 (Apr. 2008), pp. 906–925.

[606] D. Horan et al. "Multiwavelength Observations of Markarian 421 in 2005-2006". In: ApJ 695 (Apr. 2009), pp. 596–618.

[607] J. Aleksić et al. "The 2009 multiwavelength campaign on Mrk 421: Variability and correlation studies". In: A&A 576, A126 (Apr. 2015), A126.

[608] H. Z. Li et al. "Multiband Variability Analysis of Mrk 421". In: PASP 128.7 (July 2016), p. 074101.

[609] M. L. Ahnen et al. "Long-term multi-wavelength variability and correlation study of Markarian 421 from 2007 to 2009". In: A&A 593, A91 (Sept. 2016), A91.

[610] S. Sahu, L. S. Miranda, and S. Rajpoot. "Multi-TeV flaring from blazars: Markarian 421 as a case study". In: *European Physical Journal C* 76, 127 (Mar. 2016), p. 127.

[611] R. F. Green, M. Schmidt, and J. Liebert. "The Palomar-Green catalog of ultraviolet-excess stellar objects". In: ApJS 61 (June 1986), pp. 305–352.

[612] F. Aharonian et al. "Evidence for VHE γ-ray emission from the distant BL Lac PG 1553+113". In: A&A 448 (Mar. 2006), pp. L19–L23.

[613] J. Albert et al. "Detection of Very High Energy Radiation from the BL Lacertae Object PG 1553+113 with the MAGIC Telescope". In: ApJ 654 (Jan. 2007), pp. L119–L122.

[614] M. Ackermann et al. "Multiwavelength Evidence for Quasi-periodic Modulation in the Gamma-Ray Blazar PG 1553+113". In: ApJ 813, L41 (Nov. 2015), p. L41.

[615] E. Sobacchi, M. C. Sormani, and A. Stamerra. “A model for periodic blazars”. In: MNRAS 465 (Feb. 2017), pp. 161–172.

[616] J. Aleksić et al. “PG 1553+113: Five Years of Observations with MAGIC”. In: ApJ 748, 46 (Mar. 2012), p. 46.

[617] E. Aliu et al. “VERITAS Observations of the BL Lac Object PG 1553+113”. In: ApJ 799, 7 (Jan. 2015), p. 7.

[618] A. Abramowski et al. “The 2012 Flare of PG 1553+113 Seen with H.E.S.S. and Fermi-LAT”. In: ApJ 802, 65 (Mar. 2015), p. 65.

[619] J. K. Adelman-McCarthy et al. “VizieR Online Data Catalog: The SDSS Photometric Catalog, Release 7 (Adelman-McCarthy+, 2009)”. In: *VizieR Online Data Catalog* 2294 (June 2009).

[620] A. Neronov, D. Semikoz, and I. Vovk. “Discovery of VHE gamma-ray emission from 4C +21.35 with Fermi”. In: *The Astronomer’s Telegram* 2617 (May 2010).

[621] M. Mose Mariotti. “MAGIC detects a VHE flare from 4C +21.35 (PKS 1222+21)”. In: *The Astronomer’s Telegram* 2684 (June 2010).

[622] R. A. Ong. “Discovery of VHE Gamma-Ray Emission from the Fermi-LAT Source PKS 1424+240”. In: *The Astronomer’s Telegram* 2084 (June 2009).

[623] Wystan Benbow. “VHE Blazar Discoveries with VERITAS”. In: *ArXiv e-prints* (Sept. 2011).

[624] A. Abramowski et al. “H.E.S.S. discovery of VHE γ-rays from the quasar PKS 1510-089”. In: A&A 554, A107 (June 2013), A107.

[625] G. Paturel et al. “Comparison LEDA/SIMBAD octobre 2002. Catalogue to be published in 2003.” In: *LEDA, 0 (2002)* (2002).

[626] Y. T. Tanaka et al. “Fermi Large Area Telescope Detection of Bright γ-Ray Outbursts from the Peculiar Quasar 4C +21.35”. In: ApJ 733, 19 (May 2011), p. 19.

[627] R. Mirzoyan. “ATel 7542: MAGIC detects an increased activity from PKS 1510-089 at very high energy gamma-rays”. In: *The Astronomer’s Telegram* 7542 (May 2015).

[628] M. L. Ahnen et al. “Multiwavelength observations of a VHE gamma-ray flare from PKS 1510-089 in 2015”. In: *ArXiv e-prints* (Oct. 2016).

[629] M. De Naurois. “Increased VHE activity from PKS 1510-089 detected with H.E.S.S.” In: *The Astronomer’s Telegram* 9102 (May 2016).

[630] R. Mirzoyan. “Title: MAGIC detects exceptionally high activity from PKS 1510-089 at very high energy gamma-rays”. In: *The Astronomer’s Telegram* 9105 (June 2016).

[631] H. Mühlig. “Morozov, V. A., Methods for Solving Incorrectly Posed Problems. Berlin-Heidelberg-New York-Tokyo, Springer-Verlag 1984. XVIII, 257 S., 5 Abb., DM 118,—. ISBN 3-540-96059-7 — Translation from the Russian”. In: *Zeitschrift Angewandte Mathematik und Mechanik* 66 (1986), pp. 316–316.

[632] A. N. Tihonov. “On the solution of ill-posed problems and the method of regularization”. In: *Dokl. Akad. Nauk SSSR* 151 (1963), pp. 501–504.

[633] A. N. Tihonov. “On the regularization of ill-posed problems”. In: *Dokl. Akad. Nauk SSSR* 153 (1963), pp. 49–52.

[634] J. Honerkamp and J. Weese. “Tikhonovs regularization method for ill-posed problems”. In: *Continuum Mechanics and Thermodynamics* 2 (Mar. 1990), pp. 17–30.

[635] H. Akaike. “A New Look at the Statistical Model Identification”. In: *IEEE Transactions on Automatic Control* 19 (1974), pp. 716–723.

[636] S. Kullback and R. A. Leibler. “On Information and Sufficiency”. In: *Ann. Math. Statist.* 22.1 (Mar. 1951), pp. 79–86.

[637] Gideon Schwarz. “Estimating the Dimension of a Model”. In: *Ann. Statist.* 6.2 (Mar. 1978), pp. 461–464.

[638] A. R. Liddle. “Information criteria for astrophysical model selection”. In: MNRAS 377 (May 2007), pp. L74–L78.

[639] Ken-Ichi Kamo, Hirokazu Yanagihara, and Kenichi Satoh. “Bias-Corrected AIC for Selecting Variables in Poisson Regression Models”. In: *Communications in Statistics - Theory and Methods* 42.11 (2013), pp. 1911–1921.

[640] Kenneth P. Burnham, David R. Anderson, and Gary C. White. “Evaluation of the Kullback-Leibler Discrepancy for Model Selection in Open Population Capture-Recapture Models”. In: *Biometrical Journal* 36.3 (1994), pp. 299–315.